



Helena Cristina Lopes Rocha

Smart Composite Parts with Multifunctional
Properties Ready to Fly

Universidade do Minho
Escola de Engenharia





Universidade do Minho
Escola de Engenharia

Helena Cristina Lopes Rocha

Smart Composite Parts with Multifunctional
Properties Ready to Fly

Tese de Doutoramento
Programa Doutoral em Ciências e Engenharia de
Polímeros e Compósitos

Trabalho realizado sob a orientação de
Professor Doutor João Pedro Lourenço Gil Nunes
Doutor Ugo Lafont

Janeiro de 2023

DIREITOS DE AUTOR E CONDIÇÕES DE UTILIZAÇÃO DO TRABALHO POR TERCEIROS

Este é um trabalho académico que pode ser utilizado por terceiros desde que respeitadas as regras e boas práticas internacionalmente aceites, no que concerne aos direitos de autor e direitos conexos.

Assim, o presente trabalho pode ser utilizado nos termos previstos na licença abaixo indicada.

Caso o utilizador necessite de permissão para poder fazer um uso do trabalho em condições não previstas no licenciamento indicado, deverá contactar o autor, através do RepositóriUM da Universidade do Minho.

Licença concedida aos utilizadores deste trabalho



**Atribuição
CC BY**

<https://creativecommons.org/licenses/by/4.0/>

Acknowledgments

This thesis was only possible with the support of various people and institutions, to whom I would like to express my sincerest appreciation.

First and foremost, I am deeply grateful to my supervisors, Professor João Pedro Nunes and Dr. Ugo Lafont, for their continuous support, guidance, and patience throughout the last years.

I would like to express my sincere gratitude and honor to have been supervised by Dr. Christopher Semprimoschnig. His technical knowledge and guidance during the first years of my PhD studies will always be dearly remembered.

I would like to extend my gratitude to the Institute for Polymers and Composites (IPC) – University of Minho, PIEP – Innovation in Polymer Engineering and the European Space Agency (ESA) for the opportunity to conduct my research and studies at their facilities.

I would like to express my appreciation for the support provided by the Stratosphere company. I am grateful to Christophe Fernandes and Nelson Ferreira for their technical support.

To everyone in PIEP and, in particular to Paulo, Mimoso, Rafael, Joana, Andreia, Rosa, Miguel and Ângelo, I would like to thank their friendship and useful discussions.

I would like to express my appreciation to my office and department colleagues Luís, Raquel, Joana, Filipa, Ângela, Alexandra, Cláudia, Andreia and Daniela for the friendship.

I would like to express my sincere thanks to everyone that somehow contributed to my work and pleasant stay at the European Space Research and Technology Centre (ESTEC). I would like to offer my special thanks to Ugo, Riccardo, Ana, Gabor, Shumit, Neil, Prema, Graham, Kristien, Laurence, Kenneth, Ricardo, Bruno and Nuno. Thanks to all of you this was really a wonderful time.

I am deeply grateful to Eng. Pedro Vieira and Sr. Joaquim Jorge, from Amtrol-Alfa, for their availability and support to conduct the pressure tests.

I would like to thank ESA for the grant number 4000123315/18/NL/MH/mg, under the Networking/Partnering Initiative (NPI) program, the European Regional Development Fund for the grant number NORTE-01-0145-FEDER-000015 and the European Union's Portugal 2020 program for the founding of ACE project, that allowed me to conduct this dissertation.

My sincerest gratitude goes to my parents and sister for all the support and unconditional love.

To Pedro, I will forever thank his understanding, patience, support, encouragement and love at all times.

STATEMENT OF INTEGRITY

I hereby declare having conducted this academic work with integrity. I confirm that I have not used plagiarism or any form of undue use of information or falsification of results along the process leading to its elaboration.

I further declare that I have fully acknowledged the Code of Ethical Conduct of the University of Minho.

Resumo

A utilização de compósitos poliméricos, em aplicações estruturais avançadas nas indústrias aeroespacial e aeronáutica, sofreu um forte aumento nas últimas décadas. Estes materiais têm substituído os metais, com o objetivo de aumentar as propriedades mecânicas a uma baixa massa e, conseqüentemente, reduzir o consumo de combustível, emissões de CO₂ e custos. Comparativamente aos metais, que geralmente falham devido a fadiga, a falha de materiais compósitos é ainda difícil de prever. Assim, as estruturas de compósito requerem o uso de fatores de segurança elevados, para obedecer às exigentes regras de segurança destas indústrias avançadas, o que dificulta o alcance do objetivo final de redução de massa. A monitorização da integridade das estruturas (SHM) é considerada uma abordagem válida para superar estes desafios, mas também para otimizar as operações de manutenção, em vez de seguir um cronograma predefinido de manutenções.

Este trabalho estudou duas metodologias de SHM diferentes para detetar e localizar danos em compósitos poliméricos reforçados com fibra de carbono (CFRP). O trabalho inicial avaliou o uso de (1) sensores óticos de rede de Bragg (FBG) para monitorização do processamento e deteção de dano de impacto pouco visível (BVID) e a (2) capacidade de *self-sensing* dos CFRP para detetar BVID através de tomografia por impedância elétrica (EIT). Estes estudos foram conduzidos a nível laboratorial, em pequenas amostras de teste.

A um segundo nível, este trabalho implementou um sistema SHM numa peça real de engenharia, um reservatório de pressão com invólucro compósito (COPV) para armazenamento de hidrogénio. Dada a maior maturidade e precisão dos sensores FBG, esta tecnologia foi escolhida para monitorizar a peça selecionada. Esta capacidade foi demonstrada pela monitorização dos processos de enrolamento e cura, de testes de impacto para demonstrar a deteção e localização de BVID e de testes de pressão cíclica, que se assemelham a ciclos de carga e descarga de combustível. Esta tese reporta também o desenvolvimento do COPV, a sua modelação por elementos finitos (FEM), fabricação e testes de rutura para validação da análise FEM.

Palavras-chave: Dano de impacto pouco visível; Monitorização da Integridade Estrutural; Reservatório de Pressão com Invólucro Compósito; Sensor de rede de Bragg; Tomografia por Impedância Elétrica.

Abstract

Polymer composites have had increased usage in the last few decades in highly advanced structural applications in aircraft and aerospace industries. These materials have been successfully used to replace metals, aiming to increase the mechanical properties at decreased weight and consequently, also reduce fuel consumption, CO₂ emissions and costs. The failure mechanisms of composite materials are not yet as predictable as for isotropic materials, such as metals, which usually fail due to fatigue cracking. Thus, composite structures require the use of much higher safety factors, to accomplish the exigent safety rules of such advanced industries, which contradicts the ultimate purpose of using composites to reduce weight. Structural Health Monitoring (SHM) is considered a valid solution to overcome such challenges, but also to optimize maintenance operations as needed, instead of following a predefined maintenance schedule.

This work studied two different SHM methodologies to detect and locate damage on Carbon Fibre Reinforced Polymer (CFRP) composites. The initial work assessed the use of (1) optical fibre Bragg grating (FBG) sensors for processing monitoring and Barely Visible Impact Damage (BVID) detection and (2) the self-sensing capability of CFRP composites to detect BVID through the Electrical Impedance Tomography (EIT) technique. These studies were conducted at laboratory level on small coupon test specimens.

At a second level, this work implemented a SHM system on a real-life engineering part, a Composite Overwrapped Pressure Vessel (COPV) for hydrogen storage to be used in a fuel-cell system for an Unmanned Aerial Vehicle (UAV). Given the higher maturity and accuracy of FBG sensors over self-sensing EIT, FBG sensors technology was chosen to monitor the full life cycle of the selected part. This capability was demonstrated by monitoring the winding and curing processes, through drop-weight impact testing to demonstrate the capability of BVID detection and localisation, and through pressure cycling testing to resemble the real-life operational charge and discharging cycles of a COPV. This thesis also reports the development of the COPV through Finite Element Modelling (FEM) analysis, its manufacturing process and burst pressure testing for FEM analysis validation.

Key words: Barely Visible Impact Damage; Composite Overwrapped Pressure Vessel; Electrical Impedance Tomography; Fibre Bragg Grating sensors; Structural Health Monitoring.

List of Contents

Acknowledgments	iii
Resumo	v
Abstract	vi
List of Acronyms	xii
List of Figures	xiv
List of Tables	xxii
1. Introduction	1
1.1. Motivation	1
1.2. Thesis Outline and Methodology	2
2. State of the Art	4
2.1. Introduction.....	4
2.2. Impact Damage on Composite Materials.....	4
2.3. Structural Health Monitoring of Composite Materials	7
2.3.1. Sensors for Structural Health Monitoring	8
2.3.1.1. Fibre Optic Sensors.....	9
2.3.1.2. Piezoelectric Sensors	17
2.3.1.3. Piezo-resistive sensors and Self-monitoring Composites	25
2.3.2. In-situ Process Monitoring.....	32
2.3.2.1. Cure Monitoring	33
2.3.2.2. Mould filling in Liquid Composite Moulding Processes.....	37

2.4.	Composite Overwrapped Pressure Vessels	40
2.4.1.	Introduction	40
2.4.2.	Manufacturing of Composite Overwrapped Pressure Vessels.....	42
2.4.3.	Instrumentation of Composite Overwrapped Pressure Vessels	46
2.5.	Outlook and trade-off	48
2.6.	Objectives	50
3.	Theoretical Background.....	51
3.1.	Introduction.....	51
3.2.	Optical Fibres	51
3.3.	Electrical Impedance Tomography for Damage Localisation Monitoring.....	51
3.4.	Design of Composite Overwrapped Pressure Vessels.....	53
3.4.1.	Netting Theory	54
3.4.2.	Finite Element Modelling.....	55
3.4.3.	<i>Autofrettage</i>	59
4.	Materials and Experimental Procedures	60
4.1.	Introduction.....	60
4.2.	Materials.....	60
4.2.1.	Raw Materials.....	60
4.2.2.	Optical Fibres	61
4.3.	Experimental Procedures.....	62
4.3.1.	Production of CFRP Laminates by Vacuum Assisted Resin Infusion	62
4.3.1.1.	Embedding Optical FGB Sensors into CFRP Laminates	63
4.3.1.2.	Preparation of CFRP Laminates for Electrical Impedance Tomography	65
4.3.2.	Analysis of the Curing Reaction	67
4.3.2.1.	Differential Scanning Calorimetry Analysis	67
4.3.2.2.	Cure Analysis Using Optical FBG Sensors	69

4.3.3.	Damage Production and Detection	70
4.3.3.1.	Low Velocity Impact Testing	70
4.3.3.1.1.	Impact Damage Monitoring Using Optical FBG Sensors	71
4.3.3.1.2.	Impact Damage Monitoring using Electrical Impedance Tomography.....	72
4.3.3.2.	Through-thickness holes damage for Detection by Electrical Impedance Tomography.....	72
4.3.4.	Non-Destructive Ultrasonic Inspections.....	72
4.3.4.1.	Impact specimens with Optical FBG Sensors	72
4.3.4.2.	Impact Specimens used in Electrical Impedance Tomography Studies	73
4.3.5.	Development of a Smart Composite Overwrapped Pressure Vessel	73
4.3.5.1.	Design of the Composite Overwrapped Pressure Vessel	74
4.3.5.1.1.	Raw Materials Characterization.....	74
	Production of Composite Specimens	74
	Production of Aluminium Specimens.....	76
	Tensile Testing.....	77
	Compression Testing	78
	Density Measurements	78
4.3.5.1.2.	Finite Element Modelling	78
4.3.5.1.3.	Winding Patterns	79
4.3.5.2.	Production of the Smart Composite Overwrapped Pressure Vessels	80
4.3.5.2.1.	Liner	80
4.3.5.2.2.	Embedment of Optical FBG Sensors for Process and Structural Health Monitoring	81
4.3.5.2.3.	Tape Winding Process	85
4.3.5.2.4.	Curing.....	86
4.3.5.2.5.	Autofrettage	87
4.3.5.3.	Testing of the Composite Overwrapped Pressure Vessel.....	87
4.3.5.3.1.	Burst Pressure Testing	87

4.3.5.3.2.	Cyclic Pressure Testing	87
4.3.5.3.3.	Impact Testing and Damage Localisation	88
5.	Results and Discussion	91
5.1.	Introduction.....	91
5.2.	Embedded FBG Sensors for Cure and Impact Damage Monitoring.....	92
5.2.1.	Curing Studies.....	92
5.2.1.1.	Resin Curing kinetics.....	92
5.2.1.2.	Epoxy Infusion and Cure Monitoring using Optical FBG Sensors	95
5.2.1.3.	CFRP Cure Monitoring using Optical FBG Sensors	98
5.2.1.4.	Residual Strains measured by Optical FBG Sensors	102
5.2.2.	Low Velocity Impact Studies.....	104
5.2.2.1.	Selection of Impact Energies for Production of Barely Visible Impact Damage	104
5.2.2.2.	Low Velocity Impact Monitoring in CFRP Laminates with Embedded FBG Sensors	106
5.2.2.3.	Influence of Optical Fibre diameter on Low Velocity Impact Resistance.....	114
5.3.	Electrical Impedance Tomography for Damage Localisation.....	116
5.3.1.	Detection and Localisation of Through-thickness Holes	116
5.3.2.	Detection and Localisation of Impact Damage	118
5.4.	Smart Composite Overwrapped Pressure Vessel	124
5.4.1.	Development of the Composite Overwrapped Pressure Vessel.....	124
5.4.1.1.	Raw Materials Properties.....	124
5.4.1.2.	Winding Patterns.....	127
5.4.1.3.	Finite Element Analysis	128
5.4.1.4.	Burst Pressure Testing.....	130
5.4.1.5.	Autofrettage and Cyclic Pressure Testing	131
5.4.2.	Monitoring System of the Smart Composite Overwrapped Pressure Vessel	132

5.4.2.1.	Optical Fibre Sensors Embedment.....	132
5.4.2.2.	Winding and Cure Monitoring	135
5.4.2.3.	Impact Test Monitoring.....	138
5.4.2.4.	Cyclic Pressure Testing Monitoring	140
6.	Conclusions	145
7.	Recommendations for Future Work	150
	References.....	152
	Annexes	168
A1.	Plastic true stress and strain of the aluminium liner	168
A2.	Materials Data Sheets.....	170

List of Acronyms

BOTDR	Brillouin optical time-domain reflectometry
BVID	Barely visible impact damage
CCD	Cross correlation distance
CF	Carbon fibre
CFRP	Carbon fibre reinforced polymer
CNT	Carbon nanotubes
COPV	Composite overwrapped pressure vessels
CTE	Coefficient of thermal expansion
CWL	Central wavelength
DAQ	Data acquisition
DMA	Dynamic mechanical analyser
EFPI	Extrinsic Fabry-Perot interferometer
EIT	Electrical impedance tomography
EMI	Electromechanical impedance
ESA	European Space Agency
ESTEC	European Space Research and Technology Centre
FBG	Fibre Bragg grating
FC	Fuel cells
FCEV	Fuel cell electric vehicles
FEA	Finite element analysis
FEM	Finite element modelling
FOS	Fibre optic sensors
FRP	Fibre reinforced polymer
GF	Glass fibre
GFRP	Glass fibre reinforced polymer

GN	Gaussian-Newton
GNP	Graphene nanoplatelets
HDPE	High-density polyethylene
IPC	Institute for Polymers and Composites
LbL	Layer-by-layer
LCM	Liquid composite moulding
LDOF	Large diameter optical fibre
MFC	Macro fibre composite
MWCNT	Multi-walled carbon nanotube
NDE	Non-destructive evaluation
NPI	Networking/Partnering Initiative
OF	Optical fibre
OTDR	Optical time-domain reflectometry
PIEP	Innovation in Polymer Engineering
PLA	Polylactic acid
PVDC	Polyvinylidene chloride
PVDF	Polyvinylidene fluoride
PWAS	Piezoelectric wafer active sensors
PZT	Lead zirconate titanate
RF	Radio frequency
RMSD	Root mean square deviation
ROTDR	Raman optical time-domain reflectometry
SDOF	Small-diameter optical fibres
SHM	Structural health monitoring
SWCNT	Single-walled carbon nanotube
TOA	Time of arrival
TRL	Technology readiness level
UAV	Unmanned aerial vehicle
VARI	Vacuum assisted resin infusion
2D	2-dimensional
3D	3-dimensional

List of Figures

Figure 1: Schematic representation of delaminations orientations resulting from impact [15]	6
Figure 2: Schematic representation of damage on (a) thick laminates with a pine tree pattern and (b) thin laminates with a reversed pine tree pattern [15]	6
Figure 3: Schematic of a curve of transmitted energy versus time during low velocity impact test. Adapted from [17].	7
Figure 4: Schematic of cross-sectional area of an optical fibre	10
Figure 5: Schematic representation of an OF with two FBG sensors, with illustrative graphs of the input light spectrum, transmitted spectrum with notch corresponding to the Bragg wavelength seen in the peak of the reflected spectrum. Illustration of the Bragg wavelength shift, as the grating period is increased or decreased, when OF is under tension or compression, respectively.....	12
Figure 6: Micrograph of the cross-section of an 8-ply unidirectional composite laminate embedded with FOS [32]	14
Figure 7: Cross-sectional images of CFRP laminates embedded with (a) standard LDOF and (b) SDOF with FBG sensors [34].....	15
Figure 8: SHM of GF/epoxy composite by PZT sensor: (a) PZT sensor; (b) blank GF/epoxy composite (left) and with embedded PZT (right). Adapted from [47].	18
Figure 9: (a) guided wave based sensor network with an effective area of 122 mm x 122 mm; (b) full expansion of the guided wave based sensor network to an area of 630 mm x 630 mm. Adapted from [60].	23
Figure 10: (a) percentage of electrical resistance change on the locations with the highest variations during a cycling fatigue test; GFRP panel after failure; thermograms of the GFRP composite at different cycles: (c) 100, (d) 1000, (e) 10 000 and (f) right after fracture [82].	28

Figure 11: (a) SEM micrograph of CNT grown on glass fibre for strain sensing and (b) carbon/epoxy composite panel with embedded sensors [85].....	30
Figure 12: Strain monitoring during cure reaction of a prepreg laminate [40]	34
Figure 13: Composite structure being manually inspected with an inspecting device, schematically represented on the right side, by the inductive coupling between the transducer coil in the piezoelectric transducer and transmitting and receiving coils in the inspecting device [9]	36
Figure 14: Vacuum infusion process monitoring of a stiffened GF reinforced epoxy composite: (a) top view photograph of the experimental setup with sensor locations representation; (b) schematic representation of the flexible sensors integration in the stiffened polymer composites (c) photograph of the produced composite with embedded flexible sensors; dielectric constant measurements at the (d) preparation and resin infusion stage and during the (e) cure reaction stage. Adapted from [96].	38
Figure 15: numerical and experimental data of a resin infusion process for the production of a glass fibre/polyester resin composite: (a) pressure profiles; (b) numerical and experimental normalized capacitance; and resin volume fraction and position plots at the initial detection by dielectric sensors (c) S1, (d) S2, and (e) S3 at different positions of the preform [98].....	39
Figure 16: Schematic representation of the different structure types of pressure vessels [106].	42
Figure 17: Schematic representation of the wet filament winding process [115].....	43
Figure 18: Schematic representation of winding patterns: (a) circumferential, (b) helical and (c) polar [107]	44
Figure 19: Stress behaviour of liner and composite overwrap and their contribution to overall strain vs. pressure behaviour of the COPV during <i>autofrettage</i> and following deloading and loading cycles [121].....	45
Figure 20: (a) SMART Layer strips embedded on bottle during filament winding process; (b) finished bottle. Adapted from [129].....	48
Figure 21: (a) Orientation of the membrane loads in the hoop (N_θ) and meridional (N_ϕ) directions of a cylinder; (b) free-body diagram of fibres in a helical layer, relative to the hoop and meridional directions. Adapted from [138].	54

Figure 22: Modelled equivalent stress vs. equivalent displacement during elastic behaviour prior to damage initiation and (positive slope) and during damage evolution (negative slope) [142] 57

Figure 23: Schematic representation of the optical fibre configuration depicting the isolation of the FBG_{T-CAP} at the far end of the optical fibre into a capillary tube, where epoxy resin is used to close both ends, and the FBG_{S+T} is in direct contact with the resin/laminate 62

Figure 24: Schematic representation of the VARI process and FBG monitoring set up 63

Figure 25: Schematic representation of OF location through the thickness of the laminate 64

Figure 26: Composite specimens with embedded (a) SDOF and (b) LDOF for low velocity drop-weight impact testing..... 64

Figure 27: Schematic representation of the locations of through-thickness holes A and B, having progressively larger diameters of 2, 4.5 and 6 mm. The green dots represent the location of the electrodes contact with the CFRP for EIT measurement. 65

Figure 28: Boundary electrodes configuration: (a) electrical connection of a boundary electrode at the thickness of the specimen, (b) electrical insulation and fixation of the electric wire on the top surface of the specimen, (c) top surface of a quasi-isotropic specimen subjected to an impact, and (d) bottom surface of the same specimen. Note that the electric wires were facing upwards during impact testing and drilling to avoid detachment. 66

Figure 29: Electrical impedance tomography equipment..... 67

Figure 30: Drop-weight impact test setup: (a) OF interrogation equipment and impact testing machine; (b) impact support fixture with toggle clamps and impactor on a CFRP laminate with embedded OF..... 70

Figure 31: Schematic of approximate impact locations on specimens containing (a) SDOF and (b) LDOF. Numbers 1 and 2 represent the locations of the first and second impacts, respectively. 71

Figure 32: Iterative work steps for the development of the COPV 74

Figure 33: (a) plate-shaped steel mandrel, (b) tape winding over the steel mandrel and (c) final wound composite structure for specimens production 75

Figure 34: (a) as cut and (b) instrumented dog-bone shaped aluminium specimens cut out from the aluminium liner..... 76

Figure 35: Liner Surface Contour. Squares represent the beginning/end of a frame. Some of them are identified.	80
Figure 36: Picture of the 6061-T6 Aluminium liner	81
Figure 37: (a) Pin produced by additive manufacturing and (b) pin glued to the closed liner dome	81
Figure 38: Schematic representation of the FBG sensors location on the liner surface.....	82
Figure 39: Schematic representation of the configuration of the polyimide coated optical fibre having an 8-FBG sensor array, for BVID detection capability demonstration. The scheme is not drawn to scale.....	82
Figure 40: (a) Ingress point of the optical fibre in the pin and placement at the closed dome and (b) placement of FBG1 at the circumferential section.....	83
Figure 41: Optical fibre fixed on the (a) dome and (b) circumferential section of the liner surface with epoxy adhesive.....	83
Figure 42: Schematic representation of the configuration of the 4-FBG sensor array optical fibres for the preliminary study on embedding methodologies: (a) optical fibre with inscribed bare FBG sensors; (b) optical fibre with inscribed FBG sensors, which are protected in a 200 μm diameter microtube; (c) optical fibre with inscribed bare FBGs and a 750 μm diameter Teflon cable, 3 cm long, protecting the mid-section of the optical fibre in between FBG sensors. The schemes are not drawn to scale.....	85
Figure 43: Liner with fixed optical fibre with (a) epoxy adhesive and (b) localised unidirectional composite layer buffer for added protection.....	85
Figure 44: Filament winding machine Gislotica and in-situ strain monitoring with FBG sensors .	86
Figure 45: Burst test setup: (a) safety chamber and control equipment; (b) COPV holder	87
Figure 46: Cyclic pressure test and OF monitoring setup at Amtrol-Alfa.....	88
Figure 47: (a) Drop-weight impact testing setup with optical interrogation system and (b) COPV support	89
Figure 48: Measured heat flow during dynamic DSC experiment between -30 and 250 $^{\circ}\text{C}$ of the uncured resin	92

Figure 49: Measured heat flow during isothermal DSC experiments at 70, 80, 90 and 100 °C 93

Figure 50: (a) Friedman plot for calculation of activation energy at different conversions presented in (b) 94

Figure 51: Comparison of experimental curing conversion data and Friedman method fitting ... 94

Figure 52: Isothermal curing predictions for temperatures between 17 and 25 °C 95

Figure 53: Ambient cure monitoring of the epoxy resin system through FBG sensors and type-K thermocouple 96

Figure 54: Measured heat flow during heat 1 and 2 of the heat-cool-heat DSC cycle after room temperature curing of the resin system 96

Figure 55: Post cure monitoring of the epoxy resin showing (a) the CWL shift measured by the FBG sensors and (b) respective calculated strain and temperature shift, and resin temperature measured by a type-K thermocouple 97

Figure 56: Measured heat flow during heat 1 and 2 of the heat-cool-heat DSC cycle after post curing of the resin system 98

Figure 57: Strain measured during initial 12 min of cure monitoring on a specimen with OF at M-45 location 99

Figure 58: Room temperature cure monitoring of specimens with SDOF at (a) T0, (b) B0 and (c) M-45 location. Note that the strain scales have been zoomed in to better show the strain variation; the strain at time zero starts with strain values around zero, as the wavelength value at time zero of infusion was considered to be the reference Bragg wavelength. 100

Figure 59: Post cure monitoring of specimen with SDOF at location B0: (a) CWL change measured on FBG_{T-CAP} and FBG_{S+T} and, (b) correspondent calculated strain and temperature variation, and imposed temperature profile recorded by the oven 101

Figure 60: Wavelength spectrum of a free SDOF, as received, and of the same optical fibre placed in between the carbon fibre plies in the VARI set up..... 103

Figure 61: Contact force measured in each impact energy test made on the reference CFRP laminate..... 105

Figure 62: Example of (a) indentation marks on the top surface resulting from the first and second impact events, and of (b) small bump on the bottom laminate surface..... 107

Figure 63: First impact with energy of 30.0 J on specimens with SDOF: (a) impactor load vs. time curves, (b) strain measured by the FBG _{S+T} at the moment of impact, and (c) developed residual strains	108
Figure 64: Phased array ultrasonic analysis of SDOF in location B0 prior to (a) and after (b) the first impact and of SDOF in location M-45 prior to (c) and after (d) first impact.....	109
Figure 65: Second impact with an energy of 20.0 J on specimens with SDOF: (a) impactor load vs. time curves, (b) strain measured by the FBG _{S+T} at the moment of impact, and (c) developed residual strains	110
Figure 66: Impactor contact force for LDOF during the (a) first impact with 30.0 J and (b) second impact with 20.0 J.....	111
Figure 67: First (30.0 J) and second (20.0 J) low velocity impacts on specimens with a LDOF having a single FBG _{S+T} in location T0: (a), (c) measured load during the impact for LDOF 001 and 002, respectively, and (b), (d) corresponding changes on the FBG spectra.....	112
Figure 68: Phased array ultrasonic observations of specimens with an LDOF 001 (top) and 002 (bottom) with a single FBG _{S+T} in location T0: (a) and (d) before impact, (b) and (e) after the first impact, and (c) and (f) after the second impact	113
Figure 69: Reconstructed EIT images using GN algorithm of a quasi-isotropic specimen with through-thickness holes of different diameters A and B: (a) A: 2 mm; (b) A: 4.5 mm; (c) A: 6 mm; (d) A: 6 mm, B: 2 mm; (e) A: 6 mm, B: 4.5 mm; (f) A: 6 mm, B: 6 mm. The green dots represent the connection points of each electrode.	116
Figure 70: Reconstructed EIT images using GN algorithm of an unbalanced specimen with through-thickness holes of different diameters A and B: (a) A: 2 mm; (b) A: 4.5 mm; (c) A: 6 mm; (d) A: 6 mm, B: 2 mm; (e) A: 6 mm, B: 4.5 mm; (f) A: 6 mm, B: 6 mm. The green dots represent the connection points of each electrode.	117
Figure 71: Impact load vs time curves on (a) quasi-isotropic and (b) unbalanced specimens and respective energy vs time curves (c) and (d)	119
Figure 72: Reconstructed EIT images using GN algorithm of different quasi-isotropic composite specimens exposed to drop-weight impact events with impact energies of 20.0 J (left), 30.0 J	

(middle), and 49.5 J (right). The green dots represent the connection points of each electrode.
 120

Figure 73: Reconstructed EIT images using GN algorithm of different unbalanced composite specimens exposed to drop-weight impact events with impact energies of 15.0 J (left), 30.0 J (middle), and 49.5 J (right). The green dots represent the connection points of each electrode.
 121

Figure 74: Ultrasonic C-scan inspection of quasi-isotropic composite specimens exposed to drop-weight impact events with impact energies of 20.0 J (top left), 30.0 J (top right), and 49.5 J (bottom) 122

Figure 75: Ultrasonic C-scan inspection of unbalanced composite specimens exposed to drop-weight impact events with impact energies of 15.0 J (top left), 30.0 J (top right), and 49.5 J (bottom) 122

Figure 76: Ultrasonic C-scan inspection of the quasi-isotropic composite specimen Q 20J(1) exposed to impact event with energy of 20.0 J at different thickness depth, from left to right: between 2.5 – 2, 2 – 1.5, 1.5 – 1, 1 – 0.5 and 0.5 – 0 mm..... 123

Figure 77: Ultrasonic C-scan inspection of the unbalanced composite specimen U-15J(3) exposed to impact event with energy of 15 J at different thickness depth, from left to right: between 2.5 – 2, 2 – 1.5, 1.5 – 1, 1 – 0.5 and 0.5 – 0 mm..... 124

Figure 78: circumferential (89°) and helical (15°) patterns created by CADWIND® software . 127

Figure 79: Hashin and Rotem's damage initiation criteria for fibre tensile mode of the first internal circumferential layer 128

Figure 80: Elastic strain of the helical layers in the circumferential direction of the COPV 129

Figure 81: Plastic strain of the liner..... 129

Figure 82: Axial displacement (U, U1) of the liner at burst. Units of U, U1 in mm..... 130

Figure 83: COPV after burst test..... 131

Figure 84: Spectra of an optical fibres with 8 FBG sensors, embedded into a COPV, taken after major processing steps..... 133

Figure 85: Spectra of optical fibres, embedded into COPV, taken after major processing steps. Comparison of different OF constructions/configurations: (a) Ormocer® OF with bare FBG sensors;

(b) Ormocer® OF with FBG sensors protected in 200 µm diameter microtube; (c) Ormocer® OF with bare FBGs and a 750 µm diameter Teflon tubes, 3 cm long, protecting the mid-section of the OF in between FBG sensors; and (d) bend-insensitive optical fibre with FBG sensors protected in 200 µm diameter microtube. These configurations can be revisited in Figure 42.	134
Figure 86: Bend-insensitive OF spectrum after <i>autofrettage</i> process.....	135
Figure 87: Strain change on FBG sensors, during COPV winding process.....	136
Figure 88: Curing monitoring of the COPV by embedded OF.....	138
Figure 89: Smart COPV with embedded FBG sensors.....	138
Figure 90: Real and predicted Impact locations on the flat projection of the COPV cylindrical region.....	139
Figure 91: Barely visible impact damage on the COPV surface: (a) matrix crack and (b) small bump.....	140
Figure 92: Examples of strain measured by the FBG sensors during pressure cycling test at different stages of the test with different values of maximum pressure: (a) cycles number 8050 – 8058 between 3 – 350 bar; (b) cycles number 396 – 404 between 3 – 400 bar; (c) cycles number 393 – 401 between 3 – 450 bar; and (d) cycles number 347 – 354 between 3 – 500 bar.....	141
Figure 93: Relation between the maximum cyclic pressure and measured strain by FBG sensors.....	142
Figure 94: Optical spectra change between maximum and minimum pressure values of cyclic pressure testing with different maximum pressure value: (a) cycle number 8292 between 3 and 350 bar; (b) cycle number 82 between 3 and 400 bar; (c) cycle number 437 between 3 and 450 bar; and (d) cycle number 10 between 3 and 500 bar.....	143
Figure 95: Last pressure cycles between 3 – 500 bar, before failure.....	144
Figure A1: Strain change on an OF with 8 FBG sensors, during COPV winding process.....	169

List of Tables

Table 1: Characteristics summary of different fibre optic sensor types	11
Table 2: Comparison of the different sensing approaches using nanocarbon materials and self-sensing CFRP composites.....	32
Table 3: Measured residual strain values during ambient curing and post curing by the embedded small diameter and large diameter FBG sensors on CFRP laminates.....	104
Table 4: Absorbed energy and maximum contact force for each level of energy used in the impact tests performed on the reference CFRP laminate.....	105
Table 5: Residual strains measured by embedded LDOF in each of the studied through-thickness locations after the first and second impacts.....	111
Table 6: Residual strains measured by embedded LDOF in each of the studied through-thickness locations after the first and second impacts. The impact location was on top of the FBG sensors.	114
Table 7: Percentage of absorbed energy and critical load values measured on impacts at 20.0 and 30.0 J energy levels.....	115
Table 8: Elastic properties of the aluminium 6061-T6 in the liner.....	124
Table 9: Properties of the ITS50/RCX0125 composite, used in the FEM analysis.....	126
Table 10: Burst pressure test results.....	130
Table 11: Number of endured pressure cycles by the COPVs.....	131
Table 12: Error (in mm) between the real and predicted impact location.....	139
Table A1: Plastic true stress and strain of the 6061-T6 aluminium liner	168

Chapter 1

Introduction

1.1. Motivation

The use of high-performance fibre reinforced polymer (FRP) composites in spacecrafts and aircrafts, including civil and military airplanes, helicopters, and business jets, has been increasing in the past decades to replace metallic structures. For example, the Airbus A350-XWB and Boeing 787 commercial aircrafts have reached more than 50% in weight of composite materials. The replacement of metals by FRPs intends to increase the mechanical performance/ weight ratios of structural parts, which allows reducing fuel consumption and CO₂ emissions and, therefore, increment the sustainability and decrease costs. This replacement is very auspicious as composites applied in aircraft and aerospace structures exhibit simultaneously higher strength and modulus, provided by the reinforcing fibres, and lower weight [1].

Although composite materials hold promising achievements, their failure still is very difficult to predict. Failure may be caused by complex and several more mechanisms, such as breakage and/or misalignment of fibres, macro or micro-cracking of the matrix, material and stress discontinuities, fibre/matrix debonding and delamination, than those occurring in conventional materials [2]. Oppositely, homogeneous and isotropic conventional materials, such as metals, tend to fail due to excessive loading or development of cracks, which propagate in predictive way during fatigue loading [1]. Despite composites being less prone to fatigue damage than metals, it might still occur as they may face harsh environmental conditions during their lifetime. The fatigue behaviour does not only depend on matrix and fibre, but also on the layup sequence used, which may be extremely diverse and variable from part to part, making it very difficult to get reliable data that could be generically applied to any part [1], [3]. Another drawback of aerospace composites is their propensity to barely visible impact damage (BVID), as discussed in section 2.2 of this document. The eventuality of unpredicted failures occur on a composite aircraft structure often requires an engineering over-design to comply with the rigorous and exigent safety rules of aerospace/aircraft industry, particularly in the case of civil airplanes. This commonly leads to the

use of over-thicknesses and counteracts the initial purpose of using composites to reduce weight [4], [5]. Thus, the implementation of structural health monitoring (SHM) systems is essential to ensure that advanced composite structures are intervened as needed upon damage, helping to extend their service lifetime in the harsh aerospace environment [6]. Furthermore, many periodic non-destructive evaluation (NDE) inspections can also be avoided and inspection and repair operations will be much more focused on areas of need [7]. SHM is an interdisciplinary area including areas such as material science, mechanics, computer science and electronics, but also requiring knowledge of the structure operational behaviour and its history [8].

With the increasing trend of applying polymer composites, the implementation of SHM systems is essential to ensure that such structures are intervened as needed upon damage and for extending their lifetime in the harsh space environment they are exposed to [6]. Structural health monitoring systems, through surface mounted or embedded sensors, can detect critical parameters, such as strain or temperature changes, to monitor the in-service structural health of composite parts and, in some cases, their manufacturing process itself as well. The continuous acquired data may provide useful information to timely detect and locate early damage in an aircraft structure, limiting maintenance operations to the minimum necessary, and at the same time, increasing its lifetime [1]. This provides a clear alternative to existing NDE techniques, which are typically used at the end of major processing steps and are limited by the size of the structure [9]. Moreover, SHM may be used in areas inaccessible to NDE technologies and in the acquisition of long-term data that may enable the implementation of new design rules [10].

1.2. Thesis Outline and Methodology

This thesis consists of seven main chapters as described below:

- In this first chapter, the motivation for the performed work and the thesis outline is presented;
- The second chapter reviews the state of the art of structural health monitoring technologies. Three main sensing technologies are addressed: fibre optic sensors, piezoelectric sensors and piezoresistive sensors and self-monitoring composites. Process monitoring strategies and the main challenges of SHM systems are briefly highlighted. The conducted review on sensors for composites monitoring purposes resulted in the selection of the two sensing strategies, which were initially tested at laboratory level. The development of composite overwrapped pressure vessels (COPV) for hydrogen storage is

also reviewed in this chapter, as this was the full-scale part selected to implement the SHM system. Lastly, based on the conducted state of the art review, the main objectives of this work are presented;

- The third chapter presents the theoretical background on which this dissertation was based on, including theoretical background of the two studied sensing technologies and design of the COPV;
- The fourth chapter describes all the materials and sensors used in this work and the taken experimental procedures;
- Chapter 5 presents and discusses the obtained results. At first, the results concerning process monitoring and impact detection, at specimen level, for the two studied sensing technologies, are presented. These findings are followed by the test results to demonstrate the SHM system on a real-engineering part, the 1-litre type III COPV.
- The main conclusions of the work carried out are presented in Chapter 6 and;
- The recommendations for future work are, finally, given in Chapter 7.

Chapter 2

State of the Art

2.1. Introduction

This chapter reports the conducted state-of-the-art review that supports the basis of this dissertation. The impact resistance of composites, an important issue impairing the employment of composite materials is initially discussed. Afterwards, sensing methodologies are discussed as a mean to timely detect impact damage and monitor the structural health condition of structures. Moreover, the capabilities of some of the addressed sensing methodologies for process monitoring are also discussed. The state-of-the-art of pressure vessels for hydrogen storage is also assessed, as this was the case study of this work to integrate a sensing system for SHM. The objectives of this work are presented at the end of this chapter.

2.2. Impact Damage on Composite Materials

Extensive effort has been done to study the impact properties of composite materials, since any damage created during their lifetime, either on maintenance operations or in-service, might drastically compromise compression after impact strength of the structure [11]. Understanding impact behaviour of composite materials is particularly important for low energy impact events, because it can produce internal delaminations with barely visible surface damage, that may go undetected during visual inspections [12], [13].

Impact can be classified according to the impactor velocity. Low velocity impacts comprise impactor velocities ranging from 4 – 10 m/s, with energies up to 50 J, occurring when tools are dropped on structures during manufacture or in-service. Intermediate velocity impacts are characterized by velocities between 100 – 150 m/s. Examples are debris strikes on the runway, with impact energies around 50 J, and bird strikes but with higher impact energies. High velocity impacts are in the range 300 – 2000 m/s, with impact energies ranging between 10 – 20 kJ. These impacts are characteristic of artillery and missile fragments, weighing just a few grams. The impact event is so rapid, leaving the structure with no time to flexure or shear as a whole, and full

penetration of the structure is possible to happen. Hypervelocity impacts occur with impact velocities ranging from 30 – 70 km/s, when micrometeorites strike satellites or spacecrafts. The impact lasts for nanoseconds and results in vaporization of both micrometeorite and structure. Protective shielding may prevent this, allowing only a gaseous cloud hitting the payload [14].

Damage caused by flying debris on the runway during aircraft take-off and landing can be simulated by a gas gun, while damage caused by bigger projectiles at low velocity, such as a hand tool dropping on a composite structure, can be simulated by drop-weight impact testing [15].

Reproducibility of impact test parameters must be carefully considered. The initial kinetic energy of the projectile is an important test parameter. However, it should be accounted that, although the same level of initial kinetic energy can be produced by either using a projectile with large mass with low initial velocity or a projectile with lighter mass with higher initial velocity, a completely different structure response might be obtained [15].

Evaluation of impact damage extent is challenging. It is often evaluated by the area of delamination. By plotting the area of delamination against the impactor initial kinetic energy, after a threshold value has been exceeded, a proportional increase of that area with the kinetic energy is usually observed. The delamination area, usually measured by ultrasonic C-scans, corresponds to the observed damaged area. Other techniques such as X-rays and infrared thermography may be used for the same purpose [15].

Aircraft and aerospace composites are prone to BVID. It may occur during manufacturing or maintenance operations, in situation as drop of a hand tool, or in-service due to heavy hail. These occurrences may ultimately lead to front face damages, and to much more concerning events, such as transverse cracks, delaminations and/or fibres breakage that may be completely undetected by the human eye [16].

Low velocity impact damage on polymer composites usually cause a combination of failure mechanisms that can absorb a good amount of energy: delaminations resulting from mode II shear, matrix cracking resulting from transverse shear and fibre breakage [12]. Delaminations present a high concern since they can cause severe strength reduction [15]. Delaminations are characterized by debonding of adjacent laminas, which were previously shown by experimental studies to happen between plies of different fibre orientations. The delamination presents an elongated oval shape or "peanut" shape with its major axis along the direction of the fibres in the lower ply of the two adjacent plies, as depicted in Figure 1 [15].

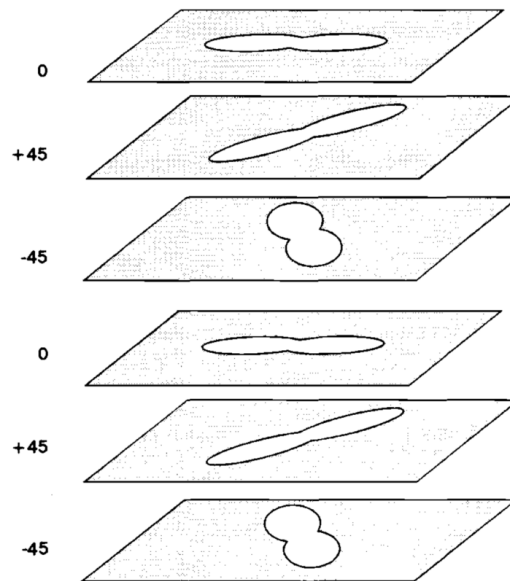


Figure 1: Schematic representation of delaminations orientations resulting from impact [15]

Impact damage produces not only a local indentation at the impact site, but also a global response that depends on the whole structure stiffness. Indentations caused by relatively small loads on stiff structures, may produce matrix cracks and delaminations able to redistribute the contact pressure over a wider area, while on lower stiffness structures, the contact pressure would be confined to a few tenths of a millimetre [14].

Impact damage initiates with matrix cracks, which can be either tensile cracks or shear cracks, and may then produce delaminations at ply interfaces. Thick laminates have matrix cracks first produced in the impacted layer due to the high and localised contact stresses developed. Then, matrix cracks and delaminations develop inwards, forming a pine tree pattern, as shown in Figure 2 (a). Thin laminates, on the other side, have matrix cracks first produced in the outermost surface to the impacted layer, resulting from bending stresses in these locations. In this case, damage develops upwards, where matrix cracks and delaminations form a reversed pine tree pattern, as illustrated in Figure 2 (b) [15].

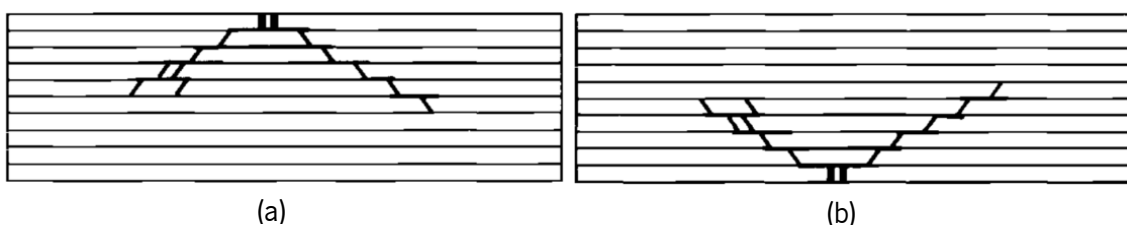


Figure 2: Schematic representation of damage on (a) thick laminates with a pine tree pattern and (b) thin laminates with a reversed pine tree pattern [15]

BVID is usually simulated through low velocity impact events. Figure 3 schematically shows a characteristic curve of transmitted energy versus time during low velocity impact event. The absorbed energy corresponds to the inelastic component of energy that was dissipated in the form of heat and damage during impact, being therefore utilized to produce fibres breakage, delaminations and matrix cracks. On the other hand, the elastic component of energy was expended in the impactor rebound [17].

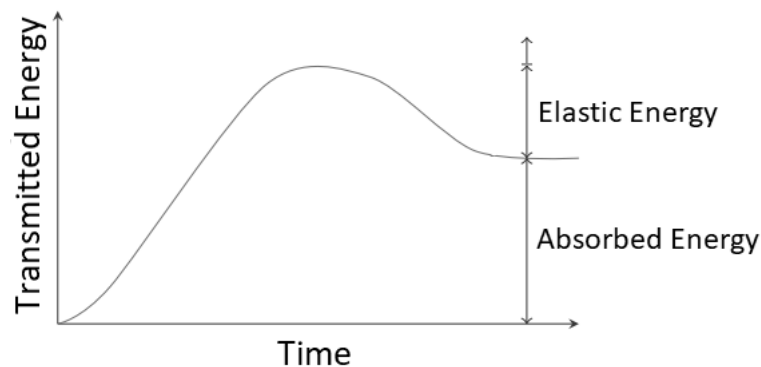


Figure 3: Schematic of a curve of transmitted energy versus time during low velocity impact test. Adapted from [17].

2.3. Structural Health Monitoring of Composite Materials

Full damage assessment and monitoring of a structure implies that certain sequential information levels are followed in the SHM methodology so that the most adequate corrective measures for repairing it may be taken in-time, in order to ensure compliance with the required levels of standard performance and safety, as predefined in the structural design. Thus, a complete SHM methodology encompasses damage detection capabilities in a mere qualitative way, on a first level, pointing of the likely damage location, on a second level, damage assessment for severity evaluation, on a third level, and only then, it can make predictions of, for example, structural safety and residual life, on a fourth level. Additionally, damage classification, with a method that provides information about the damage type, can be pointed as a third level, that may ease the implementation of damage assessment and, especially predictions, that would then be on a fourth and fifth level, respectively. Predictions (fifth level) are not possible without knowledge of damage type [18].

The data treatment of a SHM system must include signal processing, feature extraction and pattern processing, to finally lead to decision making. The first stage related to sensing has to do with data acquisition. In the second stage, signal processing entails data preparation for feature extraction (in third stage). Signal processing includes data cleaning, such as filtering for noise removal, spike removal through median filtering, outlier data points removal and missing data treatment, and

optionally, a pre-processing stage for data dimension reduction. Signal processing must be taken according to experience and engineering judgement. During feature extraction, the attributes of the different found damage types are enhanced while the regular background pattern (of the structure without damage) is suppressed. At a low damage level, the features of the different damage types may be hardly noticed as they may be hidden by the features of the regular background pattern. Therefore, caution must be taken to not to discard damage contained in data information while the data volume is reduced and feature extraction is performed. Afterwards, pattern processing comprises an algorithm which is capable of determine the damage condition, based on the features of the damage. Several algorithms, such as neural network, may be found in the literature. It is important to notice that a trade-off between the damage features resolution and the ability of the algorithm to reject noise is necessary. In case that the raw data is entirely noise-free with the slightest data fluctuation of the regular operating condition, will allow even small damages to cause detectable variations. Contrarily, when high noise level is present, distinguishing oscillations due to noise or damage will be hard, unless severe damage was introduced. At last, the decision making stage needs to consider the outputs of the algorithm of the pattern recognition stage to decide whether actions are needed and what actions they are [18].

An initial assessment of the operational conditions is necessary to develop the SHM system itself. The diverse nature of mechanical solicitation taking place in aircraft structures at the different stages of a flight, requires systems capable of acquiring data with a wide scan rate range, ranging from hundreds to thousands of hertz. Such requirement arises from the fact that operational strains, to detect nonconformities on the predicted fatigue life, involve measurements in the order of thousands of $\mu\epsilon$ and can be achieved at low scan rate, whereas the detection of impact damage or delamination needs a high scan rate system, that can detect acoustic waves propagating in the structure [6].

Although many techniques have been proposed for SHM of aerospace structures, their in-service reliability is not fully developed yet. Some of these techniques are summarized in the sections below.

2.3.1. Sensors for Structural Health Monitoring

A sensor for SHM should fulfil a few basic specifications: (1) it should only monitor the real damage condition of the host structure and be independent to changes in the environment; (2) it should transmit the acquired signals reliably; (3) it should produce as little impairment as possible on the

host structure; (4) it should survive the surrounding work environment for at least as long as the service life of the host structure; and (5) it should be easy to handle, attach, integrate and operate. Furthermore, sensors for SHM of aerospace and aeronautic structures require additional features, such as small dimensions, light weight, long service life with ageing resistance, low power consumption, good signal-to-noise ratio, compact wiring or wireless construction, and preferably have low cost [19].

2.3.1.1. Fibre Optic Sensors

The occurrence of damage may result in a change of strength and stiffness, which can be revealed by fibre optic strain sensors by a change in their optical properties, such as intensity, wavelength, phase or state of polarization, following a linear relation with the mechanical axial strain [20]–[23]. Fibre optic sensors (FOS) can be either embedded or bonded to the structure. FOS present several advantages, they are immune to electromagnetic interference, small, light, durable, and have high bandwidth, which allows multiplexing sensors in the same optical fibre (OF) [6], [24]. Despite FOS can be made of simple cheap telecom OF, the optoelectronic interrogation systems used for measurement and processing of the optical signals are still very costly [6]. The sensitivity of OF to moisture and chemicals require them to be coated by a polymeric film for protection, making the outer-diameter of the fibres very large, greater than at least ten times that of the diameter of the reinforcing fibres in the composite material [25].

Optical fibres are composed of a silica core of higher refractive index to restrain the light within itself, surrounded by a silica cladding of lower refractive index, and externally protected by a coating of polymeric materials, as previously mentioned. A schematic representation of the cross-sectional area of an OF is presented in Figure 4. Depending on the diameter of the internal core, the OFs are classified as single-mode, with a core diameter of about 10 μm and capability to carry only one mode of the light wave, and multimode fibres, with core diameters varying from 50 to 100 μm , allowing to carry more than one mode of the light wave. While multimode OF sensing range can be greater, they have lower accuracy and require higher light intensity, as opposed to single-mode OF, which can reach a distance of about 40 to 50 mm away from the sensor, with higher sensitivity, required for strain measurements [26]. Chambers et al. [27] reported an fibre Bragg grating (FBG) sensor capable of detecting residual strain from a low velocity impact event with an energy of 0.33 J, 10 mm away from the damaged area.

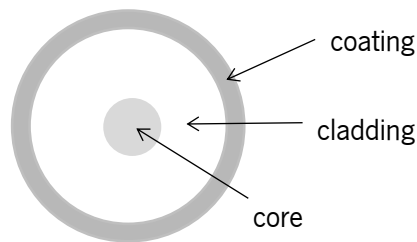


Figure 4: Schematic of cross-sectional area of an optical fibre

Fibre optic sensors can be classified according to their spatially-resolved measurement type as: interferometric sensors having single-point detection; grating-based sensors having quasi-distributed capabilities, able to make discrete measurements at sensor locations; and distributed sensors that can make measurements at any location along the fibre length. Interferometric sensors work based on an intrinsic or extrinsic cavity located along the fibre [28], which reflects a different optical phase between two interference light waves when physical changes occur in the host structure [20]. Common interferometric sensors are Fabry-Perot sensors, characterized by its high strain resolution, as high as $0.15 \mu\epsilon$, with strain measurement ranging up to $\pm 5000 \mu\epsilon$, at operating temperatures from -40 to $+250$ °C, and being very compact with no weight penalty to the structure. However, they cannot be easily multiplexed. Another well-known example are low coherent interferometric sensors (SOFO sensors), yet they are not suitable for SHM of aircraft structures as they work best for measurement of deformations at a low speed, $0.1 - 1$ Hz [20], whereas aircraft structures require measuring systems capable of reading deformations ranging from hundreds to thousands of hertz, to monitor both operational deformations and impact damage [6]. Distributed sensors are designated as optical time-domain reflectometry (OTDR), Raman optical time-domain reflectometry (ROTDR), and Brillouin optical time-domain reflectometry (BOTDR) as they are based on Rayleigh, Raman and Brillouin scattering principles, respectively. External loads cause changes in the magnitude of the reflected signal in the core/cladding interface, which can be directly related to a mechanical strain [20]. ROTDR based sensors can measure temperature with a resolution of 0.2 °C with a distance range of about 8 km, while BOTDR can measure both temperature and strain with a spatial resolution from 1 to 4 m and distance range of 30 km, which can be extended up to 200 km. A few grating-based sensors have been reported in the literature, but FBG sensors present the most matured technology [20]. FBG sensors have proved to be able to monitor low impact damage, either under static or dynamic deformation [27]. FBG sensors have the advantage over other types of FOS of being intrinsic sensing elements, as the obtained signal is encoded directly in the wavelength form, easing

wavelength division multiplexing [24]. With multi-point measurements provided by grating-based sensors and distributed sensors, a large area of the structure can be monitored with reduced wiring, keeping it a light weight structure, as opposed to traditional strain gauges or piezoelectric sensors [6], [24]. Table 1 highlights and compares the main characteristics of the aforementioned sensor classifications.

Table 1: Characteristics summary of different fibre optic sensor types

Type of sensor	Advantages	Disadvantages	Observations	Applications
Interferometric Fabry-Perot sensor	High strain resolution	Hardly multiplexed, cross temperature-strain sensitivity, fragile	Numerous cavity solutions possible for cross temperature sensitivity issue	Strain, temperature, vibration, cure monitoring
Grating-based sensors (e.g. FBG)	Discrete measurements of strain and temperature over large areas and at selected needed locations, well know technology	Cross temperature-strain sensitivity, limited damage severity and location assessment	Typical strain sensitivity of 1.2 pm/ $\mu\epsilon$ and temperature sensitivity of 10 pm/ $^{\circ}\text{C}$	Temperature and strain measurements, low velocity impact damage detection, damage localisation, cure monitoring
Distributed sensors	Measurements at any location along the fibre length, potential to monitor an entire aircraft, suitable for monitoring of large area composites	Expensive interrogation systems, spatial resolution in the cm to m range	Careful sensing technology selection for each specific application is needed	Strain, temperature, vibration, delamination

Due to the widespread use and research on FBG sensors, this section is focused on this technology for SHM. An FBG sensor consists in a narrowband reflector [29], obtained through a grating with a refractive index different of that of the core material, by writing it into the fibre core surface, exposing the side of the fibre to ultraviolet light, working as wavelength specific mirror. These sensors are multiplexed by inscribing grating of such nature with periodically different refractive indexes and, consequently, different Bragg wavelengths. The FBG sensor length can be as small as 1 mm [30]. FBG can be directly inscribed into the fibre without affecting the fibre diameter and are suitable for an extensive range of applications requiring small diameter probes, such as strain

mapping of advanced composite materials. The operating principle of FBG sensors is depicted in Figure 5.

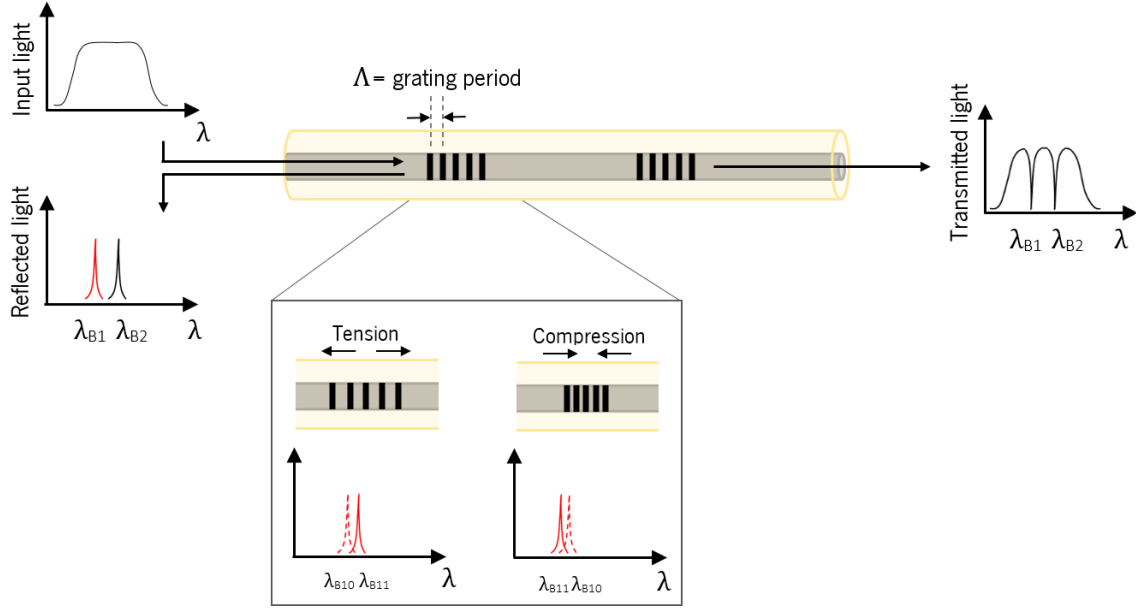


Figure 5: Schematic representation of an OF with two FBG sensors, with illustrative graphs of the input light spectrum, transmitted spectrum with notch corresponding to the Bragg wavelength seen in the peak of the reflected spectrum. Illustration of the Bragg wavelength shift, as the grating period is increased or decreased, when OF is under tension or compression, respectively

FBG sensors are based on the Bragg's law, where the Bragg wavelength, λ_B , which is the reflected wavelength by a set of periodic gratings, is dependent on the effective refractive index of the grating, η_{eff} , and on the grating period, Λ , according to equation 1 [6].

$$\lambda_B = 2\eta_{eff}\Lambda \quad (1)$$

When a local deformation is induced, it leads to a variation on the grating period, resulting in a change on the reflected Bragg wavelength, allowing to detect the local strain, resorting to equation 2 [6].

$$\frac{\Delta\lambda_B}{\lambda_B} = (1 - \rho_e)\varepsilon \quad (2)$$

being ε the longitudinal strain and ρ_e the photo-elastic coefficient of the fibre core material. For silica core fibres ρ_e is 0.22 and for a typical grating with a central wavelength of 1550 nm, the strain sensitivity is about 1.2 pm/ μm [6].

The capability of FBG sensors to detect BVID has been demonstrated. A residual strain as low as 3 μe has been detected by an FBG after an impact of 0.33 J, which did not produce any delamination or matrix cracking. Moreover, the residual strain increased to 25 and 605 μe for

impacts with energies of 1.67 and 2.99 J, respectively, which lead to matrix cracking and delaminations. Fibre breakage was also detected by microscopic analysis and ultrasonic C-Scan in the samples exposed to 2.99 J impact energy [27]. It should be added that the impact energy that produces detectable damage depends on the properties and structure of the composite laminate, and on the distance between the FBG and the impact location and, thus the same impact energy can induce very distinct damage severity on composites having different lay-up configuration. In some cases, damage location has also been assessed by the time of arrival (TOA) method. Hafizi et al. [21] reported the use of a two-channel system, an optical fibre with two NIR-FBG sensors, for impact location on a 4 mm thick glass fibre (GF)/ epoxy composite laminate. The TOA method, considering a one-dimensional structure with two sensors, allows calculating the linear impact location through the following equation.

$$l_2 = \frac{1}{2} \times (\Delta t \times C_g + L) \quad (3)$$

where l_2 is the distance between sensor 2 and impact location, Δt is the time difference between the arrival of the signal peaks of each sensor, C_g is the group velocity of the waves travelled on the sample, determined from the dispersion curves of the sample, and L is the distance between the sensors. Additional investigations of the signals utilising continuous wavelet transform, allowed to conclude that this system was able to locate linear impact sources with a relative error under 10%. Entire structures can be instrumented with multiple FBG sensors. Güemes et al. [31] have instrumented a lattice structure, envisioned for space applications, having a height of 1100 mm and diameter of 800 mm, and produced by automatic tape-laying process, with 36 FBG sensors. Strain values were acquired while the structure was fatigue loaded under compression. Although an initial failure broke a few bars, at -330 kN, the structure preserved its load-carrying capacity. The results revealed that minor production defects caused an irregular strain distribution that led to a nonlinear behaviour under fatigue loading.

Although SHM of composite materials can bring a great advantage towards damage monitoring and safety, an adequate installation of this technology is imperative. A few concerns associated to the FBG technology are discussed below.

An improper embedding of FOS in the composite may lead to degradation of the mechanical properties and higher risk of failure of the composite material. Theoretically, the strength and modulus degradation of the composite material depend on the angle between the optical fibre and reinforcing fibres direction in the adjacent plies, overall laminate thickness, diameter of the optical

fibre and material of protective coating of the optical fibre [3]. The degradation of the mechanical properties is usually more noticeable the higher the angle between the optical and reinforcing fibres of adjacent plies. “Eye” patterns or voids in the resin, which are defects that may serve as trigger points of premature failure by delamination, may be produced when the optical fibre is embedded transversely to the reinforcing fibres, as it can be seen in Figure 6. Yet it will only be relevant for structures with high density of fibre optical sensors. On the contrary, there will be a uniform consolidation around the optical fibre if they are placed parallel to the fibres of reinforcement, resulting on minimal defects and lower impairment of the composite mechanical properties, as the OF itself can also carry load [3].

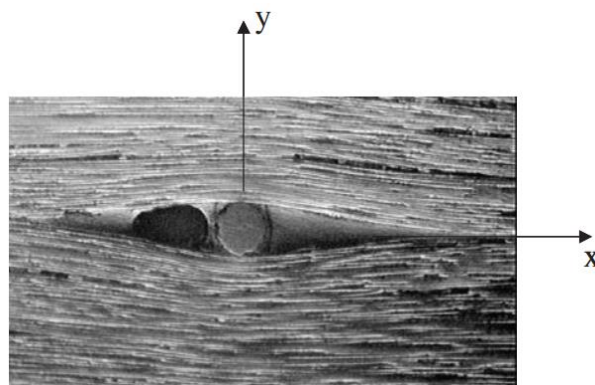


Figure 6: Micrograph of the cross-section of an 8-ply unidirectional composite laminate embedded with FOS [32]

The fact that OFs have outer-diameters of about 10 to 15 times larger than the traditional carbon or glass fibre reinforcements raises some concern [3]. This issue has been surpassed by utilizing small-diameter optical fibres and a few studies have been reported in the literature with laboratory developed small-diameter optical fibres (SDOF) [33], [34]. Commercial SDOF solutions, such as the T60 Small Diameter Fibre FBG from Technica [35], are still very scarce. Figure 7 compares typical large diameter optical fibre (LDOF) with a SDOF, which are laid parallel to the reinforcing fibres of the carbon fibre reinforced polymer (CFRP) composite. It is possible to observe that the LDOF leads to poor consolidation of the reinforcing CF and formation of matrix rich regions [34].

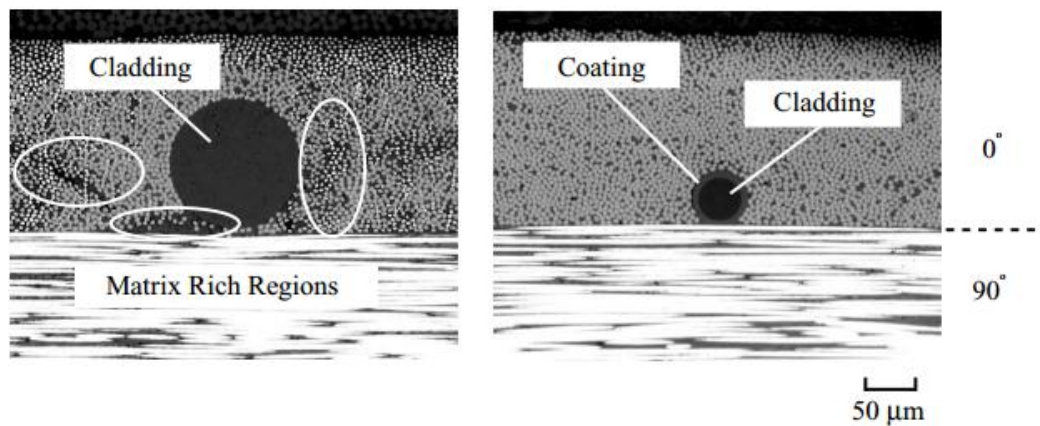


Figure 7: Cross-sectional images of CFRP laminates embedded with (a) standard LDOF and (b) SDOF with FBG sensors [34]

The success of the embedding process of FBG sensors in composite structures is limited, as the signal may be weakened and the OF may break easily. Ramly et al [36] embedded FBG sensors into sandwich composite structures, where the shifts of wavelength before and after embedment were generally lower than 1 nm, yet the signal showed a power drop within the OF after embedment. Optical connectors well suited for both industrial manufacturing processes and operational testing conditions are required to ease the integration of optical fibres, specially at the ingress-egress points. Giraldo et al. [37] have reported the development of a trimmable optical connector which was integrated in a specimen simulating a root joint of a lower wing. The optical connector includes a connecting component that is embedded in the composite material, where the OF is hold and centred, and a protective element to seal and prevent the entry of resin into the connecting component. When the structure is cured and before trimming, the protective element can be removed and a second connecting component can be installed for the optical fibre to be interrogated. Another simple solution could be surface mounting the FOS. Although they would be directly exposed to the operational environment, encapsulating protective materials could be used. Goossens et al. [38] have proposed the embedment of Ormocer® coated FBG sensors in a 1.0 mm diameter GFRP cylindrical profile, along the full length of the OF, for mechanical strength, with a 0.2 mm thick high-density polyethylene (HDPE) outer sheath, to inhibit humidity and oil ingress. The encapsulated FOS were pre-strained and adhesively bonded to thermoplastic CFRP specimens using a bi-component epoxy adhesive specially designed for optical fibres, and subsequently exposed to an annealing procedure to eliminate residual strains between the FOS and the protective GFRP coating. The instrumented specimens were then subjected to thermal and pressure cycles, humidity and hydraulic fluid exposure and fatigue testing, to mimic in-flight operational conditions.

After testing, the specimens showed a positive shift of Bragg wavelength, which shows that a pre-strain is still applied on the encapsulated FOS and that the epoxy adhesive bond has not been damaged, although this could also be the result of increased temperature when the measurements were taken.

The Bragg wavelength shift is also affected by temperature and still is difficult to compensate for it without impairment of the fibre resolution [39]. Some approaches have been developed to compensate for the sensor sensitivity regarding temperature. The easiest one comprises an additional strain free reference FBG sensor, where the temperature is measured, only useful if all FBG sensors are exposed to the same temperature. The method may be applied to both surface mounted and embedded sensors. If a strain free area is not accessible, a reference FBG sensor can be encapsulated in a capillary [6]. Glass capillaries have been demonstrated to be better suitable for temperature sensitivity isolation than stainless steel capillaries. The FBG sensor in a glass capillary has barely shown any sensitivity to heating rate changes and had the lowest thermal lag, when compared to FBG sensors in stainless steel capillaries [40]. FBG sensors of different grating structures, such as tilted FBG sensors [41], chirped FBG sensors [42], [43], and birefringent FBG sensors [44], having various and independent peaks, have also been investigated to decouple strain and temperature influence on the wavelength shift. This latter approach may be valuable for applications requiring precise strain and temperature measurements at different points of the structure, with minimal OF length, whereas the use of strain free reference FBG sensor or encapsulated FBG sensor may not measure accurate temperature values if the temperature is not uniform in the whole structure. The temperature sensitivity of FBG sensors is about 10 pm/°C.

The high sensitivity of FBG sensors to minor strains and temperature variations has fostered their wide use and acceptance for damage detection and cure monitoring, as discussed in section 2.3.2.1. However, the embedding procedure and sensor placement should be carefully considered with special attention paid to the ingress and egress points of the OF in the host structure. This can be particularly problematic when using vacuum bagging techniques, such as the vacuum assisted resin infusion process. Solving the strain-temperature cross sensitivity issue is essential for accurate strain measurements. Although the use of a capillary encapsulated FBG sensor is the most straightforward and cost-effective approach, special care must be taken when closing both ends of the capillary in order to impede resin flowing in to the loose OF extremity inside the capillary. The very localised sensing nature of FBG sensors is advantageous for evaluation of localised damage but hinders the assessment of the overall structural condition.

2.3.1.2. Piezoelectric Sensors

A piezoelectric material produces an electric charge when stressed, known as the direct piezoelectric effect, which confers it capabilities for sensing and measuring changes in forces, displacements, or velocities. Reciprocally, a piezoelectric material also presents a deformation when subject to an electric field due to a phenomenon known as the converse piezoelectric effect, allowing to serve as an actuator and acoustic source generator [45]. These are characteristic effects of dielectric materials with asymmetric crystalline structures, which may also occur in some ceramics, polymers, and crystals, such as quartz, lithium sulphate, tourmaline and Rochelle salt. Ferroelectric ceramics, such as lead zirconate titanate (PZT), and some polymers, such as polyvinylidene fluoride (PVDF), polyamides, polyimide and polyvinylidene chloride (PVDC), can be poled to obtain piezoelectric properties, by reorienting their crystal structure or crystallites, respectively. The poling process consists in applying a high electric field at an elevated temperature, and then the material is allowed to cool down with the electric field maintained in order to keep the orientation state. The piezoelectric properties are lost when the material is again subjected to a high mechanical stress or electric field capable of reorient the structure and make it symmetric, or when it is heated above its Curie temperature [45], [46].

Piezoelectric sensors offer high mechanical strength and operation for a wide frequency range and are able to fulfil demanding applications, at low price and with small sizes. Piezoelectric sensors can be either surface mounted or embedded, for superior longevity and higher sensitivity to damage, in a host structure without prejudice of its own mechanical properties. Masmoudi et al. [47] compared the performance of surface mounted and embedded piezoelectric sensors on unidirectional and cross-ply E-glass fibres/epoxy composites produced by hand lay-up and examined the effect of the sensors on the mechanical properties of the host structure due to fatigue loading by acoustic emission. Acoustic emission is a highly sensitive technique for real time damage monitoring that analyses the transient ultrasonic waves generated as damage develops in the loaded structure, which are detected by the PZT sensors. The characteristics of the acoustic emission signals (energy, amplitude, rise time, counts and duration) are analysed to identify damage mechanisms. Figure 8 (a) shows the piezoelectric sensor with a diameter of 5 mm and thickness of 0.5 mm and Figure 8 (b) shows a reference E-glass fibre/epoxy composite specimens and analogous composite specimen with an embedded sensor in the neutral plane during manufacturing. Three stages of acoustic activity were distinguished in the composite for specimens with and without embedded sensor during fatigue tests. The first stage is characterized by an

intense acoustic activity, attributed to the initiation of micro-cracks and its proliferation, with signal amplitudes between 43 – 95 dB. In the second stage, a reduction in the acoustic activity occurs, where the spread of micro-cracks, and likely fibre-matrix debonding, occur, corresponding to about 85% of the composite lifetime. The signals had amplitudes between 60 – 98 dB. The last stage is characterized by a brief and intense acoustic activity, having high energy signals with amplitudes exceeding 88 dB. In this stage there is a fast spread of micro-cracks, becoming more localised and leading to fibre breakage and, in the case of the cross-ply composites, also to delamination. The specimens reach complete failure at this point. The advantage of using embedded sensors is evident when comparing the number of acoustic events sensed by them and by the surface mounted ones. The specimens with surface mounted and embedded sensor measured in total, respectively, 35×10^3 and 30×10^4 acoustic events in total in the unidirectional laminates and 33×10^3 and 59×10^3 acoustic events in the cross-ply composites. It was also observed that the unidirectional laminate withstood without breaking to a slightly higher number of cycles by using the embedded piezoelectric sensor than the surface-mounted one, while the cross-ply laminates reached rupture at the end of the same number of cycles. Damage initiation locations and cracks in the laminates with embedded piezoelectric sensors occurred far from the sensors location, showing that these sensors themselves did not promote damage initiation. Nevertheless, this study does not represent a real and large structural part, where, generally, a large number of sensors is used.

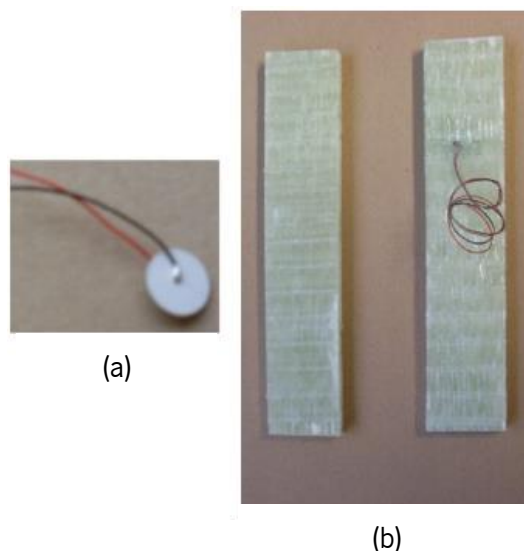


Figure 8: SHM of GF/epoxy composite by PZT sensor: (a) PZT sensor; (b) blank GF/epoxy composite (left) and with embedded PZT (right). Adapted from [47].

A PZT sensor network covering large areas of a structural part requires lengthy and heavy cabling that may be harmful to its performance. Three approaches can be implemented to reduce the length of lead wires of PZT sensors network. The PZT sensors in the same row or column can be connected either in series, parallel or heterogeneous way, with a mixture of in series and parallel connection, to form a single continuous sensor. These strategies allow reducing the cabling length as opposed to if every single sensor of the network would have its own lead wire connected to a single channel of the monitoring system. They were already tested by using a lightweight and low power consumption impact region monitor system based on a PZT sensors network and guided waves that was validated on a composite wing box of an unmanned aerial vehicle (UAV), where the sensors were placed on the inner surface of the composite skin [48].

Piezoelectric wafer active sensors (PWAS) have also been exploited on SHM of aerospace composites with multipoint measurements, as they are inexpensive, of small size and require simple instrumentation. PWAS consist of an array of PZT disks or squares and can be both surface mounted on or embedded into the composite structure [49]. However, PWAS may present weak driving force/displacement, brittleness, and their use at high temperatures or under high strains/voltages may result in a non-linear response and hysteresis [19].

Commonly, two detection approaches are used with PWAS, electromechanical impedance (EMI) (standing Lamb waves), adequate for near-field damage detection, and propagating Lamb waves for far-field damage detection [49]. The EMI technique makes use of PZT transducers that under an electric field actuate and produce a harmonic force on the host structure, to stimulate a structural response, the electromechanical impedance (or admittance) “signature” [50]. Usually, the real part of impedance or admittance can be used for damage detection, while imaginary part of impedance or admittance can be used for detection of transducer debonding [51]. The electromechanical admittance signature is dependent on the length, width, thickness, and orientation of the PZT transducer, but also on the stiffness, mass, and damping of the host structure, allowing to sense structural damage, when changes on the impedance of the PZT, $Z_E(\omega)$, are detected. The EMI can be measured by impedance analysers or LCR (Inductance L, Capacitance C, and Resistance R) meters [50]. This technique utilizes high-frequency structural excitations, typically, higher than 30 kHz, with a sinusoidal source V_x , with angular frequency ω , to produce a current I . The electrical impedance of the PZT may be calculated by [52]:

$$Z_E(\omega) = \frac{V_X}{I} = \frac{1}{j\omega a} \left(\bar{\epsilon}_{33}^T - \frac{Z(\omega)}{Z(\omega) + Z_a(\omega)} d_{3x}^2 \hat{y}_{xx}^E \right)^{-1} \quad (4)$$

where $Z_a(\omega)$ and $Z(\omega)$ are the mechanical impedances of the transducer and monitored structure, respectively, $\bar{\epsilon}_{33}^T$ the dielectric constant, \hat{y}_{xx}^E the Young's modulus, d_{3x}^2 the electric field constant, a the geometric constant and j the imaginary unit.

Some overall-statistics damage metrics were developed to evaluate the damage extent, through the differences on the admittance or impedance signature between the pristine and damaged state. Damage indexes, such as the root mean square deviation (RMSD) and cross correlation distance (CCD), are scalar numbers that give a metric of the damage in the structure. RMSD and CCD can be calculated following equations 5 and 6, respectively [53].

$$RMSD = \sum_{i=1}^n \sqrt{\frac{(R(i)_D - R(i)_R)^2}{R(i)_R^2}} \quad (5)$$

$$CCD = 1 - \sum_{i=1}^n \frac{[R(i)_R - \bar{R}_R][R(i)_D - \bar{R}_D]}{\sigma_R \sigma_D} \quad (6)$$

where $R(i)_R$ and $R(i)_D$, at the i^{th} sample, are the resistances of the PZT transducer in reference and damaged state, respectively, \bar{R}_R and \bar{R}_D are the averaged values for reference and damaged state, respectively, and σ_R and σ_D are the standard deviations for the reference and damaged state, respectively. Although being simple and frequently used, the RMSD index is dependent on outside effects other than actual damage, such as temperature changes, as it shifts the impedance spectrum up and down [54].

Wandowski et al. [53] used electromechanical impedance technique to study delamination detection and localisation in CFRP prepregs. The influence of temperature on the statistic damage metrics was evaluated as well. Delaminations of different sizes were induced through a chisel that was hit in between layers of the sample. The samples were 100 x 100 x 3.5 mm in size and were evaluated in the frequency range between 1 and 50 kHz at four conditions, no damage at 22 °C, no damage at 24 °C, and two conditions with different size of delamination at 22 °C. The effect of temperature was observed as a vertical shift on the resistance characteristic and a small horizontal shift on the frequency. The RMSD index was calculated, where the sample without damage at 22 °C served as reference condition. The small increase in temperature of 2 °C produced a high value of RMSD, of about 700, showing high sensitivity of RMSD to temperature. Although the RMSD

value for the sample with the smallest delamination, circa 1300, is higher than the RMSD value for the sample exposed for the small temperature change, it would be difficult to discern damage from a temperature variation in a real-life situation with a smaller delamination. The CCD value of the sample exposed to the temperature variation is much smaller than that of samples with delamination, being around 0.004, 0.04 and 0.06, for the sample without damage at 24 °C, and for samples with progressively larger delaminations, having as reference the sample without damage at 22 °C. The high RMSD value for the small temperature variation is due to its sensitivity to horizontal and vertical shifts of the spectrum, while the CCD index is only sensitive to horizontal shifts. With another set of samples, of dimensions 600 x 200 x 3.5 mm, the effect of temperature was further evaluated in the frequency band between 1 and 20 kHz, as damping effect was observed for higher frequencies, resulting in wide resonant peaks with low amplitude. It was observed that the resonant peaks are shifted in frequency for different temperatures, and those shifts are dependent on the frequency. For that, the authors propose an algorithm for temperature compensation based on cross correlation, where the CCD index is applied to narrow bands of frequency but covering the total analysed frequency band. Thomas and Khatibi [55] evaluated the integrity of surface mounted and embedded PWAS on CF/epoxy composites under repeated impact loading, resorting to electromechanical impedance and capacitance measurements. Both methods revealed the superior integrity of embedded PWAS. EMI analysis, generally, showed a higher RMSD for samples with surface mounted PWAS than samples with embedded PWAS. For instance, the RMSD of specimen with surface mounted PWAS was 6.51 after the 3rd impact with 7J impact energy, while the RMSD of the specimen with embedded PWAS was 0.46 after the 9th impact with the same impact energy. The capacitance measurements of samples with embedded PWAS revealed that the sensors can survive various impact events of different energies, keeping the capacitance values between 1 – 1.05, except for impact energies of 10 J, where the sensor showed a capacitance of about 0.7 after the 9th impact event, revealing some extent of damage. Regarding surface mounted PWAS, an impact energy of 5 J produced a capacitance increase after the 3rd impact event, from 1 to about 1.05, associated with partial debonding, with subsequent decrease in the following events, reaching a capacitance of about 0.6 in the 9th event. The specimen with surface mounted PWAS subjected to an impact energy of 7 J had similar response and the specimen subject to an impact energy of 10 J reduced the capacitance to about 0.5 just after the 1st impact.

PWAS transducers can both receive and transmit Lamb waves through the composite structure, serving as both sensor and actuator, respectively, through in-plane strain coupling [19]. Lamb waves require simple instrumentation: a signal generator, a digitizing oscilloscope, and a PC [19], [49]. As guided waves can propagate through long distances, few meters, it is possible to detect damage over a large area of a structure, using just a few transducers [56], allowing to detect structural anomalies, such as cracks, corrosions and delaminations in thin-wall structures [57], and to monitor even holes, notches and degradation of lap joints [56]. However, some disadvantages exist. Signal interpretation is very challenging as Lamb waves are dispersive and present simultaneously symmetric and anti-symmetric wave modes that overlap each other. Some approaches to discern a 'clean' single propagation mode are reported in the literature, by appropriately locating PZT, promoting interactions between different Lamb wave modes, resulting in their minimization or even elimination, and consequently, on the enhancement of a single propagation mode [56].

Piezoelectric powder and piezoceramic fibres incorporated into epoxy resin to form poled film sheets, known as piezocomposite transducers, have been developed to overcome the brittleness of traditional PZT sensor/arrays, but also enhancing sensor flexibility for surface conformability in curved structures. An example of a piezocomposite transducer is the macro fibre composite (MFC), developed by NASA back in 1992, for applications like structural control, vibration suppression and guided wave activation. The transducer is composed of unidirectional piezoceramic fibres, covered on both upper and lower surfaces by inter-digitated electrodes and protecting epoxy film [58]. While the activating motion of a traditional PZT sensor is across its thickness, the activating motion of a MFC is along its piezoceramic fibres, leading to a driving force that can be three times higher on MFC than on PZT [19].

Other flexible sensors are available on the market, such as the SMART Layer™ produced by Acellent Technologies, Inc. PWAS are connected by a printed conductive pattern on a thin flexible dielectric film for electrical insulation, that can be either embedded or surface attached on the composite. It is suitable for both metallic and composite structures and comes with an epoxy adhesive film on one side of the layer for convenient surface bonding. The SMART Layer™ embedment is done during manufacturing where the sensing system is placed as an extra ply. The SMART Layer™ can be co-cured with several composite materials, as it can sustain temperatures as high as 200 °C [59].

Wang et al. [60] reported the development of a stretchable sensor network based on guided Lamb waves. The authors claim that the stretchability of the system allows scaling it up so that it can be applied on aircraft smart skins. The sensors were produced by flexible printed circuit process and consist of 11 PZT elements and 11 micro radio frequency (RF) connectors on a polyimide substrate with copper metalized serpentine-based fractal interconnects, produced by laser cutting, that are connected to the PZT elements and RF connectors, through reflow welding. The serpentine-based fractal interconnects can pass on the signals or bear the tensile deformation. The network has an effective area of 122 mm x 122 mm and thickness of 0.12 mm (Figure 9 (a)), which can stretch up to an area of 630 mm x 630 mm (Figure 9 (b)). The stretched sensor network was bonded to the surface of a CF composite laminate with stiffeners, of 1000 mm x 1000 mm x 3.4 mm, using epoxy adhesive. The sensor network system demonstrated to be suitable for the application of both active and passive guided wave sensing methodologies for impact monitoring. The time-of-flight of the signals was used to construct damage imaging that revealed to accurately locate impact damage positions. However, impact damage sensitivity cannot be evaluated as the impact energy was not mentioned in the paper.

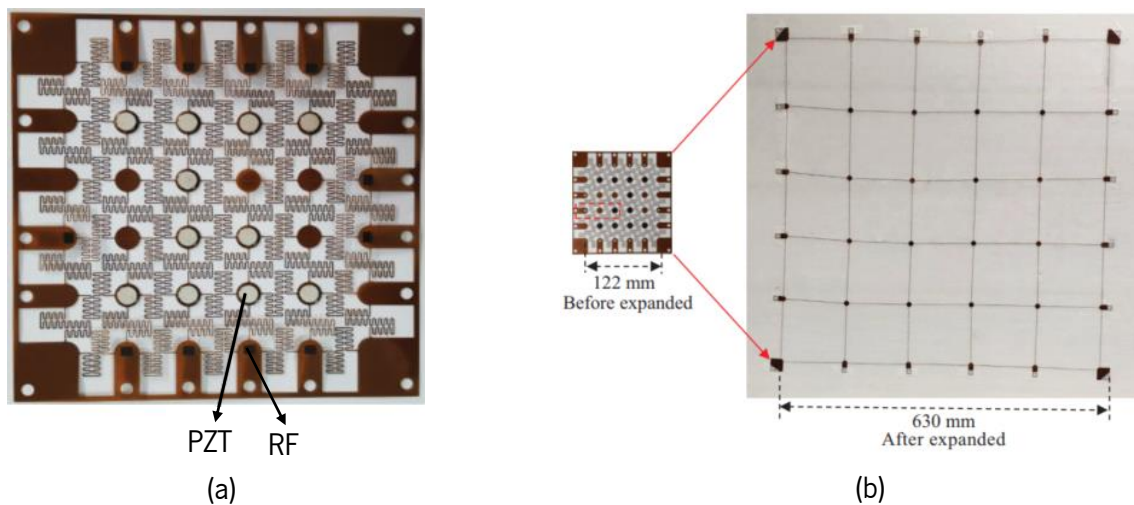


Figure 9: (a) guided wave based sensor network with an effective area of 122 mm x 122 mm; (b) full expansion of the guided wave based sensor network to an area of 630 mm x 630 mm. Adapted from [60].

Another alternative to traditional PZT are piezopolymers, such as PVDF or PVDC, offering lightweight, conformability and high voltage-generating piezo coefficient. However, PVDC is mainly found in sensing applications for the food packaging industry. Oppositely to PZT, PVDF has low stiffness and therefore low strain-generating piezo coefficient [57]. PVDF sensors can assume varied shapes. Jung and Chang [61] developed PVDF grid fabric sensors, where some CF tows were removed from dry CF fabrics and replaced by PVDF film stripes in a grid fashion. The grid is

formed by two PVDF stripes laminated with conductive copper tape, of smaller width, in between, to prevent electrical contact between the CF and the copper electrode. The fabric sensors were embedded into CF/epoxy prepregs as a regular layer. Following frequency analysis of Lamb waves, different failure modes produced by low velocity drop-weight impact tests were discerned: matrix micro-cracks with frequencies between 50 – 170 kHz, with 170 – 220 kHz, fibre-matrix debonding with 220 – 300 kHz and fibre breakage with 300 – 500 kHz. The extent of accumulated damage from consecutive impact events was estimated resorting to a failure index. Lambinet and Khodaei [62] reported the successful detection of artificial damage on adhesively bonded patch repair on CF composite laminates through the use of ring shaped PVDF sensors. The presence of distinct damages was detected using EMI and Lamb wave analysis, although damage location was not identified.

This review shows how versatile PZT sensors are. PZT sensors can be used on their own or in arrays, or even assembled in flexible films, following multiple constructions, or stretchable grids. The direct piezoelectric effect and the converse piezoelectric effect allow that PZT transducers can be used in both passive and active sensing methodologies. While an active sensing approach can assess the structural condition of a part at any time, a passive sensing approach only provides information about damage as it occurs. The level of damage detection is highly dependent on the used sensing technique. Acoustic emission is a highly sensitive technique, but it requires the structure to be loaded to create an acoustic emission event. It can only detect damage that releases energy, such as translaminar cracks, fibre breakage, delamination, fibre-matrix debonding and matrix cracks, whereas a stable crack, not spreading, is not detectable. Electromechanical impedance is also very sensitive to damage, but can be affected by environmental factors, such as temperature. This technique can only assess the current state of a structure by comparison with a baseline condition and can only give indication of damage extent resorting to statistic metrics. Lamb waves can monitor large areas of a structure and are able to detect internal damages, such as cracks, delaminations, matrix cracks, fibre breakage and porosity, in thin structures, as well as impact damage. While it can perform well on flat laminates, its applicability on real structures of more complex shapes is still limited. Damage location is also possible. All these techniques require skilled technicians to accurately evaluate data and associate it to the exact type of damage.

2.3.1.3. Piezo-resistive sensors and Self-monitoring Composites

Piezo-resistive materials respond with a change of electrical resistance when subject to a mechanical stress/strain [63]. Traditional commercially available piezo-resistive sensors are based on metallic films that present poor flexibility and stretchability, or semiconductor materials that, even though they present great piezo-resistive sensitivity, they present reduced mechanical properties [64]. The use of carbon based materials, such as CF [65] and nanocarbon materials such as carbon nanotubes (CNT) [66], graphene [67]–[70] and graphite [71], might be a promising approach for sensing applications in SHM of aerospace composites. Furthermore, these nanocarbon materials may also introduce a reinforcing effect by improving the mechanical properties of the composite structure. While CF can be self-sensing, the nanocarbon materials can be incorporated in the FRP composites following different approaches, namely, nanocarbon reinforced matrix or nanocarbon in between prepreg layers, nanocarbon coated fabric, nanocarbon containing polymer film and nanocarbon coated fibre sensors, to take advantage of their piezo-resistive properties for sensing applications.

CFRP composites can make use of a self-sensing approach, by utilizing the CF themselves as sensors to monitor damage by measuring induced changes in the intrinsic electrical conductivity of the fibres. This approach avoids introducing sensors in the CFRP, preventing the impairment of the mechanical properties of the host composite. Nevertheless, this approach is generally limited to damages involving fibre breakage, which usually happen as the part approaches the end of its service life, instead of detecting early damages that might happen in the resin, such as matrix cracks or debonding, that would allow for early preventive measures. A few recent studies [65], [72]–[74] have demonstrated the applicability of electrical impedance tomography (EIT) for detection and localisation of laboratory made damages, such as drilled holes, drill rivets, superficial cuts, embedded razor blades, and local indentation, on CFRP composites. Several electrodes are installed on the CFRP boundary and current is injected through a pair of electrodes, while the resultant voltage is measured in the remainder boundary electrode pairs, allowing to construct a tomographic image of the conductive medium [75]. The implementation of EIT in polymer composites is limited to carbon fibre (CF) composites and conductive nanoparticle containing composites, such as glass fibre composites having carbon black, carbon nanotubes or metal-based particles modified matrices [66], [72], [76], [77]. The application of EIT to monitor anisotropic materials such as composites is still at a low technology readiness level (TRL) and has only recently been exploited in the literature. Despite of its poor spatial resolution, EIT is susceptible to minor

conductivity variations [72], which makes it a promising technique for detection of damages that would disrupt the conductive network, including cracks and delaminations created during low velocity impact events.

To ease detection of early matrix related damage on CFRP, or on insulating glass fibre reinforced polymer (GFRP) composite, matrix reinforcement or surface functionalization of reinforcing fibres with electrically conductive nanocarbon materials are valid solutions. CNT offer great properties that makes them a primary choice for reinforcement of matrix resins. The advantages of CNT are now well known, they do not only have great mechanical strength and high electric conductivity, but they also have high aspect ratio allowing to obtain a very low percolation threshold, at as low wt% as 0.1, without altering significantly the properties of the matrix resin [78]. When a crack spreads in the composite, the electric conductive percolating network of CNT will be disrupted, making the damage detectable by an increase in the electrical resistivity [79]. The resistance of the CNT network is dependent on the CNT intrinsic resistance and on the intertube resistance, which arises from the contact resistance between connected CNT, and from the electrical conduction in between CNT separated by sub nanoscale gaps, known as the tunnelling effect. Therefore, as CNT structure does not change with deformation, making the CNT intrinsic resistance insignificant, the resistance changes of nanocomposites due to deformation is attributed to the contact resistance in between connected CNT and to the changes in the tunnelling current. The tunnelling effect taking place at a sub nanoscale makes any small deformation likely detected [66]. A study reported by Zhang et al. [80] showed enhanced stability of the sensing signals by introducing CNT in between layers of CF prepregs, as the sensing mechanism was due to tunnelling current in the percolated network of CNT in the resin-rich areas, instead of physical contact among the conductive CFs of the prepreg material. Moriche et al. [68] evaluated graphene nanoplatelets (GNP) reinforced epoxy nanocomposites and multiscale GNP reinforced epoxy/GF composites, produced by hand lay-up. Initial GNP/epoxy nanocomposites allowed to find the percolation threshold at about 8 wt%, much higher than threshold values reported for CNT. Yet, the GFRP composites were produced with 12 wt% GNP on the epoxy matrix. Flexural test revealed that while the 12 wt% GNP/epoxy nanocomposite had improved properties when compared to the neat resin, the multiscale GNP-GFRP composite had inferior mechanical strength and strain at break than the GFRP composite. This is explained by the poor interface between the GF and the GNP reinforced epoxy. GNP agglomerates lessen the interlaminar shear strength of the multiscale composite, easing delamination during flexural testing.

Some studies have shown the prospect of damage detection through nanocarbon material matrix reinforcement. Baltopoulos et al. [81] reported the use of EIT to create different regions of voltage distribution, in different parts of GFRP, by injecting current at different points of the CNT network, dispersed in matrix resin. A defect in the GFRP will produce a disturbance in the electrical path of the CNT network, which will be seen by the current source as a change on the total apparent resistance, and by the voltage meter as a change in the local current flow. The authors assume a 3-dimensional (3D) CNT homogeneous network in the polymer matrix that allows monitoring several damage modes, drilled hole, notch and indentation, in the composite laminate. The low electric conductivity of the glass fibres and epoxy matrix allow to use very low current (10^{-5} A) capable of producing measurable voltage changes to detect damages, in contrast to previous studies on CFRP that required a higher current (0.1 A). A recent technique was proposed by Naghashpour et Hoa [82], with MWCNT reinforced epoxy for damage location assessment. GFRP composite laminates with 0.30 wt% MWCNT reinforced epoxy were produced by hand layup and autoclave curing. The laminates were about 813 x 356 x 1.9 mm and had a 24-point grid, separated by 76.2 mm, made of an electrically conductive paste of silver and epoxy, which was surface mounted on the GFRP panel. Electrodes were obtained by connecting electrical wires to the grid points. The behaviour of the panels was analysed in fatigue tests by monitoring their strain and electrical resistances and measuring their temperature distribution by infrared thermography. A broken GFRP panel, after a tension-tension cycling test, with an electrically conductive grid on its surface can be seen on Figure 10 (b). Figure 10 (a) shows the percentage of electrical resistance change on the locations with the highest variations, A, B and C as indicated on Figure 10 (b). At first, location C presents the maximum electrical resistance change, being then overtaken by location B, until when, at about 4000 cycles, the percentage of electrical resistance change in location A started to increase, being where the final failure of the composite eventually occurred. Figure 10 (c) to (f) shows the thermograms of the GFRP panel at different cycles, 100, 1000, 10 000 and right after fracture, respectively. The authors claimed that this study allows to experimentally monitor the random initial matrix cracking happening in the composite panels.

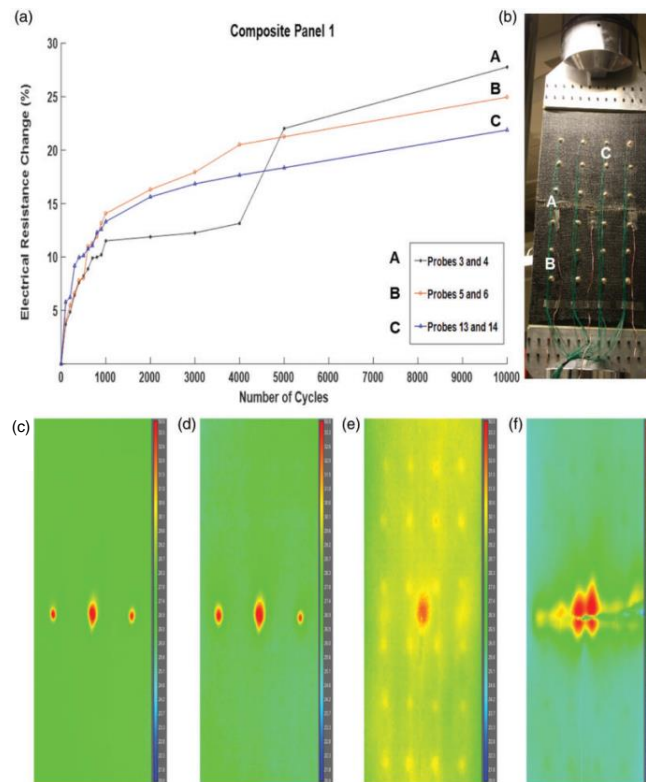


Figure 10: (a) percentage of electrical resistance change on the locations with the highest variations during a cycling fatigue test; GFRP panel after failure; thermograms of the GFRP composite at different cycles: (c) 100, (d) 1000, (e) 10 000 and (f) right after fracture [82]

Sometimes the incorporation of CNT in the matrix resin might be difficult to homogenize and may lead to highly viscous resins, even at concentrations as low as 1.5 wt%, making the production of such composites by, for example, resin infusion, a challenging process. The use of CNT containing polymer film sensors may be a feasible alternative, although it may raise concerns regarding sensor fragility, weak van der Waals CNT/polymer bonding, and poor adhesion of the sensor to the host structure. Nag-Chowdhury et al. [25] reported the production of multi-walled carbon nanotube (MWCNT)/epoxy film sensors, produced by spray layer-by-layer (LbL) deposition technique, and their embedding into GFRP laminates during resin infusion. The authors stated that the sensitivity of the CNT based sensors could easily be adjusted by the content of CNT and number of deposited layers in the LbL process. During cyclic tensile tests, the electrical resistance of the embedded sensors followed the induced strain curve, for low values of strain in the elastic region, and came to zero after unloading of the first cycle. As soon as the plastic region was achieved, the sensors presented a residual resistance after unloading of the second cycle, which can be explained by crack re-opening and new damage accumulation, allowing the sensors to monitor the residual strain accumulation. After five cycles, accumulated damage resulted in the rupture of the composite and sensor, with the disruption of the conductive percolated CNT network. Takeda and

Narita [83] produced CFRP substrates and bonded them with a MWCNT based epoxy adhesive layer, where different MWCNT concentrations, between 0.32 and 1.3 wt%, were tested, to be used in aerospace structures. The specimens were subject to mode I loading for crack monitoring with a double cantilever beam, while the electrical resistance of the joint was being recorded with a digital ultrahigh resistance/micro current meter. Naturally, the increase on MWCNT content results in increased electrical conductivity, but the fracture toughness of the adhesive joint decreased for MWCNT at 0.65 wt%. The crack extension could be measured by the resistance change. Jan et al. [69] reported a graphene nanosheets/ thermoplastic polyurethane composite film to be surface mounted on GF/epoxy composites produced by vacuum assisted resin infusion. The composite film had 12 wt% of graphene nanosheets, as this volume fraction showed an increased conductivity. A composite film strip of 3 cm x 0.25 cm was glued to the middle of the surface of each 300 cm x 25 cm composite specimen. The relative resistance measured by the graphene composite film was able to follow the amplitude of the imposed strain loading during cyclic tensile testing, though showing mechanical hysteresis as the relative resistance curve was drifting towards lower values, and some signal noise was also observed.

Another simple alternative approach to CNT reinforced resins is the use of CNT fibre [84] or CNT coated glass fibre sensors [85], [86]. Alexopoulos et al. [84] embedded CNT fibres into GFRP produced by resin infusion without prejudice of the mechanical properties of the final laminate. The specimens were exposed to cyclic tensile tests and the applied loading and electrical resistance change on the CNT fibre were observed to be correlated in a parabolic way. Residual electrical resistance was observed for high values of applied loading, due to accumulated damage. Sebastian et al. [85] reported chemical vapour deposition grown CNT on top of glass fibres, to be used as sensors for SHM of CF/epoxy composites (Figure 11). The fuzzy fibre sensors were electrically isolated in between two layers of plain weave E2 glass fibres and embedded in the midplane of the conductive composites. The reported system presented comparable sensitivity to conventional strain gages, with the advantages of being easily embedded into the composite and being able to sense a large area and at locations not easily read by strain gages. Another study conducted by Luo et al. [86] reported the embedment of single-walled carbon nanotube (SWCNT) spray coated glass fibre sensors into GFRP, for both process monitoring and in-service SHM. The SWCNT coated fibres were able to perform in-situ cure monitoring during the vacuum bagging production of the GFRP laminates, by revealing electrical resistance changes in accordance with the curing temperature program. At the strain-softening transition, the piezo-resistivity behaviour of fibre

sensor systems switches from negative to positive, corresponding to micro-cracks opening and propagation in the epoxy matrix and fibre delaminations, depicted by an increase in the electrical resistance of the sensors due to the disruption of the conductive CNT network. The sensor was able to detect composite failure, which happened at a large strain of 5.1%, allowing to perform SHM with early detection of micro-cracks, preventing catastrophic failures.

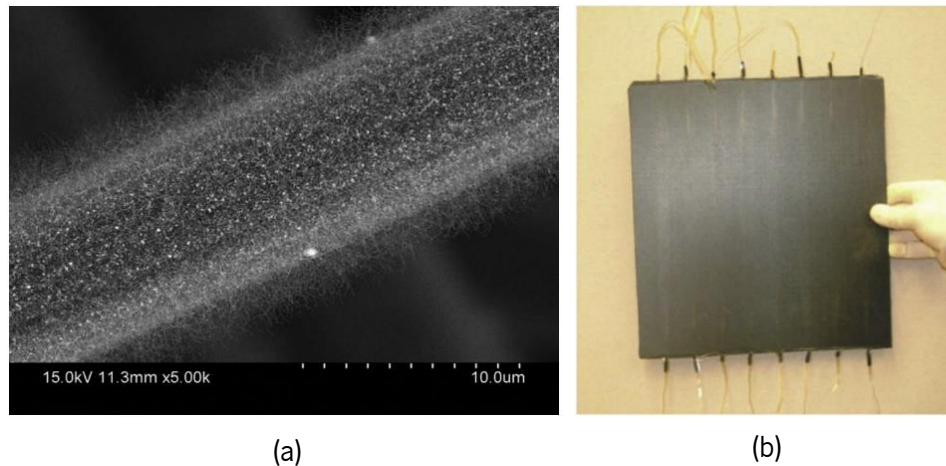


Figure 11: (a) SEM micrograph of CNT grown on glass fibre for strain sensing and (b) carbon/epoxy composite panel with embedded sensors [85]

Similar outcomes can be attained using graphene and graphite. Many works report the production of sensors consisting of graphene/ graphite coated fibres, mainly but not only limited to glass fibres [62], [67], [71], [76], [87]. Luo and Liu [71] have reported the production of a graphite nanoplatelet spray coated single filament glass fibre sensor, obtained by an aqueous dispersion of graphite nanoplatelets and a surfactant agent, following a drying, washing, and ambient drying process. The graphite nanoplatelet sensor was embedded in GFRP laminates produced by vacuum bagging of $0^\circ/90^\circ$ E-glass prepreg. Piezo-resistivity was measured during cyclic tensile testing on a dynamic mechanical analyser (DMA), allowing to calculate the gauge factor of the sensor, which revealed to be 17, although it became only 2.42 when embedded in the GFRP laminate. Piezo-resistivity measurements during fatigue tensile testing on the DMA were also used to verify the longevity of the sensor for SHM of composites. A tensile test was taken to failure to demonstrate the ability of the sensor to detect damage. During the initial elastic deformation, the sensor increases its resistivity linearly, and when the composite enters plastic deformation, the resistivity continues to decrease but at a lower rate. As the composite reaches failure, resistivity increases drastically. Additionally, the sensor was able to monitor the 2-stage curing process during production of the laminates, which is discussed in section 2.3.2.1. The authors claim that the developed sensor can

be easily embedded on composites of more complex shapes at any required location and orientation in a non-invasive way, thanks to its continuous form. Nevertheless, further research work is required in order to make the sensors suitable for conductive composite materials, such as CFRP. It should be pointed that the reported work has used very small sample sizes. Balaji and Sasikumar [67] have reported the use and embedment of a reduced graphene oxide coated glass fibre sensor for real-time strain monitoring, as well as residual strength and damage accumulation estimation based on statistical analysis, on GFRP composites during uniaxial tensile testing. The sensor showed a linear piezoresistance with strain and applied force in low strains up to 3.7% (elastic region), explained by the tunnelling effect and an effective conduction path. For higher strains, the sensor showed nonlinear response, with step increments, explained by the breakdown of the conductive path as micro-cracks spread in the composite. The divergence of piezoresistance from the elastic behaviour was used to statistically estimate damage accumulation and residual strength of the GFRP composite. Upon failure of the specimen, either by fibre pull-out or matrix failure, the reduced graphene oxide-based sensor showed a sharp increase of piezoresistance, but further work is needed to associate the failure mechanism with the piezoresistance change. Montazerian et al. [70] reported the production of a graphene-coated spandex fibre sensor with a protective stretchable silicone sheath for monitoring the hot press manufacturing of GF/polypropylene prepreg composites. The sensors were embedded in the midplane of 2 and 4-ply laminates and their suitability for SHM was assessed by three-point bending testing with imposed increasing strain amplitude. The sensors could follow the variation in the elastic strain amplitude, measure a change in the residual resistance in the fourth and fifth cycles, due to progressive failure with imposed loading, and identify failure fracture with the disruption of the conductive fibre sensor. Table 2 summarizes the main advantages, disadvantages and damage detection accomplishments of the above described methods using carbon based sensing approaches. Scaling up laboratory specimen to real large-scale structures and understanding and attributing sensing signals to specific failure modes of composites is still very challenging. Some research work, though still at a low TRL, have shown promising results towards damage location, through CNT reinforced matrix. The low percolation thresholds attained with CNT, compared to graphene and graphite, make this the most favourable nanocarbon reinforcing material for piezoresistive sensing, easing composite processing, and minimizing nanocarbon material agglomeration.

Table 2: Comparison of the different sensing approaches using nanocarbon materials and self-sensing CFRP composites

Sensing Technique	Advantages	Disadvantages	Damage detection
Self-sensing composite	No need for sensors	Limited to close to failure damage detection, limited to conductive fibre composites, mainly limited to flat or almost flat samples	fibre breakage, damage location using electrical resistance tomography at low TRL
Nanocarbon material matrix reinforcement	Percolation at low volume percentages for CNT	Difficult composite processing	Detection of early matrix dominated failure modes, damage location assessment possible
Fibre/fabric coating	Easy processing	Cannot assess damage location and size, limited to insulating fibre reinforced composites	Detection of early matrix dominated failure modes
Film sensor	Applicable to both insulating and conductive fibre composites	Poor adhesion bonding of sensor to host structure, fragile	Elastic strain, residual strain, and rupture by relative resistance change

2.3.2. In-situ Process Monitoring

Commercial aircraft industry has moved in the direction of polymer composite materials, replacing metallic materials, to produce lighter, less part-count and more complex structures, allowing to reduce fuel consumption and carbon dioxide emissions and ultimately decrease costs [1], [88]. Further cost savings may be achieved by composite manufacture through liquid composite moulding (LCM) techniques, replacing autoclave manufacturing [88]. Vacuum assisted resin infusion (VARI) is one of the LCM technologies [89] that has proved to be well-suited to produce advanced structural parts for aircraft and aerospace industries, as it allows the manufacturing of large components with good reproducibility, mechanical properties and having, simultaneously, high fibre and low void contents. It is also an eco-friendly and inexpensive technology. Monolithic panels of aircraft wings can be produced through VARI to fit the structural component, reducing the number of parts and fasteners, and consequently the complexity of the final structure [90].

Cure and process monitoring may provide the knowledge to keep up with the increasing demand for advanced FRP composites in aerospace industry, with ever desired improved performance and reliability. Other composite manufacturing technologies, like the traditional filament winding or

more recent forms of winding technologies, can also benefit from process monitoring for improved reliability. Often, sensors used for structural health monitoring of aerospace composites can be taken advantage of, to firstly use them for monitoring of the processing procedure of polymer composites, which can also be beneficial for quality assurance.

2.3.2.1. Cure Monitoring

During production of thick structural FRP for load bearing applications, uniform curing throughout the thickness of the part should be attained to produce high quality parts and reduce scraping volumes and consequently decrease costs. By monitoring the cure reaction, the electric power can be adjusted, which helps optimizing processing time, reducing costs, and avoiding thermal degradation once the curing exothermic reaction may be auto-accelerated. Very distinct sensing approaches for cure monitoring of composites are discussed in the following paragraphs.

As FBG sensors are sensitive to thermal strain can be used for monitoring thermoset curing reactions. The strain can be associated with thermal expansion at the time that the thermosetting resin warms up due to the beginning of its own exothermic reaction, followed by a negative strain due to polymerization shrinkage as the resin starts to cure, and finally, higher negative strain may be developed as further shrinkage happens upon cooling. An optical fibre placed in a transverse direction to the reinforcing fibres will measure high compressive strains, since the matrix plays a large contribution on the properties of the transverse direction, while lower strain variation happens in the same direction of the reinforcing fibres. A study published by Boateng [40] followed the strain development during the curing procedure of prepreg laminates, involving a heating stage, isothermal curing period at 100 °C for 100 min, and cooling stage, using bare and encapsulated FBG sensors (Figure 12). The data acquired by the encapsulated FBG sensors was taken to find the mechanical strain imposed in the FBG sensors during the cure reaction. At the end of the isothermal period, the strain values were about 220 and 60 $\mu\epsilon$, as measured by an FBG sensor embedded in a perpendicular direction and by an FBG sensor embedded parallelly to the reinforcing fibres, respectively, while at the end of the cooling stage, the same sensors measure strain values of about -760 and close to zero $\mu\epsilon$, respectively. As the temperature increases in the heating stage, a strain increase is recorded in both sensors due to thermal expansion suffered by the resin, though this effect is more pronounced on the FBG embedded perpendicularly to the reinforcing fibres. Initiation of chemical shrinkage due to polymerization is observed at around 25

min in the FBG sensor embedded parallelly to the reinforcing fibres, while it is unclear whether it starts at 30 or 42 min in the FBG sensor embedded perpendicularly to the reinforcing fibres.

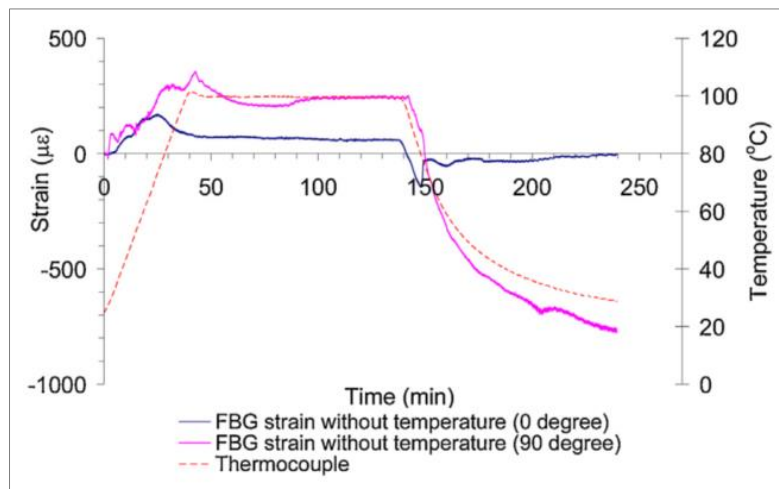


Figure 12: Strain monitoring during cure reaction of a prepreg laminate [40]

Chehura et al. reported an initial strain increase as thermal expansion occurs when resin is heated, followed by a negative strain owing to polymerization shrinkage as curing initiates and, lastly, further negative strain is developed as further shrinkage may happen and the resin cools down [91]. Leng et al. evaluated extrinsic Fabry-Perot interferometer (EFPI) sensors and FBG sensors for cure monitoring of CFRP prepregs. A thermocouple was embedded for cure temperature monitoring. EFPI sensors revealed three curing stages, starting with an increase of compressive strain, followed by a somewhat even strain region, where most of the curing reaction occurred, finishing with a last growth of the compressive strain as matrix shrank upon cooling. The wavelength shift curve of the FBG sensor showed a similar shape to the temperature curve measured by the thermocouple during curing, showing that the temperature has a higher contribution to the Bragg wavelength shift than the mechanical shrinking strain. The curing stages were also identified in the curve of FBG wavelength shift [92]. Kang et al. embedded two FBG/EFPI hybrid sensors in perpendicular directions into unidirectional, symmetric cross-ply and fabric graphite/epoxy laminate prepregs, which were autoclave cured. High compressive strains were measured by the sensors located in the transverse direction to the fibres, whereas low compressive strains were measured by the sensors positioned in the same direction of the fibres. The authors attribute this behaviour to the large role of the matrix on the transverse properties of the composite material [93].

Chilles et al. [9] proposed the embedment of inductively coupled piezoelectric sensors on GF reinforced epoxy prepreg for cure monitoring and further damage detection. The sensor system

consisted of a piezoelectric transducer electronically connected to an inductance coil, and an inspection device containing a transmitting and a receiving coil, which are connected to the input and output of an ultrasonic instrumentation, allowing wireless communication (Figure 13). A bulk wave generating system was used to monitor 10.4 mm thick composite plates and a guided elastic wave generating system was used to monitor thinner composite plates, with a thickness of 3.31 mm. The initial curing phase of the thick sample could not be characterized due to the low viscosity of the resin at this stage, while the embedded sensor using the guided wave system detected the edge reflections prior to initiation of the curing reaction, as the guided waves propagated along the fibres. The temperature increase led to the reduction of the resin viscosity, increasing the attenuation of the guided ultrasonic waves until they were no longer detectable. As curing progressed, the edge reflections became again detectable. Both systems proved to be suitable for the last phase of cure monitoring. Dielectric analyses were employed for comparison. The measurement of the imaginary impedance maximum was only possible when the dielectric sensor became wet by the resin. With the increase of temperature and decrease of resin viscosity, the imaginary impedance maximum decreased. The imaginary impedance maximum increased with the progression of the curing reaction. A steep increase due to the sudden decrease of ionic mobility during cure revealed resin gelation. The end of cure is identified by a constant value of the imaginary impedance maximum. Commercial dielectric analysers, such as the DEA 288 Ionic from Netzsch, enables cure monitoring in both laboratory and industrial scales, making use of implantable or reusable dielectric sensors. The reusable sensors can be even indefinitely mounted on a press or mould surface. The sample is placed in contact with the dielectric sensor. The sinusoidal voltage is applied forcing the positively charged particles in the sample to move towards the negative pole and vice versa, and dipole molecules are aligned, producing a sinusoidal current with a phase shift. As curing progresses, the sample viscosity increases and, consequently, the mobility of the charge carriers decreases, expressed by a decrease of amplitude and increase of phase shift in the current signal [94]. However, the use of dielectric sensors and analysers is limited to cure monitoring and cannot be used for damage monitoring.

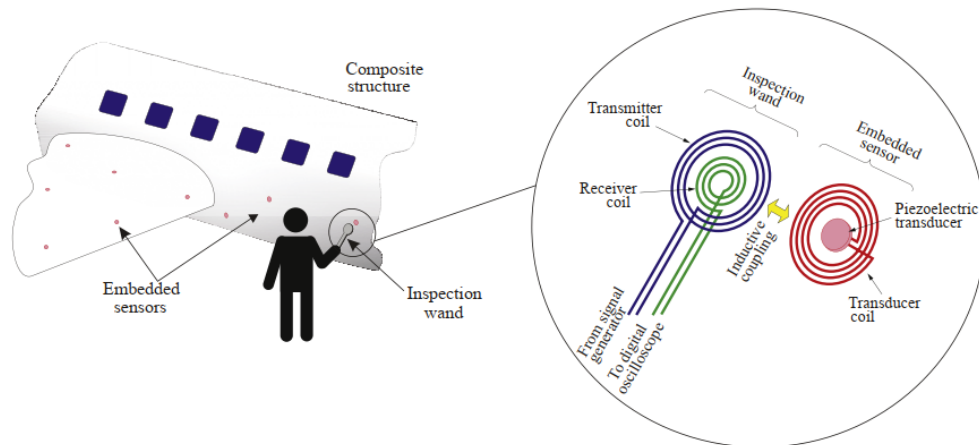


Figure 13: Composite structure being manually inspected with an inspecting device, schematically represented on the right side, by the inductive coupling between the transducer coil in the piezoelectric transducer and transmitting and receiving coils in the inspecting device [9]

Luo and Liu [71] have reported the production of a piezo-resistive sensor consisting of graphite nanoplatelet coated single filament glass fibre sensor, already described in section 2.3.1.3, and its use for cure monitoring. The sensor was embedded in GFRP prepreg laminates and was able to monitor the 2-stage cure of the vacuum bagging process. The sensor showed a steep increase of the resistivity, from 199.7 k Ω to 572.1 k Ω , as the temperature was increased from ambient temperature to 143 °C, due to the physical and chemical changes of the matrix. As the temperature increased, the viscosity of the resin decreased which makes it easier for the resin to fill in the gaps in between the graphite nanoplatelet particles at the fibre sensor surface and their contact to be further distant or disrupted and, consequently, induce an increase of the sensor resistance. The temperature ramp is followed by an isothermal stage, where cross-linking bonds further occur leading to the increase of resin viscosity and shrinking. During this stage, the resistance of the sensor decreased initially, from 572.1 k Ω to 466.1 k Ω , and was kept constant for the remainder isothermal period, with a value of 403.6 k Ω , which was explained by the interparticle graphite nanoplatelet contacts being closer together again.

The analysed sensing approaches were able to identify the completion of the cure reaction, generally by a plateau of the measured parameter, leading to enhanced properties of the composite. Although the reviewed sensing approaches are able to identify all the curing stages of composites, optical fibre sensors, namely FBG sensors, can evaluate the residual strain resulting from the matrix shrinkage due to curing happening in the isothermal and the cooling down period. This is a valuable information that can be useful to find the best curing cycle for certain aerospace

parts where precise processing control is necessary to comply with demanding dimensional accuracy requirements.

2.3.2.2. Mould filling in Liquid Composite Moulding Processes

Distinct sensing approaches, including the ones discussed in the section 2.3.1, have been shown to be suitable for mould filling and flow front monitoring on the production of polymer composites through LCM techniques. Ali et al. [95] developed a sensing technique based on the piezo-resistive properties of a reduced graphene oxide thin coating applied on glass fabrics for flow front monitoring in the resin infusion process. The proposed sensing technique was able to monitor the resin infusion process of an epoxy resin. As the infusion began there was a sudden decrease of relative resistance, and as the resin flow progressed the resistance started to increase, due to the spring-back effect of the preform caused by the resin pressure gradient, which makes up for the dielectric properties of the resin flowing in. When the preform is fully impregnated and the injection line is closed, the resistance decreases until the pressure equilibrates. When the pressure settles, curing starts and the resistance starts to increase, due to the insulating layers of cured resin around the fibres. This sensing technique may provide valuable information for LCM manufacturing methods, especially for techniques involving two closed rigid mould tools, such as RTM. The graphene coating provided insights about the compaction condition of the reinforcements, flow front progression and cure reaction as well, due to changes in the electrical resistance of the fabric. Yang et al. [96] produced flexible sensors by photolithography on polyimide-copper film substrate and with integrated temperature sensors, able to make simultaneous measurements of both capacitance and temperature. The sensors were employed for the resin infusion process of stiffened GF reinforced epoxy composites (Figure 14 (a) – (c)). They were able to monitor the vacuum seal, shown by an increase of dielectric constant ϵ' from 1 to 2, as the vacuum imposed a tighter contact between the sensors and glass fibres (blue shade in Figure 14 (d)) and, one hour later, the resin flow front, identified by the sudden increase of ϵ' from 2 to around 6 or 8 as the resin flowed in and the air in between fibres was replaced by liquid resin (purple shade in Figure 14 (d)). In the following curing time ϵ' was kept approximately constant, apart from sensors 6 and 8 where the ϵ' variation indicated a vacuum leak. Additionally, the system was able to monitor the curing rate by the rate of change of the dielectric constant ϵ' , the progression of the internal temperature, and resin solidification (Figure 14 (e)). While the authors claim that the sensors are capable of detecting delamination during SHM, it is unclear whether the sensors themselves are responsible for promoting this type of damage in the first place.

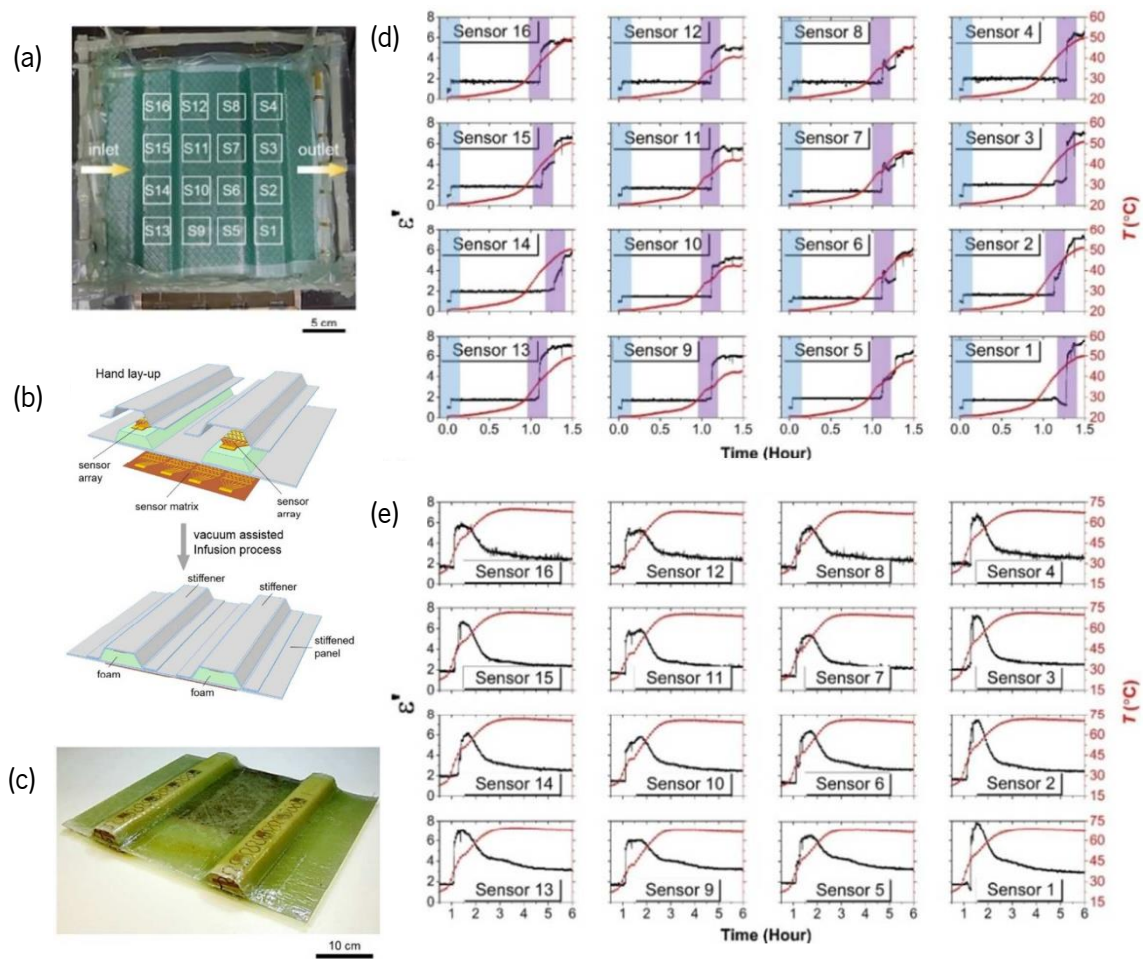


Figure 14: Vacuum infusion process monitoring of a stiffened GF reinforced epoxy composite: (a) top view photograph of the experimental setup with sensor locations representation; (b) schematic representation of the flexible sensors integration in the stiffened polymer composites (c) photograph of the produced composite with embedded flexible sensors; dielectric constant measurements at the (d) preparation and resin infusion stage and during the (e) cure reaction stage. Adapted from [96].

Alternatively, the sensors can be applied on the mould surface and reused for several cycles. Carlone and Palazzo [97] reported the use of shielded dielectric sensors on the bottom die in contact with the preform to monitor the flow front progression in LCM process, where glass fibre weave was used as reinforcement and synthetic oil as resin replacement to prevent variations on the dielectric properties due to cure. The proposed sensing approach was combined with numerical simulations and were able to monitor both unsaturated flow front (flow developed in between tows, regarded as extra-tow flow, leading to the preform impregnation) and saturated flow front (flow developed inside each tow, regarded as the intra-tow flow, leading to the preform saturation). For reduced void content the fluid/resin should be able to fill and saturate the preform, whereas there is usually a short period of time between the unsaturated and saturated flow front. The sensors were able to detect the arrival of the fluid in the sensing area by a sharp increase of capacitance, and measure the arrival time, and to detect the time of full saturation in that same area, when the

capacitance was no longer varying. Carlone et al. [98] have used the concept of capacitance variation as a sensing approach. Each dielectric sensor consisted of two flat electrodes placed parallelly on the bottom and top mould surfaces, to form a capacitor, where the central insulating material is the reinforcing glass fibres, polyester resin, and air in between the moulding surfaces. The extra-tow flow front progression was numerically modelled by bulk permeability simulations and was experimentally shown by the progressively increased time of arrival on the three sensors installed on the mould surfaces. The saturation rate was also computed, which allowed to find a good agreement between the experimental and numerical (sum of intra-tow flow and extra-tow flow) normalized capacitance data. The experimental and numerical data of an experiment is presented in Figure 15.

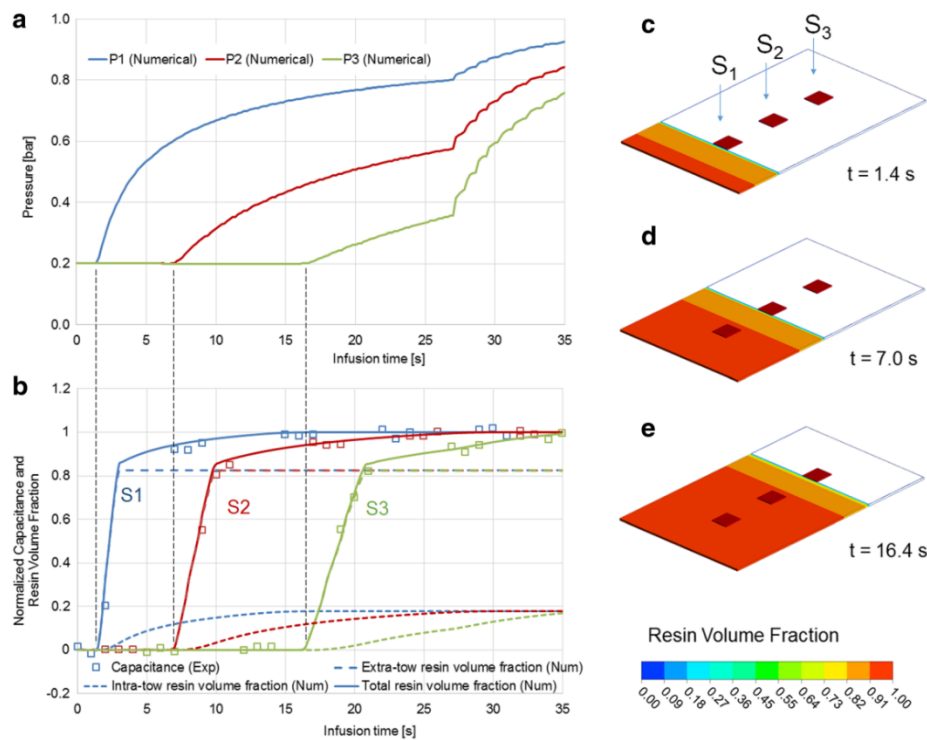


Figure 15: numerical and experimental data of a resin infusion process for the production of a glass fibre/polyester resin composite: (a) pressure profiles; (b) numerical and experimental normalized capacitance; and resin volume fraction and position plots at the initial detection by dielectric sensors (c) S1, (d) S2, and (e) S3 at different positions of the preform [98]

Only a limited number of research works address the mould filling monitoring in electrically conductive CFRP composites. Qing et al. [99] exploited the concept of the SMART Layer™, addressed in section 2.3.1.2, and employed a PZT sensor network on a flexible polyimide substrate with a printed circuit to connect the PZT sensors. The resin flow path could be followed by measuring the first arriving Lamb waves signals in between different pairs of PZT transducers. As the sensing path becomes wet by the resin, higher energy attenuation of the Lamb waves is

measured, until the signal stabilizes at a low amplitude value when the preform is fully filled. It was also possible to follow the curing reaction. A study carried out by Wang et al. [100] monitored resin infusion processing of composite laminates made of unidirectional CF fabric arranged in 0 and 90° directions and epoxy. Fresnel's optical fibre sensors monitored the refractive index of the resin during impregnation and curing to evaluate flow front progression and cure reaction. Type-K micro-thermocouples were used for temperature reading. A combination of these two sensors in the midplane of the laminate allowed to distinguish five stages of the process. In stage 1, the infusion stage, it is observable the resin arrival by a sudden decrease on the OF signal as the reflected light is decreased by the presence of the resin around the sensor, and through a temperature minimum. In stage 2 there is a temperature increase. The curing stage corresponds to stage 3, with a 2h isothermal at 180 °C. At the beginning of this stage there was a temperature peak, accompanied by an increase in the reflected light intensity, due to an increase on the resin density, as it changed from liquid to solid in the exothermal curing reaction. The resin was considered cured when there were no further changes on reflected light intensity. Upon cooling, stage 4, the resin shrinks, and its density increases, resulting in higher reflected light intensity. In stage 5, corresponding to the end of the resin infusion process, there is a stabilization of the temperature and reflected light intensity. A dielectric sensor [101] consisting of two twisted copper wires, each coated with an insulating material, to impede contact between copper and reinforcing CF, is able to monitor the flow front progression and cure reaction in the RTM process. A voltage is applied to produce an electric field between the wires, which goes through the gaps between the wires. The authors were able to calculate the flow front position, i.e., the instantaneous length of wetted sensor, by the linear admittance measured by the sensor. However, this concept can only be applied after the experimental calculation of admittance of the sensor in the dry and wetted condition, provided that the same reinforcement layup configuration and pressure profile in the impregnation stage is used. This can be a limiting issue in the production of a small number of high end large composite parts, where large material scraping, and increased costs could result.

2.4. Composite Overwrapped Pressure Vessels

2.4.1. Introduction

It is estimated that around 20% of the global carbon dioxide emissions are produced by burning fossil fuels in internal combustion engines. Since the 1970s owing to the oil crash, and particularly in the last decade, additional research efforts have been done to find replacements for fossil fuels

for the transportation sector, aiming to constrain global warming to 1.5 °C [102]. Fuel cells (FC) are an emergent hydrogen-powered propulsion system, which may help to lessen climate changes [103]. FC are expected to be widely used in the automotive industry in a near future. Large automotive companies, like Toyota, Hyundai and Honda, are commercializing fuel cell electric vehicles (FCEV) [102]. In comparison to battery electric vehicles, FCEV have faster refuelling times (around 3 – 5 min) with a 600 km autonomy, superior longevity (> 200 000 km), reducing associated anxiety and providing superior driver experience, and safety [102]. The exploitation of hydrogen powered technologies is not only foreseen in the automotive industry. Hydrogen powered UAV [104] are being developed and even Airbus has recently announced its pursue of hydrogen powered aircrafts with the ZEROe concept, with hydrogen combustion through modified gas turbine engines and hydrogen FC [105]. For the implementation of hydrogen powered systems, pressure vessels for hydrogen storage are needed. Among the existing solutions, COPVs are the most weight efficient option [106].

There are four construction types of pressure vessels for hydrogen storage. These are schematically represented in Figure 16. Type I pressure vessels are completely made of metal and mainly used in industrial applications at pressures between 20 and 30 MPa. This is a low efficiency design as it can only store circa 1% of its weight with hydrogen. Types II, III and IV are COPVs, i.e. they have a liner and a composite overwrap. The type II COPV has a thick metal liner with a fibre/resin composite overwrap around the cylindrical part. Type III and type IV pressure vessels have a composite overwrap all around the liner, typically a CFRP composite. Type III pressure vessels have thin metallic liners, while type IV pressure vessels have polymeric liners [106]. The most common material for the production of metallic liners is the aluminium alloy 6061 [107], but 7060 alloy, stainless steel and chromium molybdenum steel are also used [108]. Thermoplastics such as PEEK [109], polyamide 6 [110], [111], polyethylene terephthalate [112] and HDPE [113] are being explored for the production of polymeric liners.

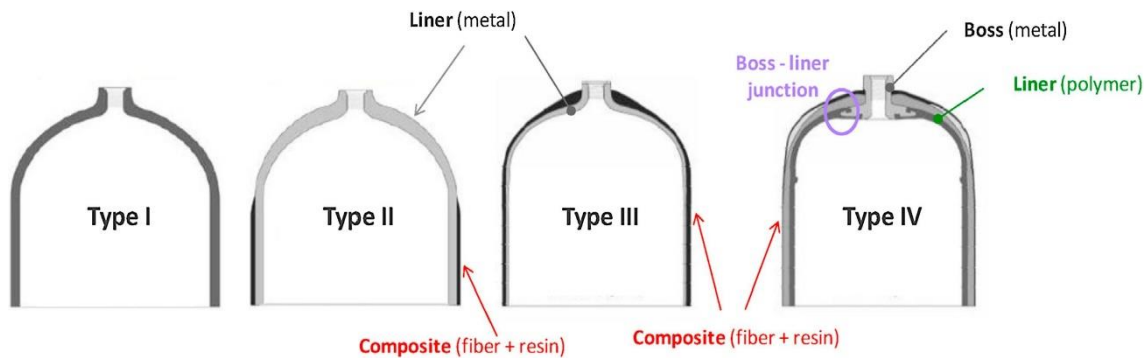


Figure 16: Schematic representation of the different structure types of pressure vessels [106]

2.4.2. Manufacturing of Composite Overwrapped Pressure Vessels

As shown in Figure 16, composite overwrapped pressure vessels consist of a liner and a composite overwrap. A seamless metallic liner is usually produced by deep drawing and spinning. A circular plate is progressively deep drawn, with several intermediate anneals, and using dies of progressively bigger sizes to form the dome. Afterwards, the open end is spun to form the second dome and neck. Alternatively, the metallic liner can be produced by spinning of both extremities of an extruded tube. This methodology involves a heat treatment and machining of the neck to produce the thread to accommodate the pressure regulator device [107]. Polymeric liners are usually produced by rotational moulding [109], [110], or blow moulding [112]. The production of liners through rotational moulding can be economically advantageous due to the low cost of the moulding tools, which is beneficial for small series production, as typically occurs in the aerospace industry [109].

However, herein focus will be given to the production of the composite overwrap. Filament winding is an automated process for the manufacturing of hollow composite structural parts with high fibre content, such as pipes and COPVs, that may find application in the aeronautic, automotive, and civil engineering. This technique uses a revolving mandrel as a moulding surface, where the continuous fibres are wound around of, following a certain pattern, to produce the fibre composite overwrap. The mandrel may be collapsible or soluble, being discarded at the end of the production process. Nevertheless, the mandrel is commonly an integral part of the COPV for mechanical reinforcement and fluid containment, as in the case of type III or type IV COPVs. There are numerous variants of the winding technology, they are mainly divided into dry and wet winding. In the conventional wet filament winding, the continuous dry fibre rovings are unwound and aligned in a comb device before being impregnated in the liquid resin bath. A nip roller device removes the excessive resin, just before the impregnated rovings are laid over the mandrel, as positioned by

the pay-out eye in the sideways moving carriage. Figure 17 shows a schematic representation of this process. During winding, enough fibre tension should be imposed on the fibres being wound onto the mandrel or onto previous layers, to ensure adequate compression, resulting in lower void content in the composite overwrap and taking advantage of the full stiffness and strength of the wound fibres [114].

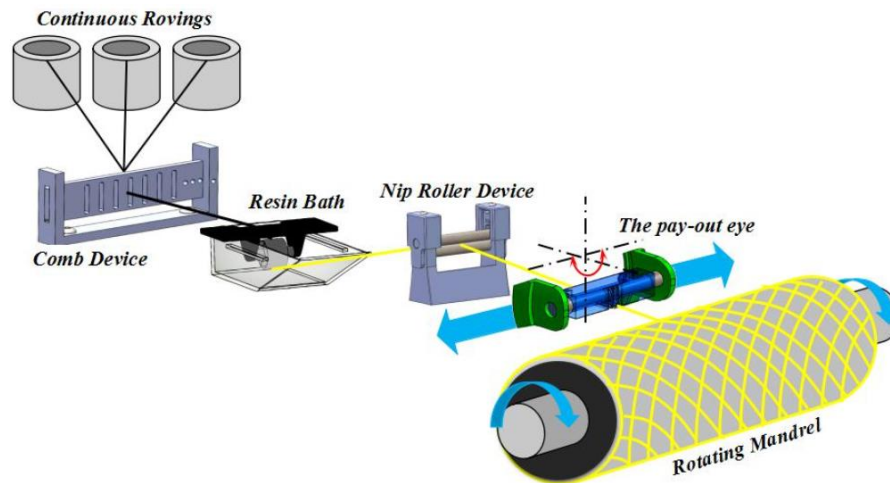


Figure 17: Schematic representation of the wet filament winding process [115]

Several forms of dry winding have recently emerged, as a result of different forms of pre-impregnated materials. For instance, narrow slit prepreg tapes can be wound around the mandrel [109], [110]. The winding of thermoplastic tape requires the addition of heating devices and compressing rollers to the winding setup to ensure proper compaction of the accumulated tape layers. Winding of thermoplastic prepreg tape is often accomplished with 6-axis robotic winding setup as it can easily follow the mandrel contour and ensure proper compaction of the tape being laid over [116]. In a similar setup to that of the one used in wet winding, the dry fibres may be wound around the liner and, only later, the dry wound fibre preform is impregnated by, for instance, VARI process [117].

There are three types of winding patterns: circumferential, helical, and polar. These are schematically represented in Figure 18. In a traditional filament winding machine, the carriage velocity is synchronized with the rotational velocity of the mandrel axis in certain ways to produce the different winding patterns. The circumferential or hoop winding pattern is characterized by winding angles very close to 90° , relative to the mandrel longitudinal direction. The circumferential winding is achieved with the carriage moving sideways by a distance corresponding to the width of the feeding roving filaments while the mandrel completes a full revolution around its axis, until the

full cylindrical part of the mandrel is covered. While the carriage is progressing to the side, the pay-out eye is static. Helical winding comprises angles between 5° and 80° , relative to the mandrel longitudinal direction. This pattern is achieved by having the mandrel axis rotating continuously, while the carriage moves sideways. The ratio between the mandrel rotational velocity and carriage longitudinal velocity is controlled to obtain a certain winding angle. The minimum winding angle of a COPV is defined by the polar opening of each dome [118]. The polar winding pattern is characterized by small winding angles, close to zero, relative to the mandrel longitudinal direction [107]. In polar winding, the fibres are laid over the mandrel with the carriage moving sideways with the pay-out eye tilted at the desired winding angle, while the mandrel axis rotates a distance corresponding to the width of the filaments. The fibres are laid side by side until the desired layers are produced. By definition, each helical or polar layer consists of two wound fibre plies, while a circumferential layer consists of only one wound fibre ply [114]. Whereas type II COPVs are produced by solely circumferential winding, type III and type IV COPVs are produced by a combination of circumferential and helical or polar winding patterns [108].

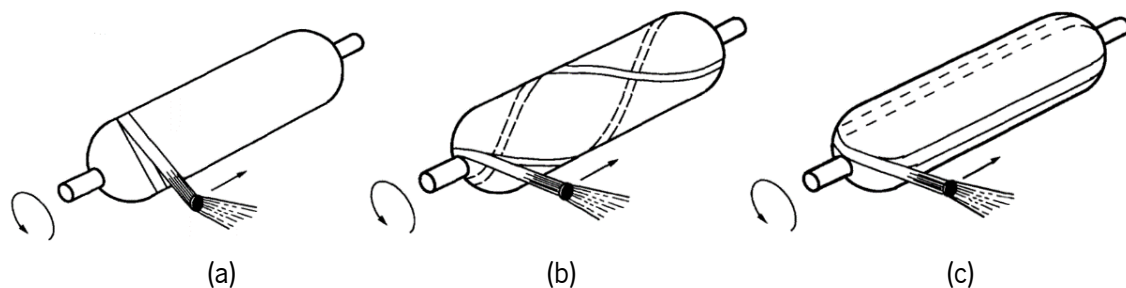


Figure 18: Schematic representation of winding patterns: (a) circumferential, (b) helical and (c) polar [107]

Commonly, the production of COPVs uses carbon fibres, glass fibres or aramid fibres, or a combination of those. Carbon fibres are preferred for storage pressures above 35 MPa, commonly found in hydrogen storage applications, due to their high specific strength [108], [119]. So far, the majority of the COPVs use thermoset resins, such as epoxy, phenolic or polyester. Nevertheless, epoxy is preferred owing to its good processability by filament winding due to its low viscosity, good mechanical properties and chemical stability [108]. Besides to thermoplastic liners used in type IV vessels, thermoplastic matrices are also being explored to produce the composite overwrap. Villalonga et al. [110] reported the production of a type IV COPV for hydrogen storage up to 70 MPa. The liner was produced by reactive rotational moulding of polyamide 6 monomers, where polymerization and forming took place simultaneously, preventing thermal oxidation. The composite overwrap was made of T700 carbon fibre and polyamide 6 prepreg tape. The equipment

for the production of the overwrap included an infrared heating system to preheat the tape to a temperature just below the melting temperature of the matrix and another one to heat the tape above the melting temperature. The compaction of the layers was ensured by a compression roll. Murray et al. [109] reported the production of a type IV COPV for cryogenic fuel vessels for space applications. The liner was made of PEEK and produced by rotational moulding, and the composite overwrap was made of CF/PEEK tape and produced by laser assisted tape-placement.

After processing, the cured type III pressure vessels are subjected to an *autofrettage* process. In this process, a permanent plastic deformation is imposed on the green load sharing elastic liner, by pressurizing it above P_y , the pressure at which the metallic liner is stretched past the yielding point (see Figure 19). After deloading, the composite overwrap has a tensile preload, while the liner becomes preloaded in compression, resulting on an improved fatigue strength of the COPV [120]. Figure 19 shows the link between stress/pressure and strain in a COPV and its components, when subjected to loading and unloading. The green lines represent *autofrettage* process loading. There is a linear increase of pressure up to P_y in the COPV (left side graph), at which the liner has a stress of σ_l^y , (right side graph). Above P_y , there is a variation on the strain/pressure curve slope of the COPV and on the strain/stress curve slope of the liner. If the pressure is further increased, burst occurs (red lines). The blue line represents both loading and unloading up to the maximum working pressure, p_h , after the *autofrettage* process. In the right side graph, it is possible to see the permanent residual compressive stress in the liner, σ_l^R , after deloading, due to the plastic deformation imposed by *autofrettage*. [121]. The middle graph shows the linear behaviour of the composite overwrap, where it is possible to see the residual tensile stress after *autofrettage*, σ_c^R . The theoretical background for the calculation of the minimum pressure P_y that causes yielding of the liner, after the COPV has been cured, is presented in section 3.4.3.

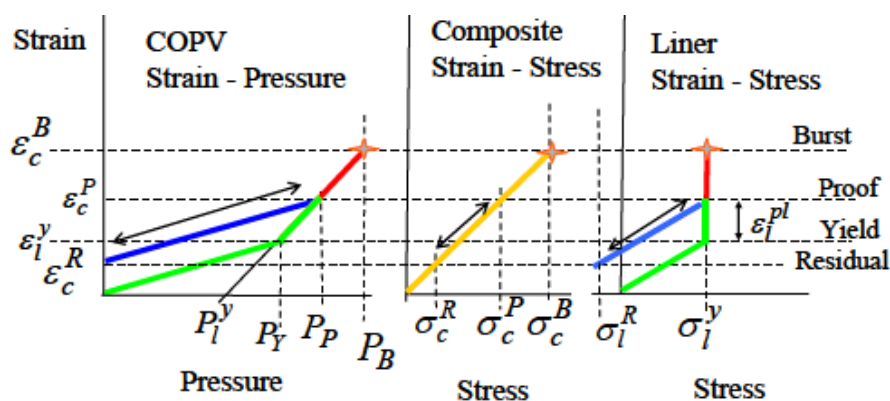


Figure 19: Stress behaviour of liner and composite overwrap and their contribution to overall strain vs. pressure behaviour of the COPV during *autofrettage* and following deloading and loading cycles [121]

2.4.3. Instrumentation of Composite Overwrapped Pressure Vessels

The complexity of loading schemes, the array of construction solutions provided by different manufacturers, and material degradation in the COPV pose some reliability issues on the performance of these systems. Periodic inspections through traditional non-destructive inspection methods such as ultrasonic inspection, radiography, acoustic emission, shearography and visual inspection might miss crucial information, for accurate assessment of the structural condition of the COPV. In contrast, instrumentation of composite pressure vessels and the implementation of structural health monitoring systems provides additional safety, with the acquired continuous data enabling the detection of critical behaviour and defects. The measurement of strain/pressure and temperature during operation may enable the evaluation of stress/strain and temperature distribution, onset and propagation of delamination and fracture, leakage detection, etc. [8]

The real-time detection of damages such as BVID or fibre breakage may prompt the immediate repair or inactivation of the COPV before burst may happen. Several studies have reported the instrumentation of COPV for structural health monitoring [122], [123], impact damage detection [124], [125] and a few of them have also reported the use of the same sensors for monitoring of the manufacturing process [117] and curing procedure [8]. The instrumentation of COPV is mainly restricted to fibre optic based sensors [8], [117], [123]–[128]. Back in 2010, Frias et al. [122] have compared the performance of FBG and PVDF piezoelectric sensors embedded in different locations of the steel liner/composite overwrap interface, to monitor the strain in both longitudinal and circumferential directions. The PVDF and FBG sensors showed good agreement under cyclic internal pressure loading up to 40 bar. However, this COPV construction is not optimal for high pressure hydrogen gas storage applications.

Sensors should be integrated at places of higher strains, which usually happens in between the liner and first layer of the composite overwrap or in between different layers of the composite overwrap. Gaşior et al. [8] have embedded FBG sensors on the surface of the polyethylene liner of a type IV COPV for hydrogen storage at 700 bar for automotive applications. Three optical fibres having 4 FBG sensors each were placed in the axial direction of the liner, separated by an angle of 120°. The sensors enabled the control of the manufacturing step, by the measurement of strain during winding and curing. The suitability of the system for operation monitoring was demonstrated during pressure cyclic testing. Saeter et al. [124] embedded a network of optical fibre distributed Rayleigh backscattering sensors, in between layers of hoop wound layers. The authors tested two configuration networks for impact damage detection: (1) a grid with OF running in the longitudinal

and hoop direction within a region of $3 \times 3 \text{ cm}^2$; and (2) a spiral placed in the hoop direction, although with a pitch angle different of that of the wound CF layers. While the grid network could evaluate the damage extent in two directions, the authors disclosed this was a labour-intensive procedure. The spiral network demonstrated to be suitable for damage location and severity assessment. With the carbon fibres bearing most of the loading in the COPV, it is advantageous that strain is measured along the carbon fibres direction. Nevertheless, challenges concerning practical integration of OF, due to their fragility, intrusiveness (producing ply defects), and inability to contour some geometric characteristics like hard curvatures should not be disregarded [122], [124].

The use of the SMART Layer was also demonstrated to be adequate for impact damage detection and location on filament wound composite structures that could be employed on solid rocket motor cases and liquid fuel bottles [129]. Eight strips were embedded into a filament wound composite bottle with an aluminium liner, each strip having five PZT sensors of 6.35 mm diameter and 0.25 mm thickness. Four strips were embedded one layer above the liner and four strips one hoop layer below the surface of the bottle. The distance between two neighbouring PZT sensors was 140 mm on the cylindrical section and 114 mm on the dome section of the bottle, and 153 mm in hoop direction, producing a square grid of sensors spread over the bottle. Some of the stripes can be seen in Figure 20, as well as the finished bottle. The diagnostic system forwards an electric signal to the PZT actuators, which consequently produce a stress wave that propagates through the structure, per converse piezoelectric effect. This mechanical excitation is detected by the PZT sensors, by piezoelectric effect. The health condition of the structure over time is assessed by using the diagnostic software that collects the sensor signals over time and compares them with a baseline signal set, following the Lamb wave approach. The difference between baseline and after impact damage signals produces a scatter signal, which can be used to locate and determine the extent of the produced damage. The scatter signals for all defined actuator-sensor paths can be processed to render an image that shows the location and size of the damage. An impact damage with an area of about 12 mm x 20 mm was successfully located by the diagnostic software.

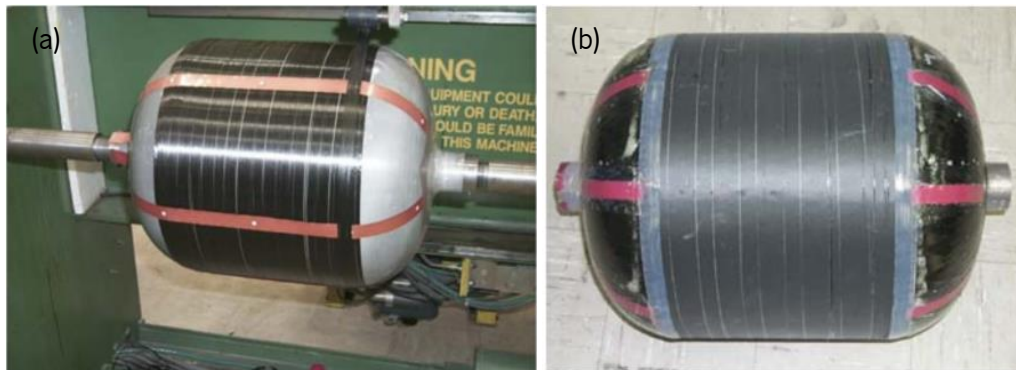


Figure 20: (a) SMART Layer strips embedded on bottle during filament winding process; (b) finished bottle. Adapted from [129].

2.5. Outlook and trade-off

Although research on SHM is already being conducted for many years, the technology transfer to industrial application is held back on the fact that laboratory work has mostly been done on simple beam and plate structures. However, most of real problems are only observed on real complex structures, often exposed to harsh and changing environmental conditions [10].

The development and implementation of SHM systems requires a multidisciplinary approach to evaluate each specific case. The best sensing approach can only be chosen once analysed the specificity of the structure, including shape, size, constituent materials, loading condition and manufacturing technology, operational environment, expected damage location and type and maintenance. Even though it is possible to predict the locations prone to fatigue, unpredictable and random impact events may challenge the design of the sensor network. Sensor location at strategic sites of the structure should be optimised to better detect damage. While surface mounted sensors are more convenient to attach, maintain and replace, their accuracy might be affected by ambient noise as the sensors are directly exposed to the environment. Oppositely, embedded sensors have higher sensitivity, signal-to-noise-ratio, stability, durability, and repeatability, as they are protected from the environment. However, embedded sensors may face high pressures and temperatures during composite manufacturing, leading to short-circuits in the sensor system. It should also be considered that embedding a large number of sensors and wires may prejudice the mechanical properties of the host structure. The choice between active and passive sensing systems should also be carefully considered. Active sensing system require an input signal, thus allowing the structure to be continually monitored or assessed at a given time. However, an active SHM system brings the disadvantage of requiring an extra component, a signal generating hardware, increasing

power consumption and complexity of the system. On the contrary, passive sensing systems only require the sensors to monitor the host structure condition. However, this approach can only detect damage as it occurs and does not allow to assess the structural condition of a part at any required time [130].

An effective structural health monitoring system must be able to detect early matrix related damage such as matrix cracks and debonding, allowing to take early preventive measures upon need. The analysed literature shows that fibre optic sensors, in particular FBG sensors, are able to detect subtle damages produced by low velocity impact events. The sensing techniques commonly used with piezoelectric sensors (electromechanical impedance, Lamb waves and acoustic emission) are all sensitive to damage. Within the wide range of piezo-resistive sensing approaches, nanocarbon matrix reinforcement, fibre coated based sensors, and film sensors can detect early matrix dominated damage. Nanocarbon based piezo-resistive sensing are encouraging approaches that may bring the advantage of mechanical reinforcing effect, yet they may bring increased difficulties to the manufacturing processes.

Many sensors can be taken advantage of from the beginning of the production process and embedding procedure for cure monitoring purposes. Understanding sensor/host material interaction is fundamental to select a suitable location of the embedded sensors for cure monitoring. For instance, embedding FOS in the transverse direction of the reinforcing fibres can be advantageous for resin cure monitoring as the resin gives a high contribution to the transverse direction and produces higher compressive strain, as opposed to the longitudinal direction where the composite properties are mainly affected by the reinforcing fibres. However, the embedment of FOS in the longitudinal direction along the reinforcing fibres produces the least impairment of the mechanical properties of the host composite structure.

Considering the literature survey conducted on sensing methodologies for process and SHM of polymeric composites, two sensing methodologies were selected to be initially studied at laboratory scale. First of all, the decision of adopting active sensing technologies was made, based on the premise that the sensing system should be able to assess the structural condition of an aeronautic component at any time. The selected sensing technologies are:

- Optical FBG sensors

FBG sensors were selected due to their compatibility with composites fabrication, ability to monitor the fabrication process itself and curing, reduced cabling as several FBG sensors can be multiplexed in the same OF, minimizing mechanical impairment of the structure when low density of OF is used, and capability of impact damage detection.

- EIT on CFRP composites, using the piezo-resistive properties of CF

The use of EIT does not interfere with the fabrication process of composites, since this only requires that electrodes are fixed at the boundary of the laminate and, thus, the final mechanical properties of the composite are not affected either. Additionally, this is a very cost-effective approach.

2.6. Objectives

The ultimate objective of this work was to implement a SHM system on a real engineered CFRP part used in aerospace applications. The SHM system must assess the overall condition of the structure, detect impact damage and, preferably, be able to monitor the production and curing processes as well.

To achieve the basic objective of this work, first, different sensing methodologies were exploited in CFRP laminates at laboratory scale. Separate studies were conducted on the different sensing methodologies to:

- evaluate the overall capability of the considered techniques to comply with the above mentioned objectives in terms of sensing data and its usefulness;
- develop integration methodologies with minimal interference with the production process;
- assess their effect on the mechanical performance of the part/specimen, when compared to the non-instrumented reference part/specimen.

The studied technologies were compared, and the most favourable sensing technology further developed for a real engineering application. For that, the structural design, material selection and optimisation of production process were carried out.

Chapter 3

Theoretical Background

3.1. Introduction

This chapter presents the theoretical background that supported the execution of the work reported in chapters 4 and 5.

3.2. Optical Fibres

As mentioned in section 2.3.1.1, FBG sensors are sensitive to both mechanical and thermal strain and the encapsulation of FBG sensors in capillaries can be used to decouple the mechanical and thermal contributions to the total strain. By subtracting the change of central wavelength measured on the encapsulated FBG sensor (FBG_{T-CAP}), $\Delta\lambda_T$, the portion of central wavelength change due to the effect of mechanical strain alone on the bare FBG sensor (FBG_{S+T}), $\Delta\lambda_S$, the imposed mechanical strain variation, $\Delta\varepsilon$ ($\mu\varepsilon$), and temperature change, ΔT ($^{\circ}\text{C}$), may be calculated by equations 7 and 8, respectively.

$$\Delta\varepsilon = \Delta\lambda_S \times S_\varepsilon \quad (7)$$

$$\Delta T = \Delta\lambda_T \times S_T \quad (8)$$

where S_ε is the strain sensitivity and S_T is the temperature sensitivity [131]. The used FBG sensors had strain and temperature sensitivities of 1.2 pm/ $\mu\varepsilon$ and 10 pm/ $^{\circ}\text{C}$, respectively, as given by the optical fibre manufacturers.

3.3. Electrical Impedance Tomography for Damage Localisation Monitoring

Different methodologies for structural health monitoring, detection and localisation of damage in composite structures have been already explored in the literature. Although different types of sensors are well developed, such as optical fibre-based sensors and piezoelectric sensors, they need to be embedded in the composite structure during manufacturing, imposing pauses in the manufacturing process, and leading to potential effects on the mechanical performance of such structures [3]. As EIT technique reconstructs tomographic images of the spatial electrical

conductivity distribution, instead of intrusive sensors, it only requires the use of surface electrodes. A number of electrodes are mounted along the boundary of the electrically conductive composite part, being the electric current inserted through a pair of electrodes, and the resulting voltages measured in the remainder consecutive pairs of electrodes [75].

Static electrical impedance tomography reconstruction algorithms can present some measurement errors, as EIT is more sensitive to changes close to the boundary than to changes happening within the medium. A minor error on the electrode positioning may produce the same voltage measurements as a severe inhomogeneity found in the middle of the medium. Thus, dynamic imaging reconstruction algorithms are good alternatives, because a conductivity image at instant t_2 is calculated from the difference of voltage data v_2 at that instant and the previous measured voltage data v_1 at time t_1 [132]. Imaging can be regarded as a linear problem, using an algorithm for difference EIT. Difference data, y , from difference EIT is calculated according to equation 9 [133].

$$[y]_i = [v_2]_i - [v_1]_i \quad (9)$$

The conductivity of the medium is modelled through a finite element model, which decomposes it into n_N elements, represented by the conductivity vector $\sigma \in \mathbb{R}^{n_N}$. The vector of conductivity change x can also be calculated by difference EIT, by the difference between the current conductivity distribution σ_2 and the reference conductivity distribution σ_1 , as presented in equation 10 [133].

$$x = \sigma_2 - \sigma_1 \quad (10)$$

The forward problem in difference EIT, i.e. finding the boundary voltage data from the reference conductivity, can be linearly solved by equation 11 [133].

$$y = Jx + n \quad (11)$$

where J is the Jacobian matrix and n is the measurement noise.

A one-step difference GN algorithm was used to solve the EIT inverse problem and for image construction. These approaches can calculate the conductivity as a linear matrix in a fast way, enabling real-time image reconstruction. The one-step GN algorithm looks for the minimized solution \hat{x} of the sum of the quadratic norms as stated in equation 12 [133].

$$\|y - J\hat{x}\|_{\Sigma_n^{-1}}^2 + \|x - x^0\|_{\Sigma_x^{-1}}^2 \quad (12)$$

being x^0 the expected conductivity changes of the element, being zero in difference EIT, $\sum n$ the covariance matrix from the measurement noise, n , and $\sum x$ the anticipated image covariance.

The linearized and one-step inverse solution is presented in equation 13 [133].

$$\hat{x} = (J^T W J + \lambda^2 R)^{-1} J^T W y \quad (13)$$

where W and R , given by equations 14 and 15, respectively, are heuristically calculated. R is regularization matrix, and λ is the hyperparameter given by equation 16.

$$W = \sigma_n^2 \Sigma_n^{-1} \quad (14)$$

$$R = \sigma_x^2 \Sigma_x^{-1} \quad (15)$$

$$\lambda = \frac{\sigma_n}{\sigma_x} \quad (16)$$

being σ_n the average amplitude of the measurement noise and σ_x the initial amplitude of the change in conductivity.

Differently from the studies reported in the literature, which use twill or plain fabrics [72], [73], [74], [134]–[136], the present work was conducted on unidirectional carbon fibre fabrics, having different layup configurations. It is relevant to study composites with this fabric construction, as it is frequently used in advanced application, such as aerospace and aeronautics. Unidirectional fibres are expected to contribute to a much higher anisotropy than twill or plain fabrics. Two different layup laminates were produced by VARI process: a quasi-isotropic laminate, which is expected to present closer characteristics to an isotropic material, and an unbalanced laminate, having more fibre layers in one orthogonal direction, contributing to an additional level of anisotropy that EIT has never assessed before in the literature. The performance of EIT to detect damage on those laminates was compared. More details on the laminate configuration are presented in section 4.2.1.

3.4. Design of Composite Overwrapped Pressure Vessels

There are, essentially, two failure mechanisms in COPV, being intralaminar damage the main contributor to COPV's mechanical performance deterioration, that leads to burst. On the other side, interlaminar damage, in the form of delamination, can be neglected as two adjacent composite layers keep pressing against each other while being pressurized. As internal pressure increases,

matrix cracking and interface debonding increase and only when a significant amount of fibre breakage abruptly occurs, the COPV burst is observed [137].

3.4.1. Netting Theory

The preliminary design of a composite overwrapped pressure vessel can be done resorting to the netting theory, prior to performing more complex finite element modelling (FEM) analysis. The netting theory is based on a few assumptions: the vessel walls work as a membrane, not carrying any out of plane bending nor shear loading; the loads are fully supported by the fibres, where resin contribution is not considered; and there is no interaction between layers wound at different winding angles [138].

The membrane loads in the hoop and meridional directions, N_θ and N_ϕ , respectively, are represented in Figure 21 (a). The fibre load carrying in a helical layer is presented in Figure 21 (b). For load equilibrium, equations 17 and 18 need to be satisfied.

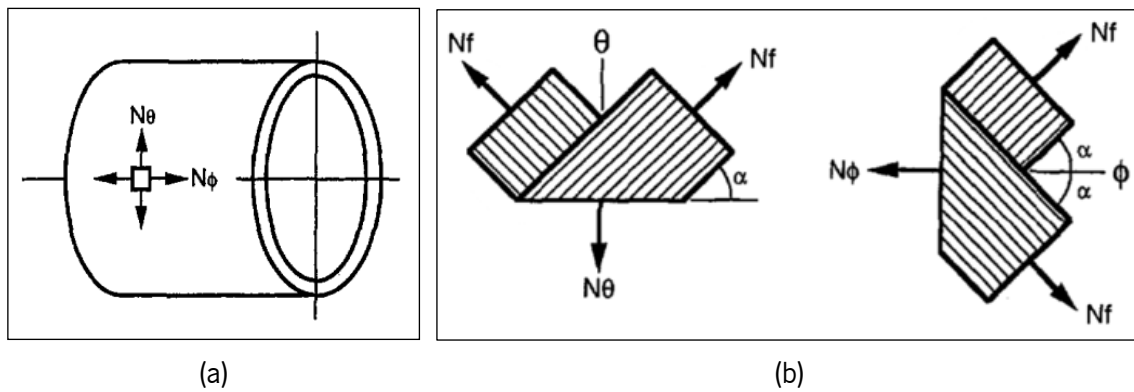


Figure 21: (a) Orientation of the membrane loads in the hoop (N_θ) and meridional (N_ϕ) directions of a cylinder; (b) free-body diagram of fibres in a helical layer, relative to the hoop and meridional directions. Adapted from [138].

$$N_\phi = 2N_f \cos^2 \alpha \quad (17)$$

$$N_\theta = 2N_f \sin^2 \alpha \quad (18)$$

being N_f the load supported by the fibres in that helical layer, wound with winding angle α .

The membrane loads in a pressure vessel, of diameter D , and with an internal design pressure P_D , can be calculated by equations 19 and 20.

$$N_\phi = \frac{P_D \times D}{4} \quad (19)$$

$$N_\theta = \frac{P_D \times D}{2} \quad (20)$$

The admissible design stress, σ_{ut} , can be calculated from the ultimate strength of the unidirectional composite, X_t , and safety factor, SF , as stated in equation 21 [139].

$$\sigma_{ut} = \frac{X_t}{SF} \quad (21)$$

The total thickness of the helical layers, $t_{\alpha f}$, and of the hoop layers, t_{90f} , can be calculated according to equations 22 and 23.

$$t_{\alpha f} = \frac{N_{\theta}}{\sigma_{ut} \cdot \cos^2 \alpha} \quad (22)$$

$$t_{90f} = \frac{N_{\theta} - N_{\phi} \cdot \tan^2 \alpha}{\sigma_{ut}} \quad (23)$$

The total thickness of the composite overwrap can be calculated by equation 24.

$$t = \frac{t_{\alpha f} + t_{90f}}{FVF} \quad (24)$$

where FVF is the fibre volume fraction. Finally, the number of helical and circumferential layers, n_h and n_c , respectively, can be calculated according to equations 25 and 26.

$$n_h = \frac{t_{\alpha f}}{FVF \cdot t} \quad (25)$$

$$n_c = \frac{t_{90f}}{FVF \cdot t} \quad (26)$$

3.4.2. Finite Element Modelling

Nowadays, COPVs are designed resorting to FEM analysis to optimize the composite layup configuration. Moreover, FEM analysis can assist the selection of sensors location for SHM, by identifying the most critical areas in the structure.

Given the small thickness of the composite overwrap, when compared to its radius, the composite overwrap can be modelled by shell elements. Abaqus offers two types of shell elements for modelling: conventional shell and continuum shell elements. Conventional shell elements are defined by the local planar dimensions, surface normal, and initial curvature of a discretised reference surface. Thus, the elements thickness is defined by the inputted section properties, rather than by the element nodes. Differently, continuum shell elements discretize a three-dimensional part and the thickness is defined by the geometry of the element nodes. Nonetheless, the modelled kinematic and constitutive behaviour of continuum shell elements is similar to that

of conventional shell elements. The stress in the thickness direction is considered to be zero for conventional shells. Thus, the resulting transverse strain is accounted from the Poisson's ratio effect. Oppositely, continuum shells may present added strain besides that caused by the Poisson's effect. The conventional shell elements present the great advantage of being able to model both thin and thick shells and can model large strains, reason why this work used S4 elements. For an increased shell thickness, Abaqus software uses thick shell theory, while for lower shell thickness, it uses the Kirchhoff shell theory [140]. For the case of the optimised composite overwrap layup, given its thickness/radius ratio, the conventional shell elements are modelled as thick elements.

There are several failure criteria for damage initiation, being the Hashin's and Hashin and Rotem's failure criteria, some of the most used for composite materials. These are interactive failure criteria, which consider four damage modes: fibre breakage due to tension, fibre buckling and kinking due to compression, matrix cracking due to transverse tension and shearing, and matrix crushing due to transverse compression and shearing [141]. The failure initiation by any of the four damage mechanisms can be predicted by equations 27 – 30.

$$F_f^t = \left(\frac{\hat{\sigma}_{11}}{X^T} \right)^2 + \alpha \left(\frac{\hat{\tau}_{12}}{S^L} \right)^2, \text{ if } \hat{\sigma}_{11} \geq 0 \quad (27)$$

$$F_f^c = \left(\frac{\hat{\sigma}_{11}}{X^C} \right)^2, \text{ if } \hat{\sigma}_{11} < 0 \quad (28)$$

$$F_m^t = \left(\frac{\hat{\sigma}_{22}}{Y^T} \right)^2 + \left(\frac{\hat{\tau}_{12}}{S^L} \right)^2, \text{ if } \hat{\sigma}_{22} \geq 0 \quad (29)$$

$$F_m^c = \left(\frac{\hat{\sigma}_{22}}{2S^T} \right)^2 + \left[\left(\frac{Y^C}{2S^T} \right)^2 - 1 \right] \frac{\hat{\sigma}_{22}}{Y^C} + \left(\frac{\hat{\tau}_{12}}{S^L} \right)^2, \text{ if } \hat{\sigma}_{22} < 0 \quad (30)$$

being X_t and X_c the longitudinal tensile and compressive strength, respectively, Y_t and Y_c the transverse tensile and compressive strength, respectively, S^L and S^T the longitudinal and transverse shear strength, respectively, and $\hat{\sigma}_{11}$, $\hat{\sigma}_{22}$ and $\hat{\tau}_{12}$ the components of the global stress tensor. α is a coefficient that defines the influence of shear stress on the fibre damage initiation criterion by tensile stresses, being 0 for the use of the Hashin and Rotem's failure criterion and 1 for the Hashin's failure criterion.

However, identification of damage initiation may not be suitable for burst pressure (P_b) prediction, as the composite material has still some load bearing capabilities beyond the level of applied pressure at the step time at which first ply failure is detected. Hence, damage evolution, accounting

for stiffness degradation, can be used in FEM analysis for more accurate prediction of the final P_b . Thus, the composite overwrap layup configuration can be better optimised for weight efficiency to achieve a specified working pressure, given a defined safety factor [137]. While, before damage initiation, the composite material is modelled with a linear elastic behaviour, given its orthotropic stiffness matrix, afterwards the material response is modelled considering the damaged elasticity matrix, C_d , as given by equation 31 [142].

$$\sigma = C_d \varepsilon \quad (31)$$

where ε is the strain and C_d is given by equation 32.

$$C_d = \frac{1}{D} \begin{bmatrix} (1 - d_f)E_1 & (1 - d_f)(1 - d_m)v_{21}E_1 & 0 \\ (1 - d_f)(1 - d_m)v_{12}E_2 & (1 - d_m)E_2 & 0 \\ 0 & 0 & (1 - d_s)GD \end{bmatrix} \quad (32)$$

being d_f , d_m , d_s the damage variable for fibre, matrix and shear damage, respectively, E_1 and E_2 the elastic modulus in the fibre and matrix directions, respectively, G the shear modulus, v_{12} and v_{21} the Poisson's ratios, and D given by equation 33.

$$D = 1 - (1 - d_f)(1 - d_m)v_{12}v_{21} \quad (33)$$

As material softening may cause mesh dependency issues, Abaqus inputs a characteristic length in the model, for the constitutive law to be defined with a stress-displacement relation. The damage variable progresses in a way that the stress-displacement presents the behaviour shown in Figure 22. The initial positive slope represents the stress-displacement behaviour by the linear elastic material before damage initiation, at a displacement δ_{eq}^0 , whereas the following negative slope represents the stress-displacement behaviour considering the evolution of the damage variable, where at a displacement δ_{eq}^f the material is fully degraded considering a certain failure mode.

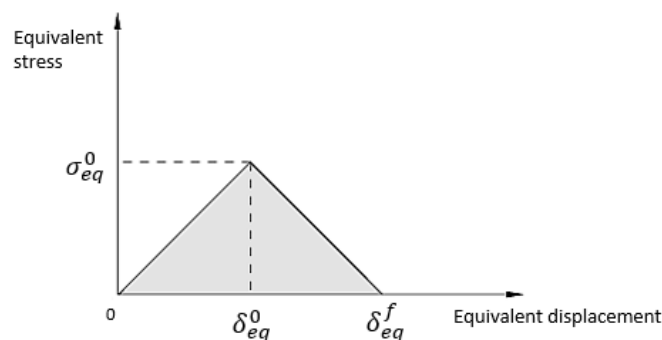


Figure 22: Modelled equivalent stress vs. equivalent displacement during elastic behaviour prior to damage initiation and (positive slope) and during damage evolution (negative slope) [142]

The metallic liner was modelled with fully integrated linear solid elements, C3D8, 8-node bricks, as excessive shear loading is not expected. The aluminium material of the liner presents an elastic-plastic behaviour. The plastic behaviour was modelled in the Abaqus software by inputting the true plastic stress/strain data. For that, the nominal plastic stress/strain data obtained from tensile tests were converted into true plastic stress/strain data. The conversion between true stress/strain and nominal stress/strain is derived through equations 34 – 40 [140]. The nominal strain, ε_{nom} , is given by equation 34.

$$\varepsilon_{nom} = \frac{l - l_0}{l_0} = \frac{l}{l_0} - 1 \quad (34)$$

By adding unity and applying the natural log to both sides of the equation, the relationship between true strain and nominal strain is obtained, as stated in equation 35.

$$\varepsilon = \ln(1 + \varepsilon_{nom}) \quad (35)$$

Considering incompressibility in both plastic and elastic deformation, equation 36 is derived.

$$l_0 A_0 = l A \quad (36)$$

Thus, the present area is related to the initial area by equation 37.

$$A = A_0 \frac{l_0}{l} \quad (37)$$

The true stress can now be defined as stated in equation 38.

$$\sigma = \frac{F}{A} = \frac{F}{A_0} \frac{l}{l_0} = \sigma_{nom} \left(\frac{l}{l_0} \right) \quad (38)$$

As equation 34 can also be written in the form presented in equation 39, the relationship between true stress and nominal stress and strain is found as presented in equation 40.

$$\frac{l}{l_0} = 1 + \varepsilon_{nom} \quad (39)$$

$$\sigma = \sigma_{nom}(1 + \varepsilon_{nom}) \quad (40)$$

3.4.3. Autofrettage

The minimum pressure P_y that causes yielding of the liner is correlated to the yield stress of the liner, σ_l^y , as stated in equation 41 [121].

$$P_y = \frac{\sigma_l^y}{E_l^*} 2(K_l + K_c) \quad (41)$$

where E_l^* is the biaxial modulus of the liner, given by equation 42, and K_l and K_c are the liner's and composite's shell stiffnesses, given by equation 43 and 44, respectively [121].

$$E_l^* = \frac{E}{(1 - \nu)} \quad (42)$$

where ν is the Poisson's ration of the liner [121].

$$K_l = \frac{t_l E_l^*}{R_l} \quad (43)$$

$$K_c = \frac{t_c E_c^*}{R_c} \quad (44)$$

where t_l and t_c are the liner's and composite's shell thickness, respectively, R_l and R_c are the liner's and composite's inner shell radius, respectively, and E_c^* is the biaxial modulus of the composite, as given by equation 45 [121].

$$E_c^* = \frac{E_f \times v_f}{2} \quad (45)$$

where E_f and v_f are the fibres' elastic modulus and volume fraction, respectively [121].

However, this methodology for *autofrettage* pressure determination is not widely adopted. Usually, the *autofrettage* pressure is determined empirically, which increases costs for design. A general guideline points at an *autofrettage* pressure that is at least 1.5 times the service pressure [143], [144].

Chapter 4

Materials and Experimental Procedures

4.1. Introduction

This chapter presents the materials and summarises the theoretical background and experimental procedures used in this work. Firstly, the experimental work for assessment of the capabilities of the preselected SHM techniques (i: optical FBG sensors and, ii: self-sensing of CFRP composites with EIT) for cure monitoring and damage detection in CFRP composite laminates is described. Specifically, the conducted initial work assessed the use of optical FBG sensors for cure monitoring and BVID detection, caused by impact loading, and damage detection and localisation by EIT technique, namely through-thickness holes and impact damage. The preliminary work conducted at laboratory specimen level allowed to select a sensing strategy that enabled the deployment of a monitoring system that can monitor the processing stage, testing and structural health as well as detect and localize impact damage on COPV for a UAV. Thus, finally, this chapter presents the development, production, and testing procedures of a composite pressure vessel prototype for high-pressure hydrogen storage, to validate and demonstrate the possibility of using embedded optical FBG sensors for process monitoring and real-time health monitoring system in-service of a real engineering component.

4.2. Materials

4.2.1. Raw Materials

A bicomponent epoxy resin system, consisting in a Biresin® CR83 resin and a CH83-6 hardener from Sika AG, Switzerland, and a unidirectional 340 g/m² carbon fibre fabric UT350 from Toray Industries Inc, Japan, having a thickness of approximately of 0.42 ± 0.05 mm, were used to produce the CFRP composite laminates in this work. Both these resin system and carbon fibre fabric have already been frequently used with success in production of aeronautic and some aerospace structural parts by using the VARI process in many other previous R&D projects.

According to the manufacturer instructions, the epoxy matrix was prepared using the resin and hardener weight proportion of 100% – 30%.

CFRP laminates having two different layup sequences were used in this work: an 8-layer quasi-isotropic laminate with layup sequence $[0/45/90/-45]_s$, and a 10-layer symmetric laminate with the layup sequence: $[0/0/45/90/-45]_s$. The quasi-isotropic and unbalanced laminates present final thicknesses of approximately 2.6 mm and 3.1 mm, respectively. While both types of laminate were used in the EIT monitoring tests, the studies carried out with optical FBG sensors only used the 10-layer laminate.

A 6 mm wide prepreg tape made of Tenax®-E ITS50 carbon fibre from Teijin, Japan, and RCX0125 epoxy resin from RED Composites, United Kingdom, was used to overwrap the aluminium alloy 6061-T6 liner of the filament wound composite pressure prototype vessel for hydrogen storage that was manufactured and tested in the present work. The prepreg tape was manufactured by Amtrol-Alfa, Portugal. The liner, which was simultaneously used as mandrel at the filament winding, was constructed in aluminium to ensure a complete permeability of the vessel and then avoiding any eventual through-thickness hydrogen releasing that, due to its very small atomic size, may occur at high pressure.

4.2.2. Optical Fibres

The preliminary work, at specimen level, used single mode polyimide coated small diameter optical fibres, with 80 μm outer diameter, from Technica. Each optical fibre had a strain and temperature sensitive FBG sensor, FBG_{S+T} , and a temperature sensitive only FBG sensor, FBG_{T-CAP} , with central wavelength (CWL) at 1540 and 1550 nm, respectively. The two sensors being 2.5 cm away from each other. Each FBG_{T-CAP} sensor was encapsulated inside a fused silica capillary tube, from Specanalítica Lda, as represented in Figure 23. The capillary was cut to be about 4 cm long and had an internal and external diameter of 150 and 363 μm , respectively. One end of the optical fibre, near the FBG_{T-CAP} , is left loose inside the capillary, and both extremities of the capillary were closed by epoxy resin, to prevent resin to go inside during the VARI process. One extremity of the capillary is glued to the optical fibre passing through. As the FBG_{T-CAP} is enclosed and can move freely inside the capillary, its CWL variation is only dependent on the coefficient of thermal expansion (CTE) of the optical fibre. On the other side, FBG_{S+T} sensors are in direct contact with the resin/laminate material, being the CWL variation dependent on the CTE of the optical fibre itself and on the mechanical strain of the surrounding material. Initial cure monitoring studies of

the resin system alone and following vacuum assisted resin infusion production of CFRP laminates, used the above described FBG sensor construction. Additionally, type-K thermocouple was used for room temperature monitoring, using the NI 9211 temperature acquisition system from National Instruments.

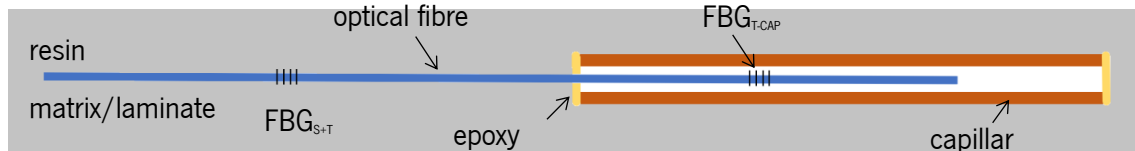


Figure 23: Schematic representation of the optical fibre configuration depicting the isolation of the FBG_{T-CAP} at the far end of the optical fibre into a capillary tube, where epoxy resin is used to close both ends, and the FBG_{S+T} is in direct contact with the resin/laminate

For comparison purposes and to evaluate whether standard diameter optical fibres impose additional residual strains on CFRP laminates, monitoring of the CFRP production was conducted using large diameter optical fibres. These were single mode 150 μm outer diameter polyimide coated optical fibres from HBK FiberSensing, Portugal, with a FBG_{S+T} sensor and a FBG_{T-CAP} sensor with central wavelengths at 1540 and 1555 nm, respectively. The FBG_{T-CAP} sensor is encapsulated into a 4 cm long microtube with a 900 μm diameter.

4.3. Experimental Procedures

4.3.1. Production of CFRP Laminates by Vacuum Assisted Resin Infusion

CFRP laminates were produced with different dimensions by using the VARI process and the setup similar to the applied to embedding the optical FBG sensors that is shown schematically in Figure 24. A glass plaque was used as bottom mould where a release agent HP7 from Marbocote was applied. Layers of carbon fibre fabric and OFs were stacked with the desired orientation. Peel ply, for easy demoulding, and flow enhancement medium, to ease resin spreading, were placed on top of the fabric layers. The inlet and outlet resin flow lines were installed and connected to a resin container and a resin catch pot, respectively. Everything was sealed with plastic bag and sealing tape before applying vacuum, at 400 mbar. The resin mixed with the hardener accordingly to the manufacturer's instructions described in the above paragraph 3.2.1 was placed in the resin container for impregnating the dry carbon fibre layers during the infusion. Vacuum was then applied for compaction, air removal and sucking the resin from the container and causing its infusion and ensuring the complete impregnation of the carbon fabrics. The laminate was cured at room temperature under vacuum for about 40 hours. Then, the laminate was removed and subjected to

post curing process at 70 °C for 8 hours at atmospheric pressure. The post-cure was performed with heating and cooling rates of about 15 °C/h to reduce temperature gradients.

The unbalanced 10-layer CFRP laminates for being monitored by using optical FBG sensors were produced with two different dimensions due to the SDOF and LDOF distinct lengths. While laminates with embedded SDOF presented dimensions of 150 × 100 × 3.3 mm, those ones with embedded LDOFs were produced with 190 × 100 × 3.3 mm to be later exposed to low velocity impact events. Differently, both CFRP laminates (the 8-layer and 10-layer one) monitored with EIT were produced with dimensions of about 500 mm × 700 mm to be later cut in several plate specimens having about 150 mm × 100 mm to be subject to drop-weight impact tests accordingly to the ASTM D7136 standard.

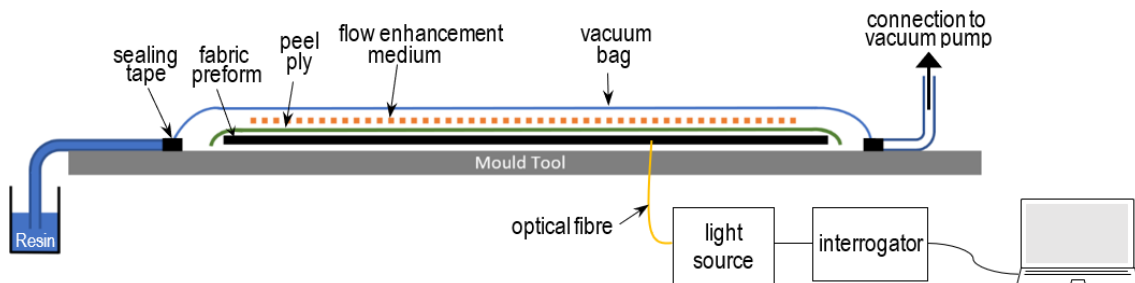


Figure 24: Schematic representation of the VARI process and FBG monitoring set up

4.3.1.1. Embedding Optical FBG Sensors into CFRP Laminates

To monitor the cure and the impact damage caused in the CFRP laminates, optical FBG sensors were embedded during their VARI processing. Before embedding the sensors into the CFRP laminates, the optical FBG sensors were firstly overwrapped with a flexible foam or a thin film and adhesive tape to become protected along their length, going from the edge of the carbon fibre fabrics to the sealing tape that holds the vacuum. Then, the peel ply was placed underneath and on top of the optical fibre wrapping to ease demoulding. To mitigate the impairment of optical fibre embedment on the mechanical properties of the composite laminates, this work used SDOF, which were placed parallel to the direction of the adjacent reinforcing fibres. Standard diameter optical fibres were also used for comparison. The wavelength shift of the FBG sensors was acquired from the beginning of the production process, to follow infusion, ambient curing and post curing stages and evaluate residual strains resultant from the production process.

Often OF-based sensors are embedded in the composite mid-plan, which is usually not where damage is created, which may lead to undervalued damage extent. In this work, the through-thickness embedding location of FBG sensors and its influence on damage detection and

severeness evaluation was assessed. The locations of the optical fibres were chosen so that they are embedded in between two layers of reinforcing fabric with the same direction, resulting in minimal defects and least impairment of the composite mechanical properties. Location M-45 was the mid-plan with the OF placed in between two CF layers oriented in the -45° direction. Location T0 was the closest to the top impact surface and location B0 was the furthest position from the impact surface, where frequent fibre breakage was observed for this thin laminate. In both locations, OF was placed in between two layers oriented at 0° . These locations for OF embedment are illustrated in Figure 25. Two samples were prepared for each studied optical fibre location.

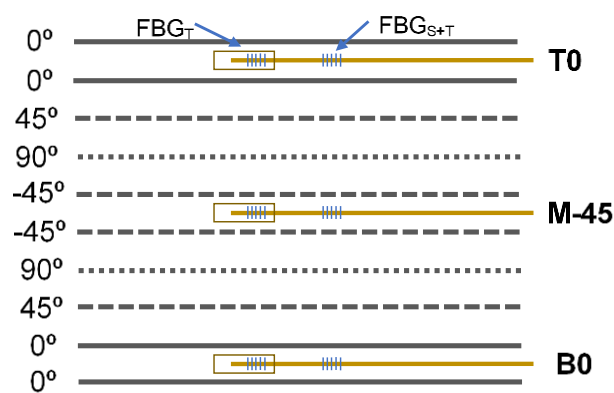


Figure 25: Schematic representation of OF location through the thickness of the laminate

Figure 26 shows pictures of produced samples with embedded SDOF (a) and LDOF (b), where it is possible to see the OF protecting materials used inside the vacuum bag.

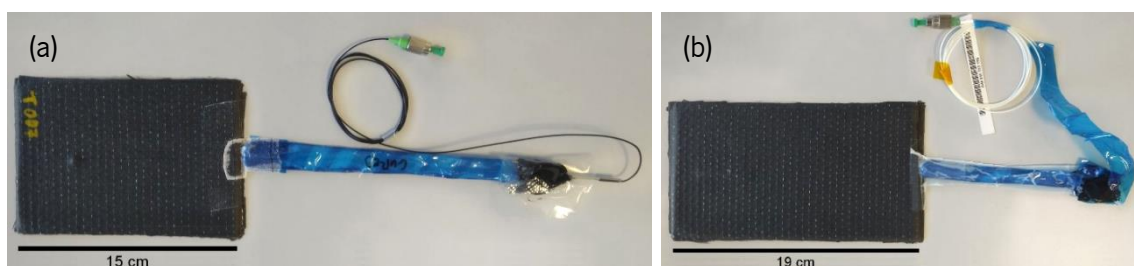


Figure 26: Composite specimens with embedded (a) SDOF and (b) LDOF for low velocity drop-weight impact testing

The FBG curing data was acquired by a I-MON 256 USB High Speed interrogation monitor connected to a DL-BP1 1501A super luminescent LED from Ibsen Photonics, having a maximum measuring frequency of 6000 Hz and an operating wavelength range of 1525 – 1570 nm. It has also a wavelength fit resolution of 0.5 pm, that translates to a strain resolution of about $0.4 \mu\epsilon$

when FBG sensors are used. The signal acquisition was taken at 50 Hz and the FC/APC optical connectors mounted in the optical fibres were plugged in to the light source.

4.3.1.2. Preparation of CFRP Laminates for Electrical Impedance Tomography

Both 8-layer and 10-layer 150 mm × 100 mm samples cut from the 500 mm × 700 mm CFRP laminates processed by VARI in the conditions previously described in paragraph 3.2.3 also had to be prepared before they could be submitted to impact testing under EIT monitoring.

To do that through-thickness holes were introduced by drilling on both composite configurations. Two through-thickness holes per configuration were performed in specific locations of the samples as represented in Figure 27. The creation of holes followed a specific sequence with EIT imaging being performed between each step. First, hole A was created with an initial diameter of 2 mm and was then increased to 4.5 and 6 mm. The increase of hole diameter aims to assess whether EIT and the GN algorithm are sensitive to damage size. Having hole A with a diameter of 6 mm, hole B was then introduced with the same diameter increase strategy: first a 2 mm diameter followed by a diameter increase to 4.5 and 6 mm. hole A and B were introduced away from the centre of the sample to avoid mirroring effect.

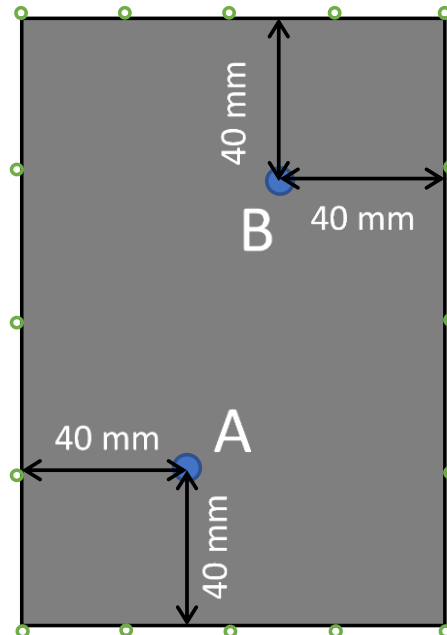


Figure 27: Schematic representation of the locations of through-thickness holes A and B, having progressively larger diameters of 2, 4.5 and 6 mm. The green dots represent the location of the electrodes contact with the CFRP for EIT measurement.

For EIT analysis, sixteen electrodes were then applied on the boundary of each specimen, as schematically represented by the green circles in Figure 27. Each sample had an electrode on each corner and 3 electrodes along each edge, spaced about 37 mm on the sample length and 25 mm on the sample width. In order to connect the electrode for measurement to the CFRP sample, first, a silver ink spot was applied on the thickness surface and left to dry for 24 hours. Next, a Kapton film was applied on the top surface of the specimen for electrical insulation, where a copper adhesive tape was placed on top of. Electric wires were finally welded. A last layer of glue was used to ensure that the electric wires would not detach during mechanical testing. The boundary electrodes configuration is also presented in Figure 28.

The EIT setup used (Figure 29) was developed by Stratosphere company. The apparatus consisted of a power supply, XPH 35-4D Dual DC from Sorensen, a 2100 digital multimeter from Keithley, and a type-k thermocouple. The adjacent current injection method was used: the current is injected in a pair of adjacent electrodes and voltage is measured on all following adjacent pairs of electrodes. The EIT image reconstruction was processed using an inverse solver with one-step difference GN algorithm, to obtain the difference between specimen condition prior to and after damage introduction. A hyperparameter λ of 1 was used during image reconstruction.

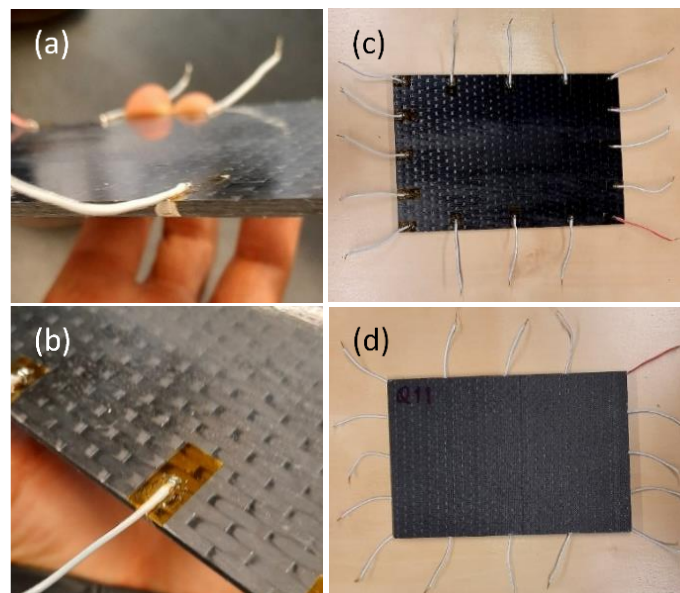


Figure 28: Boundary electrodes configuration: (a) electrical connection of a boundary electrode at the thickness of the specimen, (b) electrical insulation and fixation of the electric wire on the top surface of the specimen, (c) top surface of a quasi-isotropic specimen subjected to an impact, and (d) bottom surface of the same specimen. Note that the electric wires were facing upwards during impact testing and drilling to avoid detachment.



Figure 29: Electrical impedance tomography equipment

For the EIT measurement on specimens with through-thickness holes, each specimen was analysed by EIT before drilling to serve as reference baseline. Electrical impedance analyses were made on each specimen after each new hole has been created and increased. Regarding impacted specimens, electrical impedance analyses were also carried prior to impact testing, to serve as reference, and after impact testing.

4.3.2. Analysis of the Curing Reaction

4.3.2.1. Differential Scanning Calorimetry Analysis

A differential scanning calorimeter DSC Q20, from TA Instruments, was used to study the exothermic curing reaction of the epoxy resin resorting to multiple isothermal experiments at distinct temperatures. The DSC recorded the heat flow as a dependent experimental variable of time $H(t)$, and the enthalpy, the total heat of reaction H_T , which is found by integrating the area of heat flow of the exothermic peak. The progression of the rate of heat flow is proportional to the reaction rate $d\alpha/dt$, as described by equation 46.

$$\frac{d\alpha}{dt} = \frac{1}{H_T} \frac{dH(t)}{dt} \quad (46)$$

The reaction rate $d\alpha/dt$ (s^{-1}) of the curing reaction is generally dependent on temperature as described by the $k(T)$ function, the specific rate constant at temperature T (s^{-1}), and on the degree of conversion, α , given by the $f(\alpha)$ function, as stated by the following equation [145]:

$$\frac{d\alpha}{dt} = k(T) \cdot f(\alpha) \quad (47)$$

The temperature dependency on the reaction rate is often described by the Arrhenius law, i.e.:

$$k(T) = Z e^{-E_a/RT} \quad (48)$$

where Z is the pre-exponential factor (s^{-1}), E_a is the activation energy ($J \cdot mol^{-1}$), T is the absolute temperature (K), and R is the gas constant, $8.314 J \cdot mol^{-1} \cdot K^{-1}$.

Initially, the simple n^{th} order and accelerating (or Sestak-Berggren) reaction model equations were applied to the experimental data, following procedure B of the ASTM standard E2070-13 [145], since the isothermal DSC curves (Figure 49) presented the characteristic shape of a n^{th} order reaction. However, the Friedman model-free kinetics method [146], [147] presented a better fit with the experimental data and was used instead. This is an isoconversional method that assumes that the activation energy is independent of the temperature program, at any conversion α . To determine the value of E_a , for a certain conversion α , from each isothermal DSC experiment, equation 48 was rearranged into equation 47 and taken into its logarithmic form as:

$$\ln[d\alpha/dt] = \ln Z f(\alpha) - \frac{E_a}{R} \cdot \frac{1}{T} \quad (49)$$

Having equation 49 in the form of $y = b + mx$, it was solved through a linear regression analysis of the plot of $\ln(d\alpha/dt)$ against $(1/T)$ (often called Friedman plot), in order to obtain $-E_a/R$ as its slope (m) and $\ln Z f(\alpha)$ the y-intercept at the origin (b). Once E_a and $Z f(\alpha)$ were found, equation 50 was integrated, resulting equation 51, to find the time, t_α , to reach a conversion α , at an isothermal temperature, T_2 , for which there is no measurement available [148].

$$\frac{d\alpha}{dt} = Z e^{-E_a/RT} \cdot f(\alpha) \quad (50)$$

$$t_\alpha = \int_0^{t_\alpha} dt = \int_0^\alpha \frac{d\alpha}{[Z \cdot f(\alpha)] \cdot e^{-E_a/RT_2}} = \frac{1}{[Z \cdot f(\alpha)] \cdot e^{-E_a/RT_2}} \int_0^\alpha d\alpha \quad (51)$$

$$= \frac{\alpha}{[Z \cdot f(\alpha)] \cdot e^{-E_a/RT_2}}$$

Initially, a dynamic DSC test was performed at a constant heating rate of 10 °C/min, between -30 and +250 °C, to define the temperatures to be used in the subsequent isothermal DSC tests and measure the total enthalpy of curing. The isothermal DSC experiments were taken at 70, 80, 90 and 100 °C for progressively longer periods of time, between 3 and 6 hours, to obtain a flat line of heat flow by the end of each experiment, ensuring full conversion of the curing reaction. All DSC tests were performed under nitrogen gas with a 50 ml.min⁻¹ flow.

A big batch of about 50 g of resin and hardener were mixed in a 100% – 30% weight ratio, to ensure a good representation of the resin system. Each sample having 26 – 32 mg was placed in an aluminium crucible with a small hole in the lid and stored in a refrigerator at -15 °C to prevent curing before the DSC tests. The DSC was initially pre-heated to the isothermal temperature and only then the sample was removed from the refrigerator and quickly placed in the DSC cell. Data recording was initiated about 1 minute later as soon as the isothermal temperature was equilibrated. The Kinetics Neo software from Netzsch was used to apply the Friedman method to the experimental DSC data to obtain E_a and make isothermal predictions of the resin curing at ambient conditions, for temperatures ranging from 17 to 25 °C.

4.3.2.2. Cure Analysis Using Optical FBG Sensors

A small-diameter optical fibre (SDOF), having a FBG_{S+T} sensor and a FBG_{T-CAP} sensor, was also used to monitor the cure of the epoxy resin system alone, aiming to discern the contribution of the matrix component alone on the FBG wavelength shift during the curing stages of the CFRP composites. About 50 g of resin was poured into a plastic plate to achieve a thickness of approximately 4 mm, to resemble the resin curing behaviour that would be approximately expected in the CFRP laminate. The optical fibre was immersed in the middle area of the plate. Thermocouples were also used to measure the laboratory temperature during ambient curing and the oven temperature during post curing.

The curing degree of the resin was assessed 40 hours after ambient curing and after post curing, by measuring residual enthalpy of curing at each of these stages and comparing them to the total enthalpy of curing in the DSC. The residual enthalpy of curing was measured by the area of the exothermic peak in the first heat of heat-cool-heat DSC cycles. Samples of about 7 mg were heated from 30 to 200 °C in a first cycle, cooled down to 25°C, and again heated up to 200 °C in a second cycle. Both heating stages and cooling used a temperature ramp of 10 °C/min and a 5 min isothermal period was held at every end.

4.3.3. Damage Production and Detection

4.3.3.1. Low Velocity Impact Testing

Drop-weight impact tests were performed according to the ASTM D7136 standard [140] using Fractovis Plus impact testing equipment from CEAST, Italy, (Figure 30). The impactor had a hemispheric shape with a 20 mm diameter and a mass of 5.045 Kg. The impactor contact force on the specimen surface was recorded against time for each impact. From there, the impactor velocity $v(t)$, displacement $\delta(t)$, and absorbed impact energy $E_a(t)$, as a function of time, were calculated following equations 52, 53, and 54, respectively [14].

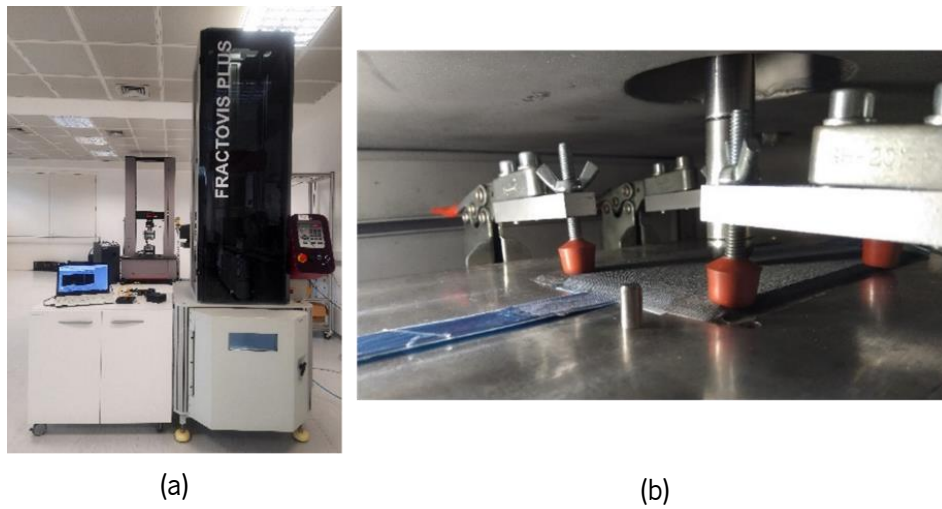


Figure 30: Drop-weight impact test setup: (a) OF interrogation equipment and impact testing machine; (b) impact support fixture with toggle clamps and impactor on a CFRP laminate with embedded OF

$$v(t) = v_i + gt - \int_0^t \frac{F(t)}{m} dt \quad (52)$$

where v_i is the initial impactor velocity, g is the gravitational acceleration, $F(t)$ is the measured load at time t , and m is the total drop mass.

$$\delta(t) = \delta_0 + v_i t + \frac{gt^2}{2} - \int_0^t \int_0^t \frac{F(t)}{m} dt dt \quad (53)$$

where δ_0 is the impactor displacement from the reference location.

$$E_a(t) = \frac{m(v_i^2 - v(t)^2)}{2} + mg\delta(t) \quad (54)$$

4.3.3.1.1. Impact Damage Monitoring Using Optical FBG Sensors

Because impact resistance is highly dependent on the materials and layup structure, initial drop-weight impact tests were performed on non-instrumented reference specimens to identify the range of impact energies that ensure BVID. A reference laminate without sensors was firstly produced and cut into samples of 150 x 100 mm. Three specimens were exposed to the following different impact energies: 13.1, 15.1, 17.5, 20.0, 25.0, 30.0 and 40.1 J. The variation of the impact energy was achieved by changing the vertical position of the impactor head between 264 and 810 mm. The results obtained from these initial impact tests allowed the range of impact energy to be selected that undoubtedly and consistently produced BVID on the composite laminate in the form of subtle bumps on the back surface, but that could still go unnoticed in real-life applications where impact event existence and location are unknown, to be used in the forthcoming tests of instrumented composites.

The instrumented samples, with embedded OF, were then subjected to an initial impact with an energy of 30.0 J and a second one with an energy of 20.0 J. Simultaneously, the FBG signals were acquired to detect the impact events and evaluate residual strain dependency on the OF through-thickness location. The first impact was located about 1 cm away from each FBG sensor in the specimens with SDOF and about 6 cm away from each FBG sensor in the specimens with LDOF. The second impact location was about 1 cm away from first impact site. Approximate impact locations are schematically represented in Figure 31.

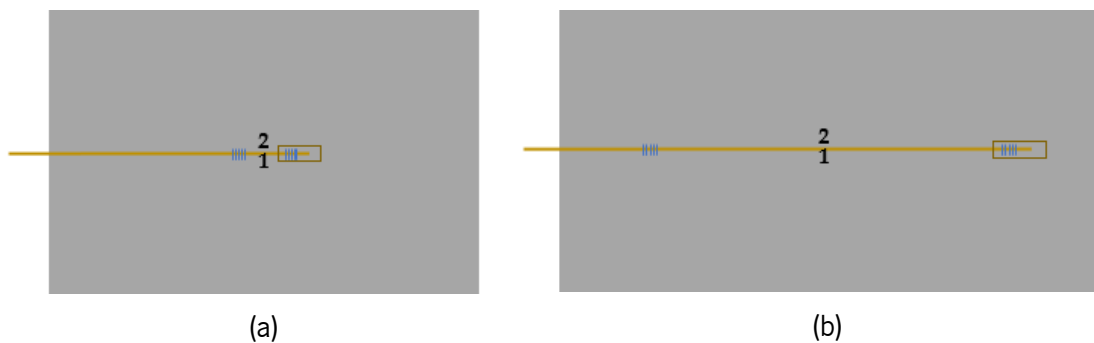


Figure 31: Schematic of approximate impact locations on specimens containing (a) SDOF and (b) LDOF. Numbers 1 and 2 represent the locations of the first and second impacts, respectively.

The DL-BP1 1501A super-luminescent LED source and I-MON 256 USB High Speed interrogation monitor were also used to record the FBG data during impact testing. Signal acquisition was taken at the maximum measurement frequency of 6000 Hz for impact detection.

Non-destructive analyses were used to evaluate the generated damage and validate the suitability of the FBG location to detect damage, as further discussed in section 4.3.4.1.

4.3.3.1.2. Impact Damage Monitoring using Electrical Impedance Tomography

Due to the different layup configurations, the two laminates had distinct impact resistance. Thus, different impact energies had to be imposed on the laminates to produce damages of comparable severity. Different levels of damage severity: unnoticed damage, barely visible damage, and more severe damage were imposed on laminates. The quasi-isotropic specimens were subjected to impact energies of 20.0, 30.0 and 49.5 J and the unbalanced specimens to 15.0, 30.0 and 49.5 J. Three specimens of each laminate configuration were exposed to each level of impact energy. Drop-weight impact tests were performed on the Fractovis Plus apparatus from CEAST, following ASTM D7136 standard. The impactor had a 20 mm diameter hemispheric head with a mass of 5.045 kg and its vertical position was adjusted, between 305 and 1000 mm, to impose the distinct levels of impact energy.

Non-destructive ultrasonic C-scan was used as a control technique for damage detection, as further discussed in section 4.3.4.2.

4.3.3.2. Through-thickness holes damage for Detection by Electrical Impedance Tomography

To evaluate the suitability of EIT with one-step difference Gaussian-Newton (GN) algorithm to detect severe visible damage, through-thickness holes were created on the CFRP laminates. Through-thickness holes were drilled with different diameters and at two locations of the specimen to evaluate the capability of EIT to detect multiple defects and its sensitivity to defect size.

4.3.4. Non-Destructive Ultrasonic Inspections

4.3.4.1. Impact specimens with Optical FBG Sensors

Non-destructive testing through phased array ultrasonics was conducted on the instrumented samples prior to and after impact testing to evaluate the induced damage and validate the OF measurements. The analyses used a Prisma ultrasonic flaw detector from Sonatest, United Kingdom, with a 5 MHz probe, 50 mm wide. The specimens were immersed in water and scans were performed at 100 mm/min.

4.3.4.2. Impact Specimens used in Electrical Impedance Tomography Studies

In the case of the samples monitored by using the EIT, the non-destructive ultrasonic C-scan technique was used to serve as a comparison and validation technique for the suitability of the EIT analysis to detect impact damage.

The analysis was conducted with the Omni Scan Sx from Olympus with a M2008 probe from Olympus, with a frequency of 0.5 MHz. The scans were performed using a two-axis encoder with 1.0 mm resolution in the axis along the length of the samples and 3.0 mm resolution in the axis along the width of the samples.

4.3.5. Development of a Smart Composite Overwrapped Pressure Vessel

This work reports the developments of a COPV for hydrogen storage to be used in a hydrogen powered fuel cell system of a UAV. A 1-litre COPV was designed for hydrogen storage at 350 bar pressure. The initial part of this work concerns the development of the COPV and the iterative working steps for its conception can be seen in Figure 32.

The materials selection and characterization step was conducted, followed by the generation of winding patterns by using CADWIND® software. The winding patterns were converted into a numerical code, compatible with the laboratorial filament winding machine, in order to make it possible to carry out preliminary tape winding experiments to validate those simulations made in CADWIND®. If the helical and circumferential winding patterns presented full coverage of the liner and of its circumferential section, respectively, the FEM analysis could proceed, thus validating the winding patterns characteristics that had been considered previously (carbon fibre orientation taken from CADWIND® simulation and layer thickness taken from the experimental winding pattern verification tests). Contrarily, if the simulated winding patterns did not provide full coverage, new winding patterns would have to be simulated and selected using CADWIND® and a new experimental verification of the winding patterns should be implemented.

Finite element analysis (FEA) simulations were run until the composite overwrap layup is optimised and has reached minimum burst pressure. At this point, the COPV can be produced according to the selected winding patterns and optimised overwrap layup configuration. Then, the COPV is exposed to burst testing in the next step. If the experimental burst pressure achieves the minimum requirement value, the COPV design is considered finalized. Otherwise, the constitutive models of the FEM were modified, a new optimisation of the composite overwrap layup performed, and production and testing iteration implemented again. Figure 32 details these iterative procedures.

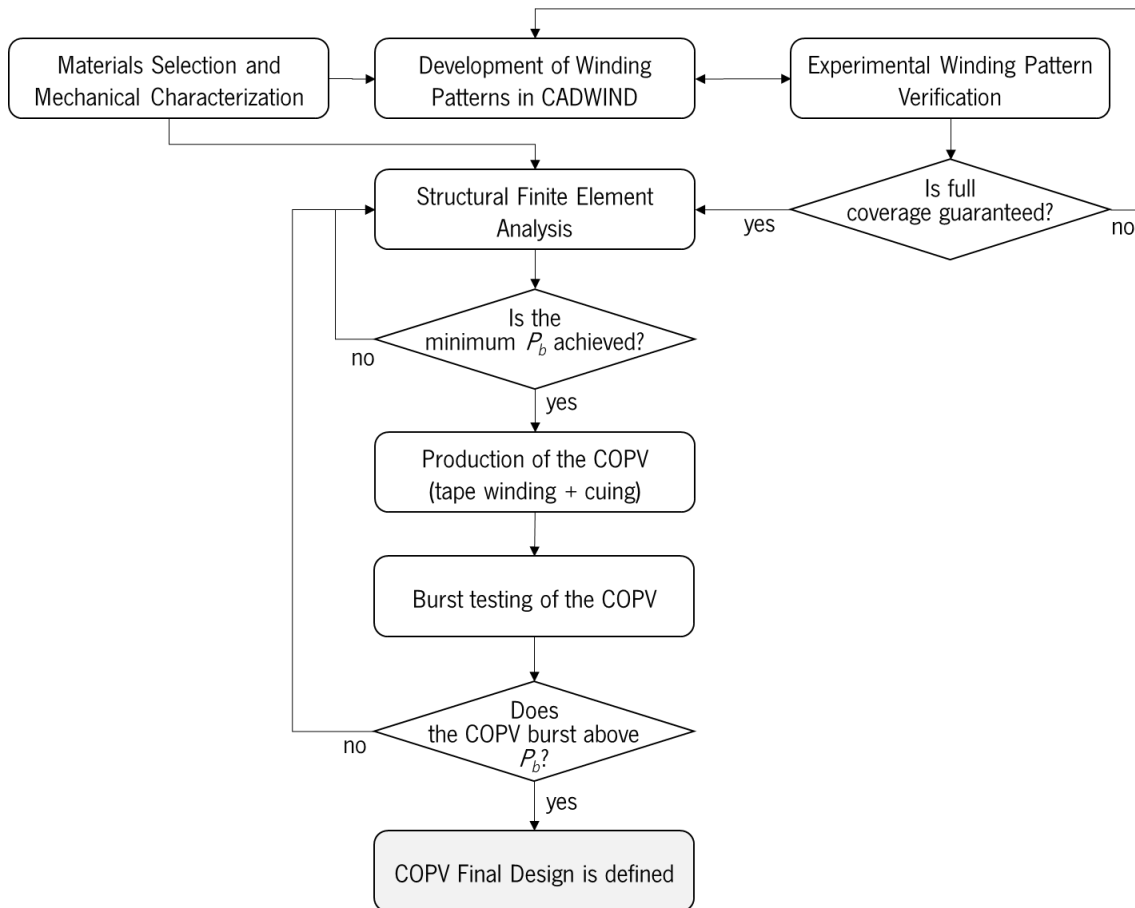


Figure 32: Iterative work steps for the development of the COPV

The second part of the work concerned to the integration of a sensing system, able to monitor the production process (tape winding process and curing schedule) and ensure the SHM, including the BVID detection and pressure cycling tests made for simulating the charging and discharging cycles during operation of the COPV. Sensors should be integrated at places subjected to higher strains, which usually happens in between the liner and first layer of the composite overwrap or in between the more dissimilar layers of the composite overwrap [8]. The FEM analysis conducted for development of the COPV helped to confirm locations where the highest strain levels would occur. The integration of optical FBG sensor arrays into COPVs is described in more detail in section 4.3.5.2.2.

4.3.5.1. Design of the Composite Overwrapped Pressure Vessel

4.3.5.1.1. Raw Materials Characterization

Production of Composite Specimens

Composite plates were produced for mechanical characterization of the ITS50 carbon fibre/RCX0125 epoxy composite. In order to produce CFRP specimens as similar as possible to the

composite overwrap of the COPV, the same prepreg tape material was wound over a plate-shaped steel mandrel of 300 mm x 300 mm x 30 mm (Figure 33 (a)) with the filament winding machine (Figure 33 (b) and (c)).

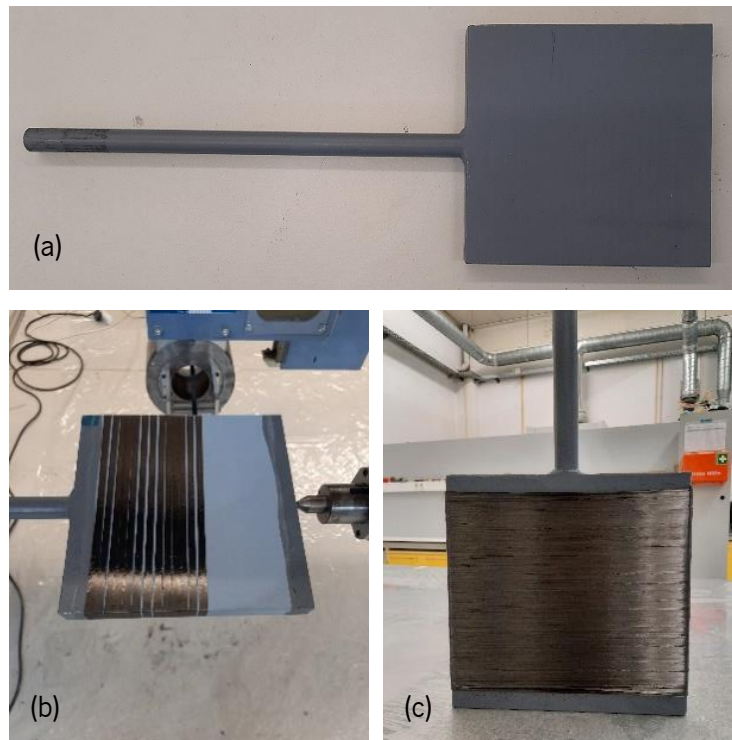


Figure 33: (a) plate-shaped steel mandrel, (b) tape winding over the steel mandrel and (c) final wound composite structure for specimens production

Like in the COPV, the winding pattern on the flat mandrel was created using CADWIND® software (see section 4.3.5.1.3 for more details). Due to limitation of the winding process, the tape was wound at $\pm 89.6^\circ$

Four layers of tape were wound around the flat mandrel. A plaque was cut from one side to produce a 1.45 mm thick laminate to produce specimens with carbon fibres at 0° . The remaining part of the wound composite was fixed to the flat mandrel to wound three more layers, resulting a 2.74 mm thick laminate with seven layers. The laminate to produce tensile specimens with carbon fibres at $\pm 45^\circ$ was produced by stacking of subsequent layers of tape at 89.6° and perpendicular to that. The flat mandrel was wound four times with only one layer, and the two faces of the plate were manually cut and stacked to form an eight-layer laminate with the symmetrical stacking sequence $[0/90/0/90]_s$. Since the consolidation of the tape is lost when the layers are cut out of the mandrel, the stacked layers were cold pressed in a 100-bar hydraulic press from M.J. Amaral Equipamentos Industriais Lda.

Each prepreg plate was then vacuum bagged for curing and consolidation. A peel ply layer was placed over a glass plaque, followed by the prepreg stack, other layer of peel ply and breather fabric. The vacuum line was installed and the setup was sealed with a plastic bag and sealing tape. The system was placed in an atmospheric oven and the vacuum was set to approximately 400 mbar. The curing schedule followed the suggestions of the manufacturer. The heating program consisted of a heating ramp at 1°C/min to 90 °C, followed by an initial stage of 30 min at that temperature, followed by another ramp at the same heating rate and isothermal stage at 150 °C for 90 min. The cooling ramp was also set to 1°C/min.

Finally, the composite plates were cut to the desired dimensions by using a circular saw from Einhell and sanded for finishing.

Production of Aluminium Specimens

Dog-boned shaped specimens were cut out from the circumferential section, in the longitudinal direction, of a 6061-T6 aluminium liner, according to European standard EN 10002-1. The specimens, shown in Figure 34, were machined by the MH50-DX100 robot from Yaskawa. It is possible to see the curvature of the specimens in Figure 34 (a). The specimen grips were manually flattened with a hammer, for fixation in the test equipment. The gage length was 75 mm and the gage width was 12.5 mm. Figure 34 (b) shows some of the produced specimens with installed bidirectional strain gauges 3/350-XY41 from Omega, with a gauge factor of 2.14 for unidirectional tensile testing. More details on the tensile tests performed can be found in the next section.

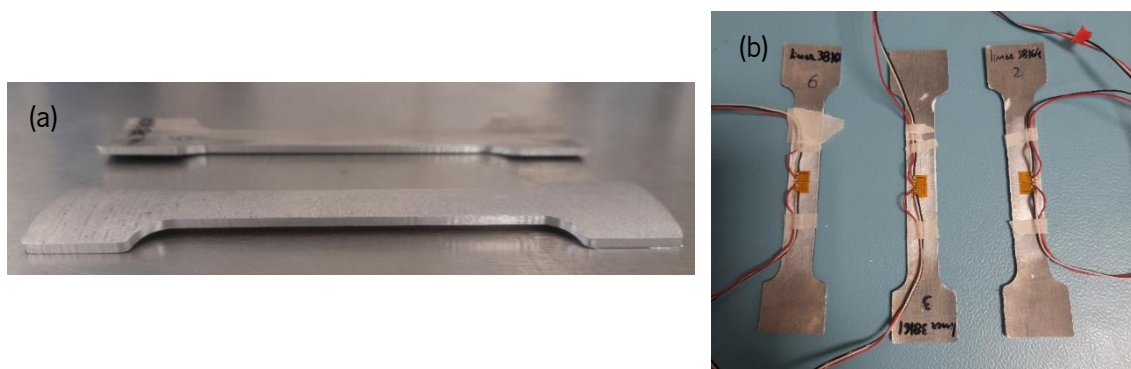


Figure 34: (a) as cut and (b) instrumented dog-bone shaped aluminium specimens cut out from the aluminium liner

Tensile Testing

Unidirectional tensile tests were conducted in a 50 kN universal testing machine Autograph AG-X from Shimadzu.

The tensile tests performed to the composite specimens were conducted according to the ASTM D3039 standard [149]. Bidirectional strain gauges, SGT-4/350-XY41 from Omega, with a gauge factor of 2.13, were mounted on all composite specimens to determine different material properties. The unidirectional specimens with carbon fibres in the longitudinal direction were tested to obtain the longitudinal tensile strength, elastic modulus E_1 and Poisson's ratio ν_{12} . These specimens measured approximately 15x250x1.45 mm. The unidirectional specimens with carbon fibres aligned in the transverse direction were tested to obtain the transverse tensile strength and elastic modulus E_2 . These specimens measured approximately 25x175x2.33 mm. The specimens with carbon fibres aligned at $\pm 45^\circ$ were tested to obtain the shear strength and modulus G_{12} . These specimens measured approximately 25x175x2.74 mm. These specimens with carbon fibre orientation at $\pm 45^\circ$ were also tensile tested according to ASTM D3518 standard. 1 mm thick glass fibre composite tabs were adhesively bonded (2-part epoxy adhesive system STRUCTIL EA 9394 from Henkel, Germany) to the specimens to prevent damage at the gripping area. The tensile tests were conducted at a speed of 2 mm/min.

The obtained results also enabled the calculation of the transverse shear modulus G_{23} by equation 55 [150].

$$G_{23} = \frac{E_2}{2(1 + \nu_{23})} \quad (55)$$

where the Poisson's ratio ν_{23} is mainly dependent on the matrix properties.

Three dog-shaped aluminium specimens were subjected to tensile testing, at a stress rate of 5 MPa/s, as suggested by the European standard EN 10002-1. These tests were performed to obtain the elastic modulus, Poisson's ratio, yield stress and hardening modulus, to be used in the FEM analysis. As mentioned in the previous section, bi-axial strain gages were also installed on the aluminium specimens. These tests allowed to obtain the elastic modulus, E , of aluminium from the slope of the tensile/strain curve in the elastic region and the *Poisson's* ratio from the slope of the transverse strain/ longitudinal strain curve.

The tensile tests on aluminium specimens were also performed on the Shimadzu Autograph AG-X, with a load cell of 50 kN.

Compression Testing

Compression tests were carried out on the CFRP specimens according to the SACMA SRM 1R-94 standard. Unidirectional specimens, of about 80x15x1.45 mm, were prepared with carbon fibres in the longitudinal and transverse direction, to obtain the longitudinal and transverse compressive strength, respectively. Glass fibre composite tabs, of about 37,6x15x1 mm, were adhesively bonded (2-part epoxy adhesive system STRUCTIL EA 9394 from Henkel) to the specimens. The tests were performed at a speed of 1 mm/min.

Density Measurements

The density of the composite material was determined by the immersion method, following the ISO 1183 standard. The mass of the sample was weighted in air and when immersed in the fluid, allowing the density to be determined by equation 56.

$$\rho_s = \frac{m_{s,A} \times \rho_{IL}}{m_{s,A} - m_{s,IL}} \quad (56)$$

being $m_{s,A}$ the sample mass in air, ρ_{IL} the density of the fluid and $m_{s,IL}$ the sample mass when immersed in the liquid. The density measurements used 2-propanol as immersion liquid, which has a density of 0.785 g/ml at 25 °C.

4.3.5.1.2. Finite Element Modelling

Abaqus Standard software was used to conduct FEA to simulate the COPV mechanical behaviour and optimize the composite overwrap layup to obtain a minimum burst pressure of 1050 bar. For that, a static analysis was made by applying a uniform pressure on the inner surface of the aluminium liner. As applied boundary conditions, the COPV was considered totally fixed at the bottleneck and tie constrained in between the liner and overwrap.

The composite overwrap was initially modelled using an orphan mesh generated by CADWIND® software, which divided the overwrap into several circumferential/ conical sections along the longitudinal axis of the overwrap, to attribute specific fibre angle and thickness of each layer in that section. However, the model did not present good correlation with the experimental burst tests. As such, the composite overwrap was then modelled as a continuum shell, using a 3D CAD drawing having the external surface of the liner as the actual internal surface of the composite overwrap, which allowed to change the mesh refinement. Additionally, the composite shell was manually divided into several section, to attribute distinct fibre angle at each of these sections, as obtained

in the CADWIND® input file. Furthermore, the thickness of each layer was attributed as measured on a preliminary wound COPV after curing. This COPV was cut half lengthwise to measure the thickness of helical and circumferential layers. Again, this was an iterative process. After measuring the thickness of each layer of the selected winding patterns and updating the thickness values in the finite element model, the composite overwrap layup configuration was optimised. In the circumferential zone of the COPV, each circumferential layer presented a thickness of approximately 0.28 mm and each helical layer presented a thickness of about 0.50 mm. The composite overwrap was modelled with a general size mesh of 1 mm, resulting 27,720 S4 linear shell elements, having anisotropic behaviour. The Hashin and Rotem's failure criterion was used for damage initiation and the linear damage evolution was considered. The liner was modelled with a general size mesh of 2 mm, resulting 26,348 C3D8 linear solid elements, with isotropic elastic-plastic behaviour. The material properties used in FEA are presented in Table 9. Except for the fracture energy properties, all composite properties were experimentally obtained from specimens produced on the flat mandrel, as described in section 4.3.5.1.1. The mechanical properties of the aluminium liner were also determined experimentally.

The FEM results were validated through burst tests. More details on the experimental procedure of these tests can be found in section 4.3.5.3.1.

4.3.5.1.3. Winding Patterns

CADWIND® software, version 10.131, from MI MATERIAL innovative GmbH, was used to generate winding patterns that would be compatible with the laboratorial winding machine and the friction characteristics of the liner material and the prepreg tape.

The 2-dimensional (2D) liner surface contour (Figure 35) was firstly fed to the software, which was previously drawn in SolidWorks 2020 CAD software. The 2D liner surface contour was divided into 41 frames, 13 on each dome, and 15 on the cylindrical zone. The frames were not equally spaced, they were defined to be more finely spaced out in the transition areas between the domes and cylindrical zone, for better control of the turning zones to create the winding patterns. More physical characteristics of the liner can be found in section 4.3.5.2.1.

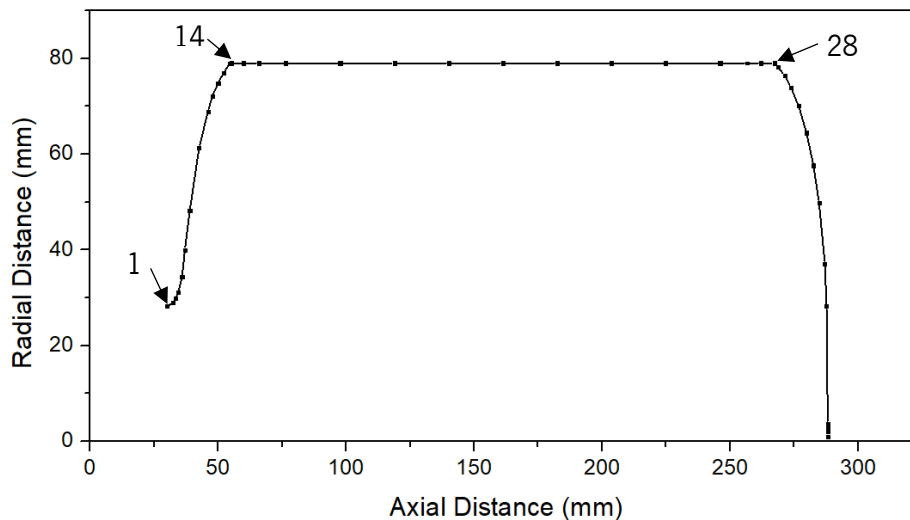


Figure 35: Liner Surface Contour. Squares represent the beginning/end of a frame. Some of them are identified.

A friction factor of 0.35 was considered for winding of the prepreg tape over the aluminium liner for both winding patterns. Finding an adequate winding pattern was an iterative process between the CADWIND® pattern simulation and the actual winding process in the laboratory winding machine. Although the unwound ITS50 carbon fibre/ RCX0125 epoxy tape had a width of approximately 6 mm, the tension in the tape during winding affected its width. Therefore, to respect the real tape width during winding and achieve full coverage of the liner by the helical winding and of the cylindrical section by the circumferential winding, the tape width was considered to be of 4 and 5 mm during CADWIND® simulations of the helical and circumferential winding patterns, respectively. The start frame, at which the machine winding cycle is initiated, the turning front zone, the frame on the dome with the bottleneck where the pattern starts to change direction, the turning back zone and the frame on the closed dome at which the pattern starts to change direction and finish the cycle, were adjusted to find suitable winding patterns.

4.3.5.2. Production of the Smart Composite Overwrapped Pressure Vessels

4.3.5.2.1. Liner

A seamless 6061-T6 aluminium liner, having a water volume capacity of 0,98 L, was purchase from Luxfer Gas Cylinders, USA. The liner has an external diameter of 78.99 mm, with a minimum thickness of 1.85 mm in the circumferential section, a total length of 287.02 mm, and a mass of 0.454 kg. A picture of the liner can be seen in Figure 36.



Figure 36: Picture of the 6061-T6 Aluminium liner

To ease the winding process, keeping the wound tape in place and preventing sliding, a pin of polylactic acid (PLA) was produced by additive manufacturing (of Prusament PLA filament from Prusa Polymers, Czech Republic) and glued to the centre of the closed dome of the liner by using a Loctite EA3450 epoxy adhesive from Henkel, Germany (Figure 37). Exceptionally, as described in section 4.3.5.2.3, the winding monitoring studies used a long steel bolt, instead, to fix the interrogator to the liner. Additionally, the pin also provided support to the optical fibres and optical connectors at the ingress/egress point of the composite overwrap.

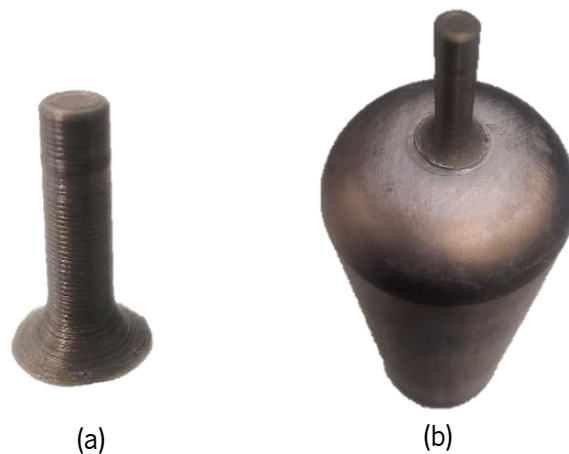


Figure 37: (a) Pin produced by additive manufacturing and (b) pin glued to the closed liner dome

4.3.5.2.2. Embedment of Optical FBG Sensors for Process and Structural Health Monitoring

Sensors should be integrated at places where the highest strains are developed, which usually happens in between the liner and first layer of the composite overwrap or in between the most dissimilar composite overwrapped layers [8]. As it may be seen in section 5.4.1.3, the FEA of the developed COPV showed that the highest strain level is at the internal circumferential layer of the composite overwrap.

Having the aim of BVID detection in mind, a FBG sensor array was configured to be embedded in the liner/overwrap interface with enough spatial sensing range to enable damage detection and localisation in the circumferential section of the COPV. A single optical fibre was designed to be

wound around the liner and have 8 FBG sensors equally spaced throughout the circumferential section of the liner. The FBG sensors were positioned along three lines running in the axial direction of the liner, distanced by 120° , and with an axial distance of 26 mm in between consecutive sensors, as schematically represented in Figure 38. Moreover, having the FBG sensors fixed on the external surface of the liner, prior to composite overwrap winding, also allowed to monitor the winding and curing processes as well. The FBG sensors were fixed on the liner at 90° to its axial direction, to be aligned with the internal circumferential layers.

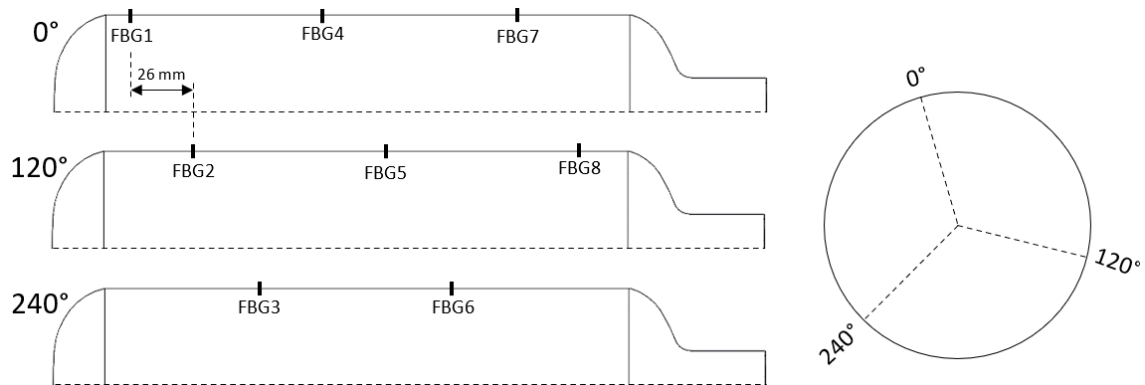


Figure 38: Schematic representation of the FBG sensors location on the liner surface

The OF had 8 FBG sensors inscribed at each 0.09 m distance. The OF had FC/APC connectors with $750\ \mu\text{m}$ diameter teflon lead-in/out cable and $500\ \mu\text{m}$ diameter transition tube (configuration presented in Figure 39). The FBG sensors presented the following central wavelengths: 1535.0, 1539.2, 1543.4, 1547.6, 1551.8, 1556.0, 1560.2 and 1564.4 nm.

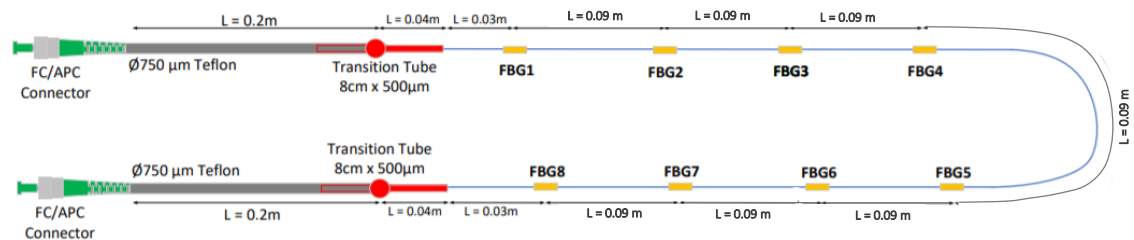


Figure 39: Schematic representation of the configuration of the polyimide coated optical fibre having an 8-FBG sensor array, for BVID detection capability demonstration. The scheme is not drawn to scale.

The embedment of optical fibres into FRP laminates is very challenging, where the main issues are found in the egress/ingress point of the optical fibre in the composite [37]. Thus, the OF was positioned in a way to be as much aligned as possible with the wound carbon fibres and minimize shear loading on the OF. The extension of optical fibre running from the ingress point at the pin up to the dome/circumferential section interface and from there to FBG1 follows approximately the orientation of the carbon fibres. The helical layer covers the liner in the dome section and the

optical fibre was bonded in a similar orientation (see Figure 40 (a)). From the dome/circumferential section interface to FBG1, the optical fibre is almost oriented perpendicularly to the longitudinal axis of the liner (see Figure 40 (b)), approximately the same orientation of the carbon fibres in the circumferential layer, the first layer in contact with the liner in the circumferential section.

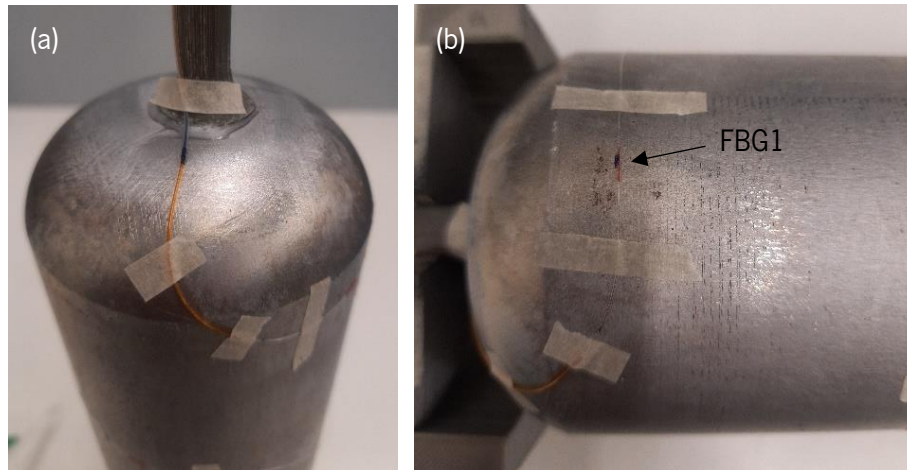


Figure 40: (a) Ingress point of the optical fibre in the pin and placement at the closed dome and (b) placement of FBG1 at the circumferential section

The first trials simply fixed a 150 μm diameter polyimide coated optical fibre with inscribed bare FBG sensors (schematic of configuration in Figure 42 (a)) on the external liner surface with the bi-component epoxy adhesive X120 from HBM, Germany (see Figure 41). The adhesive was either let to cure at room temperature for 40 hours or cured at 60 $^{\circ}\text{C}$ for 3 hours. After curing of the adhesive, the tape winding process and curing schedule for the production of the COPV followed as usual.

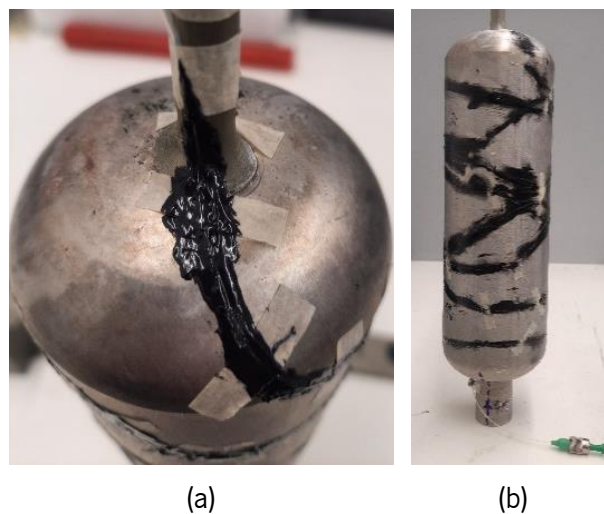


Figure 41: Optical fibre fixed on the (a) dome and (b) circumferential section of the liner surface with epoxy adhesive

In two COPVs, a high temperature polyester adhesive tape was also placed on top of the cured epoxy adhesive X120 to further protect the OF in the following manufacturing steps.

The following tests used 4-FBG sensing arrays to minimize costs. The next tested embedding strategies looked, primarily, into ways to further protect the optical fibre from the compressive and shear loads of the liner and composite overwrap and used Ormocer® coated optical fibres instead of polyimide coated ones. The Ormocer® coated optical fibres have higher diameter, 195 μm , but they present superior mechanical strength and temperature stability. Besides bonding of the optical fibre with epoxy adhesive X120, as described in the previous methodology, the following trials had the OFs covered with a unidirectional flax fibres/epoxy prepreg tape (see Figure 43), to act as a buffer. This protection was vacuum bagged and cured in an atmospheric oven for 24 hours at 70 °C. At this stage, three optical fibre configurations were tested:

- (a) the same configuration applied in previous trials (Figure 42 (a)) to verify whether the localised unidirectional composite layer protection would be enough;
- (b) a second configuration, where the FBG sensors were protected with a 200 μm diameter microtube for added protection of the sensors (Figure 42 (b)) and;
- (c) a third configuration where 750 μm diameter, 3 cm long, Teflon tube was placed in the optical fibre in between the inscribed bare FBG sensors (Figure 42 (c)). The Teflon tube was intended for extra protection of the mid-section of the optical fibre in between FBG sensors, which is the section where the optical fibre is oriented at a higher angle relatively to the carbon fibres in the circumferential layer, where optical fibre breakage is likely to happen.

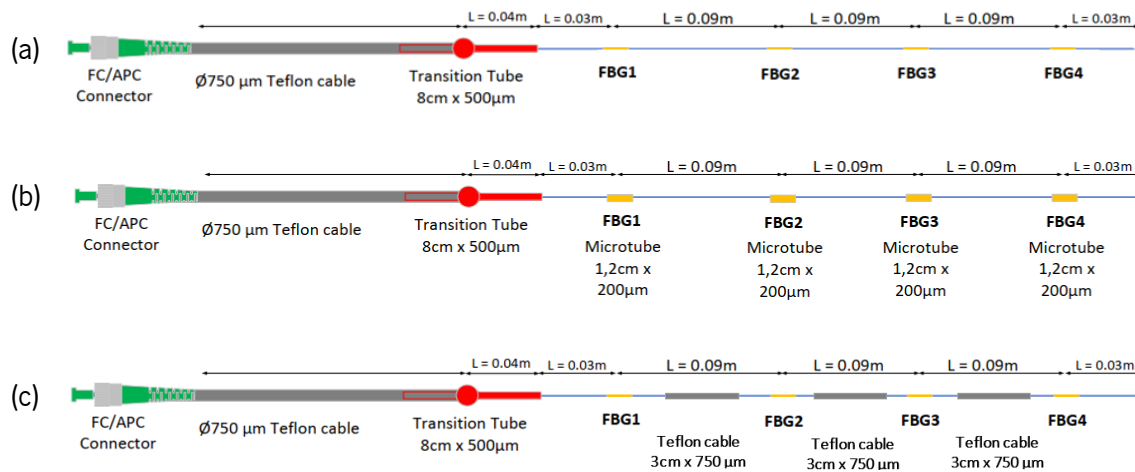


Figure 42: Schematic representation of the configuration of the 4-FBG sensor array optical fibres for the preliminary study on embedding methodologies: (a) optical fibre with inscribed bare FBG sensors; (b) optical fibre with inscribed FBG sensors, which are protected in a 200 µm diameter microtube; (c) optical fibre with inscribed bare FBGs and a 750 µm diameter Teflon cable, 3 cm long, protecting the mid-section of the optical fibre in between FBG sensors. The schemes are not drawn to scale.

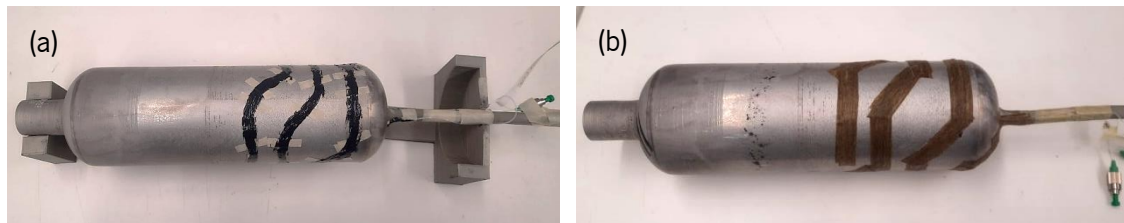


Figure 43: Liner with fixed optical fibre with (a) epoxy adhesive and (b) localised unidirectional composite layer buffer for added protection

A further trial was performed with a 4-FBG sensor array inscribed in a bend-insensitive OF, with the same configuration as illustrated in Figure 42 (b). As in the previous trials, the OF was fixed to the liner surface with epoxy adhesive X120 and protected with unidirectional fibre buffer layer. The bend-insensitive OF has a different configuration of a traditional one. An optical trench, made of a lower refractive index material, is applied between the OF core and cladding, to reflect the lost light back into the OF core material [151].

All optical FBG sensor arrays were purchased from HBK Fibersensing, Portugal.

4.3.5.2.3. Tape Winding Process

A laboratory filament winding equipment manufactured by Gislotica, Portugal, was used to produce the COPV. This equipment has six axes of movement: three linear moving carriage axes (vertical, horizontal left-right and horizontal back-forward), a rotating spindle axis, where the liner is fixed, and two other rotating axes, one around the linear vertical carriage axis and one around the fibre pay-out eye, along the linear horizontal back-forward carriage axis.

The composite overwrap was produced by winding the prepreg tape around the aluminium liner. The CADWIND® software was used to generate the numerical code to be introduced into the winding equipment command for each pattern (circumferential, helical and angle combinations). As mentioned before in section 4.3.5.1.3, the winding patterns were manually adapted to wind the desired number of layers.

After production of suitable winding patterns, the interrogator system from Ibsen Photonics, comprising the DL-BP1 1501A super-luminescent LED source and I-MON 256 USB High Speed interrogation monitor, was used to acquire the FBG data during production, at a sampling rate of 50 Hz. The winding procedure was monitored by fixing the optical interrogator to the liner. A long steel bolt with threads on the end was adhesively bonded (Loctite EA3450 epoxy adhesive from Henkel, Germany) to the centre of the closed dome of the liner. A support for the interrogator was produced by additive manufacturing and screwed to the bolt. The optical fibre was connected to the interrogator and the power and USB cables were connected to the electricity socket and laptop, respectively, through a rotary joint that was fixed to the additive manufactured support, as it can be seen in Figure 44.

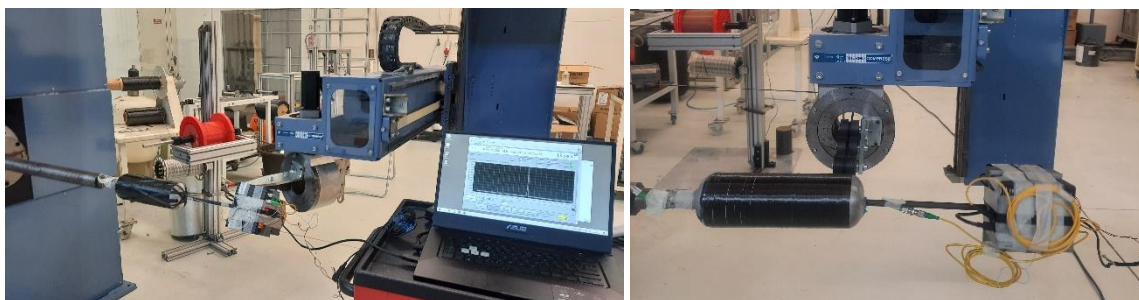


Figure 44: Filament winding machine Gislatica and in-situ strain monitoring with FBG sensors

4.3.5.2.4. Curing

The curing schedule of the COPV followed the suggestion of the resin manufacturer, as also proceeded for curing of the composite plates for material characterization, as described in section 4.3.5.11. Accordingly, the COPV was initially subjected to a pre-curing stage of 30 min at 90 °C, followed by a period of 90 min at 150 °C. After winding and prior to curing, the COPV was wrapped with a 31.7 mm wide polyester shrink tape A 575 from Airtech to maintain the consolidation of the composite overwrap during curing. This shrink tape was selected because it starts to shrink at 79 °C, which occurs prior to the pre-curing stage at 90 °C, and is thermally resistant up to 204 °C. In some cases, the COPV was also vacuum bagged for consolidation during curing.

Curing monitoring was also conducted with the interrogator system from Ibsen Photonics, at a sampling rate of 50 Hz.

4.3.5.2.5. Autofrettage

After curing, the COPVs were subjected to the *autofrettage* process. A pressure above that calculated according to the method presented in section 3.4.3 was used. Thus, the *autofrettage* process was conducted at a pressure of 600 bar for 2 min.

Exceptionally, the COPVs submitted to burst testing were not subjected to the *autofrettage* process and were directly pressure tested from atmospheric pressure up to the burst pressure.

4.3.5.3. Testing of the Composite Overwrapped Pressure Vessel

4.3.5.3.1. Burst Pressure Testing

Burst pressure tests were conducted at Amtrol-Alfa, Portugal, in an in-house built setup (Figure 45). The COPV is filled with distilled water and then connected to the pumping system inside a protective chamber. The internal pressure is then manually increased until burst. Three COPVs, as recommended by the EN12245 European standard, were subjected to burst testing to validate the FEM simulation.

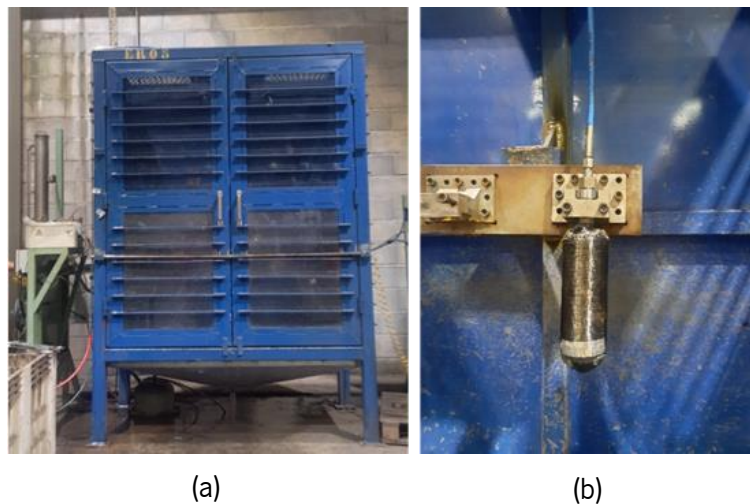


Figure 45: Burst test setup: (a) safety chamber and control equipment; (b) COPV holder

4.3.5.3.2. Cyclic Pressure Testing

Cyclic pressure testing was also conducted at Amtrol-Alfa, Portugal. The COPV is filled with distilled water and antifreeze agent and then connected to the pumping system. The COPV is placed and tested inside of a protecting chamber. Two COPVs were subjected to cyclic pressure testing, between 3 and 525 bar until failure, to evaluate the lifetime of the COPV, as suggested by the

EN12245 European standard. It should be mentioned that the EN12245 standard recommends that the lower pressure value of the cycle does not exceed 10 % of the higher pressure and shall not exceed 30 bar. However, the used setup cannot limit the lower cyclic pressure to that range of values and reaches the minimum pressure of 3 bar.

A smart COPV, with embedded optical FBG sensors, was subjected to 18190 pressure cycles between 3 and 350 bar, to resemble the operational fuel charging and discharging cycles. To reach failure sooner and evaluate the suitability of the FBG sensors to monitor different pressure levels, the smart COPV was then subjected to 1000 pressure cycles between 3 and 400 bar, 1000 pressure cycles between 3 and 450 bar and, lastly, to pressure cycles between 3 and 500 bar until failure. Each cycle lasted for about 7 – 15 seconds. The FBG data during test was acquired by the interrogator system from Ibsen Photonics, at a sampling rate of 100 Hz. The testing setup can be seen in Figure 46.



Figure 46: Cyclic pressure test and OF monitoring setup at Amtrol-Alfa

4.3.5.3.3. Impact Testing and Damage Localisation

Drop-weight impact tests were performed using the Fractovis Plus impact testing equipment from CEAST. The impactor had a hemispheric shape with a 20 mm diameter and a mass of 5.045 Kg. The performed impacts had an energy of 15 J, as the impactor head was at a vertical distance to the impact sight of 305 mm. The COPV was placed in a custom-built concave steel support and fixed with clamps. The drop-weight impact testing setup can be seen in Figure 47.

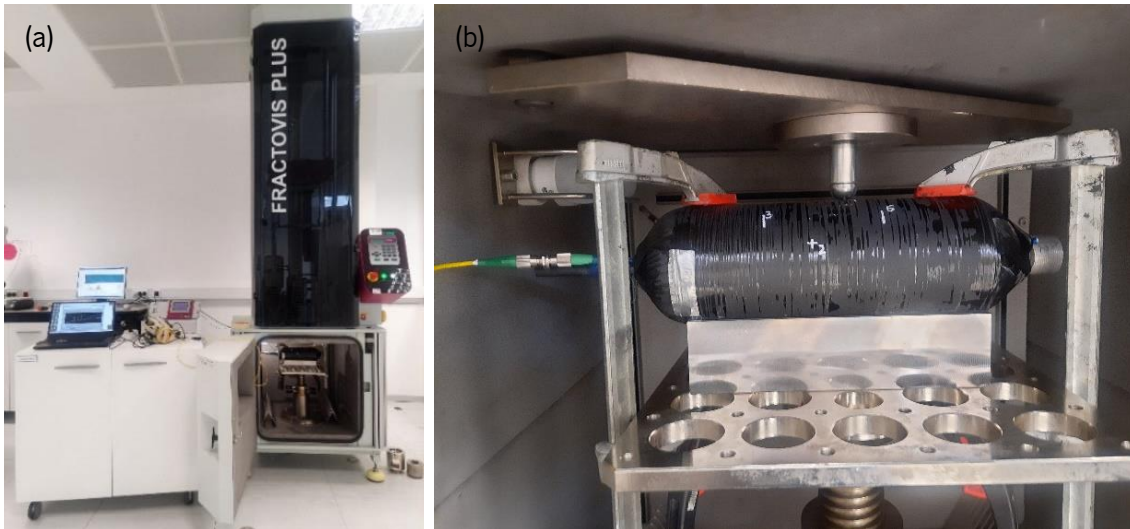


Figure 47: (a) Drop-weight impact testing setup with optical interrogation system and (b) COPV support

A simple method, based on the residual strain amplitude, similar to the one reported by Hiche et al. [152], was used to predict damage location on the circumferential section of the COPV. This method assumes that FBG sensors closer to the impact sight measure higher residual strain values.

The residual strain values measured by each sensor after impact are normalized to calculate the strain ratio, r_{ij} , between each pair of sensors, according to equation 57.

$$r_{ij} = \frac{\bar{\varepsilon}_j}{\bar{\varepsilon}_j + \bar{\varepsilon}_i} \quad (57)$$

being $\bar{\varepsilon}_j$ and $\bar{\varepsilon}_i$ the normalized absolute maximum strain obtained from FBG_{*i*} and FBG_{*j*} sensors, respectively.

For impact detection, only the four sensor pairs with highest strain magnitude, M_{ij} (equation 58), were used.

$$M_{ij} = \bar{\varepsilon}_j + \bar{\varepsilon}_i \quad (58)$$

The cylindrical coordinates (ρ , φ , z) of each FBG sensor were initially inputted to calculate the linear surface distance between each of the selected sensor pairs, d_{ij} , following equation 59.

$$d_{ij} = \sqrt{(z_j - z_i)^2 + \left((\Phi_j - \Phi_i) \left(\frac{\pi \rho}{180} \right) \right)^2} \quad (59)$$

The relative distance between FBG_i, of the FBG_i/FBG_j sensors pair and the expected impact location, I_d , was calculated according to equation 60.

$$I_d = r_{ij} \times d_{ij} \quad (60)$$

The cartesian coordinates of the relative impact locations ($(I_{ij})_x$, $(I_{ij})_y$) were recorded, using the nearest FBG sensor as origin of the coordinate axes, considering the 2D flat projection of the cylinder region (as it can be seen in the results and discussion section, 5.4.2.3, Figure 90). The cartesian coordinates of the predicted impact location, $(I(p)_x$, $I(p)_y$), are finally obtained from the average of the relative impact positions obtained from the four FBG sensor pairs previously selected, as given by equation 61.

$$[I(p)_x, I(p)_y] = \left[\frac{\sum_{k=1}^4 (I_{ij}^k)_x}{4}, \frac{\sum_{k=1}^4 (I_{ij}^k)_y}{4} \right] \quad (61)$$

Chapter 5

Results and Discussion

5.1. Introduction

This chapter presents the main results of this work, and it is divided in the three main following sections: i) monitoring of CFRP laminates by optical FBG sensors, ii) monitoring of CFRP laminates by EIT and, iii) development of a smart COPV prototype for hydrogen storage. The latter section is divided in two subsections, the first concerning to the COPV product development, including its structural design, production and testing, and the second one dealing with the integration and implementation of an optical sensing system for real-time monitoring of the production process and structural health condition.

The first section (section 5.2) starts with the results concerning the exploitation of FBG sensors, early on from their integration into the CFRP laminates, when being prepared for the VARI production, until their use to monitor their room temperature curing process and post processing in an oven. To assist the interpretation of the FBG sensors measurements during curing of the CFRP laminates and the resin system alone, curing kinetics studies conducted on the epoxy resin, using the DSC analysis, are presented in this section. This section also presents and discusses the recorded data from FBG sensors embedded into host CFRP laminate specimens subjected to LVI tests, for BVID detection capability purposes.

The second section (section 5.3) presents results and discusses the suitability of using the EIT technique to detect and locate damages in CFRP laminate specimens, namely, severe damage in the form of through-thickness holes and impact damage of different severities. The last section shows and discusses the main results for the validation of the embedded optical FBG sensing system in the developed COPV prototype for hydrogen gas storage. At first, the results of the test to demonstrate the process monitoring (winding and curing) capabilities are analysed. Then follows the analysis of the cyclic pressure testing results to evaluate the suitability of the sensing system for initial testing and development of prototypes and, also, of life cycle monitoring as this test resembles the charging and discharging cycles during the operation of the COPV. Lastly, the results

of drop weigh impact tests are investigated to assess the capability of the optical sensing system to detect and locate BVID.

The third section reports the development of the smart COPV, its modelling, production and testing for validation of the structural finite element model, and the implementation of a monitoring system. Given the higher maturity and wider capabilities of FBG sensors, as reported in the results obtained in the mentioned earlier work of this thesis, these sensors were selected to be integrated in the COPV to enable its production monitoring and structural health monitoring, including for impact damage detection and location and operating loads monitoring. These results are presented in section 5.4.

5.2. Embedded FBG Sensors for Cure and Impact Damage Monitoring

5.2.1. Curing Studies

5.2.1.1. Resin Curing kinetics

As described in section 4.3.2.1, a dynamic DSC analysis was performed on the uncured resin between -30 and +250 °C to define the temperatures to be used in the subsequent isothermal DSC tests and measure the total enthalpy of curing. The obtained curve is presented in Figure 48.

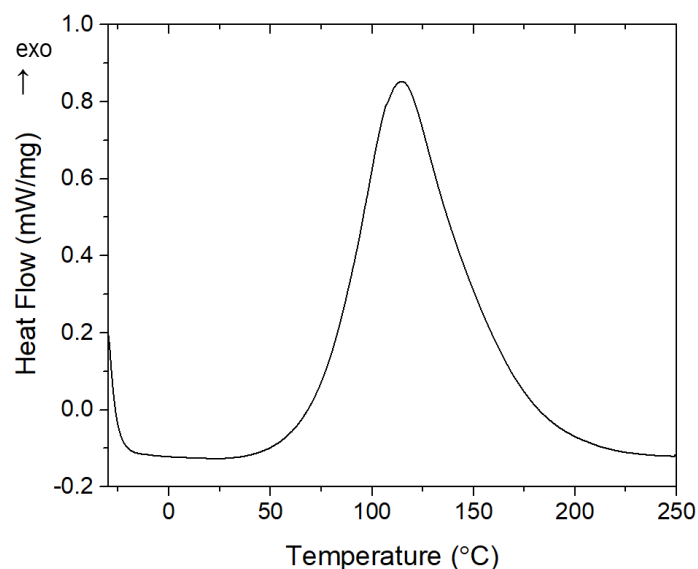


Figure 48: Measured heat flow during dynamic DSC experiment between -30 and 250 °C of the uncured resin

The enthalpy of the curing reaction was found to be 373.0 J/g, by integrating the area of heat flow of the exothermic peak. The selected temperatures for the isothermal DSC experiments are below the exothermic curing peak at 115 °C.

The curing kinetics of the epoxy resin system alone was firstly evaluated by isothermal DSC studies, using the model-free isoconversional Friedman method previously described in section 4.3.2.1. The isothermal DSC experiments showed the peak of exothermic curing right at the beginning of each isothermal test (see Figure 49), which is the typical curve shape of a n^{th} order reaction. Therefore the experimental data was initially modelled by the n^{th} order reaction model equation and then by the Sestak-Berggren model equation [145]. Nonetheless, as described in section 4.3.2.1, the Friedman model-free kinetics method was used because it presents better fitting than the model-based approaches. Experimental and model differences arise attending to high rate that curing occurs at the beginning of each isothermal DSC test, which makes impossible to measure the heat flow before the temperature has stabilized at the set isothermal temperature.

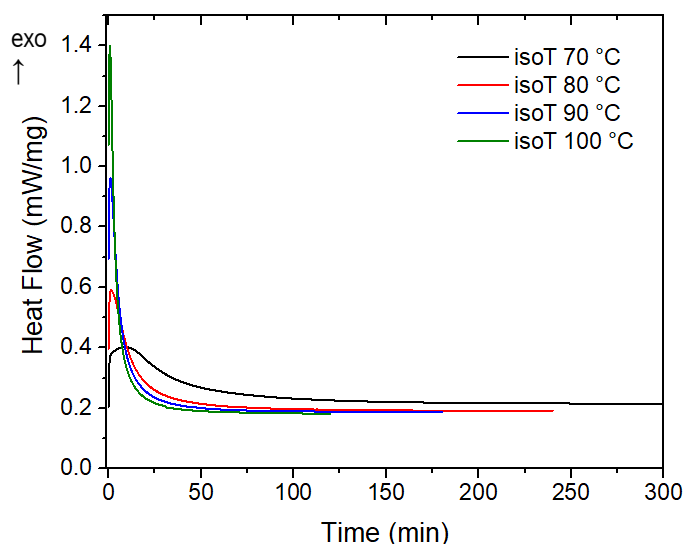


Figure 49: Measured heat flow during isothermal DSC experiments at 70, 80, 90 and 100 °C

The Friedman plot (Figure 50 (a)) was then constructed to allow calculating E_a by using the linear regression of each conversion line as it is presented in Figure 50 (b). As may be seen, the curing reaction has a higher heat flow and thus higher conversion rate at the beginning of the isothermal, which results in a higher E_a at that point. The maximum activation energy was calculated to be about 73.5 kJ/mol at $\alpha = 0.01$, decreasing to about 13.4 kJ/mol at $\alpha = 0.99$. As the curing reaction progresses, being generally a diffusion-controlled process, the mobility of the molecules decreases after the gel point, resulting in lower reaction rates and lower E_a [153].

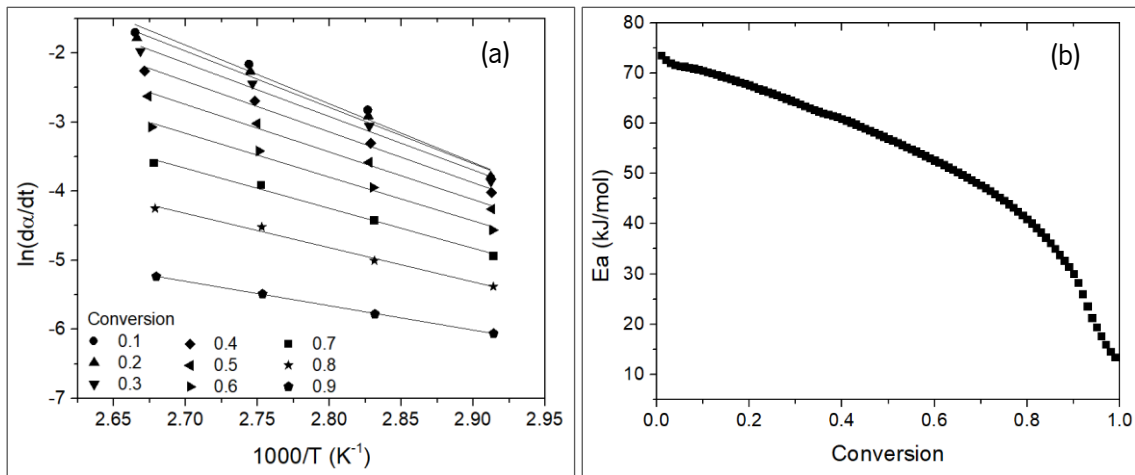


Figure 50: (a) Friedman plot for calculation of activation energy at different conversions presented in (b)

As Figure 51 shows, a good agreement was found ($R^2 = 0.995$) between experimental data and the theoretical fit plotted using the values determined for E_a and y-intercepts, which gave confidence to make isothermal predictions for the curing of the epoxy system for lower temperatures.

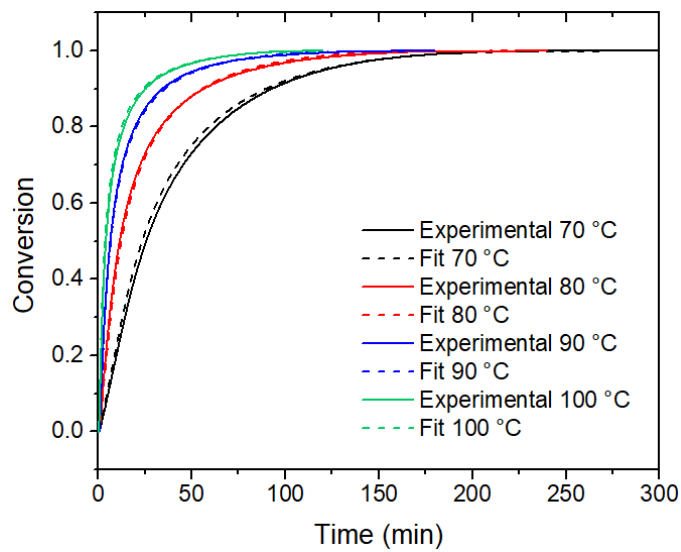


Figure 51: Comparison of experimental curing conversion data and Friedman method fitting

Isothermal curing predictions for temperatures between 17 – 25 °C, are shown in Figure 52. The predictions show that, a small temperature difference of 8 °C can result in a time difference of about 22.4 hours to reach full curing, varying from 52.8 hours at 17 °C to 30.4 hours at 25 °C.

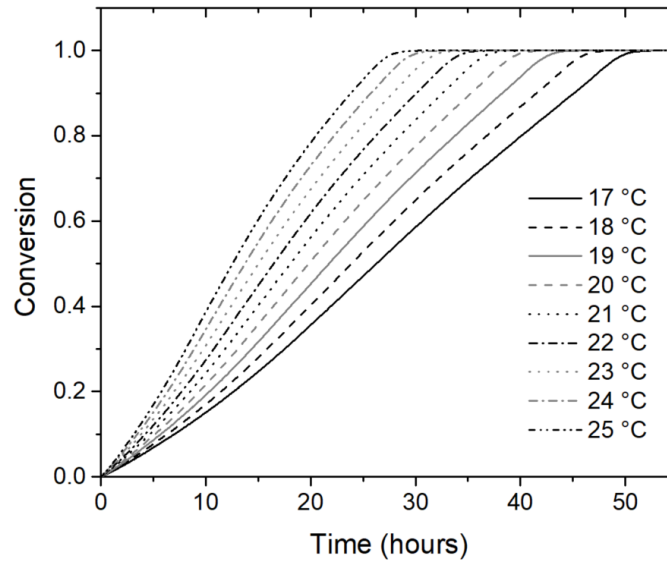


Figure 52: Isothermal curing predictions for temperatures between 17 and 25 °C

5.2.1.2. Epoxy Infusion and Cure Monitoring using Optical FBG Sensors

As previously described in section 3.2, the curing of the epoxy system alone was monitored resorting to a bare and encapsulated FBG sensor ($\text{FBG}_{\text{T-CAP}}$). These experiments aimed to validate the use of the FBG sensors for cure monitoring. Figure 53 shows the strain and temperature change calculated from the FBG wavelength shift data during the cure monitoring of the resin system (black line) and the laboratory temperature measured by a type-K thermocouple (blue line). Following an initial strain decrease as the FBG sensors stabilize in the casted epoxy resin, the strain starts to increase, due to the developing network of covalent bonds, reaching a maximum of approximately $92 \mu\epsilon$ after 18.3 hours. A decrease of temperature is measured by the encapsulated $\text{FBG}_{\text{T-CAP}}$ sensor, which is explained by the initial temperature difference between the optical fibre and resin. Afterwards, the resin shrinkage due to crosslinking leaves the FBG under compressive strain, allowing to calculate a strain to decrease by about $322 \mu\epsilon$, when it reaches a strain value close to $-230 \mu\epsilon$ at 40 hours of ambient curing. The $\text{FBG}_{\text{T-CAP}}$ sensor revealed to be highly sensitive to the laboratory temperature variations, as it can be observed by the temperature increase measured by both $\text{FBG}_{\text{T-CAP}}$ sensor and thermocouple variation measured between 16 – 20 hours.

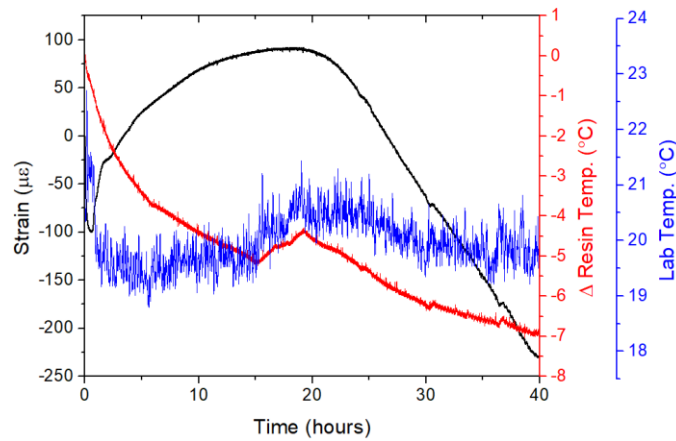


Figure 53: Ambient cure monitoring of the epoxy resin system through FBG sensors and type-K thermocouple

At the time data recording was stopped, the resin has hardened but was not fully cured, since strain was still showing a downward progression. Looking at the isothermal curing predictions in Figure 52 for temperatures between 19 and 20 °C, full curing would be expected to only occur after 41 – 44 hours. According to these same predictions, 40 hours of ambient curing at 19 °C would result in a conversion of 0.93, while at 20 °C the conversion would be 0.99. Yet, a DSC test performed on a small sample of the room temperature cured resin allowed to calculate a residual enthalpy of curing of about 108.2 J/g, which corresponds to a curing conversion of 0.71 (see Figure 54). Such conversion difference can be due to distinct localised curing degrees in the resin sample and to the small size and unrepresentative sample used in the DSC test. The glass transition is visible in the heat 2 of Figure 54 at an onset temperature of 93.42°C and with a mid-temperature of 98.66°C.

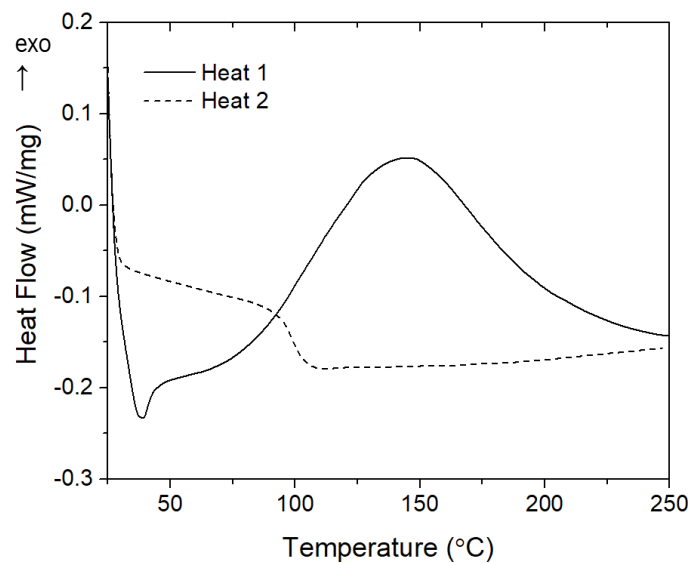


Figure 54: Measured heat flow during heat 1 and 2 of the heat-cool-heat DSC cycle after room temperature curing of the resin system

Further curing was inferred by the FBG measurements in the post curing process, as it can be seen in Figure 55. The epoxy resin was subjected to the post curing process, as suggested by the supplier, at 70 °C for 8 hours, using one heating and cooling rate of about 15 °C/h.

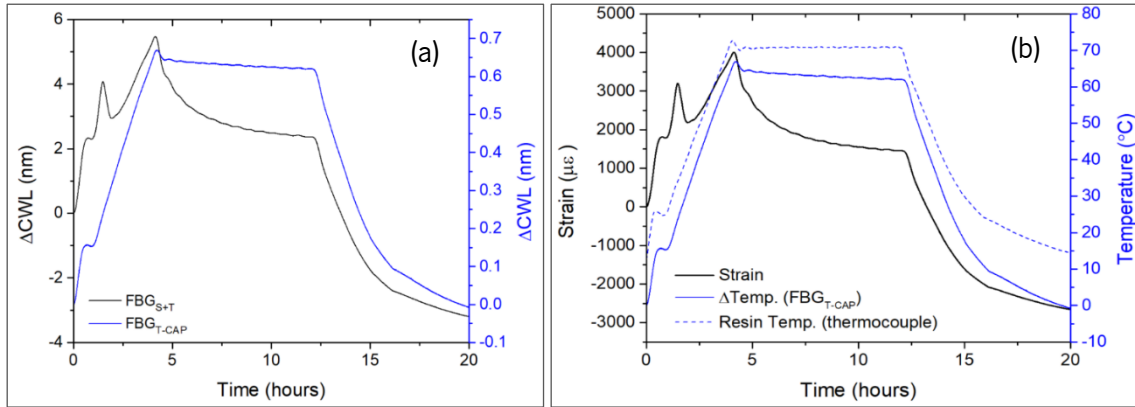


Figure 55: Post cure monitoring of the epoxy resin showing (a) the CWL shift measured by the FBG sensors and (b) respective calculated strain and temperature shift, and resin temperature measured by a type-K thermocouple

During the initial part of the heating stage, the strain measured by the FBG sensor changes as temperature changes, due to the resin thermal expansion/contraction. During the heating stage, when the thermocouple was reading a temperature of approximately 35 °C at about 1.56 h, the strain decreased for about 25 minutes, while the resin kept warming up following the imposed heating rate. This demonstrates that shrinkage due to crosslinking is taking place. While at around 2 hours of post curing the strain starts to increase again, it is noticeable that the slope of strain curve is not as high as the slope of the temperature curve, showing that cure shrinking, and resin thermal expansion are competing at this moment. The strain reaches a maximum of 4004 $\mu\epsilon$ at the beginning of the isothermal period. During the isothermal period, the strain decreases slowly, showing that crosslink bonds are still forming, while thermal expansion stops as the temperature is kept constant. As the strain was still slightly decreasing, it indicates that the resin plate did not cure completely by the end of the isothermal period. As temperature is decreased in the cooling stage, thermal contraction acts on the FBG_{S+T} sensor and compressive strain is imposed on it. A compressive strain of about -2762 $\mu\epsilon$ was calculated at the end of the post curing process. The shape of CWL shift curve of the FBG_{S+T} sensor (Figure 55 (a)) closely matches the shape of the strain curve (Figure 55 (b)), showing that the effect of mechanical strain is stronger than the effect of temperature for such a sample made of neat resin, as opposed to what is observed for the CFRP laminates in Figure 59. The ambient curing produced much lower compressive strains than the post curing procedure, showing that higher temperatures lead to higher residual strain.

A DSC test was performed to a small sample of the post-cured resin to evaluate the curing conversion degree. A residual enthalpy of curing of about 4.6 J/g was measured in the tenuous exothermic bump in the first heating step of Figure 56. That reveals a conversion degree of 0.99, reaching almost full conversion. The glass transition is already visible in the heat 1 as the exothermic curing reaction is almost insignificant during the DSC test. The glass transition has its onset at 81.87 °C and its mid temperature is at 86.10 °C. The glass transition is seen at higher temperatures in heat 2, it has an onset temperature of 95.01 °C and a mid-temperature of 101.93 °C. Higher curing degree provides the higher glass transition.

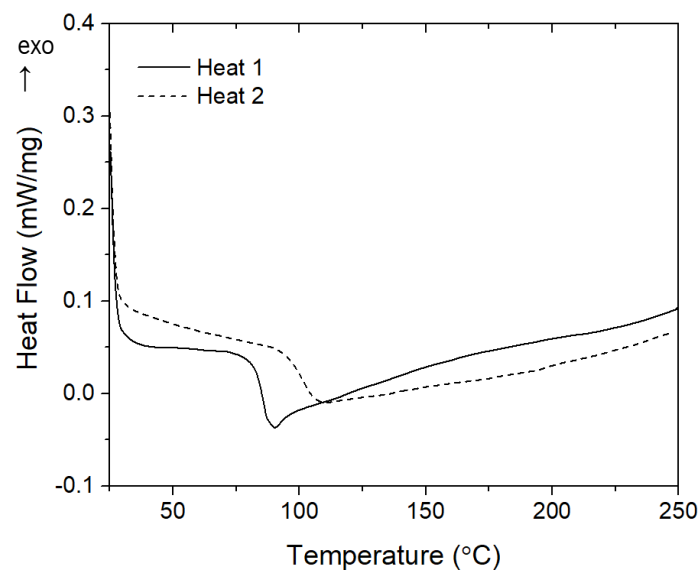


Figure 56: Measured heat flow during heat 1 and 2 of the heat-cool-heat DSC cycle after post curing of the resin system

5.2.1.3. CFRP Cure Monitoring using Optical FBG Sensors

The FBG sensors were used to monitor the VARI process, right from the beginning, prior to resin infusion. A slight strain increase, in the order of 20 to 50 $\mu\epsilon$, was observed as resin started flowing into the dry fibres at the beginning of the vacuum infusion process. The pressure increase puts the FBG_{S+T} sensor under tensile strain. Figure 57 shows an example of strain monitoring on a specimen having the optical fibre located in between the two -45° layers at the CFRP laminate mid-plane (M-45 location, see Figure 25 in section 4.3.1.1) up to 12 minutes past beginning of signal acquisition. The small peak is followed by a steep decrease of strain as the resin fills in the voids in between the dry carbon fibre reinforcement, compressing the FBG_{S+T} sensor, and an inflection point is visible. Following the step decrease, strain stays relatively constant for the remaining time of ambient curing. This behaviour was observed among all the specimens, except for the sample shown in Figure 58 (a).

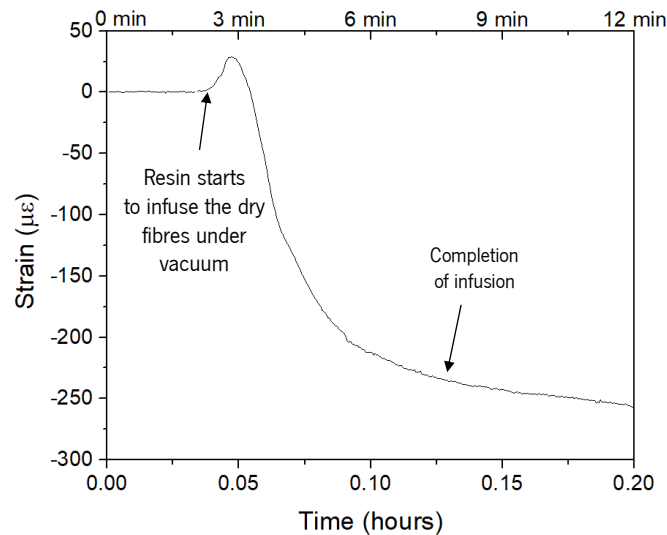


Figure 57: Strain measured during initial 12 min of cure monitoring on a specimen with OF at M-45 location

All the temperature sensitive FBG sensors revealed to be very sensitive to room temperature variations induced by the daily laboratory activities. The thermocouple measuring the laboratory temperature allowed to conclude that the temperature changes measured by the $\text{FBG}_{\text{T-CAP}}$ sensors are due to temperature fluctuations in the laboratory and are not produced by the curing reaction of the resin. Examples of strain and temperature change curves, measured by the $\text{FBG}_{\text{T-CAP}}$ sensors located between the two 0° oriented layers at the upper (T0) and lower (B0) CFRP laminate plies and into its mid-plane -45° oriented layers (M-45), during the full room temperature curing process for specimens with small diameter optical fibre at (a) T0, (b) B0 and (c) M-45 locations (see Figure 25 in section 4.3.1.1), as well as the laboratory temperature, are presented in Figure 58. While, generally, most of the samples showed a strain plateau (indicated by a two-sided arrow in Figure 58 (b) and (c)) after the sudden strain decrease after resin fill up, the sample shown in Figure 58 (a), with the FBG sensor at T0 location, showed a strain increase starting at about 3 hours. Although the wavelength variation data of the temperature sensitive FBG sensors was used to compensate for the temperature effect on the $\text{FBG}_{\text{S+T}}$ sensors, some degree of temperature influence on the strain curves is still noticeable (indicated with arrow signs), which may explain some fluctuations observed in the strain curves. The FBG sensors take very localised measurements and the CWL shift produced on the $\text{FBG}_{\text{T-CAP}}$ sensor may not entirely match the CWL shift produced by temperature on the $\text{FBG}_{\text{S+T}}$ sensor. On the other side, as the temperature increases or decreases, the laminate may expand or shrink, producing a tensile or compressive strain, respectively, on the $\text{FBG}_{\text{S+T}}$ sensor. Yet, about 27.2 hours after infusion, strain starts to decrease in the FBG sensor at T0 location. Similarly, the FBG sensor at B0 location (Figure 58 (b)) starts to present a strain

decrease at 28.6 hours. The FBG sensor at M-45 location (Figure 58 (c)) presents a strain decrease much earlier, at around 12.6 hours. These are a wide range of values that differ from -5.7 hours to +10.3 hours compared to the 18.3 hours after which compressive strains were applied on the resin system alone.

It is noticeable the difference between the strain curve of the CFRP laminates cured under vacuum and of the resin system cured at ambient pressure. Considering the cure of CFRP laminates under vacuum, after infusion, the produced compressive strains are only in the range of 20 to 30 $\mu\epsilon$, in contrast to the cure monitoring of the resin system alone at ambient conditions, where a compressive strain of about 322 $\mu\epsilon$ was measured. It can be attributed to the high level of compactness imposed on the carbon fibre fabric by the vacuum pressure and to the small amount of resin when compared to the neat resin system. A correlation between optical fibre positioning along the laminate thickness and FBG ability to monitor curing was not found.

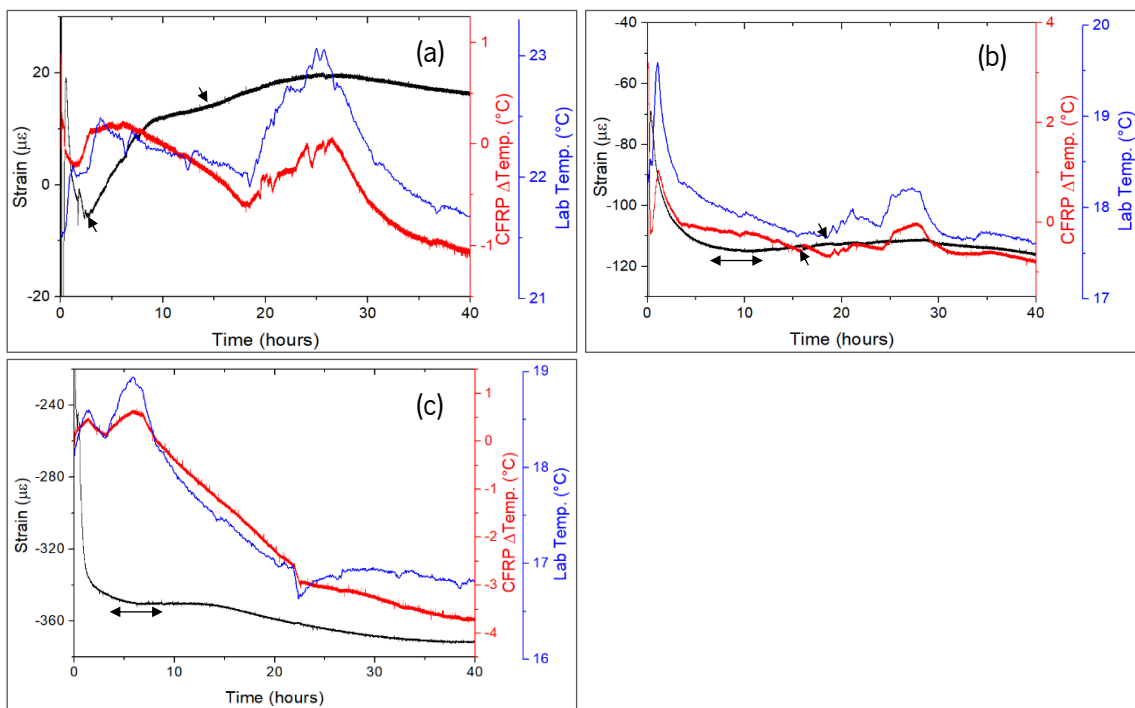


Figure 58: Room temperature cure monitoring of specimens with SDOF at (a) T0, (b) B0 and (c) M-45 location. Note that the strain scales have been zoomed in to better show the strain variation; the strain at time zero starts with strain values around zero, as the wavelength value at time zero of infusion was considered to be the reference Bragg wavelength.

The central wavelength of the FBG sensors (Figure 59 (a)) was also recorded during post curing process, for one sample of each location studied. The developed strain and temperature change, along with the imposed temperature profile recorded in the oven, are plotted in Figure 59 (b) for a specimen with the OF embedded at location B0. As the temperature increases, the strain also

increases due to thermal expansion of the resin until it reaches a maximum point where strain starts to decrease. Just like observed in the post curing of the resin system alone, here there are further crosslink bonds forming as well, causing the resin to shrink and strain to decrease. Strain decreases during the initial 2 hours of the isothermal period and it is approximately constant for the remainder time of the isothermal step, showing that most of the curing happened up to the initial 2 hours of the isothermal period. The strain decreases upon cooling as resin shrinks and applies a compressive stress on the $\text{FBG}_{\text{S+T}}$ sensor. The slope of strain vs. time curve changes according to the cooling rate. The shape and value of the wavelength variation curve of the $\text{FBG}_{\text{S+T}}$ sensor is very similar to the wavelength variation curve of the $\text{FBG}_{\text{T-CAP}}$ sensor for most of the curing process. This shows that a large portion of the wavelength variation in the $\text{FBG}_{\text{S+T}}$ sensors is promoted by temperature variations rather than mechanical strain, oppositely to what happens in the post cure monitoring of the resin system where the $\text{FBG}_{\text{S+T}}$ sensor suffers a much higher CWL shift owing to mechanical strain. The deviation from the linear strain increase during the heating stage was observed at around 1.11 h for a period of about 6 minutes, when the temperature in the laminate raised by about $2\text{ }^{\circ}\text{C}$, as measured by the $\text{FBG}_{\text{T-CAP}}$ sensor. In turn, at that time interval, the oven registered a temperature raise from $42.2\text{ }^{\circ}\text{C}$ up to $43.6\text{ }^{\circ}\text{C}$. This strain curve perturbation is showing up at higher temperatures than in the neat epoxy plate, which happened at around $35\text{ }^{\circ}\text{C}$. At the end of cooling, the compressive strain stabilized at a value of about $-100\text{ }\mu\epsilon$, a much lower value than the one of $-2762\text{ }\mu\epsilon$ measured at the end of post curing of the resin. This can be explained by the small amount of resin in the CFRP and by the near zero CTE of the carbon fibres.

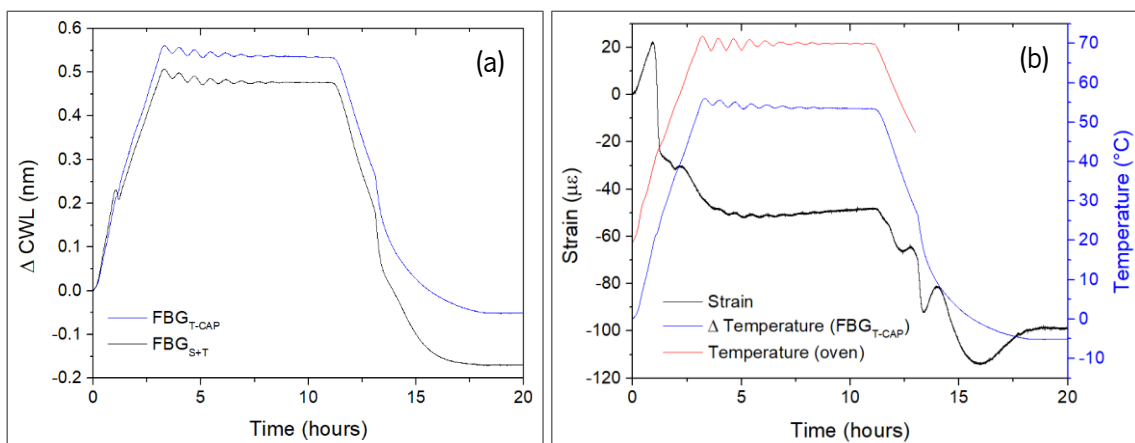


Figure 59: Post cure monitoring of specimen with SDOF at location B0: (a) CWL change measured on $\text{FBG}_{\text{T-CAP}}$ and $\text{FBG}_{\text{S+T}}$ and, (b) correspondent calculated strain and temperature variation, and imposed temperature profile recorded by the oven

FBG sensors may not be able to evaluate the curing conversion at ambient curing, but they are, certainly, a useful approach for high temperature curing resins and post curing monitoring, when the subtle temperature fluctuations measured during ambient curing, highly contributing to the shape of FBG wavelength shift, are negligible.

5.2.1.4. Residual Strains measured by Optical FBG Sensors

The use of the FBG sensors allowed to evaluate the residual strains developed at different stages of the VARI process. It was observed that the preparation of the VARI set up, fixing and placing of the optical fibre in between CF plies during preform and vacuum bag preparation already induced either compressive or tensile strain on the FBG sensors. An example of the wavelength spectrum shift is presented in Figure 60 for the SDOF placed at location B0. The Bragg wavelength of the FBG_{S+T} increased when embedded and under vacuum in the dry preform, right before infusion, when compared to the free condition (“as received” spectrum), revealing that the sensor is under tension. This condition was not observable for all the samples, some of them were under tension, others under compression, which is expected in such a manual embedding procedure. Nevertheless, as expected, most of the samples present a tensile pre-strain since they were tightly fixed to the sealing tape to be well aligned with the dry carbon fibre reinforcement. The pre-strain imposed in the VARI set up was calculated by the variation in the Bragg wavelength between the spectra of the optical fibre taken “as received” and just before infusion and resorting to equations 7 and 8. Examples of the pre-strain values observed in each optical fibre location are summarized in Table 3. It should be noted that these FBG spectra data are very localised measurements in both time and area of the sample and may not entirely represent the real residual strain. Furthermore, the spectrum wavelength resolution is very low, 0.16 nm, corresponding to a strain of about 133 $\mu\epsilon$, which may fail to accurately measure the Bragg wavelength peak. For instance, the “As received” spectrum clearly did not present a symmetric peak. To minimize erroneous strain calculation, the spectra data was fit to an areal based Gaussian function, using the *fityk* software, to find a more realistic CWL peak. Nonetheless, these pre-strains imposed by the preform preparation do not influence the final properties of the laminate and following strain measurements.

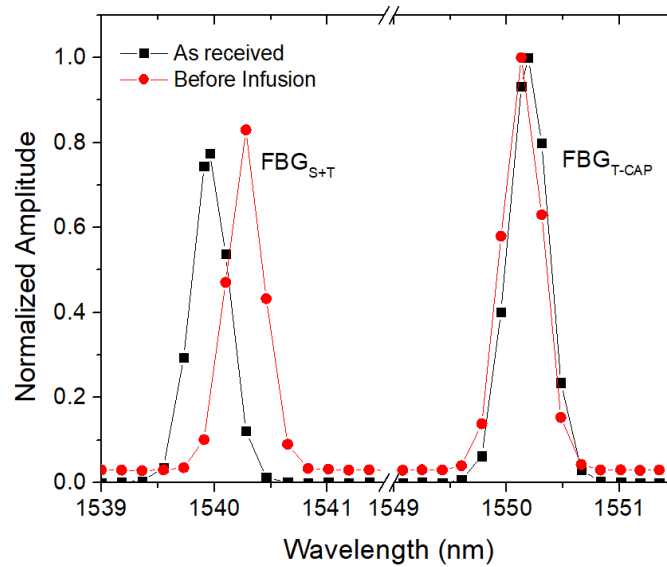


Figure 60: Wavelength spectrum of a free SDOF, as received, and of the same optical fibre placed in between the carbon fibre plies in the VARI set up

As discussed in the previous section, for the case of the specimen with OF at B0 location and for most of the samples, there was a decrease on the Bragg wavelength of the $\text{FBG}_{\text{S+T}}$ sensor during ambient curing (Figure 58 (b)) and post curing (Figure 59). This is explained by resin shrinking as crosslinking takes place during ambient curing and post curing. A comparison of the residual strains measured by FBG sensors on SDOF and LDOF in the ambient curing and post curing stages is provided in Table 3. Oppositely to the pre-strain values developed in the VARI process, the presented residual strain values produced in the ambient curing and post curing stages were obtained by continually following the variation of CWL instead of comparing the full FBG spectrum at the beginning and end of the curing stages.

Table 3: Measured residual strain values during ambient curing and post curing by the embedded small diameter and large diameter FBG sensors on CFRP laminates

Sample	Residual Strain ($\mu\epsilon$)		
	Pre-strain in the VARI set up	Ambient Curing	Post Curing
T0	158	16	-48
SDOF	B0	267	-118
	M-45	67	-372
	Average	164 \pm 82	-158 \pm 161
T0	543	-350	-156
LDOF	B0	-156	-5
	M-45	-66	-112
	Average	107 \pm 310	-156 \pm 144

The residual strains developed in the ambient curing stage were highly variable both on samples with SDOF and on samples with LDOF, with high standard deviations from the average values, $-158 \pm 161 \mu\epsilon$ and $-156 \pm 144 \mu\epsilon$, respectively. This range of values can be attributed to different vacuum pressures in the vacuum bag. The post curing procedure produced more uniform residual strain values among the samples, $-60 \pm 26 \mu\epsilon$ and $-128 \pm 25 \mu\epsilon$ for samples with SDOF and LDOF, respectively. The obtained results are comparable to the work reported by Kang et al. [93], Leng et al. [92] and Chehura et al. [91] on prepreg laminates. Moreover, it is possible to conclude that the LDOF did not contribute to higher residual strains in the final CFRP laminates.

The FBG sensors have proved to be able to follow the residual strain resulting from the processing conditions. For certain aerospace applications where tight dimension accuracies are needed, the use of FBG sensors can be beneficial to better adjust the curing temperature and cooling and heating rates to yield lower residual strains.

5.2.2. Low Velocity Impact Studies

5.2.2.1. Selection of Impact Energies for Production of Barely Visible Impact Damage

The damage imposed on non-instrumented reference specimens during drop-weight impact testing, performed accordingly to the procedure described in section 4.3.3.1.1, was evaluated to

select adequate impact energies that produce BVID. The recorded impact contact loads are plotted in Figure 61 and the averages of absorbed energy and maximum impactor contact force of three specimens for each level of energy are presented in Table 4.

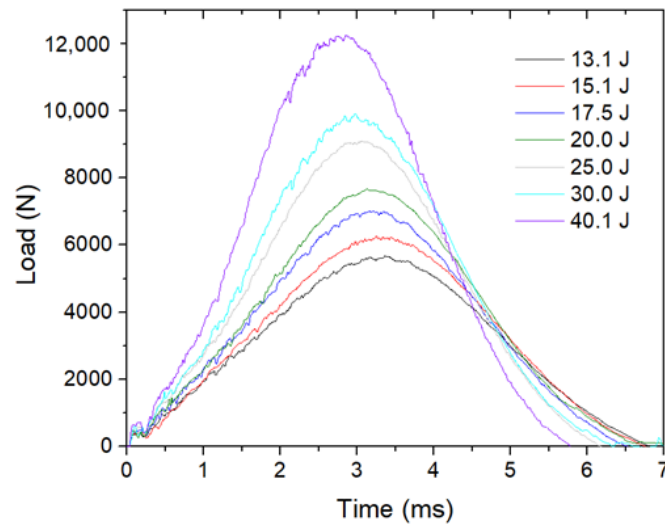


Figure 61: Contact force measured in each impact energy test made on the reference CFRP laminate.

Table 4: Absorbed energy and maximum contact force for each level of energy used in the impact tests performed on the reference CFRP laminate

Impact Energy (J)	Absorbed Energy (%)	Max. Impact Force (N)
13.1	45.5 ± 0.3	5662 ± 15
15.1	45.4 ± 0.4	6317 ± 35
17.5	46.2 ± 0.1	6986 ± 24
20.0	41.1 ± 0.3	7696 ± 50
25.0	46.5 ± 0.7	9069 ± 24
30.0	44.8 ± 0.6	9899 ± 85
40.1	54.0 ± 3.2	12189 ± 39

The maximum impact force increased with impact energy. For impact energies between 13.1 and 30.0 J, the absorbed energy did not change significantly. Although there was an increase of absorbed energy of roughly 9% for impacts with 40.1 J, the load vs. time graph in Figure 61 does not reveal severe damage. Yet, the samples exposed to impact energies of 40.1 J showed lower contact time, revealing higher stiffness.

All the samples presented an indentation at the impact spot, some of them with small matrix cracks transverse to the CF in the top layer. Some samples tested with impact energies between 13.1 and 17.5 J showed a very smooth and hardly noticeable bump on the back surface, whereas samples exposed to impact energies between 20.0 and 30.0 J presented progressively more noticeable bumps on the back surface, but that could still go unnoticed in real-life applications where impact existence and location are unknown. Contrarily, the bump produced on samples exposed to 40.1 J would likely be detected in an attentive inspection. Hence, impact energies between 20.0 and 30.0 J were selected for tests on instrumented laminates. Each sample was first exposed to an impact event of 30.0 J to ensure that BVID was consistently imposed on the sample and that the FBG sensor could detect it, and to a second impact event of lower impact energy of 20.0 J, but that could still produce BVID.

5.2.2.2. Low Velocity Impact Monitoring in CFRP Laminates with Embedded FBG Sensors

Different FBG through-thickness locations were evaluated for BVID detection. BVID was imposed by drop-weight impact testing with the energy range selected in previous section 5.2.3.1. Each sample was subjected to a first and second impact with energies of 30.0 and 20.0 J, respectively. The majority of damage was observed close to the bottom surface, where small bumps were visible (Figure 62 (b)), as also observed in the reference laminates and expected on thin composites [15]. On the impact site, only a small indentation (Figure 62 (a)) was visible. It should be noticed that the indentations observed on the top surface were very shallow, with a depth of about 0.15 mm and 0.12 mm for the cases of the first and second impact events, respectively.

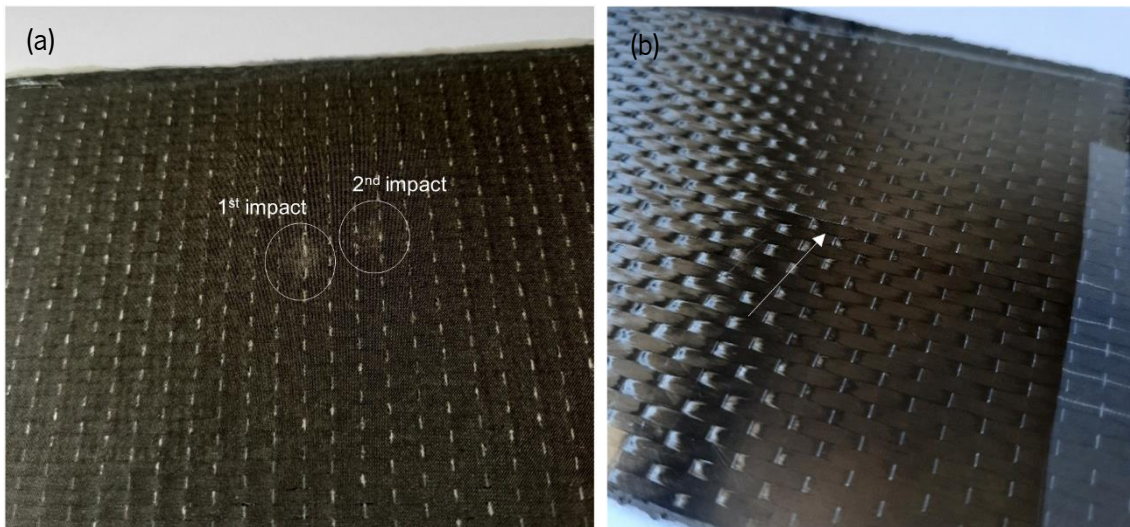


Figure 62: Example of (a) indentation marks on the top surface resulting from the first and second impact events, and of (b) small bump on the bottom laminate surface

Figure 63 presents the contact load measured by the impact setup (a) and strain ((b) and (c)) measured by the FBG sensors in the SDOF during the first impact test made at the energy of 30.0 J. The strain was null just before the impact and, at around 0.1 s the impact happened on each sample. The FBG sensors measured a sudden increase and decrease in strain during impact, lasting about 6 ms, from 0.103–0.109 s. The impact duration was very close to the one measured by the impact setup (Figure 63 (a)). This response can be attributed to the shear and compressive stresses applied at the instant of impact. The through-thickness compressive stresses on the FBG sensor extended its length, resulting in a tensile strain. This fast-changing in strain curve observed in Figure 63 (b) can be very helpful in real-life situations to identify the nature of the event causing damage. Following the fast strain changing event, for the case of the specimens with OF at the B0 and T0 locations (Figure 25 in section 4.3.1.1), the strain slowly reached a residual strain value (Figure 63 (c)). For the case of the specimen with OF at the M-45 location, the strain quickly reached a residual strain value after the sudden increase in strain upon impact, which can be explained by the lower displacement caused by the bending efforts resulting from the impact on the layers located in the laminate mid-plan, where this OF was embedded.

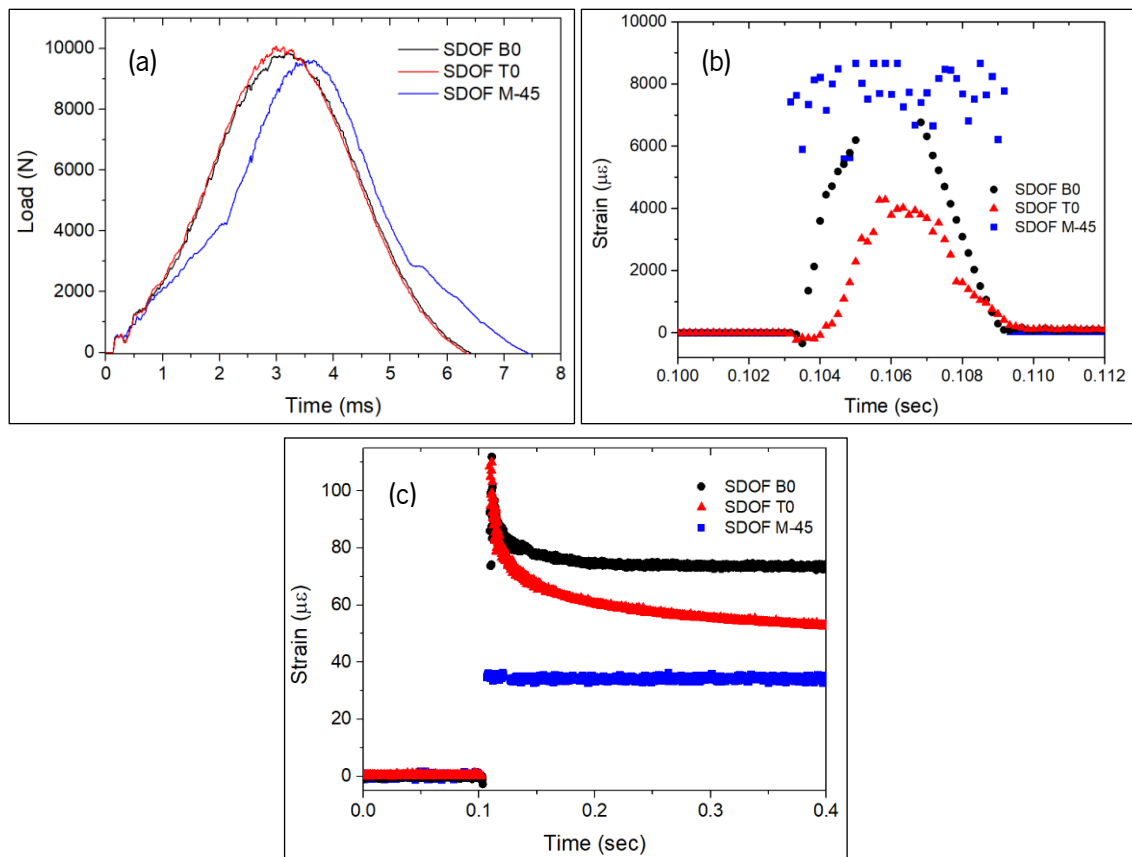


Figure 63: First impact with energy of 30.0 J on specimens with SDOF: (a) impactor load vs. time curves, (b) strain measured by the FBG_{S+T} at the moment of impact, and (c) developed residual strains

The shape of impactor contact load curve of the specimen with the SDOF at the M-45 location in Figure 63 (a) reveals that this sample suffered the highest damage extent, which was also confirmed by phased array ultrasonic observations (Figure 64). The analysed material corresponds to the middle colourful stripe, where the red colour in the top of the scale corresponds to the highest sound wave reflection, as the sound interacted with the laminate, whereas the lower part of the scale with the purplish colours corresponds to the lowest sound reflection and highest sound wave attenuation. A rectangular pattern was clear on the top surface of the laminates, which was due to the weft fibres in the CF fabric. The higher damage extent is visible in Figure 64 (d), with a whitish lower surface of the laminate. It must be noted that if one were to only evaluate the absolute values of strain measured by the FBG sensors, one could never guess that the sample with the OF in location M-45 was the most damaged one, since the SDOF in the M-45 location showed the lowest absolute residual strain value. The high extent of damage probably explains why this FBG sensor did not measure a strain value close to zero.

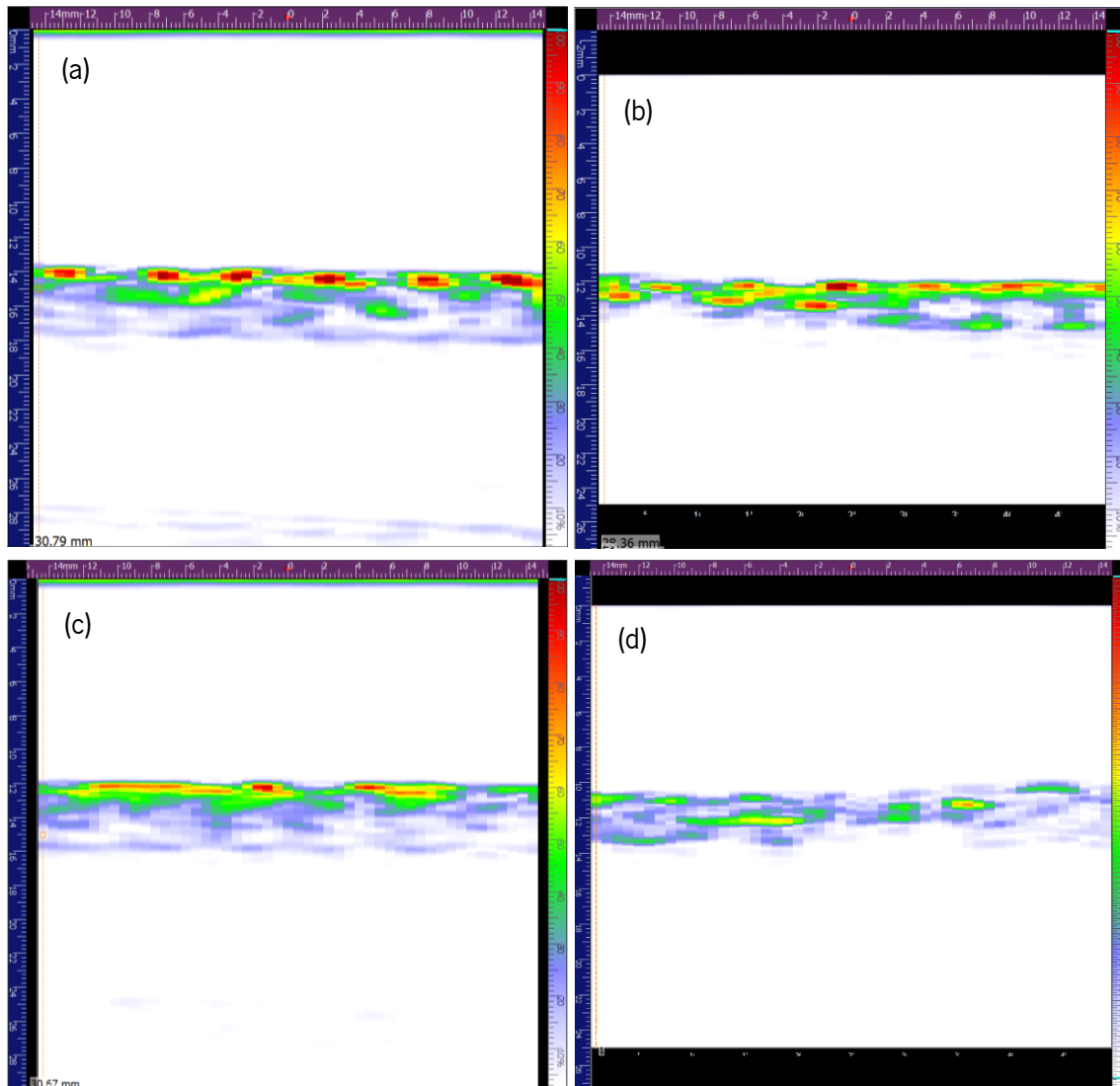


Figure 64: Phased array ultrasonic analysis of SDOF in location B0 prior to (a) and after (b) the first impact and SDOF in location M-45 prior to (c) and after (d) first impact

Again, during the second impact, the FBG sensors measured a sudden increase and decrease in strain in the specimens with OF at the B0 (in between the two bottom layers) and T0 (in between the two bottom layers) locations (Figure 65 (b)). Unexpectedly, the specimen with OF at the M-45 (mid-plan) location kept its strain approximately constant at around $8000 \mu\epsilon$ and it only decreased to about $15 \mu\epsilon$ 1.2 s after the impact, as can be seen in Figure 65 (c). The sample with FBG sensors in the B0 location measured a tensile strain of about $38 \mu\epsilon$, whereas the sample with an FBG sensor in the T0 location measured a compressive strain of about $-30 \mu\epsilon$. The FBG sensor in the M-45 location measured a rather lower residual tensile strain of about $15 \mu\epsilon$. The measured residual strains confirm the typical behaviour of a thin laminate under impact. Damage was mostly observed in the two bottom plies due to the imposed bending stresses [15], resulting in a compressive strain in the FBG in the T0 location, a tensile strain in the FBG in the B0 location, and

a rather lower residual strain in the FBG in the M-45 location. Chambers et al. [27] also reported the measurement of residual tensile strain by FBG sensors embedded below the mid-plan of CFRP after being subjected to LVI. The residual strains measured during the first impact with a higher energy revealed a different behaviour of the laminate. The strain measured by the SDOF at the B0 location was indeed a tensile strain, of about $75 \mu\epsilon$. However, the SDOF at the T0 and M-45 locations also measured tensile strains of about 48 and $34 \mu\epsilon$, respectively. The higher impact energy of 30.0 J caused a stiffer response in the laminate, with the dynamic load producing a rather complex strain-state condition with shear stresses prevailing over bending stresses. The second impact, at least for the case of the samples with OF in the B0 and M-45 locations, produced residual strain values of approximately half of the values observed in the first impacts with energies of 30.0 J.

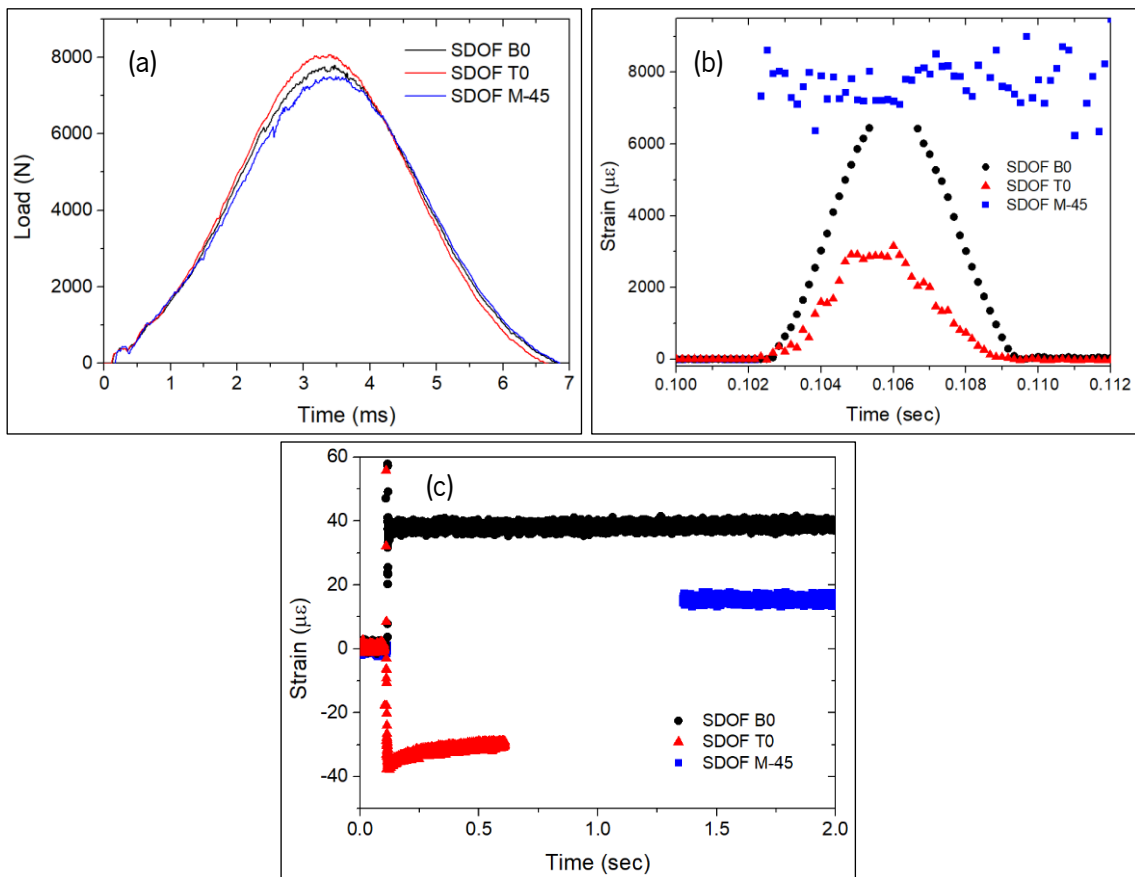


Figure 65: Second impact with an energy of 20.0 J on specimens with SDOF: (a) impactor load vs. time curves, (b) strain measured by the FBG_{S+T} at the moment of impact, and (c) developed residual strains

The measured residual strains on specimens with LDOF at each OF through-thickness location after the first and second impacts are presented in Table 5. The impactor contact load curves (Figure 66) show that the higher damage extent during the first impact was imposed in locations

B0 and T0, whereas location M-45 had more damage extent during the second impact, where critical loads (P_{cr}) were clearly observed by a sudden decrease in load. Due to technical issues with the interrogator equipment, it was not possible to acquire the real-time λ_B variation of the FBG sensors. Instead, the full FBG spectra were recorded both prior to and after impact, from which the λ_B was taken and used to calculate the imposed strain by the impact damage. The lower residual strain values measured on the first impacts, compared to the values measured by the SDOF, are explained by the larger distance between the impact sight and the FBG sensor. The LDOF in locations T0 and B0 measured approximately the same magnitude of residual strain, whereas the LDOF in location M-45 measured a lower residual strain. The second impacts, which were imposed closer to the FBG sensor, measured higher strain values. The observed behaviour was similar to that reported above for the laminates with embedded SDOF.

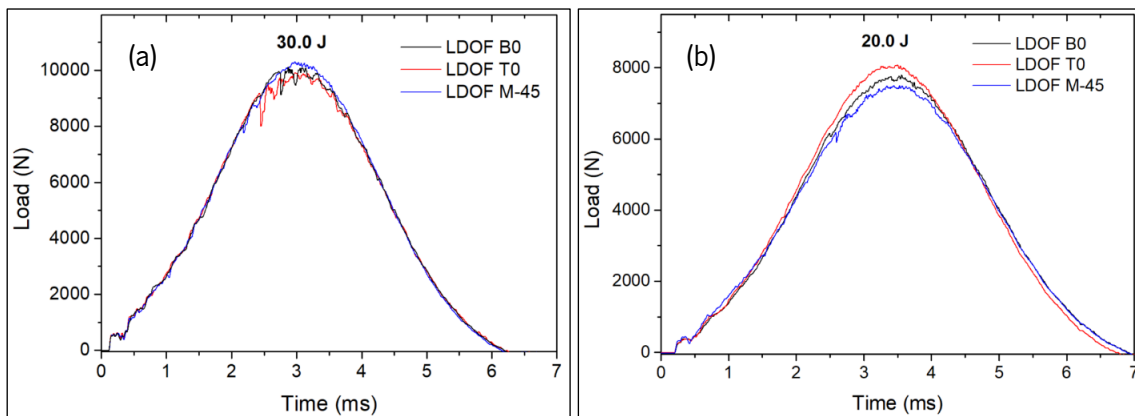


Figure 66: Impactor contact force for LDOF during the (a) first impact with 30.0 J and (b) second impact with 20.0 J

Table 5: Residual strains measured by embedded LDOF in each of the studied through-thickness locations after the first and second impacts

Sample	Strain ($\mu\epsilon$)	
	1 st Impact (30.0 J)	2 nd Impact (20.0 J)
LDOF T0	8	-26
LDOF M-45	-1	-16
LDOF B0	6	35

Two samples with LDOF (labelled sample 001 and 002) with a single FBG_{S+T} sensor embedded at each studied through-thickness OF location were also produced, where the FBG_{S+T} was in the central area of the impact sample, just below the impact site. These samples were also subjected to impacts with energies of 30.0 J and 20.0 J. The λ_B of the FBG in location T0, just one CF layer away from the impactor surface, became broader and with more peaks (Figure 67 (b) and (d)), whereas more severe damage was only observed in the first impact performed on sample 002 (Figure 67 (c)). This reveals that a non-uniform strain was applied along the grating of the FBG, as reported elsewhere [38], [154], [155]. These sensors will likely fail to measure the actual strain condition in the FBG sensor and to detect impacts that may follow. The sample had the same mechanical condition on the “After 1st impact” and “Before 2nd impact” spectra. The slight wavelength shift measured between these spectra was due to small differences in sample temperature, as those spectra were taken on different days. Like in the previous experiments, the second impact with an energy of 20.0 J produced a compressive strain in the FBG sensors in the T0 location.

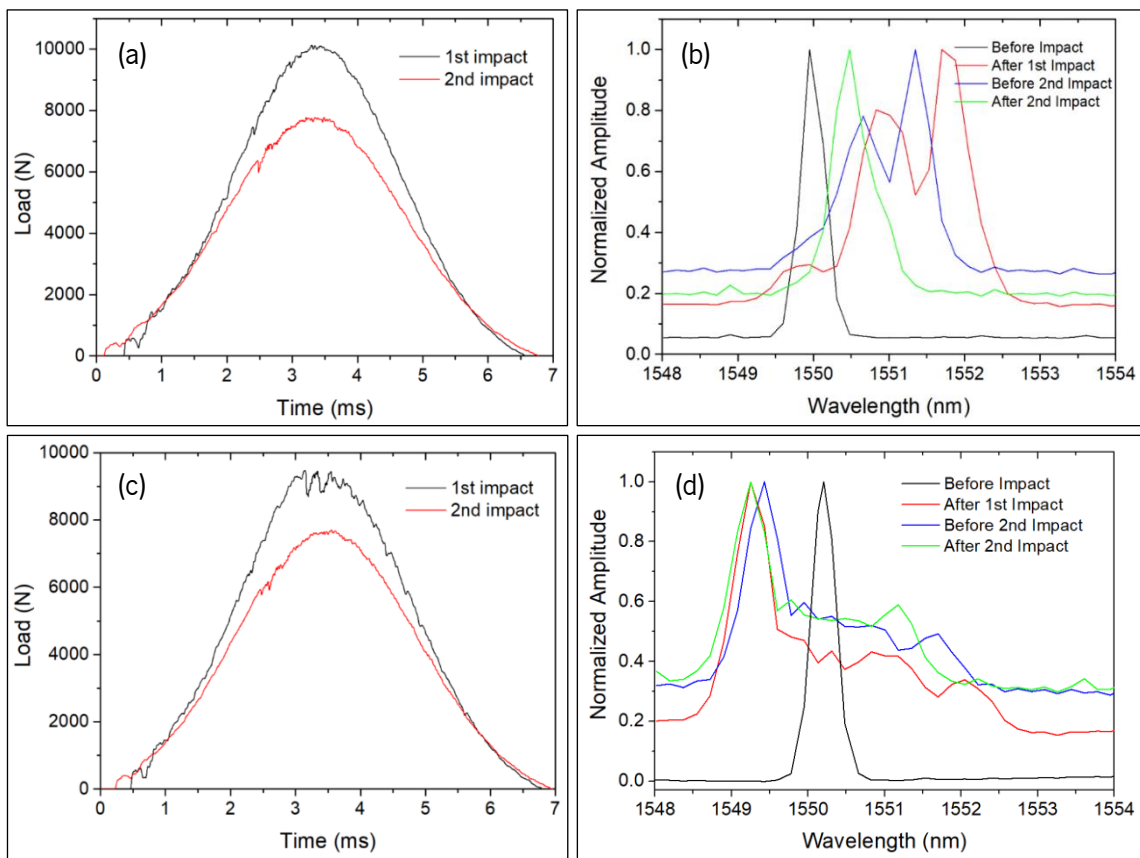


Figure 67: First (30.0 J) and second (20.0 J) low velocity impacts on specimens with a LDOF having a single FBG_{S+T} in location T0: (a), (c) measured load during the impact for LDOF 001 and 002, respectively, and (b), (d) corresponding changes on the FBG spectra

After the first impact, the FBG sensor on LDOF 001 showed a peak split with two maximums at 1550.66 and 1551.35 nm. After the second impact, the FBG sensor showed again only one maximum at 1550.48 nm, which might indicate that the non-uniform strain was no longer applied. The first impact put the FBG under tension, whereas the second impact compressed the FBG, although it still showed a λ_B above the initial condition without damage. Comparing to the original λ_B of the FBG sensor, 1549.95 nm, a tensile strain of 434 $\mu\epsilon$ was introduced. After the first impact, the FBG sensor on LDOF 002 showed a very broad peak with a bandwidth of about 3.5 nm, with a main peak at 1549.43 nm. After the second impact, the FBG sensor showed again a broad peak with about the same bandwidth. Comparing the main peaks in the spectra prior to and after the second impact, a compressive strain of $-147 \mu\epsilon$ was introduced during the second impact. However, the spectra after each impact showed the same λ_B . A strain of $-720 \mu\epsilon$ was measured after the first impact. Looking at Figure 67 (c), the first impact did in fact produce more damage than the second one. The phased array ultrasonic observations in Figure 68 show very similar damage between the two samples and it is possible to see that further damage was introduced in the second impacts, as both impacts were made about 1 cm away. The phased array ultrasonic observations were performed as reported in section 4.3.4.1.

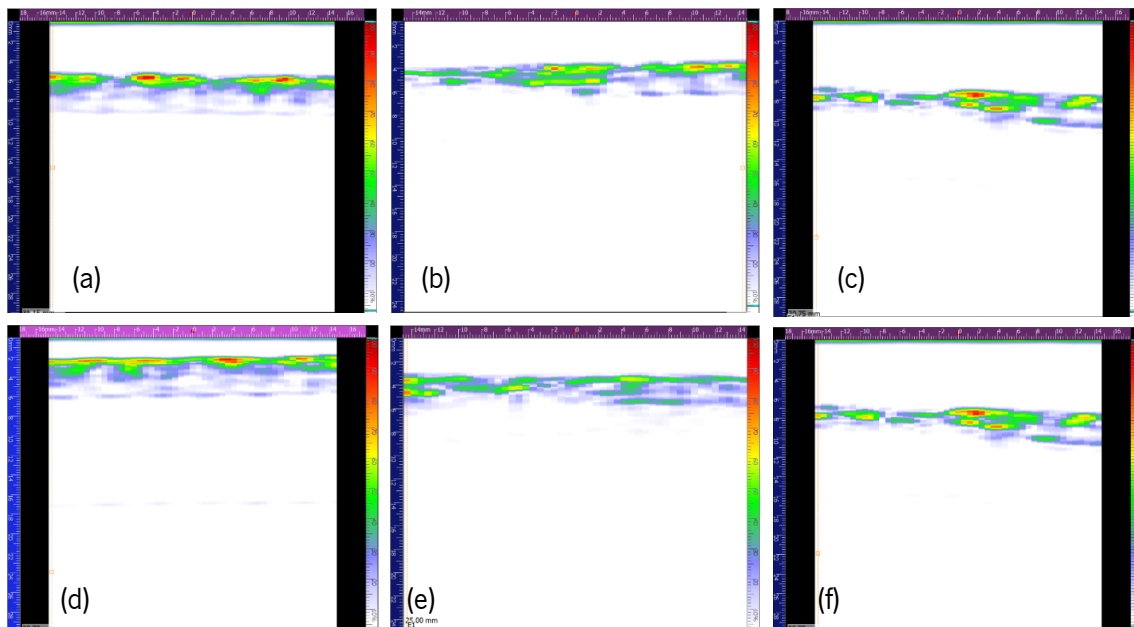


Figure 68: Phased array ultrasonic observations of specimens with an LDOF 001 (top) and 002 (bottom) with a single FBG_{S+T} in location T0: (a) and (d) before impact, (b) and (e) after the first impact, and (c) and (f) after the second impact

Samples with LDOF in locations M-45 and B0 did not have their FGB peak shape change, even though the FBG sensors were also located below the impactor site, but at lower thickness levels in the laminate. These sensors read much higher strain values (see Table 6) compared to the other samples with FBG sensors further away from the impact site. Again, the sample with LDOF in location B0 measured a higher residual strain value than the sample with LDOF in the neutral axis. The FBG sensor of the sample with LDOF in location B0 broke during the second impact of 20.0 J. As mentioned previously, thin laminates had most of the damage imposed in the bottom plies.

Table 6: Residual strains measured by embedded LDOF in each of the studied through-thickness locations after the first and second impacts. The impact location was on top of the FBG sensors.

Sample	Strain ($\mu\epsilon$)	
	1 st Impact (30.0 J)	2 nd Impact (20.0 J)
LDOF M-45	173	-8
LDOF B0	519	(FBG destroyed)

One sample of each condition, with a 2-FBG sensor array on SDOF and LDOF at each studied location, was further exposed to eight more consecutive impacts, all in the same location. Those ones with SDOFs were submitted to impacts with energies of 20.0 J, as FBG_{S+T} sensors were about 2–3 cm away from the impact location, and samples with LDOFs were exposed to impacts with energies of 25 J, as the FBG_{S+T} sensors were about 4 – 5 cm away from the impact location. All FBG_{S+T} sensors survived the 10 total impacts, but two temperature sensitive FBG sensors were damaged between the third and fifth impacts. For samples with OF in locations B0 and T0, the third impact followed the same behaviour observed in the second impact: the FBG_{S+T} in B0 location measured residual tensile strains, whereas the FBG_{S+T} in location T0 measured residual compressive ones. In most of the samples, the fourth to 10th impacts produced either tensile or compressive strains due to accumulated damage caused by precedent impacts in that same location.

5.2.2.3. Influence of Optical Fibre diameter on Low Velocity Impact Resistance

The percentage of absorbed energy and P_{cr} were compared among the instrumented laminate specimens, with the aim to evaluate whether instrumentation with SDOF or LDOF would impair the impact resistance of the laminates. As can be seen in Table 7, the non-instrumented reference

laminates showed lower absorbed impact energy than the instrumented laminates, which reveals that the embedded OF contributed to a higher level of damage in the composite specimens. However, the difference between non-instrumented and instrumented laminates was only about 5%. Moreover, it should be noted that each specimen of reference laminate was impacted only once; hence, the specimens impacted with an energy of 20.0 J were not previously impacted with an energy of 30.0 J, unlike the instrumented laminates. All LDOF-containing specimens showed a P_{cr} in the first impact (Figure 66 (a)), whereas only SDOF in the M-45 location showed a P_{cr} (Figure 66 (b)). Strong evidence of the advantage on the use of SDOF over LDOF was not observable. The almost negligible decline of impact properties, in comparison to the non-instrumented laminate, can be overcome by composite design optimisation to take full advantage of FBG sensors for BVID detection.

Table 7: Percentage of absorbed energy and critical load values measured on impacts at 20.0 and 30.0 J energy levels

Sample	Absorbed Energy (%)		P_{cr} (N)	
	30.0 J	20.0 J	30.0 J	20.0 J
LDOF T0	50.5	46.7	9148	–
LDOF B0	49.0	47.9	9952	–
LDOF M-45	47.9	48.0	8032	–
Average	49.1 ± 1.1	47.5 ± 0.2	9044 ± 787	–
SDOF T0	49.3	42.3	–	–
SDOF B0	49.9	45.9	–	6160
SDOF M-45	50.8	48.7	4255	6400
Average	50.0 ± 0.6	45.6 ± 2.6	–	6280 ± 120
Reference laminate	44.8 ± 0.6	41.1 ± 0.3	8015 ± 58	–

5.3. Electrical Impedance Tomography for Damage Localisation

5.3.1. Detection and Localisation of Through-thickness Holes

The use of EIT for visible and severe damage detection was evaluated with the introduction of through-thickness holes of different diameters, as described in section 4.3.3.2. Figure 69 and Figure 70 show the EIT images of a quasi-isotropic and an unbalanced specimen, respectively, with through-thickness holes A and B with progressive diameter increase from 2 to 6 mm in two locations. Three specimens of each layup configuration were subjected to the same damage, where similar EIT images were obtained.

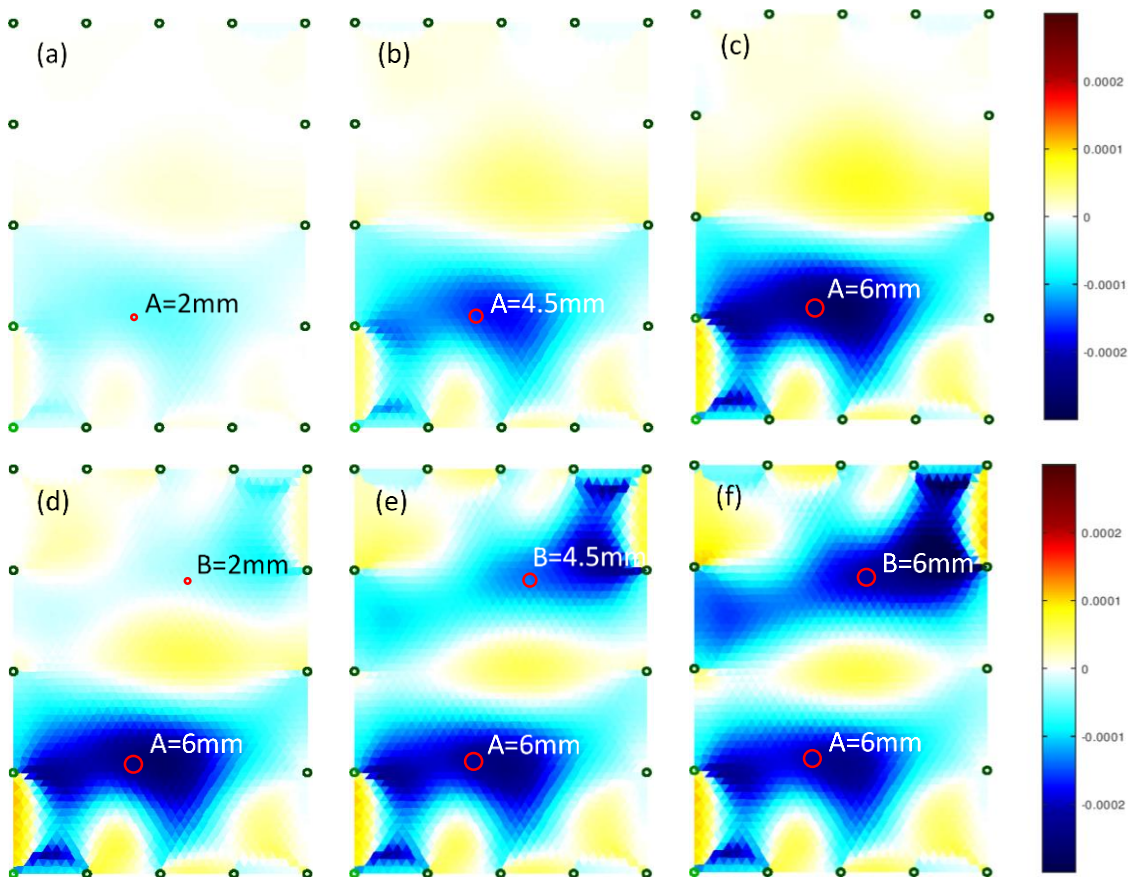


Figure 69: Reconstructed EIT images using GN algorithm of a quasi-isotropic specimen with through-thickness holes of different diameters A and B: (a) A: 2 mm; (b) A: 4.5 mm; (c) A: 6 mm; (d) A: 6 mm, B: 2 mm; (e) A: 6 mm, B: 4.5 mm; (f) A: 6 mm, B: 6 mm. The green dots represent the connection points of each electrode.

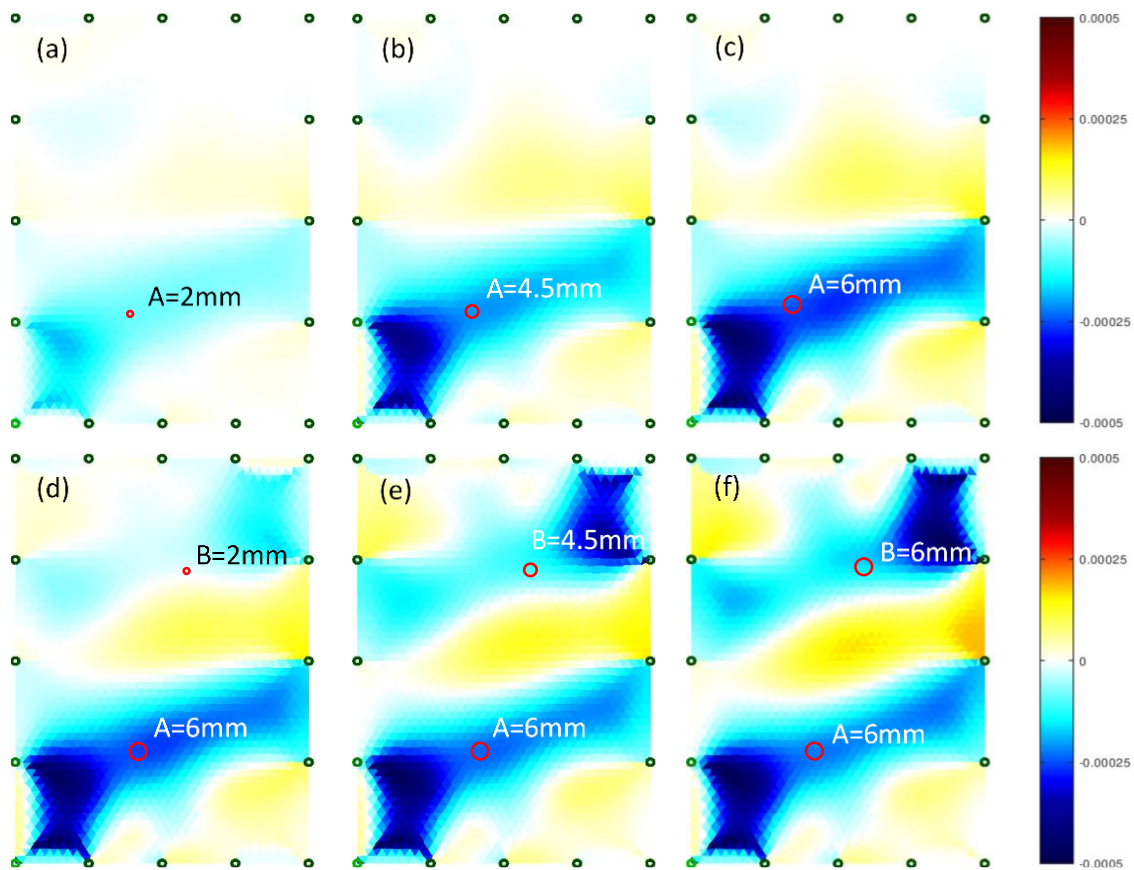


Figure 70: Reconstructed EIT images using GN algorithm of an unbalanced specimen with through-thickness holes of different diameters A and B: (a) A: 2 mm; (b) A: 4.5 mm; (c) A: 6 mm; (d) A: 6 mm, B: 2 mm; (e) A: 6 mm, B: 4.5 mm; (f) A: 6 mm, B: 6 mm. The green dots represent the connection points of each electrode.

The damaged locations can be identified by the areas where electrical conductivity was decreased (change of colour towards blue shades). Increasing intensity of the blue colour is observable in the bottom area of Figure 69 and Figure 70 (a) – (c), as the diameters of the through-thickness hole A increases. With the introduction of the through-thickness hole B and with the increase of its diameter, an increase of intensity of the blue colour is also observable in the top area of Figure 69 and Figure 70 (d) – (f). A decrease of electrical conductivity in the damage sight created an artefact at the closest boundary electrodes, as electrical conduction is affected from the hole location to the boundary electrodes. Yet, the increase of damage severity as the through-thickness hole diameter increases is evident in the reconstructed images. EIT was sensitive to the electrical conductivity changes enforced by the small localised damage imposed by the first through-thickness hole A with a 2 mm diameter. Moreover, the production of hole B did not interfere with the detection of hole A and two distinct damages are clearly observable. The change of electrical conductivity remains constant in the lower part of the image where the through-thickness hole A is found, while the diameter of the through-thickness hole B is being created and then increased. It is possible to see that the real location of the through-thickness holes is at the areas

where the different blue zones of lower conductivity, coming from the boundary electrodes converge. In a real engineering application, the exact location of damage could not be indicated, but it would allow to inspect only a rather smaller area of the part to find the damage. These results show the ability of EIT to detect the localised damage and its approximate location, instead of just providing an assessment of the general damage condition in the whole specimen.

5.3.2. Detection and Localisation of Impact Damage

The suitability of the EIT technique to assess impact damage was also explored. Impact tests were conducted as reported in section 4.3.3.1.2, using the drop-weight impact testing equipment presented in Figure 30, section 4.3.3.1. The contact load and energy recorded by the drop-weight impact testing setup, for the three levels of impact energy are presented in Figure 71. Given the different layup configuration of the two studied laminates and their resultant distinct impact resistance, different impact energies were used to produce unnoticed damage: 20.0 J on quasi-isotropic laminates and 15.0 J on unbalanced laminates. The same levels of impact energies were used on both laminates to produce barely visible damage (30.0 J) and more severe damage (49.5 J). The samples are labelled by “Q” or “U” depending on if they are from the quasi-isotropic or unbalanced laminate, respectively, by the value of impact energy and its number from 1 – 3, as each condition was repeated three times. For instance, sample Q-20J(1) is the first sample of the quasi-isotropic laminate subjected to an impact with an energy of 20.0 J.

The production of severe damage by impact events with energies of 49.5 J is evident by the sudden decrease of load at around 10 000 and 11 000 N in the cases of the quasi-isotropic laminates (Figure 71 (a)) and unbalanced laminates (Figure 71 (b)), respectively, and by the high absorbed energy during impact events. In fact, values of absorbed energy as high as $85.8 \pm 0.7\%$ and $88.3 \pm 1.6\%$ were determined in the case of the quasi-isotropic laminates (Figure 71 (c)) and unbalanced laminates (Figure 71 (d)), respectively.

Both quasi-isotropic and unbalanced laminates submitted to impact events with impact energy of 30.0 J show load oscillations, revealing some degree of imposed damage, with absorbed energies of $43.8 \pm 1.5\%$ and $45.9 \pm 0.6\%$, respectively. The impact events of lower impact energy produced smoother load curves, with the exception of the quasi-isotropic specimen Q-20J(1), which also showed some load oscillations. The quasi-isotropic laminates absorbed $38.0 \pm 0.7\%$ of the impact energy and the unbalanced laminates absorbed $39.9 \pm 0.7\%$.

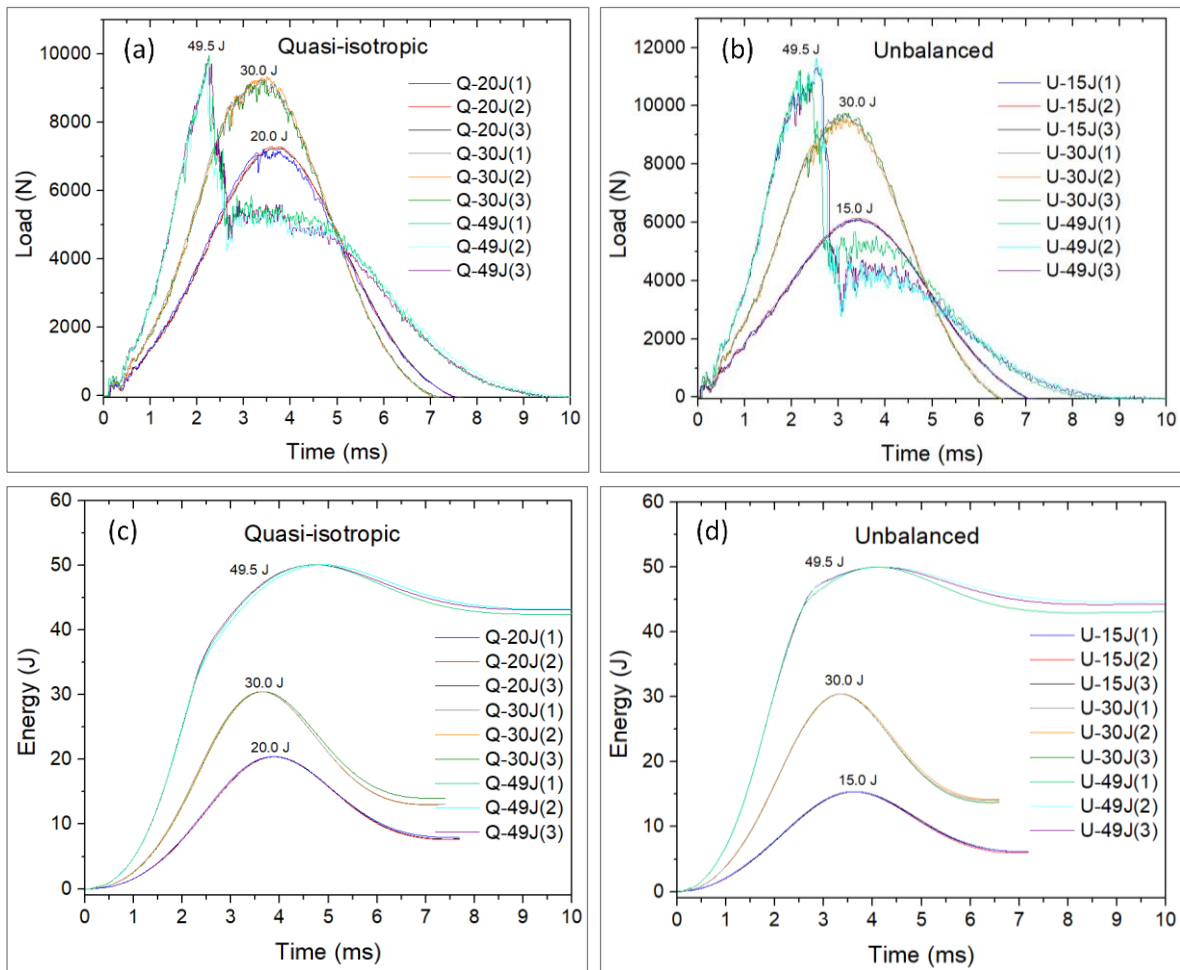


Figure 71: Impact load vs time curves on (a) quasi-isotropic and (b) unbalanced specimens and respective energy vs time curves (c) and (d)

The EIT images were able to reveal a general different shape of damage in the two laminates with different layup sequences. The quasi-isotropic laminates tend to show a change on the electrical conductivity in the central area of the specimens (Figure 72). Contrary to what was expected, some samples show an increase of electrical conductivity after damage, with yellowish and reddish regions. Yet, similarly to the tomographic images of specimens with through-thickness holes, a decrease of electrical conductivity is observed from the damaged location towards the boundary electrodes. The unbalanced laminates also show a change on the electrical conductivity in the central area of the specimens, but with a rather elongated shape (Figure 73), like the so-called “peanut” shape [15]. The unbalanced specimens consistently present a decrease of electrical conductivity after damage in the “peanut” shape regions, represented in blue colour. The ultrasonic inspections confirmed the shape of damage imposed in the laminates, with the quasi-isotropic laminates showing circular shape-like damages (Figure 74) and the unbalanced laminates showing elongated shape damages (Figure 75).

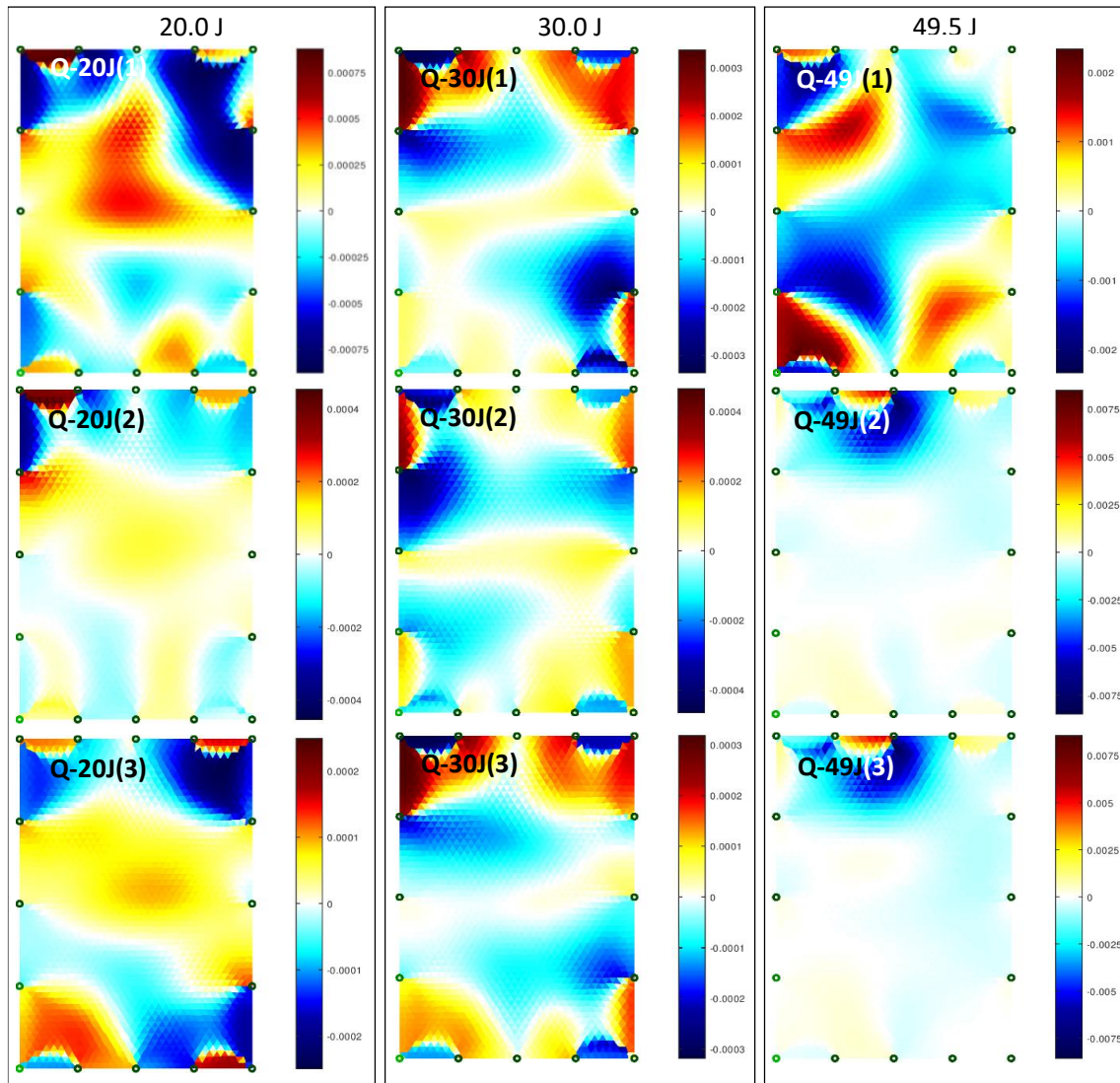


Figure 72: Reconstructed EIT images using GN algorithm of different quasi-isotropic composite specimens exposed to drop-weight impact events with impact energies of 20.0 J (left), 30.0 J (middle), and 49.5 J (right). The green dots represent the connection points of each electrode.

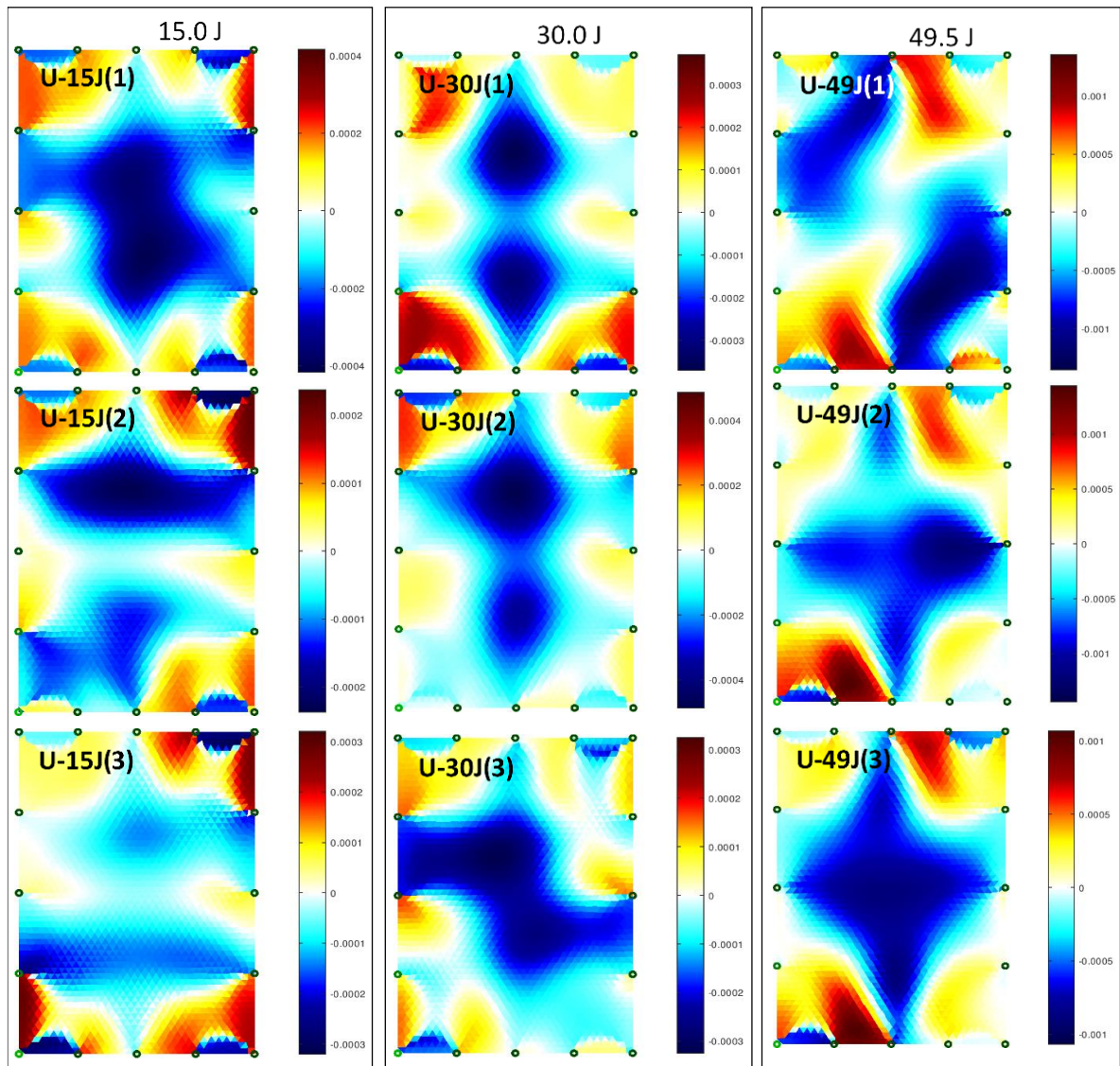


Figure 73: Reconstructed EIT images using GN algorithm of different unbalanced composite specimens exposed to drop-weight impact events with impact energies of 15.0 J (left), 30.0 J (middle), and 49.5 J (right). The green dots represent the connection points of each electrode.

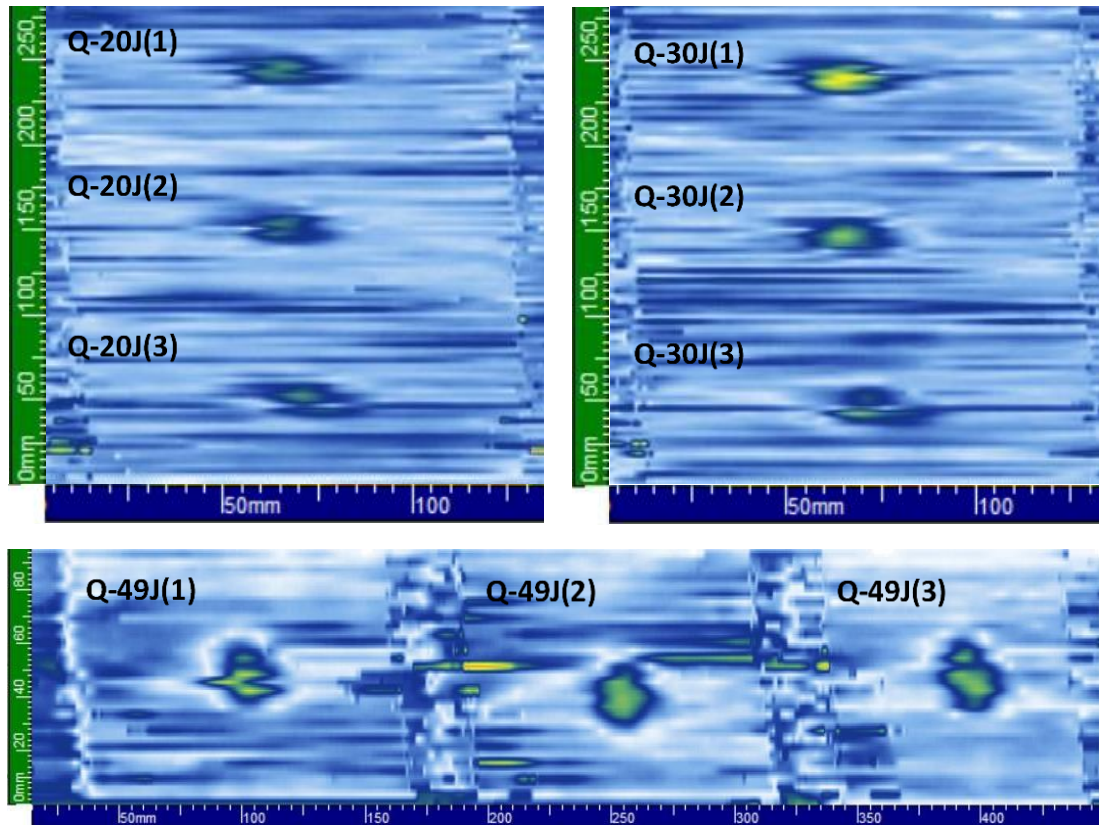


Figure 74: Ultrasonic C-scan inspection of quasi-isotropic composite specimens exposed to drop-weight impact events with impact energies of 20.0 J (top left), 30.0 J (top right), and 49.5 J (bottom)

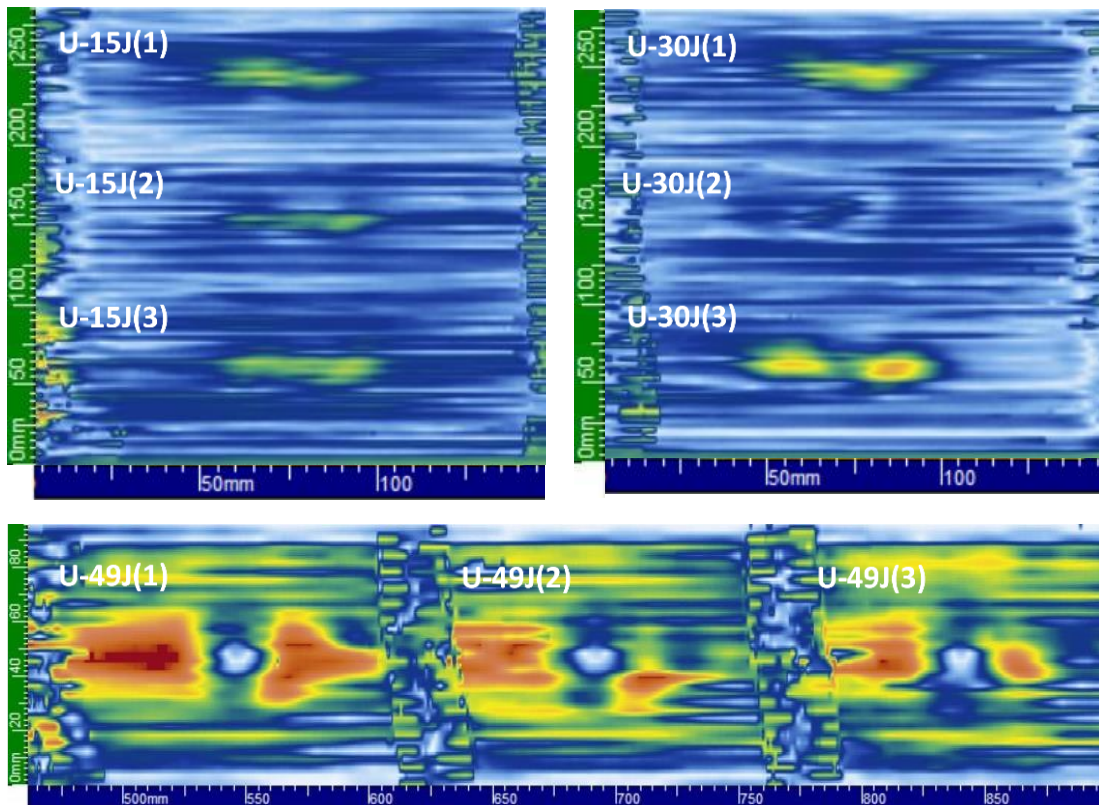


Figure 75: Ultrasonic C-scan inspection of unbalanced composite specimens exposed to drop-weight impact events with impact energies of 15.0 J (top left), 30.0 J (top right), and 49.5 J (bottom)

With the EIT technology presenting higher TRL values to evaluate isotropic materials, such as metals, it would be expected that the employment of EIT on quasi-isotropic laminates would yield more accurate results than on the unbalanced laminates. While “peanut” shape-like damage is clearly seen in the unbalanced specimens, the shape of the damages is not evident in the quasi-isotropic laminates, although it is clear that damage is present in the central area of the specimens. The higher number of layers oriented at 0° may contribute to higher electrical conductivity along the surface of the unbalanced samples, yielding more accuracy in damage shape recognition by the EIT technique. The sensitivity of EIT to the presence of damage is highlighted, but it overestimates the area of delaminations, as compared to the ultrasonic C-scan inspections. In the case of unbalanced laminates, the EIT images show 1.4 to 2 times bigger damages than those ones observed with ultrasounds. While the ultrasound techniques analyse the sound reflection that is dependent on the geometric characteristics of the damage and laminate, the EIT technique evaluates the electrical conductivity, which can be changed not only in the damage area but also around it as the electrical current will be scattered and have increased difficulty to pass on.

The slightly shorter impact event duration reveals a more rigid behaviour of unbalanced specimens, when compared to the quasi-isotropic laminates (Figure 71 (a) and (b)). The higher rigidity of the unbalanced laminate may be explained by the larger thickness and higher number of layers oriented at 0° , leading to the larger “peanut” shaped delaminations. The damage shape changes across the thickness of the laminate, and the “peanut” shape damage is only observable in the middle layers of the laminate, as it can be seen in Figure 77 on the specimen U-15J(3). Therefore, damage detection with EIT technique is independent on the through-thickness location of damage and it can detect the larger damage within the composite. The quasi-isotropic laminates, on the other side, present a rather circular shaped damage throughout the entire thickness of the laminates, as presented in Figure 76 for specimen Q-20J(1).

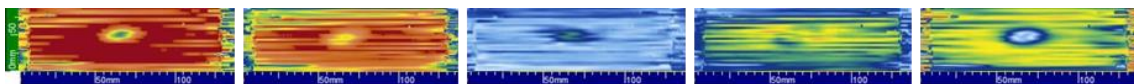


Figure 76: Ultrasonic C-scan inspection of the quasi-isotropic composite specimen Q 20J(1) exposed to impact event with energy of 20.0 J at different thickness depth, from left to right: between 2.5 – 2, 2 – 1.5, 1.5 – 1, 1 – 0.5 and 0.5 – 0 mm

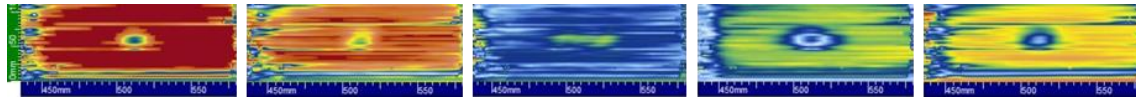


Figure 77: Ultrasonic C-scan inspection of the unbalanced composite specimen U-15J(3) exposed to impact event with energy of 15 J at different thickness depth, from left to right: between 2.5 – 2, 2 – 1.5, 1.5 – 1, 1 – 0.5 and 0.5 – 0 mm

5.4. Smart Composite Overwrapped Pressure Vessel

5.4.1. Development of the Composite Overwrapped Pressure Vessel

5.4.1.1. Raw Materials Properties

This section presents the results of the tests performed on the materials used in the production of the COPV to determine their properties. The test specimens (aluminium specimens from the liner and flat wound CFRP specimens) and all the properties presented in this section were obtained following the procedures reported in section 4.3.5.1.1. These results were used in the preliminary design, FEM analysis and calculation of the minimum *autofrettage* pressure of the pressure vessel.

Table 8 presents the elastic modulus, Poisson's ratio and yield strength of the liner material, aluminium 6061-T6. The tested specimens show some variability in their stress/strain response, resulting in a high standard deviation in the calculated elastic modulus. In fact, the FEM model used an elastic modulus of 69 GPa as reported in the literature for this material [156]–[158].

Table 8: Elastic properties of the aluminium 6061-T6 in the liner

Property	Value
E (GPa)	97.964 ± 27.566
ν	0.343 ± 0.015
σ_{yield} (MPa)	256 ± 4

Modelling of the liner material also included its plastic behaviour. For that, the true stress/true strain curves were calculated from the plastic region of an experimental stress/strain curve, using equations 35 and 40 from section 3.4.2. These values are presented in Table A1 in the annex A1 section. It should be noted that the two last lines in Table A1 were extrapolated, assuming a linear increase of the strain. These values were added to better represent the plasticity of the 6061-T6 aluminium which, in the literature, presents plastic strain values just above 10% [159]–[161]. The

early failure of the strain gauges prevented the measurement of the entire plasticity range of the material.

Table 9 presents the properties of the ITS50/RCX0125 composite used in the composite overwrap of the COPV. E is the elastic modulus, G is the shear modulus and ν is the Poisson's ratio, where the subscript 1 represents the property in the longitudinal direction of the fibres and the subscripts 2 and 3 represent the property in the transverse directions of the fibres. X_t and X_c are the tensile and compressive strength, respectively, in the longitudinal direction of the fibres and Y_t and Y_c are the tensile and compressive strength, respectively, in the transverse direction of the fibres. S is the shear strength. G_{XT} , G_{XC} , G_{YT} , G_{YC} are the fracture energies, where the subscripts x and y stand for the longitudinal and transverse direction of the fibres, respectively, and the subscripts t and c stand for tensile and compressive mode. These values of fracture energy were taken from the literature for similar material [162]. Poisson's ratio ν_{23} was considered to be 0.35, a common value found in the literature for epoxy resin [163], [164].

Table 9: Properties of the ITS50/RCX0125 composite, used in the FEM analysis

Property	Value
E_1 (GPa)	134.8 ± 9.7
$E_2 = E_3$ (GPa)	6.5
$\nu_{12} = \nu_{13}$	0.30 ± 0.02
ν_{23}	0.35 [163], [164]
$G_{12} = G_{13}$ (GPa)	6.0 ± 0.3
G_{23} (GPa)	2.3
χ_t (MPa)	1406.3 ± 443.1
χ_c (MPa)	597.0 ± 42.8
Y_t (MPa)	14
Y_c (MPa)	99.3 ± 14.3
S (MPa)	53.9 ± 0.4
G_{XT} (N/mm)	48.4 [162]
G_{XC} (N/mm)	60.3 [162]
G_{YT} (N/mm)	4.5 [162]
G_{YC} (N/mm)	8.5 [162]

It should be noted that it was only possible to test one specimen with the fibres oriented at 90° due to the fragility of the specimens. Therefore, a standard deviation value is not presented for E_2 and Y_t . It should also be noted that the obtained value of Y_c is lower than the real one, as the squareness of the fibres could not be assured, due to the nature of the winding process. Nevertheless, since this value is conservative, and the carbon fibres are mainly subjected to tensile stresses in the COPV, this result will not have a pejorative effect in the FEM analyses.

It should also be mentioned that the FEM model used a longitudinal tensile strength of 2097 MPa corresponding to the value of the specimen with greater strength, since the literature points to magnitudes of longitudinal tensile strength superior to the average value obtained in these tests [165]. The high dispersion of the values obtained experimentally, as inferred by the standard

deviation value, is due to the high number of voids in the specimens due to the insufficient compaction of the plates produced in the flat mandrel. which will not match the tensile strength properties of the same material when wound on the liner with circumferential section.

The density of the composite laminate was also determined, obtaining a value of $1.629 \pm 0.002 \text{ g/cm}^3$.

5.4.1.2. Winding Patterns

As described in section 4.3.5, several winding patterns were simulated and adjusted in CADWIND® software until a suitable pattern, in terms of fibre angle and no slippage between the prepreg tape and liner surface, was found. This was an iterative process between CADWIND® simulations and experimental tests in the laboratory winding machine. The selected circumferential pattern at 89° and helical pattern at 15° are presented in Figure 78. The helical pattern consisted of a “5 pattern”, also known as a “5-star” pattern, which can be clearly seen in Figure 78 (b). In this type of patterns, five cycles are wound in such a way to form a five-pointed star, followed by the 6th winding cycle, where the tape is placed adjacent to the first wound tape and so on. The full helical pattern selected from CADWIND® consists of 62 cycles, corresponding to two layers at $+15^\circ$ and -15° . Each helical wound layer had a thickness of about 0.50 mm. The circumferential pattern selected from CADWIND® consists of 1 cycle, corresponding to two circumferential layers.

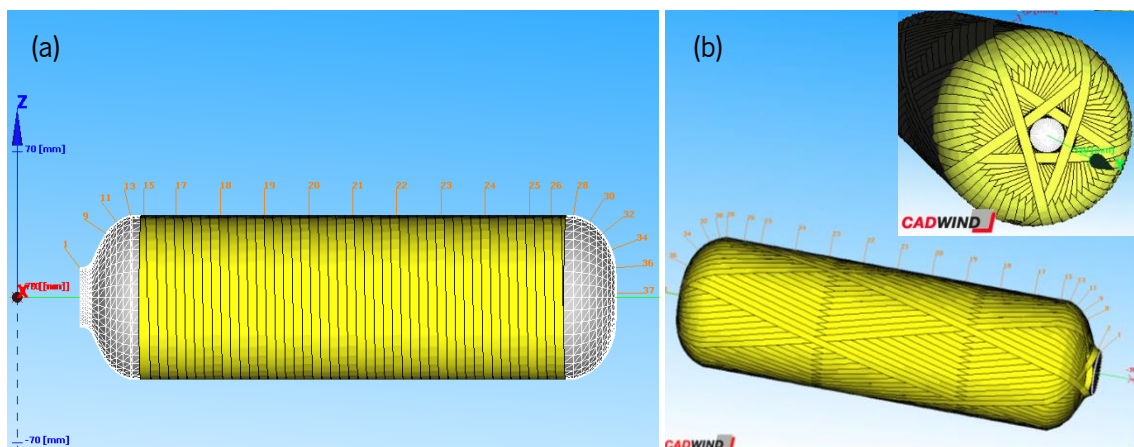


Figure 78: circumferential (89°) and helical (15°) patterns created by CADWIND® software

As it can be found in section 5.4.1.3, the optimised layup configuration was $[90_3/\pm 15_2]_S$, consisting of 3 internal circumferential layers, 4 helical layers and 3 external circumferential layers. To wound each 3 circumferential layers, the numerical code generated by CADWIND® software to run the winding machine was copied and manually changed to stop winding at the end of the first cycle to

produce just one circumferential layer and thus, wind 2 circumferential layers using the original file plus 1 circumferential layer using the adapted file.

5.4.1.3. Finite Element Analysis

The COPV was developed to satisfy the requirement of a 2 hours flying autonomy of a UAV. That was found to be accomplished with a volume capacity of 2 litres of hydrogen stored at 350 bar. For uniform weight distribution, the UAV will fly with two 1-litre capacity COPVs, placed under each wing. To achieve a design pressure of 350 bar, the COPV was designed to have a minimum burst pressure of 1050 bar, corresponding to a safety coefficient of 3, as recommended by EN12245 European standard.

As explained in section 4.3.5, the structural modelling of the COPV in Abaqus software was an iterative process. Different layups were modelled and then subjected to burst tests to validate the composite overwrap layup. The optimised layup has the layup configuration $[90_3/\pm 15_2]_S$.

The circumferential layers were the first ones to fail. Damage initiation was observed at a pressure of 1063 bar according to Hashin and Rotem's damage initiation criteria for fibre tensile mode (Figure 79).

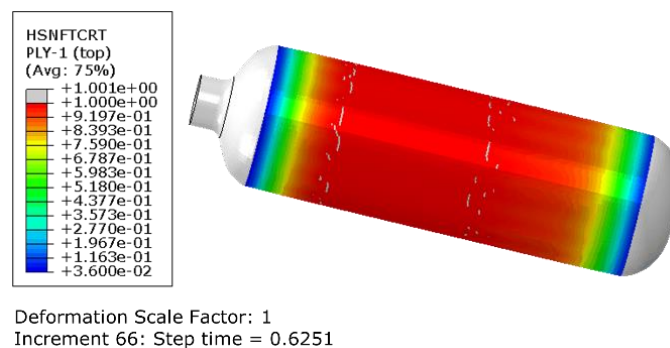


Figure 79: Hashin and Rotem's damage initiation criteria for fibre tensile mode of the first internal circumferential layer

At the point where the circumferential layers and the epoxy resin have already failed, there is a sudden stiffness loss in the circumferential direction of the COPV. That can be observed by the sudden increase of elastic strain in the helical layers in the circumferential direction (Figure 80). With that, the failure of the helical layers can be identified right after the failure of the circumferential layers, at a pressure of 1064 bar.

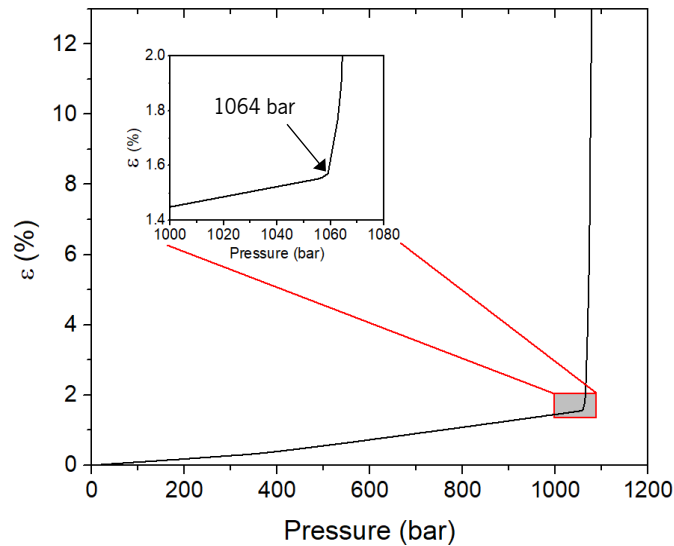


Figure 80: Elastic strain of the helical layers in the circumferential direction of the COPV

Once the stiffness of the composite overwrap is lost, the liner is the last element to expand with the applied internal pressure and burst. At last, the failure of the aluminium liner, and of the COPV as a whole, was identified at a pressure of 1069 bar, when there is a sudden increase of the plastic strain of the liner (Figure 81).

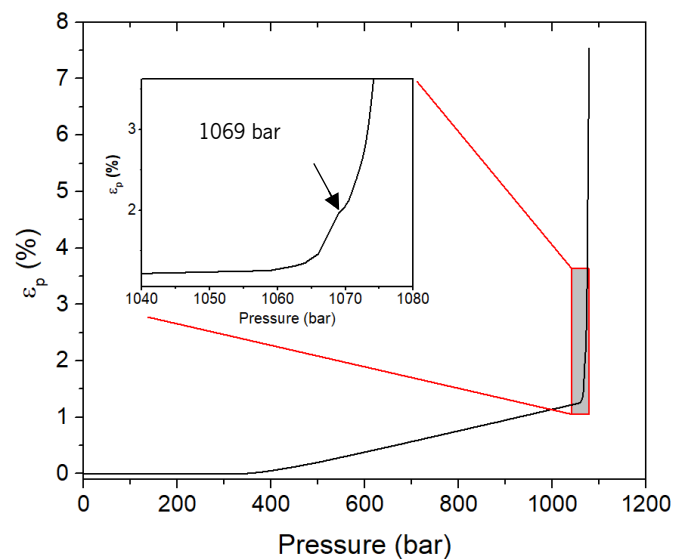


Figure 81: Plastic strain of the liner

By analysing the simulated axial displacement of the liner, it is expected that the COPV will burst safely. since the greatest displacement occurs in the circumferential zone, as it is possible to observe in Figure 82.

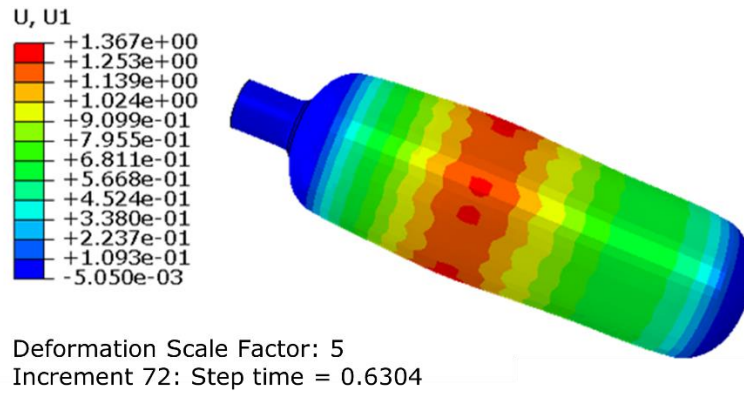


Figure 82: Axial displacement (U, U1) of the liner at burst. Units of U, U1 in mm

Additionally, the FEA were also helpful to identify the locations subjected to higher strain, assisting to define the best and most useful location for the FBG sensors.

5.4.1.4. Burst Pressure Testing

The FEM analysis was validated by experimental burst tests. The COPVs were subjected to an increasing internal pressure until rupture. The three COPVs tested showed a burst pressure of 1061 ± 26 bar, as presented in Table 10. Each COPV sample is identified by the liner fabrication number. The results revealed a very small error of 0.7% between the simulated and experimental burst pressure. An example of a tested COPV can be seen in Figure 83.

Table 10: Burst pressure test results

Sample	Burst Pressure, P_b (bar)
COPV (Liner 38245)	1075
COPV (Liner 38247)	1025
COPV (Liner 38233)	1084
Average	1061 ± 26 bar



Figure 83: COPV after burst test

5.4.1.5. Autofrettage and Cyclic Pressure Testing

Two COPVs were subject to cyclic pressure tests between 3 and 525 bar, until failure. The results are presented in Table 11. Right before the cyclic pressure tests, the COPVs were submitted to the *autofrettage* process for improved fatigue life, as discussed in section 2.4.2.

The minimum pressure P_y to cause yielding of the liner in the cured COPV was calculated to be 554 bar, according to section 3.4.3. Taking also the general guideline that the *autofrettage* pressure shall not exceed 1.5 times the maximum expected working pressure p_h , which is 787.5 bar, given a p_h of 525 bar, the COPVs were pressurized up to 600 bar. The *autofrettage* pressure was maintained for 2 minutes.

The COPV with minimum number of endured cycles, 5546 cycles, would qualify the prototype for 22 years of operation, according to the EN12245 standard, which defines that each 250 endured cycles qualify the pressure vessel to one year of operation.

Table 11: Number of endured pressure cycles by the COPVs

Sample	Number of cycles
COPV (Liner 38240)	5546
COPV (Liner 38174)	6135
Average	5840 ± 294

A smart COPV, with embedded FBG sensors, was also subject to a pressure cycling test, with different pressures ranges, to evaluate the suitability of the sensors to monitor the structural life of the COPV. The results are presented in section 5.4.2.4.

5.4.2. Monitoring System of the Smart Composite Overwrapped Pressure Vessel

5.4.2.1. Optical Fibre Sensors Embedment

As demonstrated in the initial work of this thesis, where OFs were embedded into CFRP specimens, optic FBG sensors are very accurate sensors. However, their integration into composite parts can be very challenging. In the case of COPVs, the embedded OFs are exposed to high deformations both during manufacturing and operation.

The initial OF embedment trials had the optical fibre fixed on the liner surface by epoxy adhesive X120 and covered by high temperature adhesive tape. As it can be seen in Figure 84, the 8-FBG optical fibre sensing array was able to bear the deformations developed during the manufacturing process (winding and curing). Nevertheless, some signal loss can be inferred from the spectra baseline. Moreover, when such system was subjected to the *autofrettage* process, at which the COPV is pressurized up to 600 bar, the optical fibre would soon break. In some specimens, FBG1, which was positioned closer to the closed dome of the liner, would last longer. The extension of optical fibre running from the ingress point at the pin up to the dome/circumferential section interface and from there to FBG1 follows approximately the orientation of the carbon fibres. The helical layer covers the liner in the dome section and the optical fibre was bonded in a similar orientation (see Figure 40 (a)). From the dome/circumferential section interface to FBG1, the optical fibre is almost oriented perpendicularly to the longitudinal axis of the liner (see Figure 40 (b)), approximately the same orientation of the carbon fibres in the circumferential layer, the first layer in contact with the liner in the circumferential section. Moreover, as shown in the FEM analysis (Figure 79), the extremities of the circumferential section, where FBG1 is fixed, suffer the lowest loads. FBG1 lasted to a pressure of about 200 bar, still below the working pressure. The signal of the other sensors was lost before that, at about 100 bar, which can be attributed to the misorientation of the optical and carbon fibres and the resultant shear forces on the optical fibre by the expanding liner and tensioned carbon fibres in the composite overwrap. Yet, this embedding strategy allowed to monitor the winding and curing processes, as well as impact damage prior to pressure tests.

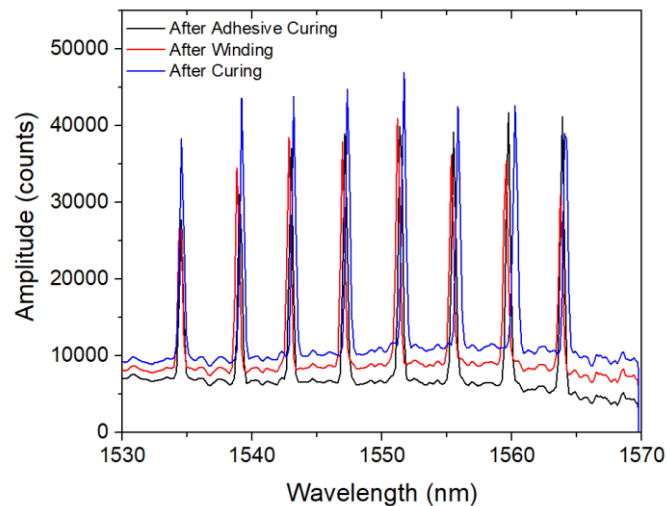


Figure 84: Spectra of an optical fibres with 8 FBG sensors, embedded into a COPV, taken after major processing steps

The spectra change at the end of major manufacturing steps of some COPVs with embedded OF protected with a localised unidirectional composite layer is presented in Figure 85. Figure 85 (a) – (c) presents the spectra change of trials with Ormocer® coated OF having different configurations. Though not promising, three of the initial four FBG sensors, which were protected by microtubes (configuration presented in Figure 42 (b)), survived the curing process. Curing of the protecting localised unidirectional composite layer over the OF (spectrum labelled as “After Prepreg Curing”) did not imposed a significant shift on the OF spectrum when compared to the previous manufacturing step at which the OF is fixed with the cured epoxy adhesive (spectrum labelled as “After Adhesive Curing”), while, unexpectedly, a significant spectrum shift is observed after composite overwrap curing. It shows that a tensile strain was imposed on the OF during curing and that it suffered signal loss. Despite the significant optical signal loss, this OF performed better in the *autofrettage* process than the previous trials without the localised unidirectional composite buffer layer. The FBG sensors survived up to 340 bar of internal pressure, showing the stiffening effect of the localised unidirectional composite protection provided to the optical fibre bonded system, reducing compression and shear loading during the *autofrettage* process.

The first FBG sensors (FBG1) in the OF with simple FBG sensors (configuration presented in Figure 42 (a) and spectra presented in Figure 85 (a)) and of the OF with Teflon tubes in between FBG sensors (configuration presented in Figure 42 (c) and spectra presented in Figure 85 (c)) were also able to sustain pressure up to approximately 340 bar in the *autofrettage* process.

Similarly to the Ormocer® coated OF, the bend-insensitive OF also presented a shift of the spectrum after curing of the composite overwrap towards higher wavelengths, showing that a

tensile strain was imposed on the OF during the curing procedure. However, its optic signal was not significantly affected. This optical fibre was able to survive the entire *autofrettage* process up to 600 bar. Its spectrum after the *autofrettage* process is shown in Figure 86. It is possible to see that FBG2 – FBG4 (second – fourth peaks) lost some amplitude counts on the *autofrettage* process, but this OF was still capable of monitoring the pressure cycling tests presented in section 5.4.2.4.

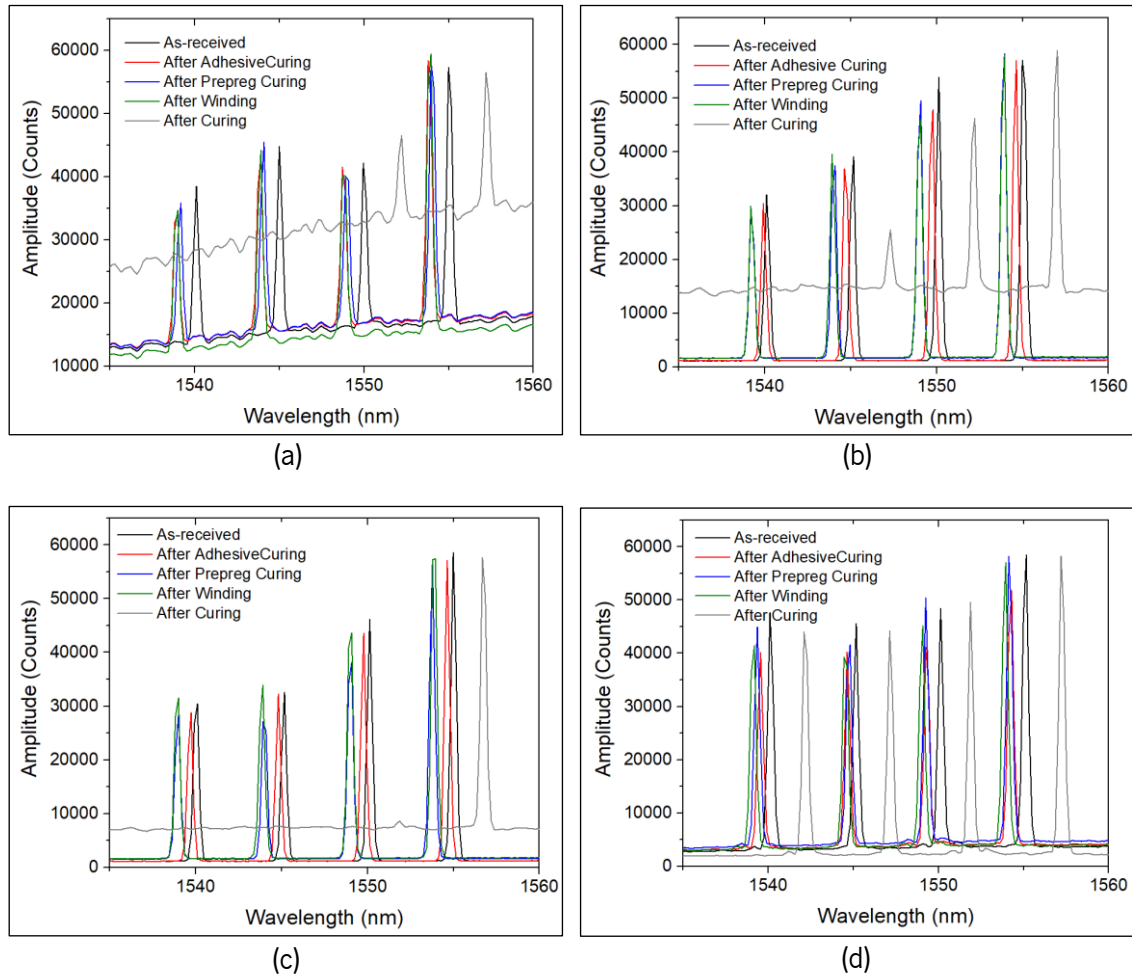


Figure 85: Spectra of optical fibres, embedded into COPV, taken after major processing steps. Comparison of different OF constructions/configurations: (a) Ormocer® OF with bare FBG sensors; (b) Ormocer® OF with FBG sensors protected in 200 μm diameter microtube; (c) Ormocer® OF with bare FBGs and a 750 μm diameter Teflon tubes, 3 cm long, protecting the mid-section of the OF in between FBG sensors; and (d) bend-insensitive optical fibre with FBG sensors protected in 200 μm diameter microtube. These configurations can be revisited in Figure 42.

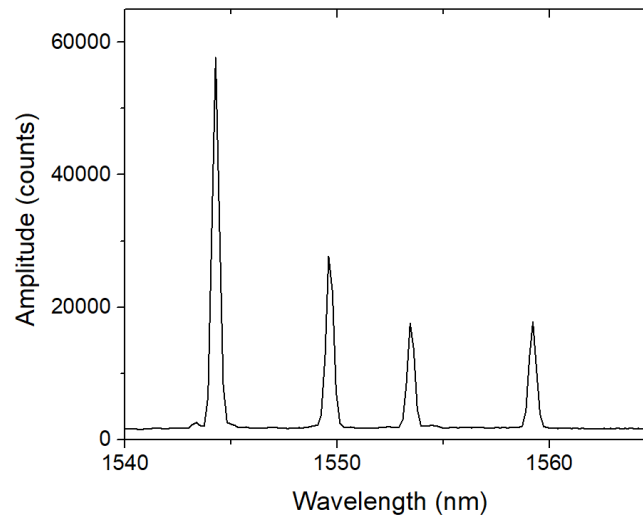


Figure 86: Bend-insensitive OF spectrum after *autofrettage* process

5.4.2.2. **Winding and Cure Monitoring**

The integration of FBG sensors on the liner surface brings the advantage of enabling monitoring of the full manufacturing process, both winding and curing processes. To monitor the winding process, the optical interrogator was fixed to the liner and an electrical rotary joint was used for data transfer, as described in 4.3.5.2.3.

Figure 87 presents the strain evolution during the tape winding process, as measured by the FBG sensors. For easier reading of the graphs, it is presented just the data for every other sensor of the 8-FBG sensing array. The complete data for all FBG sensors can be seen in Figure A1 in the annex A1 section. Except for FBG8, the FBG sensors, generally, showed a decrease of strain when the circumferential layers were wound. As winding of a layer starts, a strain oscillation is observed in all sensors, reaching higher amplitude as the carbon fibres being wound got closer to the FBG sensor. A sudden strain decrease followed as the carbon fibres covered the FBG sensor. After that, a strain recovery and plateau are observed for the remaining time of the layer deposition. Figure 87 (b) clearly shows the strain variation measured by FBG5, where the first and third internal and external circumferential layers are highlighted by the grey shadowed regions for easier identification. During circumferential winding, as the process progressed, the FBG sensors were strained at progressively later time, according to their location along the longitudinal axis of the liner, as presented in Figure 87 (c) and (d). At about 1 min after initiating data acquisition, the winding process starts and FBG8 is the first sensor to show a strain decrease, followed by FBG7 and so on. Naturally, as the second circumferential layer is wound backwards, relatively to the first circumferential layer, FBG1 is the first sensor to show another strain decrease step, followed by

FBG2 and so on. The behaviour observed in the first circumferential layer is also visible in the third one. This pattern also applies to the deposition of the external circumferential layers. It is also noticeable that strain amplitude recovery, just after the FBG sensor has been covered and compressed by the carbon fibres, is much higher during winding of the external layers than during winding of the internal circumferential layers. For the case of FBG5, it measured a strain decrease of about 51, 37 and 34 $\mu\epsilon$ after winding of the first, second and third internal circumferential layers, respectively, and of 7, 3, and 2 $\mu\epsilon$ after winding of the first, second and third external circumferential layers, respectively. As the layers are produced over the liner and FBG sensors, the previously wound layers by carbon fibres under tension work as a buffer that lessen the compression of the FBG sensors.

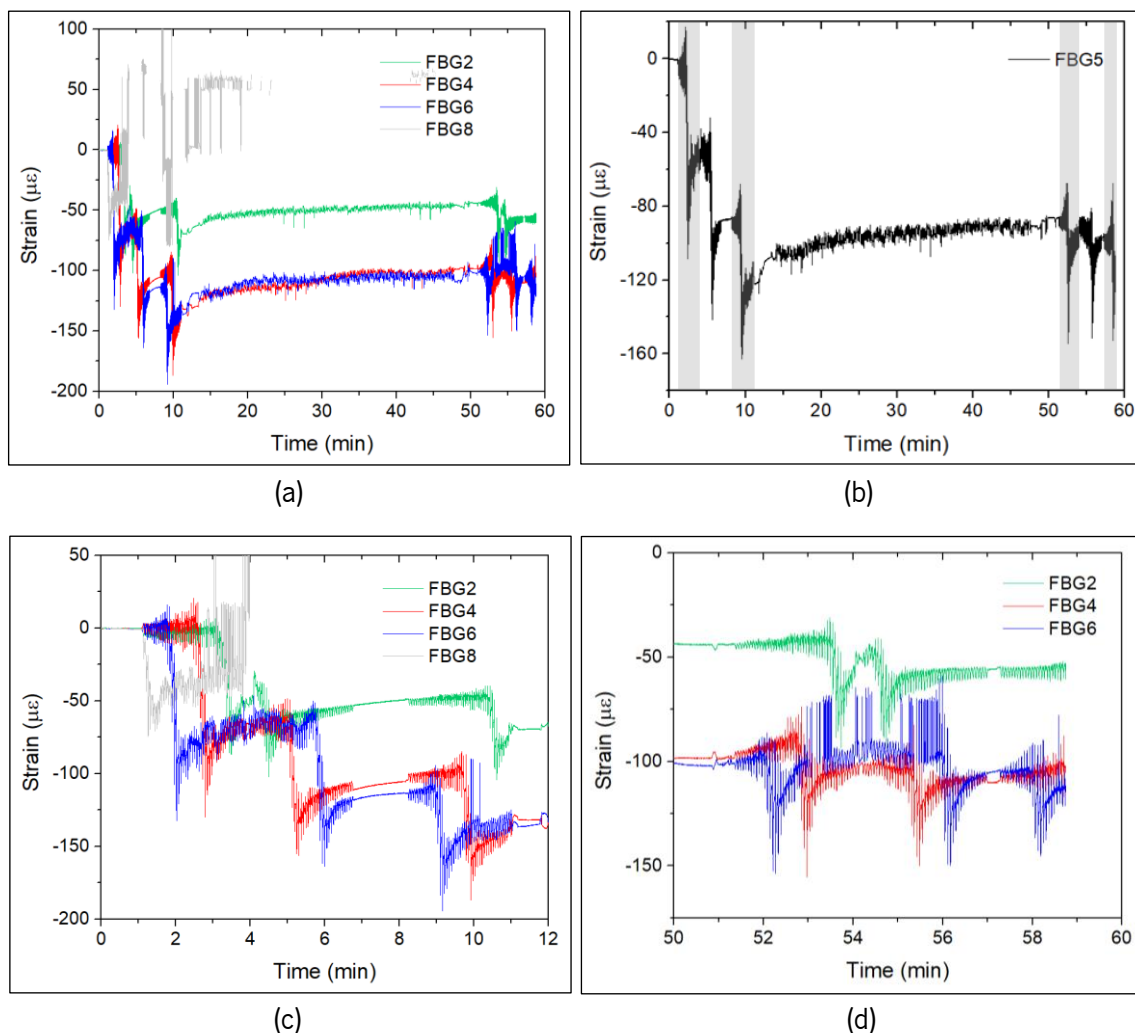


Figure 87: Strain change on FBG sensors, during COPV winding process

The winding of helical layers (between approximately the 12th and 48th min, see Figure 87 (a) and (b)) does not impose additional compression on the FBG sensors. Instead, the strain slightly increased during these steps. This can be attributed to the wound internal circumferential layers acting as a buffer to the FBG sensors, but also to the fact that the anchoring places for the carbon fibre during helical winding are the domes sections of the COPV. The times between 11 and 13.5 min and 48 and 51 min correspond to the processing steps of combined angle winding, enabling the changes from circumferential to helical winding and vice-versa, respectively, without stopping the machine neither cutting the carbon fibres at the end of winding of each layer type.

FBG8 presented a very distinct behaviour comparatively to the other FBG sensors (Figure 87 (a)). It also presented the first sudden strain decrease when the carbon fibres covered the sensor in the first wound internal circumferential layer, but afterwards, it showed tensile strains rather than compressive strains. Signal was also lost at times during acquisition. This may be explained by microbending of the OF in the vicinity of FBG8 by the wound carbon fibres. Yet, FBG8 survived the winding process.

FBG1 – FBG7 presented strain values between -51 and -106 $\mu\epsilon$ after winding.

After winding, the COPV is cured. Figure 88 presents the strain data imposed on an FBG during the curing process and the temperature on the COPV surface, measured by a type-k thermocouple, and oven temperature. The results presented here concern to an optical fibre which was fixed by epoxy adhesive X120 to the liner surface and then protected with a high-temperature adhesive tape to prevent it from breaking. Obviously, the cured epoxy adhesive and the adhesive tape on top of the OF lessen the eventual polymerization strain acting on the FBG sensors. The strain in the FBG roughly follows the temperature curve shape measured in the COPV surface. Yet, the measured strain starts to increase faster than the temperature curve, which may be attributed to the thermal expansion of the liner. Between 3.8 – 4.6 hours into the curing process, it is possible to observe that the strain is kept approximately constant, while the temperature in the COPV surface is still slightly increasing, revealing that polymerization shrinkage is counteracting the thermal expansion.

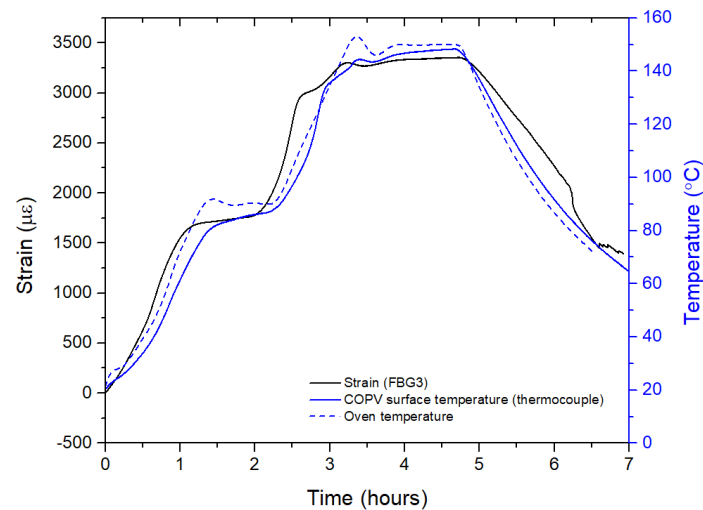


Figure 88: Curing monitoring of the COPV by embedded OF

Ideally, cure monitoring should be done with an OF without a protective buffer layer to actually measure the mechanical and thermal strain resulting from thermal expansion and polymerization. However, the OF without protection barely survived the curing procedure and suffered significant microbending during the process.

A picture of a produced COPV with embedded FBG sensors can be seen in Figure 89.



Figure 89: Smart COPV with embedded FBG sensors

5.4.2.3. Impact Test Monitoring

LVI tests were performed on the circumferential section of the COPV to demonstrate the capability of the FBG sensors to detect and locate BVID, as described in section 4.3.5.3.3.

Prediction of damage location, was achieved by a simple method, similar to the one reported by Hiche et al. [152], based on the residual strain amplitude imposed on the FBG sensors after impact. This methodology is established upon the assumption that FBG sensors closer to the impact sight suffer higher residual strain values.

Figure 90 shows a flat projection of the FBG sensors location, “real” impact locations, predicted impact locations based on the residual strain between pairs of FBG sensors and averagely predicted impact locations. Distances as small as 17 mm and up to 56 mm (Table 12) were measured

between the predicted impact locations and the “real” impact locations. These short distances quickly enable the localisation of the impact in a real-life structure and the implementation of preventive and repairing measures.



Figure 90: Real and predicted Impact locations on the flat projection of the COPV cylindrical region

Table 12: Error (in mm) between the real and predicted impact location

Impact no	Error real – predicted impact location (mm)
1	56
2	36
3	17
4	21

It should be mentioned that the differences between the “real” and the predicted impact location may arise from the misidentification of the FBG sensors location in the COPV after winding. The FBGs are fixed in the liner surface and a plastic jig mask is used to mark their position. However,

after winding, as the diameter of the COPV increased comparatively to the liner diameter, an exact identification of the FBG sensors is not possible.

These impact tests, conducted with energies of 15 J, produced BVID on the COPV surface that can be successfully detected and located by the optical fibres. A matrix crack resultant from Impact 1 can be seen in Figure 91 (a) and a small bump resultant from Impact 4 can be seen in Figure 91 (b). Impacts 2 and 3 also produced small bumps on the COPV surface but could not be well perceived on camera.



Figure 91: Barely visible impact damage on the COPV surface: (a) matrix crack and (b) small bump

5.4.2.4. Cyclic Pressure Testing Monitoring

A smart COPV, with an embedded bend-insensitive OF having a 4-FBG sensing array, was subjected to cyclic pressure testing. Prior to that, the COPV was also submitted to the *autofrettage* process. It was pressurized up to 600 bar and that pressure was kept for 2 minutes. The OF spectrum after the *autofrettage* process can be revisited in Figure 86.

Considering the design operating pressure of 350 bar, the smart COPV was, at first, pressure cycled between 3 and 350 bar, to resemble the operational charging and discharging cycles of fuel. After 18 190 pressure cycles between 3 and 350 bar, the same COPV was then subjected to 1000 pressure cycles between 3 and 400 bar, 1000 pressure cycles between 3 and 450 bar and, lastly, to pressure cycles between 3 and 500 bar until failure.

For demonstration, Figure 92 presents the strain obtained by the FBG sensors during pressure cycling testing for a few cycles conducted at different values of maximum pressure. The FBG sensors show a linear response to the applied internal strain as it can be clearly seen in Figure 93.

As expected, considering the results of the FEM analysis presented in section 5.4.1.3, FBG1, the one closest to the dome section, suffers the smallest strain gradient at each cycle, comparatively to the other FBG sensors. This is followed by FBG2, with significantly higher strain gradient at each cycle, and then FBG4 and FBG3. It would be expected that FBG4 would suffer higher strain as it is in the middle section of the circumferential zone of the COPV. This behaviour can be attributed to an increased buffer effect of the protective unidirectional fibre layer in the surroundings of FBG4. Yet, in some cycles between 3 – 500 bar, such as the ones shown in Figure 92 (d), FBG4 suffers the highest strains when at the top pressure range of the cycle, causing microbending and momentaneous signal loss.

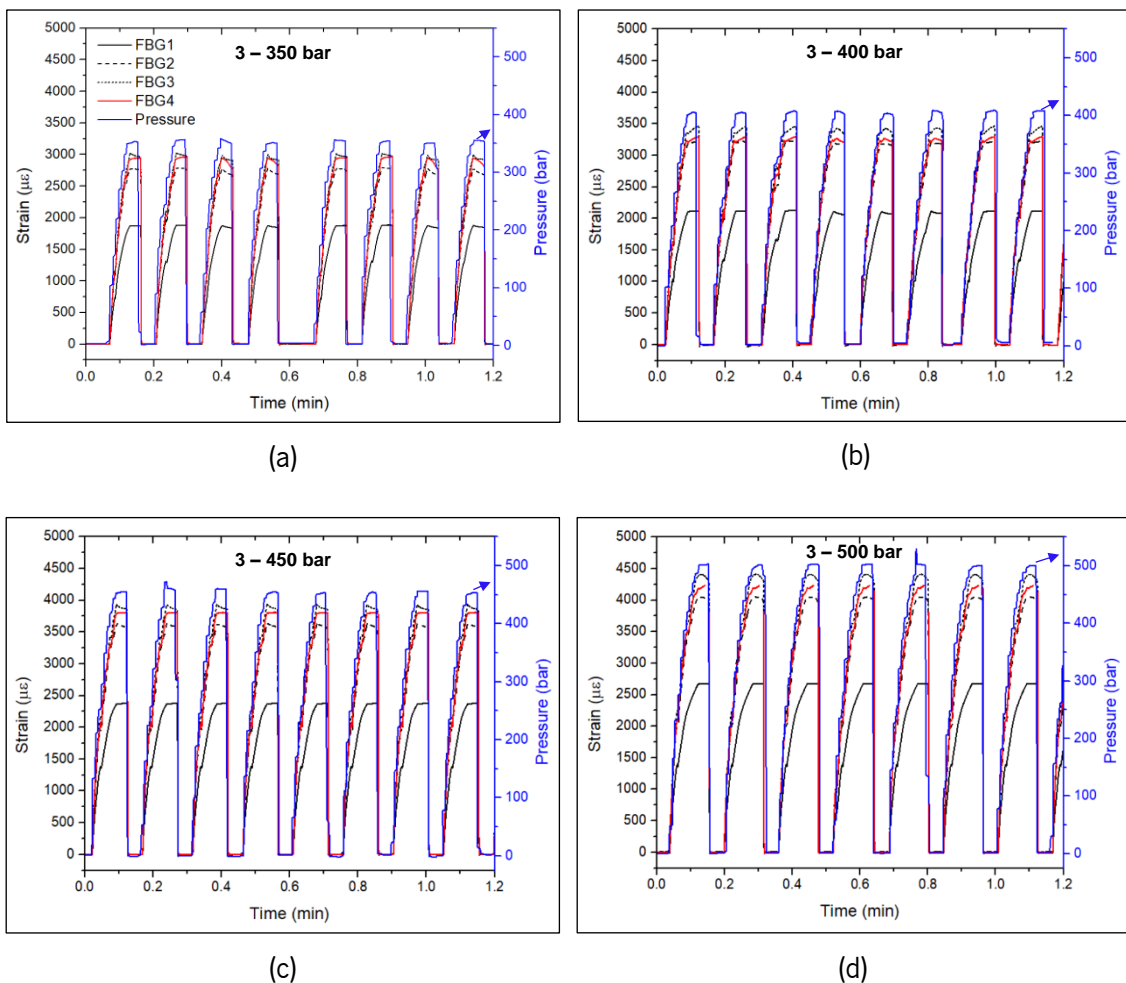


Figure 92: Examples of strain measured by the FBG sensors during pressure cycling test at different stages of the test with different values of maximum pressure: (a) cycles number 8050 – 8058 between 3 – 350 bar; (b) cycles number 396 – 404 between 3 – 400 bar; (c) cycles number 393 – 401 between 3 – 450 bar; and (d) cycles number 347 – 354 between 3 – 500 bar

FBG1 presents the smallest slope of the linear strain/pressure curve, thus, suffering a lower strain gradient as the internal pressure is increased, comparatively to FBG2 – FBG4. This behaviour can be very useful to evaluate the internal pressure and, therefore, know the level of hydrogen fuel in the COPV. This behaviour is also depicted in Figure 93.

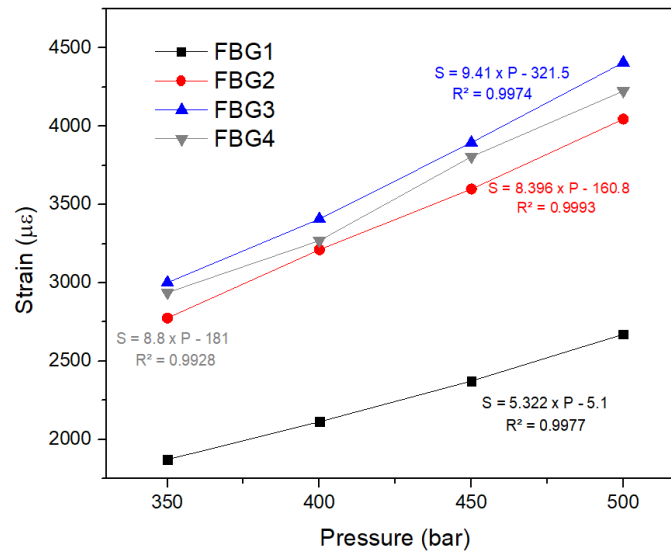


Figure 93: Relation between the maximum cyclic pressure and measured strain by FBG sensors

Figure 94 presents the spectra of the embedded optical fibre at the maximum and minimum pressures in different cycles, having different values of maximum pressure. The CWL of the 4 FBGs, for the four cyclic pressure ranges tested, remains nearly unchanged, revealing no damage as the COPV is unloaded, up to this point. Moreover, the amplitude of the spectra is kept approximately constant, demonstrating the reliability of the OF for a very high number of cycles. The spectra at the maximum pressure of each cycle shows decreasing amplitude as the value of maximum pressure increases, due to increased microbending. Nevertheless, except for the FBG4 when cycled between 3 – 500 bar, the optical interrogator was still able to continuously detect the CWL of all FBG sensors throughout the entire test.

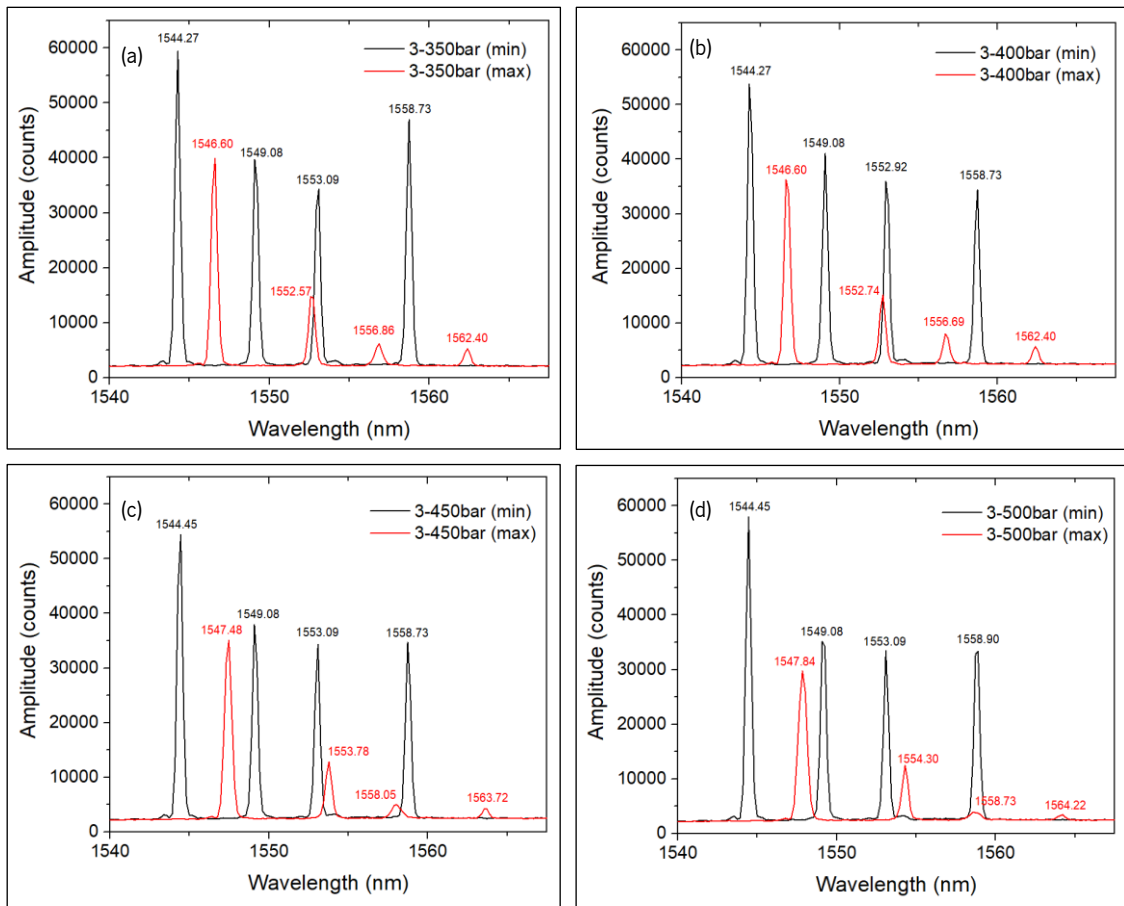


Figure 94: Optical spectra change between maximum and minimum pressure values of cyclic pressure testing with different maximum pressure value: (a) cycle number 8292 between 3 and 350 bar; (b) cycle number 82 between 3 and 400 bar; (c) cycle number 437 between 3 and 450 bar; and (d) cycle number 10 between 3 and 500 bar

The optical fibre endured the entire cyclic pressure test and was able to monitor the last cycles before failure. Figure 95 presents the strain measured by the FBG sensors, as the pressure varied in the last cycles between 3 and 500 bar. The composite overwrap provides high stiffness to the COPV, and no additional deformation due to cumulative damage is observed, making it difficult to anticipate failure. It is possible to see that, at about 1.1 min of the time period shown in Figure 95, the internal pressure in the COPV does not reach the target of 500 bar at first. A new attempt is taken by the pressure pump, and it is still possible for the COPV to endure that pressure. A few cycles later, it happens again, until at about 3.4 min the pump takes 5 trials to reach the target pressure. At about 7.4 min the COPV has built enough damage that it can no longer reach the maximum cyclic pressure. The COPV completed 790 cycles between 3 and 500 bar.

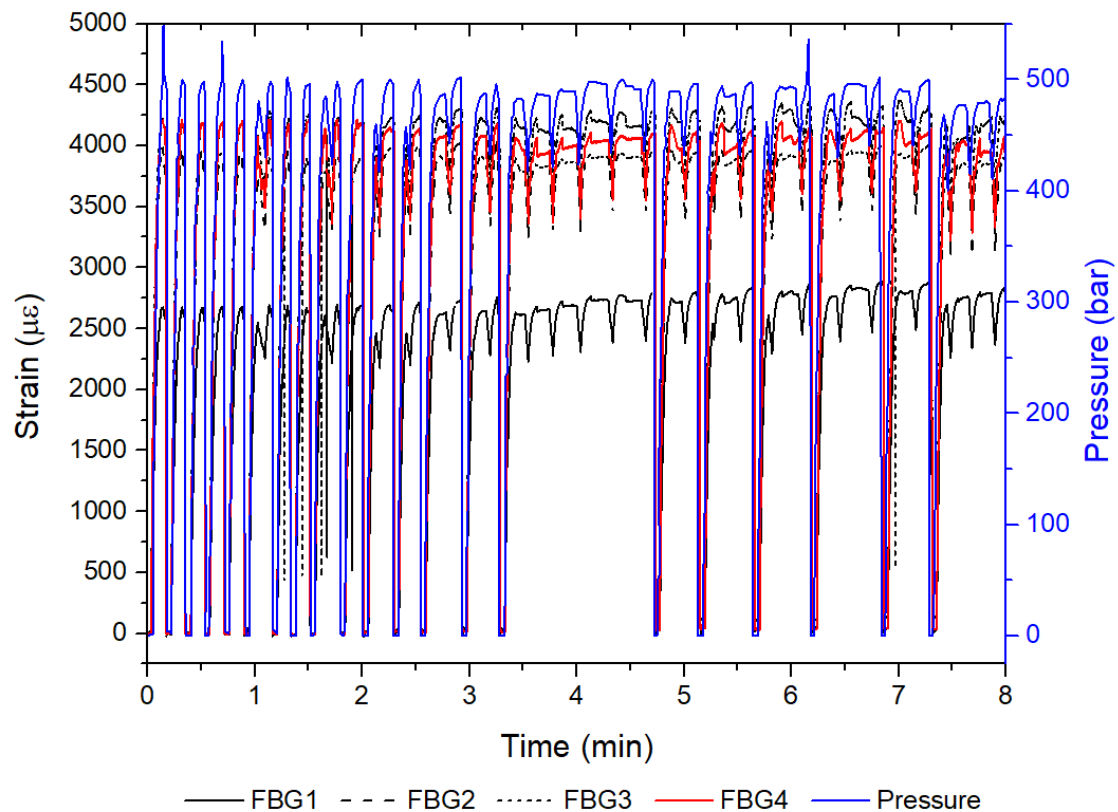


Figure 95: Last pressure cycles between 3 – 500 bar, before failure

The reported integration methodology with a bend-insensitive OF and the results presented here are very promising for the widespread use of metallic liner COPVs for storage of hydrogen or other fluid, to enable new COPV product development and reliability assurance. It should be mentioned that although the COPV failed after a total of 20 980 cycles, the FBG sensors were still intact in the end of the cyclic pressure test, showing their high fatigue strength. This number of cycles is equivalent to refuelling the COPV once a day for over 57 years.

So far, monitoring of cyclic pressure testing of metallic COPVs with embedded sensors, at such high-pressure range, has not been reported in the literature.

Chapter 6

Conclusions

This work investigated different sensing methodologies to monitor the manufacturing process and structural integrity of CFRP composites for advanced structural applications in aircraft and aerospace industries. Sensing integration was investigated as a means to detect early damage, specifically, BVID, decreasing the chances of catastrophic events.

The initial work, conducted at laboratory scale, compared and evaluated the obtained sensing data of the considered techniques, FBG sensors and self-sensing of CFRP composites with EIT technique, to infer on BVID detection and localization. Moreover, particularly for FBG sensors integration, this initial study, developed integration methodologies to minimize the interference with the production process, and assessed their effect on the mechanical performance of the specimen, when compared to the non-instrumented reference specimen.

Optical fibres were embedded into CFRP laminates prior to production by VARI. Thus, the FBG sensors were able to monitor the ambient temperature curing and post curing monitoring and evaluate the residual strains developed during the VARI process. The OFs had a free encapsulated FBG sensor for temperature compensation and a strain and temperature sensitive FBG sensor. FBG sensors proved to be able to detect a subtle increase of strain as infusion started. This was, generally, followed by a strain decrease up to the time where resin has filled up the voids in the carbon fibre fabrics. Afterwards, strain is kept approximately constant for the remainder time of ambient curing. Yet, it is possible to identify a subtle strain decrease due to curing shrinkage at distinct times of ambient curing of the CFRP samples. The temperature sensitive FBG sensors revealed to be very sensitive to room temperature oscillations. Further curing was detectable during the heating and isothermal stages of the post curing procedure.

The successful embedment and surviving the VARI process allowed to take advantage of the same FBG sensors for impact detection. Different through-thickness embedding locations of FBG sensors in CFRP laminates were studied for BVID detection. The higher energy of the first impact (30.0 J) caused a stiffer response in the CFRP, with FBG sensors in the T0 and B0 locations measuring residual tensile

strains of similar amplitude, about 50–75 $\mu\epsilon$ for samples with SDOF and 6–8 $\mu\epsilon$ for samples with LDOF. Rather lower residual strain values were measured by the FBG sensors in the mid-plan, about 35 $\mu\epsilon$ in the SDOF and $-1 \mu\epsilon$ in the LDOF. Bending of the laminate was revealed during the second impact with lower energy (20.0 J) by the residual tensile strain in the bottom layers (38 $\mu\epsilon$ in the SDOF and 35 $\mu\epsilon$ in the LDOF) and residual compressive strain in the top layers ($-30 \mu\epsilon$ for samples with SDOF and $-26 \mu\epsilon$ for those with LDOF). Besides the residual strain produced by the impact event, the FBG sensors identified the dynamic response of the CFRP with strain peaks, reaching up to 8000 $\mu\epsilon$ at the time of impact. This is particularly useful for the identification of the damage source in real-life applications, enabling improved damage severity assessment. For BVID detection in thin laminates, it is recommended that OF be embedded close to the bottom layers, where the damage condition can be more reliably evaluated, with FBG sensors being closer to the damaged layers.

For the studied density of embedded OF, the impairment of impact resistance was minimal when compared to the reference laminates. Furthermore, there was no evident advantage of the use of SDOF over LDOF, since the impacts produced comparable levels of absorbed energy in the instrumented laminates.

A sensor free methodology, the self-sensing capability of CFRP laminates with EIT and the one-step difference GN algorithm, was also evaluated for damage detection. Different types of damages, through-thickness holes and impact damage of different severities, were inflicted in the composite laminates. Two laminates with different layup configurations, a quasi-isotropic laminate and a highly anisotropic unbalanced laminate, were produced by VARI process.

The EIT was sensitive to the presence of through-thickness holes as small as 2 mm and revealed a gradually larger area with decreased electrical conductivity as the diameter of through-thickness holes increased. It was even possible to identify two distinguished localised damaged areas when two through-thickness holes were present. Similar responses were found for both laminates with different levels of anisotropy.

Each laminate configuration was subjected to three levels of impact energy to create damages with different degrees of severity, unnoticed damage, barely visible damage, and more severe damage. The EIT technique also demonstrated to be able to identify impact damage in the specimens with different levels of anisotropy, with overall distinguished damage shapes. These are encouraging results for the further investigation of EIT for damage detection in real composite parts with different

layup configurations. The unbalanced laminate revealed a slightly lower impact resistance, presenting a more rigid behaviour. The impact events on unbalanced specimens produced elongated shaped damages, roughly in the middle layers of the laminate. This elongated “peanut” shape-like damage was revealed by both EIT and ultrasound inspections. The quasi-isotropic specimens had circular shaped damages, as it was revealed by ultrasonic C-scan. However, the EIT images cannot show a well-defined damage shape, but they show changes of electrical conductivity in the central area of the specimens. Overall, the EIT images overestimate the area of damage.

The following observations derived from the initial work conducted on small coupon test specimens allowed to select the optical FBG sensors to be implemented in a SHM system for a real engineered CFRP part used in aerospace applications:

- the FBG sensors present higher maturity and sensitivity than the EIT based sensing technique;
- the FBG sensors can monitor the manufacturing process and impact damage;
- it is not possible to implement the EIT based sensing technique in a complex part without well-defined boundaries.

In the second stage of this work, a COPV for hydrogen storage to be used in a fuel cell system of a UAV was developed to then implement an optical sensing system to monitor the manufacturing process and structural integrity and detect and locate BVID. The COPV was developed to satisfy the requirement of a 2 hours flying autonomy of a UAV. For that, 2 COPVs with 1-litre capacity, for hydrogen storage at 350 bar, were considered. To achieve a design pressure of 350 bar, the COPV was designed to have a minimum burst pressure of 1050 bar, as recommended by EN12245 European standard. The COPV consisted of an aluminium liner and a CFRP composite overwrap. The composite overwrap layup was optimized in the finite element modelling Abaqus software and was validated by experimental burst pressure tests. The tested COPVs presented a burst pressure of 1061 ± 26 bar, a very small difference, 0.7%, with the simulated burst pressure (1069 bar). The optimised layup presents the following configuration: $[90_3/\pm 15_2]_S$. The composite overwrap was produced by winding of a carbon fibre reinforced epoxy prepreg tape in a filament winding machine. Different OF embedding strategies were tested. Simplified embedding strategies consisted of fixing the OF to the liner by a bi-component epoxy adhesive. However, the OF did not survive the high strains developed in the curing process. Covering the adhesive fixed OF with a high temperature

polyester adhesive tape provided a strain buffer effect to the OF, enabling the manufacturing process to be monitored, including winding and curing. The OFs were able to measure the developed strains in all the steps of the winding process and identify polymerization in the curing process.

Different OF embedding strategies were tested for implementation of an SHM system for process and structural health monitoring of the COPV. Simplified embedding strategies consisted of fixing the OF to the liner by a bi-component epoxy adhesive. However, the OF did not survive the high strains developed in the curing process. Covering of the adhesive fixed OF with a high temperature polyester adhesive tape provided a strain buffer effect to the OF, enabling the manufacturing process to be monitored, including winding and curing. The OFs were able to measure the developed strains in all the steps of the winding process and identify polymerization in the curing process.

The embedded OFs were also able to detect and locate BVID, in the form of matrix cracks and small bumps, produced by drop-weight impact tests with energies of 15 J. Errors as small as 17 mm and up to 56 mm were measured between the predicted impact locations and the “real” impact locations. These are very small errors that easily enable the localisation of the impact in a real-life structure.

Monitoring of the structural health of the COPV was accomplished by a bend-insensitive OF fixed to the liner surface by epoxy adhesive, which was then covered with a local unidirectional composite layer for reduction of shear and compressive strain on the OF, as demonstrated by the experimental cyclic pressure test. The OF was able to endure the full cyclic pressure test, remaining operational even after the failure of the COPV. In this test, the smart COPV was exposed to 18 190 pressure cycles between 3 and 350 bar, to resemble the operational charging and discharging cycles of fuel, and then to 1000 pressure cycles between 3 and 400 bar, 1000 pressure cycles between 3 and 450 bar and, lastly, 790 pressure cycles between 3 and 500 bar, when failure occurred. The bend-insensitive OF revealed a linear behaviour with the increase of internal pressure, which can be used to provide information on the level of fuel in the COPV. Moreover, having an embedded OF that can endure these large number of pressure cycles can provide safety assurance in the development of new COPV designs. Monitoring of pressure cycling tests, at such high pressure ranges, has not yet been reported in the literature for metallic COPVs.

The embedment of the bend-insensitive OF in between the aluminium liner and CFRP overwrap allowed to accomplish the ultimate objective of this work, to implement a SHM system on a real engineered CFRP part used in aerospace applications. This optical based monitoring approach can monitor the winding and curing processes for the production of the COPV, detect and locate impact damage and assess the internal pressure in the COPV. The proposed embedding approach, using a prepreg buffer material over the OF for added protection, can be employed even in space tank fuels, with adequate selection of the prepreg buffer material.

Chapter 7

Recommendations for Future Work

The results obtained in this work opened new perspectives and motivation for future work. Some considerations that may be regarded for further investigation are introduced next.

Although the EIT technique was not selected for implementation on a SHM system for the COPV, this is a very inexpensive technique and the results reported here demonstrate its sensitivity to the presence of subtle damage. This technique is highly dependent on the electrical conductivity of the material and, consequently, on the composite layup configuration. To further increase the TRL of EIT and understanding of the tomographic images, it is suggested that more layup configurations are studied and compared.

The work conducted on the SHM system for the COPV focused, essentially, on the demonstration of the OF capabilities to monitor this real-life engineering part in-operation and its manufacturing process. However, the OF could be integrated in the COPV to aid the development of its manufacturing process, namely, the *autofrettage* process. There are no standards, nor widely accepted and established rules that specify the *autofrettage* pressure and this process plays an important role on the fatigue lifetime of a COPV. Optical FBG sensors may allow to optimize the *autofrettage* pressure during development of COPV prototypes by detecting plastic deformation of the liner. This would minimize the number of experiments and save time and money on the execution of cyclic pressure testing to evaluate the effect of different *autofrettage* pressures on the fatigue lifetime of the COPV.

Other prepreg materials may be tested as a unidirectional composite buffer layer to protect the OF from shear and compressive loading.

Finally, but not less important, this work opens new perspectives on highly reliable structural health monitoring systems for FRP composite structures under great stress loads, enabled by FBG sensors inscribed into bend-insensitive optical fibres and protected by a unidirectional composite buffer layer. This embedding technique can be used in COPVs for storage of not only hydrogen but also

for other fuels, like liquid hydrogen and liquid oxygen in space applications. As temperature fluctuations are considerable in such applications, a second set of FBG sensors would be necessary for decoupling the thermal and mechanical strain. This is particularly valuable for reusable COPVs in emerging reusable launch vehicles, where the status and evolution of the COPV structural condition can be readily assessed upon return and prior to the next mission, by evaluation of FBG sensors data.

References

- [1] V. Giurgiutiu, *Structural Health Monitoring of Aerospace Composites*. USA: Elsevier, 2016.
- [2] V. Tita, J. Carvalho, and D. Vandepitte, "Failure analysis of low velocity impact on thin composite laminates: Experimental and numerical approaches," *Compos. Struct.*, vol. 83, pp. 413–428, 2008.
- [3] M. Ramakrishnan, G. Rajan, Y. Semenova, and G. Farrell, "Overview of Fiber Optic Sensor Technologies for Strain/Temperature Sensing Applications in Composite Materials," *Sensors*, vol. 16, no. 1, p. 99, 2016.
- [4] C. Boller, "Next generation structural health monitoring and its integration into aircraft design," *Int. J. Syst. Sci.*, vol. 31, no. 11, pp. 1333–1349, 2010.
- [5] H. Zhang, E. Bilotti, and T. Peijs, "The use of carbon nanotubes for damage sensing and structural health monitoring in laminated composites: a review," *Nanocomposites*, vol. 1, no. 4, pp. 177–194, 2015.
- [6] R. Di Sante, "Fibre Optic Sensors for Structural Health Monitoring of Aircraft Composite Structures: Recent Advances and Applications," *Sensors*, vol. 15, no. 8, pp. 18666–18713, 2015.
- [7] W. H. Prosser *et al.*, "Structural Health Management for Future Aerospace Vehicles," *2nd Australas. Work. Struct. Heal. Monit.*, 2004.
- [8] P. Gasior, R. Rybczynski, J. Kaleta, S. Villalonga, F. Nony, and C. Magnier, "High pressure composite vessel with integrated optical fiber sensors: Monitoring of manufacturing process and operation," in *American Society of Mechanical Engineers, Pressure Vessels and Piping Conference*, 2018, pp. 1–10.
- [9] J. S. Chilles, A. F. Koutsomitopoulou, A. J. Croxford, and I. P. Bond, "Monitoring cure and detecting damage in composites with inductively coupled embedded sensors," *Compos. Sci. Technol.*, vol. 134, pp. 81–88, 2016.

-
- [10] P. Cawley, "Structural health monitoring: Closing the gap between research and industrial deployment," *Struct. Heal. Monit.*, vol. 17, no. 5, pp. 1225–1244, 2018.
- [11] S. Abrate, "Impact on laminated composites : Recent advances," *Appl Mech Rev*, vol. 47, no. 11, pp. 517–544, 1994.
- [12] J. Kim and M. Sham, "Impact and delamination failure of woven-fabric composites," *Compos. Sci. Technol.*, vol. 60, no. 5, pp. 745–761, 2000.
- [13] S. Abrate, "Impact on Laminated Composite Materials," *Appl Mech Rev*, vol. 44, no. 4, pp. 155–188, 1991.
- [14] G. Davies and P. Irving, "Impact, post-impact strength and post-impact fatigue behaviour of polymer composites," in *Polymer Composites in the Aerospace Industry*, C. P.E. Irving, Soutis, Ed. Elsevier Ltd, 2015, pp. 231–259.
- [15] S. Abrate, *Impact on Composite Structures*. Cambridge University Press, 1998.
- [16] V. Giurgiutiu, "SHM of Aerospace Composites – Challenges and Opportunities," *CAMX Conf. Proc.*, pp. 1–15, 2015.
- [17] J. Körbelin, M. Derra, and B. Fiedler, "Influence of temperature and impact energy on low velocity impact damage severity in CFRP," *Compos. Part A*, vol. 115, no. March, pp. 76–87, 2018.
- [18] K. Worden and J. M. Dulieu-Barton, "An Overview of Intelligent Fault Detection in Systems and Structures," *Struct. Heal. Monit.*, vol. 3, no. 1, pp. 85–98, 2004.
- [19] L. Y. Z. Su, *Identification of Damage Using Lamb Waves*, vol. 49. Berlin: Springer, 2009.
- [20] Y. J. Guo H, Xiao G, Mrad N, "Fiber Optic Sensors for Structural Health Monitoring of Air Platforms," *Sensors*, vol. 11, pp. 3687–3705, 2011.
- [21] Z. M. Hafizi, J. Epaarachchi, and K. T. Lau, "Impact location determination on thin laminated composite plates using an NIR-FBG sensor system," *Meas. J. Int. Meas. Confed.*, vol. 61, pp. 51–57, 2015.
- [22] Z. Ren, J. Li, R. Zhu, K. Cui, Q. He, and H. Wang, "Phase-shifting optical fiber sensing with rectangular-pulse binary phase modulation," *Opt. Lasers Eng.*, vol. 100, pp. 170–175, 2018.
- [23] M. Maheshwari, V. G. M. Annamdas, J. H. L. Pang, A. Asundi, and S. C. Tjin, "Crack

- monitoring using multiple smart materials; fiber-optic sensors & piezo sensors,” *Int. J. Smart Nano Mater.*, vol. 8, pp. 41–55, 2017.
- [24] B. W. Jang and C. G. Kim, “Real-time detection of low-velocity impact-induced delamination onset in composite laminates for efficient management of structural health,” *Compos. Part B Eng.*, vol. 123, pp. 124–135, 2017.
- [25] S. Nag-Chowdhury, H. Bellegou, I. Pillin, M. Castro, P. Longrais, and J. F. Feller, “Non-intrusive health monitoring of infused composites with embedded carbon quantum piezo-resistive sensors,” *Compos. Sci. Technol.*, vol. 123, pp. 286–294, 2016.
- [26] G. Zhou and L. M. Sim, “Damage detection and assessment in fibre-reinforced composite structures with embedded fibre optic sensors – review,” *Smart Mater. Struct.*, vol. 11, pp. 925–939, 2002.
- [27] A. R. Chambers, M. C. Mowlem, and L. Dokos, “Evaluating impact damage in CFRP using fibre optic sensors,” *Compos. Sci. Technol.*, vol. 67, no. 6, pp. 1235–1242, 2007.
- [28] M. Hirsch, D. Majchrowicz, P. Wierzba, M. Weber, M. Bechelany, and M. Jędrzejewska-Szczerska, “Low-coherence interferometric fiber-optic sensors with potential applications as biosensors,” *Sensors (Switzerland)*, vol. 17, no. 2, pp. 1–12, 2017.
- [29] V. Giurgiutiu, “Fiber-Optic Sensors,” in *Structural Health Monitoring of Aerospace Composites*, 2016, pp. 249–296.
- [30] E. S. Kocaman *et al.*, “Monitoring the damage state of fiber reinforced composites using an FBG network for failure prediction,” *Materials (Basel)*, vol. 10, no. 32, pp. 1–19, 2017.
- [31] A. Güemes, A. Fernández-López, P. F. Díaz-Maroto, A. Lozano, and J. Sierra-Perez, “Structural health monitoring in composite structures by fiber-optic sensors,” *Sensors (Switzerland)*, vol. 18, no. 4, pp. 1–11, 2018.
- [32] K. Shivakumar and A. Bhargava, “Failure mechanics of a composite laminate embedded with a fiber optic sensor,” *J. Compos. Mater.*, vol. 39, no. 9, pp. 777–798, 2005.
- [33] R. Liu and D. Liang, “Natural frequency detection of smart composite structure by small diameter fiber Bragg grating,” *J. Vib. Control*, no. January, 2014.
- [34] S. Takeda, Y. Okabe, and N. Takeda, “Delamination detection in CFRP laminates with embedded small-diameter fiber Bragg grating sensors,” *Compos. Part A*, vol. 33, no.

- December 2013, pp. 971–980, 2002.
- [35] “T60/ Small Diameter Fiber (Thin) FBG,” *Technica*. [Online]. Available: <https://technicasa.com/t60-small-diameter-fiber-thin-fbg/>. [Accessed: 11-Dec-2020].
- [36] R. Ramly, W. Kuntjoro, and M. K. A. Rahman, “Using embedded fiber bragg grating (FBG) sensors in smart aircraft structure materials,” *Procedia Eng.*, vol. 41, no. Iris, pp. 600–606, 2012.
- [37] C. Miguel Giraldo, J. Zúñiga Sagredo, J. Sánchez Gómez, and P. Corredera, “Demonstration and Methodology of Structural Monitoring of Stringer Runs out Composite Areas by Embedded Optical Fiber Sensors and Connectors Integrated during Production in a Composite Plant,” *Sensors*, vol. 17, no. 1683, pp. 1–22, 2017.
- [38] S. Goossens *et al.*, “Aerospace-grade surface mounted optical fibre strain sensor for structural health monitoring on composite structures evaluated against in-flight conditions,” *Smart Mater. Struct.*, vol. 28, no. 6, 2019.
- [39] Y. Qiu, Q. Wang, H. Zhao, J. Chen, and Y. Wang, “Review on composite structural health monitoring based on fiber Bragg grating sensing principle,” *J. Shanghai Jiaotong Univ.*, vol. 18, no. 2, pp. 129–139, 2013.
- [40] E. K. G. Boateng, P. Schubel, and R. Umer, “Thermal isolation of FBG optical fibre sensors for composite cure monitoring,” *Sensors Actuators, A Phys.*, vol. 287, pp. 158–167, 2019.
- [41] N. J. Alberto, C. A. Marques, J. L. Pinto, and R. N. Nogueira, “Three-parameter optical fiber sensor based on a tilted fiber Bragg grating,” *Appl. Opt.*, vol. 49, no. 31, pp. 6085–6091, 2010.
- [42] R. Min, B. Ortega, and C. Marques, “Fabrication of tunable chirped mPOF Bragg gratings using a uniform phase mask,” *Opt. Express*, vol. 26, no. 4, pp. 4411–4420, 2018.
- [43] K. Markowski, K. Jędrzejewski, M. Marzęcki, and T. Osuch, “Linearly chirped tapered fiber-Bragg-grating-based Fabry–Perot cavity and its application in simultaneous strain and temperature measurement,” *Opt. Lett.*, vol. 42, no. 7, pp. 1464–1467, 2017.
- [44] R. X. Tan *et al.*, “Birefringent Bragg grating in C-shaped optical fiber as a temperature-insensitive refractometer,” *Sensors*, vol. 18, no. 3285, 2018.
- [45] J. F. Tressler, L. Qin, and K. Uchino, *Piezoelectric Composite Sensors*, no. May 2015.

- Elsevier Ltd., 2016.
- [46] K. S. Ramadan, D. Sameoto, and S. Evoy, "A review of piezoelectric polymers as functional materials for electromechanical transducers," *Smart Mater. Struct.*, vol. 23, no. 3, 2014.
- [47] S. Masmoudi, A. El Mahi, and S. Turki, "Fatigue behaviour and structural health monitoring by acoustic emission of E-glass/epoxy laminates with piezoelectric implant," *Appl. Acoust.*, vol. 108, pp. 50–58, 2016.
- [48] L. Qiu, X. Deng, S. Yuan, Y. Huang, and Y. Ren, "Impact monitoring for aircraft smart composite skins based on a lightweight sensor network and characteristic digital sequences," *Sensors*, vol. 18, no. 2218, pp. 1–27, 2018.
- [49] V. Giurgiutiu, "Piezoelectric Wafer Active Sensors," in *Structural Health Monitoring of Aerospace Composites*, USA: Elsevier, 2016, pp. 177–248.
- [50] V. G. M. Annamdas and C. K. Soh, "Application of Electromechanical Impedance Technique for Engineering Structures: Review and Future Issues," *J. Intell. Mater. Syst. Struct.*, vol. 21, no. 1, pp. 41–59, 2010.
- [51] T. Wandowski, P. H. Malinowski, and W. M. Ostachowicz, "Temperature and damage influence on electromechanical impedance method used for carbon fibre-reinforced polymer panels," *J. Intell. Mater. Syst. Struct.*, vol. 28, no. 6, pp. 782–798, 2017.
- [52] M. A. de Oliveira, A. V. Monteiro, and J. V. Filho, "A new structural health monitoring strategy based on PZT sensors and convolutional neural network," *Sensors (Switzerland)*, vol. 18, no. 9, 2018.
- [53] T. Wandowski, P. H. Malinowski, and W. M. Ostachowicz, "Delamination detection in CFRP panels using EMI method with temperature compensation," *Compos. Struct.*, vol. 151, pp. 99–107, 2016.
- [54] V. I. G. Iurgiutiu, "Electro-Mechanical Impedance Method for Crack Detection in Thin Plates," *J. Intell. Mater. Syst. Struct.*, vol. 12, pp. 709–718, 2015.
- [55] G. R. Thomas and A. A. Khatibi, "Durability of Structural Health Monitoring Systems under Impact Loading," *Procedia Eng.*, vol. 188, pp. 340–347, 2017.
- [56] M. Carboni, A. Gianneo, and M. Giglio, "A Lamb waves based statistical approach to structural health monitoring of carbon fibre reinforced polymer composites," *Ultrasonics*,

- vol. 60, pp. 51–64, 2015.
- [57] V. Giurgiutiu, *Smart Materials and Health Monitoring of Composites*. Elsevier Ltd., 2017.
- [58] Smart Material, “Smart Material - Home of the MFC,” *MFC - Macro Fiber Composite*. [Online]. Available: <https://www.smart-material.com/MFC-product-main.html>. [Accessed: 18-Dec-2019].
- [59] M. Lin, X. Qing, A. Kumar, and S. J. Beard, “SMART Layer and SMART Suitcase for Structural Health Monitoring Applications,” in *Smart Structures and Materials 2001: Industrial and Commercial Applications of Smart Structures Technologies*, 2001, vol. 4332, pp. 98–106.
- [60] Y. Wang, L. Qiu, Y. Luo, and R. Ding, “A stretchable and large-scale guided wave sensor network for aircraft smart skin of structural health monitoring,” *Struct. Heal. Monit.*, pp. 1–16, 2019.
- [61] K. C. Jung and S. H. Chang, “Performance evaluation of smart grid fabrics comprising carbon dry fabrics and PVDF ribbon sensors for structural health monitoring,” *Compos. Part B Eng.*, vol. 163, pp. 690–701, 2019.
- [62] F. Lambinet and Z. S. Khodaei, “Smart patch repair with low profile PVDF sensors,” *Key Eng. Mater.*, vol. 754, pp. 359–362, 2017.
- [63] F. Avilés, A. May-pat, M. A. López-manchado, R. Verdejo, and A. Bachmatiuk, “A comparative study on the mechanical, electrical and piezoresistive properties of polymer composites using carbon nanostructures of different topology,” *Eur. Polym. J.*, vol. 99, no. September 2017, pp. 394–402, 2018.
- [64] J. Teixeira, L. Horta-romarís, M. Abad, P. Costa, and S. Lanceros-méndez, “Piezoresistive response of extruded polyaniline/ (styrene-butadiene-styrene) polymer blends for force and deformation sensors,” *Mater. Des.*, vol. 141, pp. 1–8, 2018.
- [65] S. Nonn, M. Schagerl, Y. Zhao, S. Gschossmann, and C. Kralovec, “Application of electrical impedance tomography to an anisotropic carbon fiber-reinforced polymer composite laminate for damage localization,” *Compos. Sci. Technol.*, vol. 160, pp. 231–236, 2018.
- [66] T. C. H. Peng, Q. Li, “Carbon Nanotubes for Defect Monitoring in Fiber-Reinforced Polymer Composites,” in *Industrial Applications of Carbon Nanotubes*, vol. 437, no. June,

- Amsterdam: Elsevier, 2017, pp. 71–100.
- [67] R. Balaji and M. Sasikumar, “Graphene based strain and damage prediction system for polymer composites,” *Compos. Part A*, vol. 103, pp. 48–59, 2017.
- [68] R. Moriche, M. Sánchez, A. Jiménez-Suárez, S. G. Prolongo, and A. Ureña, “Electrically conductive functionalized-GNP/epoxy based composites: From nanocomposite to multiscale glass fibre composite material,” *Compos. Part B Eng.*, vol. 98, pp. 49–55, 2016.
- [69] R. Jan *et al.*, “Liquid exfoliated graphene smart layer for structural health monitoring of composites,” *J. Intell. Mater. Syst. Struct.*, vol. 28, no. 12, pp. 1565–1574, 2017.
- [70] H. Montazerian, A. Rashidi, A. Dalili, H. Najjaran, A. S. Milani, and M. Hoorfar, “Graphene-Coated Spandex Sensors Embedded into Silicone Sheath for Composites Health Monitoring and Wearable Applications,” *Small*, vol. 15, no. 1804991, pp. 1–12, 2019.
- [71] S. Luo and T. Liu, “Graphite nanoplatelet enabled embeddable fiber sensor for in situ curing monitoring and structural health monitoring of polymeric composites,” *ACS Appl. Mater. Interfaces*, vol. 6, no. 12, pp. 9314–9320, 2014.
- [72] J. Cagáň, J. Pelant, M. Kyncl, M. Kadlec, and L. Michalcová, “Damage detection in carbon fiber–reinforced polymer composite via electrical resistance tomography with Gaussian anisotropic regularization,” *Struct. Heal. Monit.*, vol. 18, no. 5–6, 2019.
- [73] A. Baltopoulos, N. Polydorides, L. Pambaguian, A. Vavouliotis, and V. Kostopoulos, “Damage identification in carbon fiber reinforced polymer plates using electrical resistance tomography mapping,” *J. Compos. Mater.*, vol. 47, no. 26, pp. 3285–3301, 2013.
- [74] J. Cagáň, “Hardware implementation of electrical resistance tomography for damage detection of carbon fibre–reinforced polymer composites,” *Struct. Heal. Monit.*, vol. 16, no. 2, pp. 129–141, 2017.
- [75] B. R. Loyola, V. La Saponara, K. J. Loh, T. M. Briggs, G. O. Bryan, and J. L. Skinner, “Spatial Sensing Using Electrical Impedance Tomography,” *IEEE Sens. J.*, vol. 13, no. 6, pp. 2357–2367, 2013.
- [76] T. N. Tallman, S. Gungor, K. W. Wang, and C. E. Bakis, “Damage detection via electrical impedance tomography in glass fiber/epoxy laminates with carbon black filler,” *Struct. Heal. Monit.*, vol. 14, no. 1, pp. 100–109, 2015.

-
- [77] A. J. Thomas, J. J. Kim, T. N. Tallman, and C. E. Bakis, "Damage detection in self-sensing composite tubes via electrical impedance tomography," *Compos. Part B Eng.*, vol. 177, no. 107276, 2019.
- [78] E. Thostenson and T. Chou, "Carbon Nanotube Networks: Sensing of Distributed Strain and Damage for Life Prediction and Self Healing," *Adv. Mater.*, vol. 18, pp. 2837–2841, 2006.
- [79] T. W. Chou, L. Gao, E. T. Thostenson, Z. Zhang, and J. H. Byun, "An assessment of the science and technology of carbon nanotube-based fibers and composites," *Compos. Sci. Technol.*, vol. 70, no. 1, pp. 1–19, 2010.
- [80] H. Zhang, Y. Liu, M. Kuwata, E. Bilotti, and T. Peijs, "Improved fracture toughness and integrated damage sensing capability by spray coated CNTs on carbon fibre prepreg," *Compos. Part A*, vol. 70, pp. 102–110, 2015.
- [81] A. Baltopoulos, N. Polydorides, L. Pambaguian, A. Vavouliotis, and V. Kostopoulos, "Exploiting carbon nanotube networks for damage assessment of fiber reinforced composites," *Compos. Part B Eng.*, vol. 76, pp. 149–158, 2015.
- [82] A. Naghashpour and S. Van Hoa, "A technique for in-situ detection of random failure in composite structures under cyclic loading," *J. Compos. Mater.*, vol. 53, no. 23, pp. 3243–3255, 2019.
- [83] T. Takeda and F. Narita, "Fracture behavior and crack sensing capability of bonded carbon fiber composite joints with carbon nanotube-based polymer adhesive layer under Mode I loading," *Composites Science and Technology*, vol. 146, pp. 26–33, 2017.
- [84] N. D. Alexopoulos, C. Bartholome, P. Poulin, and Z. Marioli-Riga, "Structural health monitoring of glass fiber reinforced composites using embedded carbon nanotube (CNT) fibers," *Compos. Sci. Technol.*, vol. 70, no. 2, pp. 260–271, 2010.
- [85] J. Sebastian *et al.*, "Health monitoring of structural composites with embedded carbon nanotube coated glass fiber sensors," *Carbon N. Y.*, vol. 66, pp. 191–200, 2014.
- [86] S. Luo, W. Obitayo, and T. Liu, "SWCNT-thin-film-enabled fiber sensors for lifelong structural health monitoring of polymeric composites - From manufacturing to utilization to failure," *Carbon*, vol. 76, pp. 321–329, 2014.
- [87] R. Moriche, A. Jiménez-Suárez, M. Sánchez, S. G. Prolongo, and A. Ureña, "Graphene

- nanoplatelets coated glass fibre fabrics as strain sensors," *Compos. Sci. Technol.*, vol. 146, pp. 59–64, 2017.
- [88] R. S. Pierce, B. G. Falzon, and M. C. Thompson, "A multi-physics process model for simulating the manufacture of resin-infused composite aerostructures," *Compos. Sci. Technol.*, vol. 149, pp. 269–279, 2017.
- [89] H. S. Sas, P. Šimáček, and S. G. Advani, "A methodology to reduce variability during vacuum infusion with optimized design of distribution media," *Compos. Part A Appl. Sci. Manuf.*, vol. 78, pp. 223–233, 2015.
- [90] V. A. Komarov, E. I. Kurkin, and M. O. Spirina, "Composite Aerospace Structures Shape Distortion during All Stages of Vacuum Infusion Production," *Procedia Eng.*, vol. 185, pp. 139–145, 2017.
- [91] E. Chehura, A. A. Skordos, C.-C. Ye, S. W. James, I. K. Partridge, and R. P. Tatam, "Strain development in curing epoxy resin and glass fibre/epoxy composites monitored by fibre Bragg grating sensors in birefringent optical fibre," *Smart Mater. Struct.*, vol. 14, pp. 354–362, 2005.
- [92] J. Leng and A. Asundi, "Structural health monitoring of smart composite materials by using EFPI and FBG sensors," vol. 103, pp. 330–340, 2003.
- [93] H.-K. Kang, D.-H. Kang, H.-J. Bang, C.-S. Hong, and C.-G. Kim, "Cure monitoring of composite laminates using fiber optic sensors," *Smart Mater. Struct.*, vol. 11, no. 2, pp. 279–287, 2002.
- [94] NETZSCH, "DEA 288 Ionic - Dielectric Analyzer - NETZSCH Analyzing & Testing." [Online]. Available: <https://www.netzsch-thermal-analysis.com/en/products-solutions/dielectric-analysis/dea-288-ionic/>. [Accessed: 22-Jun-2020].
- [95] M. A. Ali, R. Umer, K. A. Khan, Y. A. Samad, K. Liao, and W. Cantwell, "Graphene coated piezo-resistive fabrics for liquid composite molding process monitoring," *Compos. Sci. Technol.*, vol. 148, pp. 106–114, 2017.
- [96] Y. Yang *et al.*, "Design and Integration of Flexible Sensor Matrix for in Situ Monitoring of Polymer Composites," *ACS Sensors*, vol. 3, no. 9, pp. 1698–1705, 2018.
- [97] P. Carlone and G. S. Palazzo, "Unsaturated and Saturated Flow Front Tracking in Liquid

- Composite Molding Processes using Dielectric Sensors,” *Appl. Compos. Mater.*, vol. 22, no. 5, pp. 543–557, 2015.
- [98] P. Carlone, F. Rubino, V. Paradiso, and F. Tucci, “Multi-scale modeling and online monitoring of resin flow through dual-scale textiles in liquid composite molding processes,” *Int. J. Adv. Manuf. Technol.*, vol. 96, pp. 2215–2230, 2018.
- [99] X. Qing, X. Liu, J. Zhu, and Y. Wang, “In-situ monitoring of liquid composite molding process using piezoelectric sensor network,” *Struct. Heal. Monit.*, no. 411, 2020.
- [100] J. C. Wang, P.; Molimard, J.; Drapier, S.; Vautrin, A.; Minni, “Monitoring the resin infusion manufacturing process under industrial environment using distributed sensors,” *J. Compos. Mater.*, vol. 46, no. 6, pp. 691–706, 2012.
- [101] K. I. Tifkitsis and A. A. Skordos, “A novel dielectric sensor for process monitoring of carbon fibre composites manufacture,” *Compos. Part A Appl. Sci. Manuf.*, vol. 123, pp. 180–189, 2019.
- [102] B. G. Pollet, S. S. Kocha, and I. Staffell, “Current status of automotive fuel cells for sustainable transport,” *Curr. Opin. Electrochem.*, vol. 16, pp. 90–95, 2019.
- [103] N. C. Menon, A. M. Kruiuzenga, K. J. Alvine, C. S. Marchi, A. Nissen, and K. Brooks, “Behaviour of Polymers in High Pressure Environments as Applicable to the Hydrogen Infrastructure,” in *Proceedings of the ASME 2016 Pressure Vessels and Piping Conference*, 2016, pp. 1–14.
- [104] J. Jones, “Hydrogen-powered drones take to the skies,” *Enlit World*, 05-Jan-2022. [Online]. Available: <https://www.enlit.world/hydrogen/hydrogen-powered-drones-take-to-the-skies/>. [Accessed: 24-Sep-2022].
- [105] Airbus, “ZEROe - Zero emission.” [Online]. Available: <https://www.airbus.com/en/innovation/zero-emission/hydrogen/zeroe>. [Accessed: 06-Aug-2022].
- [106] A. M. Abdalla, S. Hossain, O. B. Nisfindy, A. T. Azad, M. Dawood, and A. K. Azad, “Hydrogen production, storage, transportation and key challenges with applications: A review,” *Energy Convers. Manag.*, vol. 165, no. April, pp. 602–627, 2018.
- [107] F. C. Shen, “A filament-wound structure technology overview,” *Mater. Chem. Phys.*, vol.

- 42, pp. 96–100, 1995.
- [108] H. Barthelemy, M. Weber, and F. Barbier, “Hydrogen storage: Recent improvements and industrial perspectives,” *Int. J. Hydrogen Energy*, vol. 42, no. 11, pp. 7254–7262, 2017.
- [109] B. R. Murray, A. Doyle, P. J. Feerick, C. O. A. Semprimoschnig, S. B. Leen, and C. M. Ó Brádaigh, “Rotational moulding of peek polymer liners with carbon fibre/peek over tape-placement for space cryogenic fuel tanks,” *Mater. Des.*, vol. 132, pp. 567–581, 2017.
- [110] S. Villalonga *et al.*, “Application of full thermoplastic composite for type IV 70MPa high pressure vessels,” in *ICCM International Conferences on Composite Materials*, 2011, pp. 1–5.
- [111] Y. Fukui, T. Katayama, and M. Mizuno, “Hydrogen Tank Liner Material and Hydrogen Tank Liner,” US 2009/0203845 A1, 2009.
- [112] M. Leavitt, “Low Cost , High Efficiency , High Pressure Hydrogen Storage.” Quantum Technologies Inc., 2010.
- [113] N. L. Newhouse, “Development of Improved Composite Pressure Vessels for Hydrogen Storage,” *Project Final Report Hydrogen Storage Engineering*. 2016.
- [114] Y. M. Tarnopol’skii, S. T. Peters, and A. I. Beil’, “Filament Winding,” in *Handbook of Composites*, S. T. Peters, Ed. London: Chapman & Hall, 1998, pp. 456–471.
- [115] M. Quanjin, R. M. Rejab, B. Zhang, and N. M. Kumar, “Filament Winding Technique: SWOT Analysis and Applied Favorable Factors,” *SCIREA J. Mech. Eng.*, no. April, 2019.
- [116] Y. Di Boon, S. C. Joshi, and S. K. Bhudolia, “Review: Filament winding and automated fiber placement with in situ consolidation for fiber reinforced thermoplastic polymer composites,” *Polymers (Basel)*, vol. 13, no. 12, 2021.
- [117] M. Lehmann *et al.*, “Infusion 4.0 – Flow Front Detection in Composite Parts with Fiber Optic Sensors,” *Dtsch. Luft- und Raumfahrtkongress 2019*, pp. 1–11, 2019.
- [118] A. M. Shibley, “Filament Winding,” in *Handbook of Composites*, G. Lubin, Ed. Springer, 1982, pp. 449–478.
- [119] D. Nash, D. Aklil, E. Johnson, R. Gazey, and V. Ortisi, *Hydrogen storage: Compressed gas*, vol. 4. Elsevier Ltd., 2012.
- [120] P. B. McLaughlan, S. C. Forth, and G.-L. L. R., “Composite Overwrapped Pressure Vessels,

-
- A Primer," *NASA/SP-2011-573*. National Aeronautics and Space Administration - Johnson Space Center, Houston, pp. 1–20, 2011.
- [121] J. C. Thesken, P. Murthy, and L. Phoenix, "Composite overwrap pressure vessels: Mechanics and stress rupture lifing philosophy," 2009.
- [122] C. Frias, H. Faria, O. Frazão, P. Vieira, and A. T. Marques, "Manufacturing and testing composite overwrapped pressure vessels with embedded sensors," *Mater. Des.*, vol. 31, no. 8, pp. 4016–4022, 2010.
- [123] C. Banks and J. Grant, "Strain Measurement Using FBG on COPV in Stress Rupture Test." NASA Marshall Space Flight Center, 2019.
- [124] E. Saeter, K. Lasn, F. Nony, and A. T. Echtermeyer, "Embedded optical fibres for monitoring pressurization and impact of filament wound cylinders," *Compos. Struct.*, vol. 210, no. July 2018, pp. 608–617, 2019.
- [125] S. W. Park, D. H. Kang, H. J. Bang, S. O. Park, and C. G. Kim, "Strain monitoring and damage detection of a filament wound composite pressure tank using embedded fiber bragg grating sensors," *Key Eng. Mater.*, vol. 321-323 I, pp. 182–185, 2006.
- [126] J. Degrieck, W. De Waele, and P. Verleysen, "Monitoring of fibre reinforced composites with embedded optical fibre Bragg sensors, with application to filament wound pressure vessels," *NDT E Int.*, vol. 34, no. 4, pp. 289–296, 2001.
- [127] L. Maurin, P. Ferdinand, F. Nony, and S. Villalonga, "OFDR distributed strain measurements for SHM of hydrostatic stressed structures: An application to high pressure H2 storage type IV composite vessels - H2E project," *7th Eur. Work. Struct. Heal. Monit. EWSHM 2014 - 2nd Eur. Conf. Progn. Heal. Manag. Soc.*, pp. 930–937, 2014.
- [128] C. E. Banks, J. Grant, S. Russell, and S. Arnett, "Strain measurement during stress rupture of composite over-wrapped pressure vessel with fiber Bragg gratings sensors," *Smart Sens. Phenomena, Technol. Networks, Syst. 2008*, vol. 6933, no. 2008, p. 693300, 2008.
- [129] X. P. Qing, S. J. Beard, A. Kumar, H. L. Chan, and R. Ikegami, "Advances in the development of built-in diagnostic system for filament wound composite structures," *Compos. Sci. Technol.*, vol. 66, no. 11–12, pp. 1694–1702, 2006.
- [130] H. Fu, Z. Sharif Khodaei, and M. H. F. Aliabadi, "An Event-Triggered Energy-Efficient

- Wireless Structural Health Monitoring System for Impact Detection in Composite Airframes," *IEEE Internet Things J.*, vol. 6, no. 1, pp. 1183–1192, 2019.
- [131] G. Ding, H. Cao, and C. Xie, "Multipoint cure monitoring of temperature and strain of carbon fibre-reinforced plastic shafts using fibre Bragg grating sensors," *Nondestruct. Test. Eval.*, vol. 34, no. 2, pp. 117–134, 2019.
- [132] A. Adler and R. Guardo, "Electrical impedance tomography: Regularized imaging and contrast detection," *IEEE Trans. Med. Imaging*, vol. 15, no. 2, pp. 170–179, 1996.
- [133] A. Adler, T. Dai, and W. R. B. Lionheart, "Temporal image reconstruction in electrical impedance tomography," *Physiol. Meas.*, vol. 28, no. 7, 2007.
- [134] J. Cagáň and L. Michalcová, "Impact Damage Detection in CFRP Composite via Electrical Resistance Tomography by Means of Statistical Processing," *J. Nondestruct. Eval.*, vol. 39, no. 2, 2020.
- [135] A. Baltopoulos, A. Vavouliotis, V. Kostopoulos, N. Polydorides, and L. Pambaguian, "Electrical tomography as a tool for non-destructive assessment of composite structures," *Emerg. Technol. Non-Destructive Test. V - Proc. 5th Conf. Emerg. Technol. NDT*, no. 2006, pp. 389–394, 2012.
- [136] A. Ampatzoglou, A. Vavouliotis, A. Baltopoulos, and V. Kostopoulos, "Non destructive evaluation of artificially induced damage in composite structures using electrical resistance/potential mapping," *Emerg. Technol. Non-Destructive Test. V - Proc. 5th Conf. Emerg. Technol. NDT*, no. 1999, pp. 381–387, 2012.
- [137] P. F. Liu, J. K. Chu, S. J. Hou, P. Xu, and J. Y. Zheng, "Numerical simulation and optimal design for composite high-pressure hydrogen storage vessel: A review," *Renew. Sustain. Energy Rev.*, vol. 16, no. 4, pp. 1817–1827, 2012.
- [138] B. W. Tew, "Preliminary Design of Tubular Composite Structures Using Netting Theory and Composite Degradation Factors," *J. Press. Vessel Technol.*, vol. 117, pp. 390–394, 1995.
- [139] R. M. Gheshlaghi, M. H. Hojjati, and H. R. Mohammadi Daniali, "Analysis of composite pressure vessels," *Fract. Nano Eng. Mater. Struct. - Proc. 16th Eur. Conf. Fract.*, pp. 335–336, 2006.
- [140] Dassault Systèmes Simulia, "Getting Started With ABAQUS Interactive Edition Version 6.8."

- United States of America, 2008.
- [141] “Damage initiation for fiber-reinforced composites - SIMULIA User Assistance 2020,” *Dassault Systems*. [Online]. Available: https://help.3ds.com/2020/english/dssimulia_established/SIMACAEMATRefMap/simamat-c-damageinitfibercomposite.htm?contextscope=all&fbclid=IwAR1lcLOzj46_vwBBGx0bjmiltGXul55aqJeUpW3r-p43BIPylkFUxkEDpRk. [Accessed: 17-Sep-2022].
- [142] “Damage evolution and element removal for fiber-reinforced composites - SIMULIA User Assistance 2020,” *Dassault Systems*. [Online]. Available: https://help.3ds.com/2020/english/dssimulia_established/SIMACAEMATRefMap/simamat-c-damageevolfibercomposite.htm?contextscope=all&fbclid=IwAR3rWAp6mUDJxpohRRTY70mpIAQdE29qJoUcfBBqS_Qw_xWQmQ4aKTkmpdA. [Accessed: 17-Sep-2022].
- [143] D. S. Son, J. H. Hong, and S. H. Chang, “Determination of the autofrettage pressure and estimation of material failures of a Type III hydrogen pressure vessel by using finite element analysis,” *Int. J. Hydrogen Energy*, vol. 37, no. 17, pp. 12771–12781, 2012.
- [144] V. Alcántar, S. Ledesma, S. M. Aceves, E. Ledesma, and A. Saldaña, “Optimization of type III pressure vessels using genetic algorithm and simulated annealing,” *Int. J. Hydrogen Energy*, vol. 42, no. 31, pp. 20125–20132, 2017.
- [145] ASTM International, “ASTM E2070-13 Standard Test Methods for Kinetic Parameters by Differential Scanning Calorimetry Using Isothermal Methods,” *ASTM Int.*, vol. i, no. Reapproved, pp. 1–12, 2018.
- [146] H. L. Friedman, “Kinetics of thermal degradation of char-forming plastics from thermogravimetry. Application to a phenolic plastic,” *J. Polym. Sci. Part C*, vol. 6, no. 1, pp. 183–195, 1964.
- [147] B. Fernandez d’Arlas, L. Rueda, P. M. Stefani, K. de la Caba, I. Mondragon, and A. Eceiza, “Kinetic and thermodynamic studies of the formation of a polyurethane based on 1,6-hexamethylene diisocyanate and poly(carbonate-co-ester)diol,” *Thermochim. Acta*, vol. 459, pp. 94–103, 2007.
- [148] G. Wuzella, A. R. Mahendran, C. Beuc, and H. Lammer, “Isoconversional cure kinetics of a

- novel thermosetting resin based on linseed oil," *J. Therm. Anal. Calorim.*, 2020.
- [149] "ASTM D 3039/D 3039M: Standard Test Method for Tensile Properties of Polymer Matrix Composite Materials 1," vol. 15. ASTM International, United States, pp. 1–13, 2002.
- [150] Y. M. Kuo, H. J. Lin, C. N. Wang, and C. I. Liao, "Estimating the elastic modulus through the thickness direction of a uni- direction lamina which possesses transverse isotropic property," *J. Reinf. Plast. Compos.*, vol. 26, no. 16, pp. 1671–1679, 2007.
- [151] P. Xu *et al.*, "Bend-insensitive distributed sensing in singlemode-multimode-singlemode optical fiber structure by using Brillouin optical time-domain analysis," *Opt. Express*, vol. 23, no. 17, p. 22714, 2015.
- [152] C. Hiche, C. K. Coelho, and A. Chattopadhyay, "A strain amplitude-based algorithm for impact localization on composite laminates," *J. Intell. Mater. Syst. Struct.*, vol. 22, no. 17, pp. 2061–2067, 2011.
- [153] J. M. Barton, "The application of differential scanning calorimetry (DSC) to the study of epoxy resin curing reactions," *Adv. Polym. Sci.*, vol. 72, pp. 111–154, 1985.
- [154] M. Salvetti *et al.*, "On the mechanical response of CFRP composite with embedded optical fibre when subjected to low velocity impact and CAI tests," *Compos. Struct.*, vol. 179, pp. 21–34, 2017.
- [155] M. Yeager, M. Todd, W. Gregory, and C. Key, "Assessment of embedded fiber Bragg gratings for structural health monitoring of composites," *Struct. Heal. Monit.*, vol. 16, no. 3, pp. 262–275, 2017.
- [156] W. Woo, H. Choo, D. W. Brown, Z. Feng, and P. K. Liaw, "Angular distortion and through-thickness residual stress distribution in the friction-stir processed 6061-T6 aluminum alloy," *Mater. Sci. Eng. A*, vol. 437, no. 1, pp. 64–69, 2006.
- [157] G. T. Yahr, "Fatigue Design Curves," *J. Press. Vessel Technol.*, vol. 119, pp. 211–215, 1997.
- [158] S. A. Meguid and Y. Sun, "On the tensile and shear strength of nano-reinforced composite interfaces," *Mater. Des.*, vol. 25, pp. 289–296, 2004.
- [159] Y. B. Guo, H. J. Chiang, J. J. Deng, and V. P. W. Shim, "Projectile impact on fabric-metal assemblies – Influence of fabric-metal sequence," *Int. J. Impact Eng.*, vol. 127, no. May,

- pp. 1–16, 2019.
- [160] R. R. Ambriz and D. Jaramillo, “Mechanical Behavior of Precipitation Hardened Aluminum Alloys Welds,” in *Light Metal Alloys Applications*, IntechOpen, 2014, pp. 35–59.
- [161] A. Dorbane, G. Ayoub, B. Mansoor, R. Hamade, G. Kridli, and A. Imad, “Mechanical Response and Evolution of Damage of Al6061-T6 under Different Strain Rates and Temperatures,” *Proc. TMS Middle East – Mediterr. Mater. Congr. Energy Infrastruct. Syst. (MEMA 2015)*, 2016.
- [162] S. S. R. Koor, A. Karimzadeh, N. Yidris, M. Petru, M. R. Ayatollahi, and M. N. Tamin, “An energy-based concept for yielding of multidirectional FRP composite structures using a mesoscale lamina damage model,” *Polymers (Basel)*, vol. 12, no. 1, 2020.
- [163] A. Elmahdy, A. Zotti, S. Zuppolini, M. Zarrelli, A. Borriello, and P. Verleysen, “Effect of strain rate and silica filler content on the compressive behavior of rtm6 epoxy-based nanocomposites,” *Polymers (Basel)*, vol. 13, no. 21, pp. 1–20, 2021.
- [164] S. Saseendran, M. Wysocki, and J. Varna, “Cure-state dependent viscoelastic Poisson’s ratio of LY5052 epoxy resin,” *Adv. Manuf. Polym. Compos. Sci.*, vol. 3, no. 3, pp. 92–100, 2017.
- [165] R. A. J. Weerts, O. Cousigné, K. Kunze, M. G. D. Geers, and J. J. C. Remmers, “Assessment of contact-induced damage mechanisms in thick-walled composite cylinders,” *J. Reinf. Plast. Compos.*, vol. 39, no. 17–18, pp. 679–699, 2020.

Annexes

A1. Supplementary Experimental Data Results

Table A1: Plastic true stress and strain of the 6061-T6 aluminium liner

True Plastic Stress (MPa)	True Plastic Strain
255.4931004	0
259.1498764	7.95E-05
270.2703552	0.000396795
277.5060658	0.000706509
284.3997365	0.001121857
290.0643842	0.001609865
298.8268298	0.002775505
303.7751189	0.004165283
310.3017253	0.006943001
315.5845075	0.011289685
318.7210306	0.014371662
322.5012672	0.018608323
326.8933709	0.023851778
332.3736458	0.030315903
338.7421421	0.038466283
343.9211055	0.048268545
374.2896	0.08
425.1618	0.14

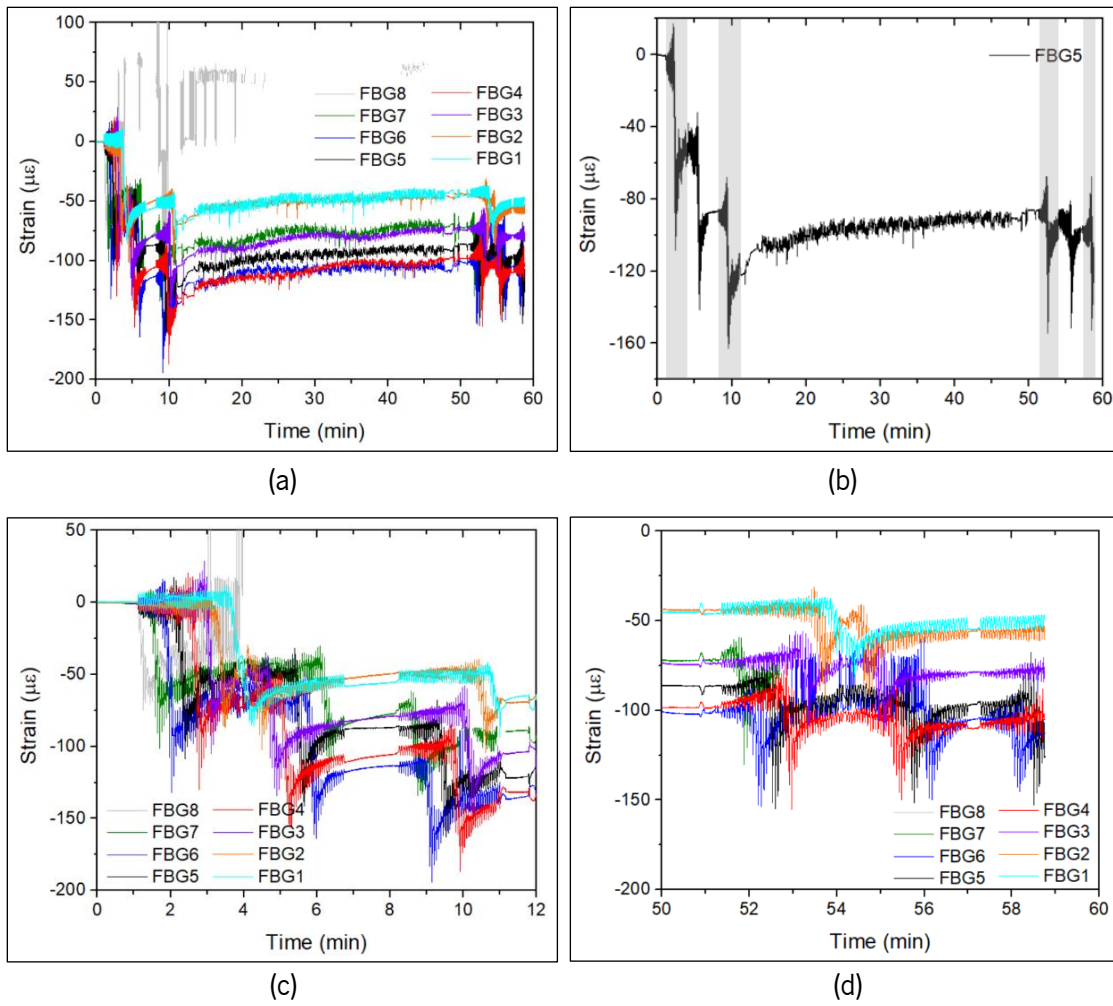


Figure A1: Strain change on a 8 FBG sensor array, during COPV winding process

A2. Materials Data Sheets

The data sheets of the following materials can be found in the next pages:

- Biresin® CR83 Composite resin system from Sika AG, Switzerland;
- Carbon fibre fabric UT350 from Toray Industries Inc, Japan, as supplied by Rebelco, Portugal;
- RCX0125 epoxy resin from RED Composites, United Kingdom;
- Tenax®-E ITS50 carbon fibre from Teijin, Japan;
- X120 strain gauge adhesive system from HBM, Germany;
- STRUCTIL EA 9394 adhesive system from Henkel, Germany;
- Loctite EA3450 adhesive system from Henkel, Germany;
- Prusament PLA filament from Prusa Polymers, Czech Republic.

Biresin® CR83 Composite resin system

Product Description

Biresin® CR83 is an epoxy resin system with extremely low viscosity designed specifically for the infusion process for the production of high performance fibre reinforced composites parts and moulds. The system has thermal properties up to 80°C. Biresin® CR83 epoxy resin has a low tendency to crystallise.

Application Areas

Biresin® CR83 is especially suited to the infusion and injection processes due to its low viscosity range. It can be used in the marine and general industrial composite areas. Due to its good wetting properties it is particularly suited for use with carbon fibre reinforcement.

Features / Advantages

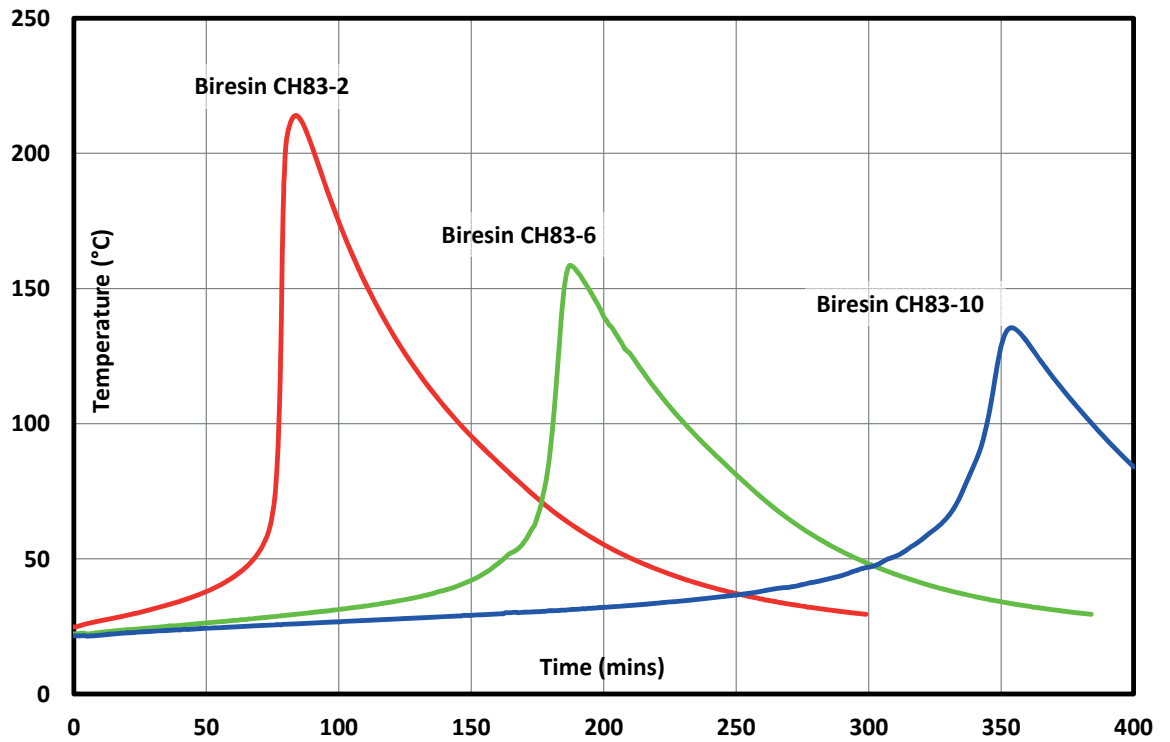
- 3 hardeners (B) give a wide range of processing times
- The reactivity can be adapted by mixing the hardeners
- Fast infusion and good wet-out of fabrics and non-wovens due to low viscosity and good wetting characteristics even at low temperatures
- All systems Germanischer Lloyd approved, Certificate No. WP 1420017 HH (attached)
- Glass transition temperatures up to 80°C dependent on curing conditions
- Carbon fibres are wet out well by all of the resin systems
- Biresin® CR83 resin (A) has a low tendency to crystallise

Physical Data	Resin (A)	Hardener (B)		
Individual Components	Biresin® CR83	Biresin® CH83-2	Biresin® CH83-6	Biresin® CH83-10
Mixing ratio, parts by weight	100	30		
Mixing ratio, parts by volume	100	36		
Colour	translucent	colourless to yellowish		
Viscosity, 25°C mPa.s	~610	<10	<10	< 10
Density, 25°C g/ml	1.14	0.95	0.94	0.95
		Mixture		
Potlife, 100 g / RT, approx. values min		60	180	300
Mixed viscosity, 25°C, approx. values mPa.s		155	170	155

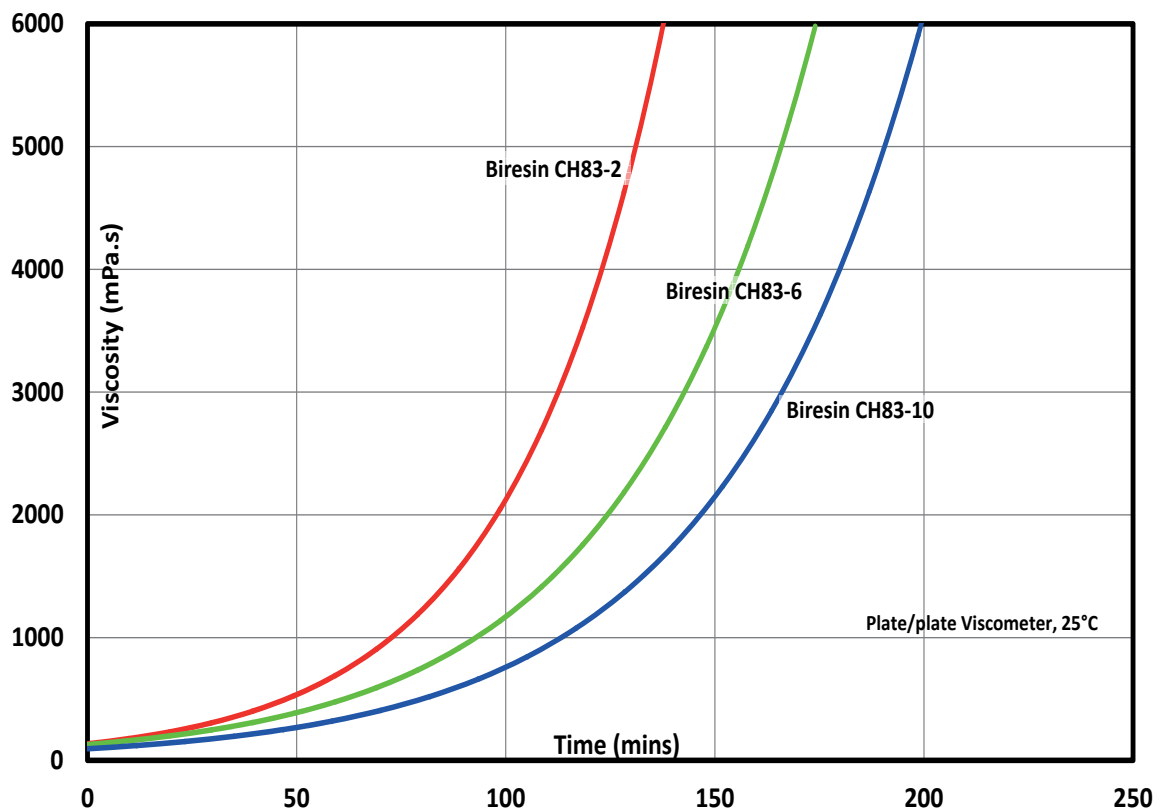
Processing

- The material and processing temperatures should be in the range 18 - 35°C.
- The mixing ratio must be followed accurately to obtain best results. Deviating from the correct mix ratio will lead to lower performance.
- The final mechanical and thermal values are dependent on the applied postcuring cycles.
- It is recommended to clean brushes or tools immediately after use with Sika Reinigungsmittel 5.
- Additional information is available in "Processing Instructions for Composite Resins".

Development of Exotherm of Biresin® CR83-Resin (A)-Hardener (B)-Mixtures, 100g / RT, insulated



Development of Viscosity of Biresin® CR83 (A)-Resin-Hardener (B)-Mixtures, 25°C



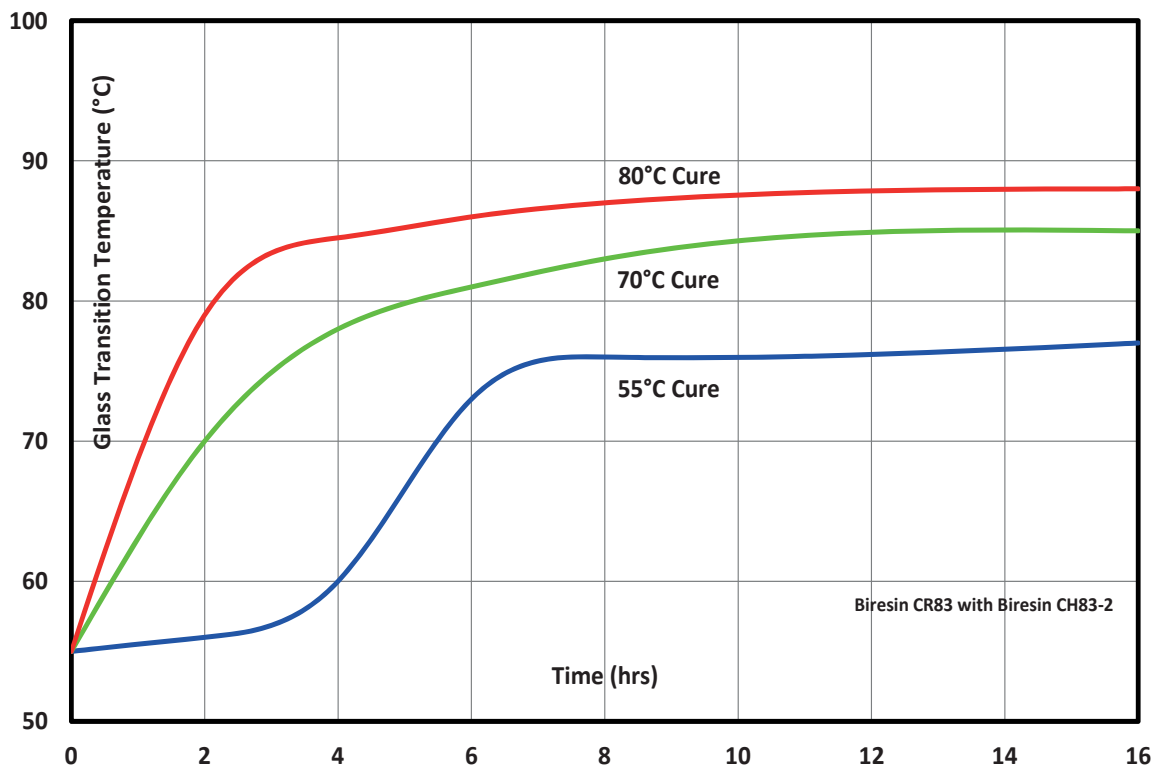
Typical Mechanical Properties of Fully Cured Neat Resin

Biresin® CR83 resin (A)	with hardener (B) Biresin®		CH83-2	CH83-6	CH83-10
Tensile strength	ISO 527	MPa	84	91	86
Tensile E-Modulus	ISO 527	MPa	2,960	3,200	3,100
Elongation at break	ISO 527	%	6.7	8.4	7.9
Flexural strength	ISO 178	MPa	129	134	131
Flexural E-Modulus	ISO 178	MPa	3,125	3,360	3,340
Compressive strength	ISO 604	N/mm ²	107	111	109
Density	ISO 1183	g/cm ³	1.15	1.15	1.15
Shore-hardness	ISO 868		D 85	D 85	D 85
Impact resistance	ISO 179	kJ/m ²	93	84	83

Typical Thermal Properties of Fully Cured Neat Resin

Biresin® CR83 resin (A)	with hardener (B) Biresin®		CH83-2	CH83-6	CH83-10
Heat distortion temperature	ISO 75B	°C	79	79	78
Glass transition temperature	ISO 11357	°C	84	80	81

Glass Transition Temperature vs. Cure Cycle



When curing a composite part, the whole of the part (including the very middle of the laminate) needs to see the cure temperature.

Packaging (net weight, kg)

Biresin® CR83 resin (A)	1,000	200	10
Biresin® CH83-2 hardener (B)		180	20
Biresin® CH83-6 hardener (B)		180	20
Biresin® CH83-10 hardener (B)		180	20

Storage

- Minimum shelf life of Biresin® CR83 resin (A) is 24 month and of Biresin® CH83-2, CH83-6 and CH83-10 hardeners (B) is 12 month under room conditions (18 - 25°C), when stored in original unopened containers.
- The tendency to crystallise with this system is very low. However, if crystallisation of the resin (A) component appears, it can be easily removed by warming up the resin for a sufficient time to at least 60°C.
- Containers must be closed tightly immediately after use. The residual material needs to be used up as soon as possible.

Health and Safety Information

For information and advice on the safe handling, storage and disposal of chemical products, users shall refer to the most recent Safety Data Sheet (SDS) containing physical, ecological, toxicological and other safety related data.

Disposal considerations

Product Recommendations: Must be disposed of in a special waste disposal unit in accordance with the corresponding regulations.

Packaging Recommendations: Completely emptied packagings can be given for recycling. Packaging that cannot be cleaned should be disposed of as product waste.

Value Bases

All technical data stated in this Product Data Sheet are based on laboratory tests. Actual measured data may vary due to circumstances beyond our control.

Legal Notice

The information, and, in particular, the recommendations relating to the application and end-use of Sika products, are given in good faith based on Sika's current knowledge and experience of the products when properly stored, handled and applied under normal conditions in accordance with Sika's recommendations. In practice, the differences in materials, substrates and actual site conditions are such that no warranty in respect of merchantability or of fitness for a particular purpose, nor any liability arising out of any legal relationship whatsoever, can be inferred either from this information, or from any written recommendations, or from any other advice offered. The user of the product must test the product's suitability for the intended application and purpose. Sika reserves the right to change the properties of its products. The proprietary rights of third parties must be observed. All orders are accepted subject to our current terms of sale and delivery. Users must always refer to the most recent issue of the local Product Data Sheet for the product concerned, copies of which will be supplied on request.

Further information available at:

Sika Deutschland GmbH

Subsidiary Bad Urach

Stuttgarter Str. 139

D - 72574 Bad Urach

Germany

Tel: +49 (0) 7125 940 492

Fax: +49 (0) 7125 940 401

Email: tooling@de.sika.com

Internet: www.sika.com



Ficha Técnica – 350 UT



350 UT

Tecido carbono Unidirecional

Características técnicas

Fibra (Teia): Fio de Carbono HS 12 K

Fibra (Trama): Fio Termoplástico 150 dtex

Peso (Total): 340 g/m² (+ 4 %)

Espessura: 0,670 mm (+ 15 %)

Fio/cm (Teia): 4,2 ± 0,3

Fio/cm (Trama): 1,5 ± 0,3

Malha: Tafetá

Os valores indicados são fornecidos com base no conhecimento actual e são apenas indicativos não podendo ser usados para elaborar qualquer especificação técnica. Para mais informações consulte os nossos serviços técnicos.

PV-GRADE Towpreg matrix RCX0125

Red Composite **PV-grade** Towpregs are a family of pre-impregnated fibre tow materials suitable for use in applications that demand a high performance, fatigue resistant resin matrix.

Typical applications include:

- Pressure Vessels
- Composite flywheels
- Defence components

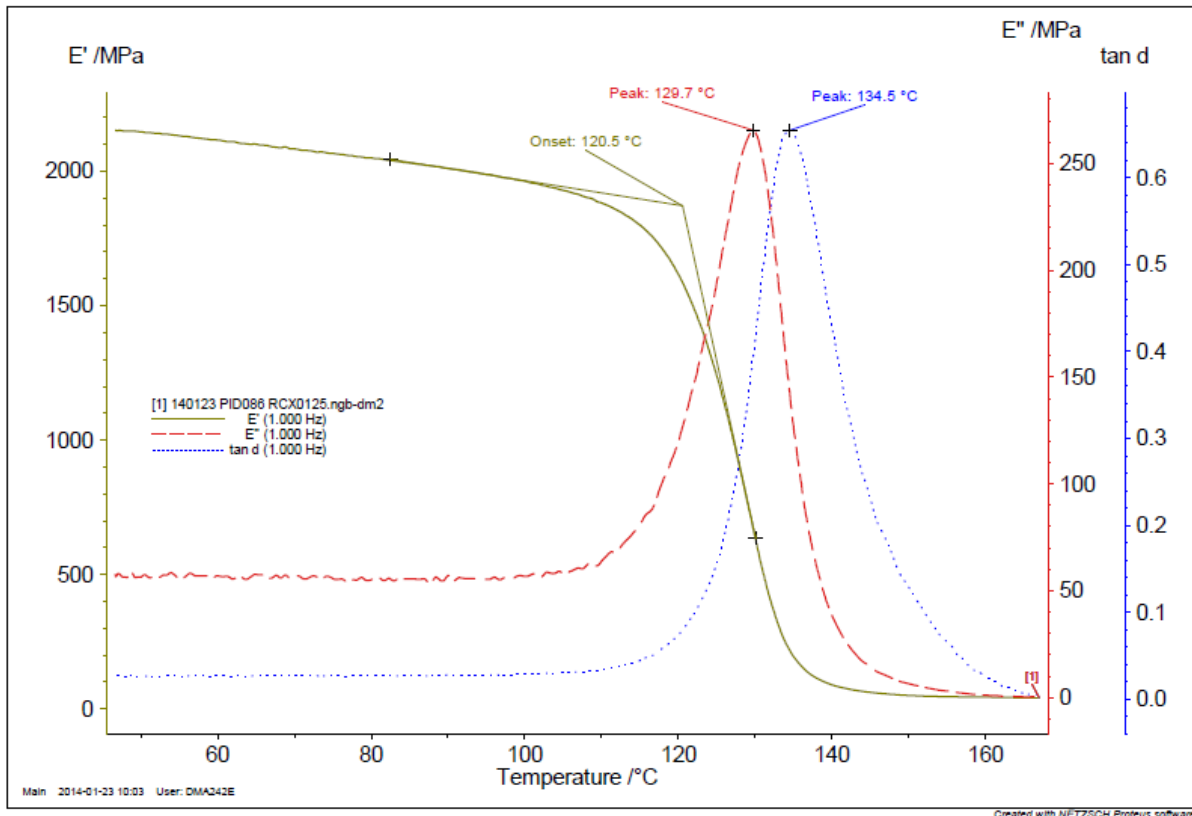
RCX0125 is an epoxy resin matrix offers high flow characteristics and robust fatigue performance. Incorporating the latest generation curing technology, the system provides highly dependable mechanical and thermal properties.

Mechanical properties

Parameter	Method	Value	Unit
Tensile strength	ISO 527-2	87.1	MPa
Tensile modulus	ISO 527-2	3.0	GPa
Tensile strain	ISO 527-2	7.2	%
Flexural strength	ISO 178	121.2	MPa
Flexural modulus	ISO 178	3.0	GPa
Flexural strain	ISO 178	12.7	%

Physical properties

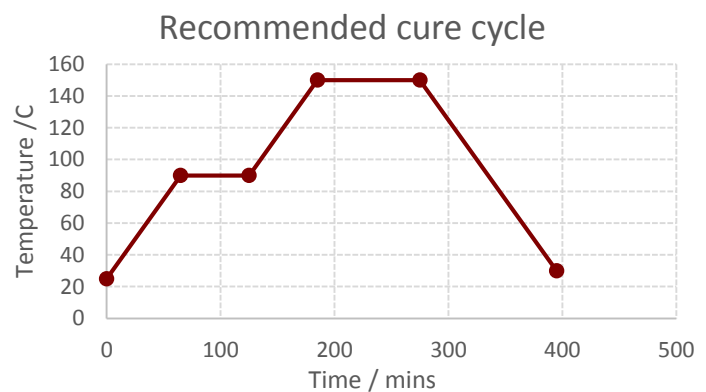
Parameter	Method	Value	Unit
Density	ISO 1183	1.20	g/cc
Tg (onset)	DMA	120.5	°C
Tg (E'' peak)	DMA	129.7	°C
Water absorption	ISO 62	Tbc	%
Tg (E'' peak) after 24 hr water boil	DMA	Tbc	°C



Suggested cure cycle

Red Composites suggest a cure cycle consisting of:

- Ramp to 90°C @ 1°C/min
- Hold @ 90°C for 60 min
- Ramp to 150°C @ 1°C/min
- Hold @ 150°C for 90 min
- Cool down



Other curing cycles may be used and it is recommended to contact Red Composites for advice, or perform state of cure testing before component manufacture begins.

Storage requirements

Red Composites PV-grade Towpreg should be stored in its original packaging in clean, dry conditions. It should be stored indoors and out of direct sunlight. Under these conditions the shelf life will be;

At ambient temperature (22°C) minimum **3 months**

In refrigerated conditions (-18°C) minimum **12 months**

If frozen, care should be taken to avoid condensation forming on the product. This is achieved by allowing to thaw thoroughly before removing the outer polythene packaging.

Product availability

Red Composites PV-grade Towpreg is offered in a wide variety of flat tow carbon, glass, aramid and other fibre types. Please contact below for details.

Contact details

Please contact Red Composites for any further details

info@redcomposites.com

www.redcomposites.com

+44 (0) 1983 241930

Values in this datasheet are typical and indicative only. They should not be used for design calculations without further validation. The data is presented in good faith, but is dependent on processing methods and conditions.

It is the responsibility of the end-user to ensure suitability of the product in final application. Red Composites take no responsibility for incorrect material selection or processing errors. Please contact Red Composites Technical Service team to discuss any application, or for assistance in identifying if this material is suitable.

Brand name	Production site	Fiber family & tensile properties	Sizing properties	Number of filaments	Nominal linear density (without sizing)	Additional information	Tensile strength [MPa]	Tensile modulus [GPa]	Elongation at break [%]	Filament diameter [µm]	Density [g/cm ³]	Sizing	Size level [%]
Tenax®-J		HTA40	E15	1K	67tex	15S	4100	240	1.7	7.0	1.77	EP	2.5
Tenax®-E		HTA40	E13	3K	200tex		4100	240	1.7	7.0	1.77	EP	1.3
Tenax®-E		HTA40	E13	3K	200tex	15Z	4100	240	1.7	7.0	1.77	EP	1.3
Tenax®-J/E		HTA40	E13	6K	400tex		4100	240	1.7	7.0	1.77	EP	1.3
Tenax®-E		HTA40	E13	6K	400tex	10Z	4100	240	1.7	7.0	1.77	EP	1.3
Tenax®-J		HTS40	E13	3K	200tex		4400	240	1.8	7.0	1.77	EP	1.3
Tenax®-J		HTS40	E13	6K	400tex		4400	240	1.8	7.0	1.77	EP	1.3
Tenax®-E		HTS40	F13	12K	800tex		4400	240	1.8	7.0	1.77	PU	1.0
Tenax®-E		HTS40	F13	12K	800tex	10Z	4400	240	1.8	7.0	1.77	PU	1.0
Tenax®-E		HTS40	F13	24K	1600tex		4400	240	1.8	7.0	1.77	PU	1.0
Tenax®-E		HTS40	F13	24K	1600tex	5Z	4400	240	1.8	7.0	1.77	PU	1.0
Tenax®-E		HTS45	E23	3K	200tex		4500	245	1.8	7.0	1.76	EP	1.2
Tenax®-E		HTS45	E23	3K	200tex	15Z	4500	245	1.8	7.0	1.76	EP	1.2
Tenax®-E		HTS45	E23	12K	800tex		4500	240	1.9	7.0	1.77	EP	1.3
Tenax®-E		HTS45	E23	12K	800tex	10Z	4500	240	1.9	7.0	1.77	EP	1.3
Tenax®-E		HTS45	P12	12K	800tex		4500	240	1.9	7.0	1.77	TP	0.5
Tenax®-E		STS40	E23	24K	1600tex		4300	250	1.7	7.0	1.78	EP	1.3
Tenax®-E		STS40	F11	24K	1600tex		4300	240	1.8	7.0	1.78	PU	0.17
Tenax®-J/E		STS40	F13	24K	1600tex		4300	240	1.8	7.0	1.78	PU	1.0
Tenax®-J/E		STS40	F13	48K	3200tex		4300	250	1.7	7.0	1.77	PU	1.0
Tenax®-J		UTS50	F13	12K	800tex		5100	245	2.1	7.0	1.78	PU	1.0
Tenax®-J		UTS50	F22	12K	800tex	S	5100	245	2.1	7.0	1.78	PU	0.8
Tenax®-J/E		UTS50	F24	24K	1600tex	DCP	5100	245	2.1	7.0	1.78	PU	2.0
Tenax®-E		ITS50	F23	24K	1600tex	D	5100	265	1.9	7.0	1.80	PU	1.0
Tenax®-E		ITS55	E23	24K	1600tex		5100	280	1.8	7.0	1.75	EP	1.2
Tenax®-J		IMS60	E13	24K	830tex		5800	290	2.0	5.0	1.79	EP	1.3
Tenax®-E		IMS65	E23	24K	830tex		6000	290	2.1	5.0	1.78	EP	1.3
Tenax®-E		IMS65	P12	24K	830tex		6000	290	2.1	5.0	1.78	TP	0.8
Tenax®-J		UMS40	F23	24K	800tex	S	4700	390	1.2	4.9	1.79	PU	1.0
Tenax®-J		UMS45	F22	12K	385tex		4600	425	1.1	4.7	1.83	PU	0.8
Tenax®-J		HTS40	A23	12K	1420tex	MC	2900	230	1.3	7.5*	2.70	PU	1.3

* inkl. 0,25 µm Nickel

- Please contact our sales team any time, for choosing the right type. The stated numbers are typical values. For design purposes please request a fiber specification.
- The export or transfer of carbon fibers can be subject to authorization, depending on end-use and final destination.

Cylindrical bobbins

		Tenax®-J		Tenax®-E
Tube length	[mm]	182	280	290
Tube internal diameter	[mm]	77	77	77
Tube weight	[g]	110	160	190
Stroke	[mm]	152	254	254

Net weight

	[kg]	0.5	1.0	2.0	4.0	6.0	8.0	10.0
External diameter	[mm]	105	120	145	180	205	225	245

(typical values)

Bobbins per packaging

		[kg]	0.5	1.0	2.0	4.0	6.0	8.0	10.0
Tenax®-J	carton	20/24	20	12	6	6	-	4	
	large packaging		-	-	-	75	60	54	

Tenax®-E	carton	-	16	11/12	6	6	3	-
	large packaging		-	150	90	69	60	-

Packaging (L x W x H)

Tenax®-J	carton	[mm]	640	x	520	x	290
	carton (4 kg)	[mm]	550	x	370	x	290
	carton (8 kg, 10 kg)	[mm]	570	x	570	x	290
	large packaging incl. palett	[mm]	1200	x	1100	x	1200

Tenax®-E	carton	[mm]	600	x	420	x	320
	large packaging incl. palett	[mm]	1000	x	1200	x	1040



X120

Adhesive

Special features

- For installing optical fibers or fiber Bragg grating based sensors


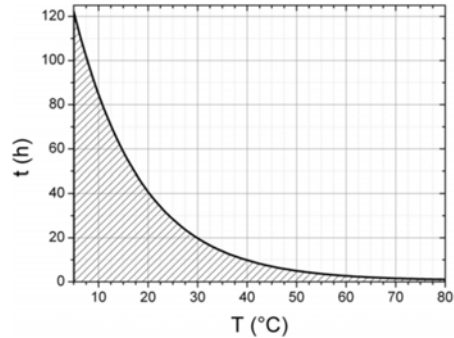
Description

The **X120** is a **bi component cold curing epoxy**, especially selected for installing **optical fibers**. It is compatible with most **fiber Bragg grating based sensors** that are to be fixed by gluing, including bare fibers. The mixture can also be used as a **protective layer** to cable paths and sensors.


The X120 is supplied in a **50 ml cartridge**, with **two mixing nozzles** and requires the usage of an **applicator** for the components mixture and application. Extra nozzles can also be ordered separately.

Benefits and applications


- Easy usage
- Excellent strain transfer

X120		Resin	Hardener	
	Material	n.a.	Epoxy resin	
	Color	n.a.	Black	
	Consistency	n.a.	Pasty	
	Viscosity ¹⁾	Pa.s	520	100
	Percentage of solids	%	100	
	Specific weight	g/cm ³	1.0	
	Mixing ration	n.a.	2	1
	Pot life ¹⁾	min	90	
	Operating temperature	°C	-55 ... 120	
	Storage temperature	n.a.	Room temperature	
	Shelf life	months	12	
	Cartridge size ²⁾	ml	50	
	Inc. mixing nozzles	un.	2	
	Curing time chart	h/°C		

Ordering information: 1-X120

Applicator			
	Cartridge size	ml	50

Ordering information: 1-APPLICATOR

Mixing nozzles			
	Units per pack	un	12

Ordering information: 1-MIXING NOZZLE

- 1) At room temperature.
- 2) For projects where high quantities of X120 is needed, bigger cartridges can be ordered. Please contact your local HBM supplier or HBM FiberSensing for a dedicated quote.

Subject to modifications.
All product descriptions are for general information only. They are not to be understood as a guarantee of quality or durability.

HBM FiberSensing S.A.
Rua Vasconcelos Costa 277 · 4470-640 Maia · Portugal
Tel. +351229613010 · Email: fibersensing@hbm.com · www.hbm.com/fs

Bringing light to measurement





LOCTITE EA 9394 AERO

Epoxy Paste Adhesive

(KNOWN AS Hysol EA 9394)

INTRODUCTION

LOCTITE EA 9394 AERO is a two-part structural paste adhesive, which cures at room temperature and possesses excellent strength to 350°F/177°C and higher. Its thixotropic nature and excellent high temperature compressive strength also make it ideal for potting, filling and liquid shim applications. LOCTITE EA 9394 AERO is qualified to MMM-A-132 Rev A, Type I, Class 3.

The mechanical properties in this data sheet are also valid for LOCTITE EA 9394S AERO. LOCTITE EA 9394S AERO is only available in Semkits and differs from LOCTITE EA 9394 AERO as it has 1 part less thixotrope in the Part B to aid packaging. All other mechanical and handling properties similar.

FEATURES

- Room Temperature Cure
- Good Gap Filling Capabilities
- 350°F/177°C Performance
- Potting Material
- Room Temperature Storage
- Outstanding Mechanical Properties
- Long Pot Life
- Low Toxicity

Uncured Properties

	<u>Part A</u>	<u>Part B</u>	<u>Mixed</u>
Color	Gray	Black	Gray
Viscosity, 77°F Brookfield, HBT	4000-8000 Poise Spdl 7 @ 20 rpm	200-700 Poise Spdl 4 @ 20 rpm	1600 Poise Spdl 5 @ 20 rpm
Viscosity, 25°C Brookfield, HBT	400-800 Pa·S Spdl 7 @ 2.09 rad/sec	20-70 Pa·S Spdl 4 @ 2.09 rad/sec	160 Pa·S Spdl 5 @ 2.09 rad/sec
Density (g/ml)	1.50	1.00	1.36
Shelf Life @ <77°F/25°C	1 year	1 year	

This material will normally be shipped at ambient conditions, which will not alter our standard warranty, provided that the material is placed into its intended storage upon receipt. Premium shipment is available upon request.



LOCTITE EA 9394 AERO

Epoxy Paste Adhesive

(KNOWN AS Hysol EA 9394)

Handling

Mixing - This product requires mixing two components together just prior to application to the parts to be bonded. Complete mixing is necessary. The temperature of the separate components prior to mixing is not critical, but should be close to room temperature (77°F/25°C).

<u>Mix Ratio</u>	<u>Part A</u>	<u>Part B</u>
By Weight	100	17

Note: Volume measurement is not recommended for structural applications unless special precautions are taken to assure proper ratios.

Pot Life (450 gram mass) 90 minutes @ 75°F/25°C
Method - ASTM D 2471 in water bath.

Application

Mixing - Combine Part A and Part B in the correct ratio and mix thoroughly. THIS IS IMPORTANT! Heat buildup during or after mixing is normal. Do not mix quantities greater than 450 grams as dangerous heat buildup can occur causing uncontrolled decomposition of the mixed adhesive. TOXIC FUMES CAN OCCUR, RESULTING IN PERSONAL INJURY. Mixing smaller quantities will minimize the heat buildup.

Applying - Bonding surfaces should be clean, dry and properly prepared. For optimum surface preparation consult the LOCTITE Surface Preparation Guide. The bonded parts should be held in contact until the adhesive is set. Handling strength for this adhesive will occur in 24 hours @ 77°F/25°C, after which the support tooling or pressure used during cure may be removed. Since full bond strength has not yet been attained, load application should be small at this time.

Dual Cartridge Application

We recommend that you do not precondition the kits, dispense adhesive at ambient temperature. If pre-heating is required for the cartridge kits, do not exceed 90°F for a maximum time of four hours.

- Do not assemble the static mixer onto the cartridge while conditioning.
 - Do not place the assembled cartridges upright in the oven.
 - Seat kit into the cartridge sleeve/tray and ensure proper placement against the gun plungers.
Misalignment during triggering of the plungers can result in kit damage.
 - Burp the adhesive at **low pressure** prior to dispensing through the static mixer.
 - Allows for both Piston, A & B sides to be equally level during initial dispensing, thus preventing an adhesive backflow.
 - It's possible that the Piston-B Side may be unlevelled with the Piston-A side due to the heating & positioning of the cartridge. The Part B resin viscosity is much lower than the Part A resin viscosity 200 ml kit failures will occur if the inlet pressure is set too high while triggering the plungers.
 - Start the plungers at **low pressure (20 psi)** then increase to the desired pressure
 - Over heating of the cartridge in an oven and then applying high pressure can result in **kit damage and/or resin blowback.**
-

LOCTITE EA 9394 AERO

Epoxy Paste Adhesive

(KNOWN AS Hysol EA 9394)

- Do not allow the adhesive to sit in the static mixer unattended for more than 90 minutes.
 - The material is curing within the static mixer and when pressure is re-applied back onto the plungers, back pressure will occur and potentially result in cartridge failure.

Failure to follow the recommended procedures stated in this TDS will void the Warranty of the Adhesive.

Note: Special precautions are recommended to minimize carbonate formation in large assemblies subject to extended open times in humid environments. A special memo is available upon request from Henkel providing users with suggestions for minimizing carbonate formation.

Curing - LOCTITE EA 9394 AERO may be cured for 3 to 5 days @ 77°F/25°C to achieve normal performance. Accelerated cures up to 200°F/93°C (for small masses only) may be used as an alternative. For example, 1 hour @ 150°F/66°C will give complete cure.

Cleanup - It is important to remove excess adhesive from the work area and application equipment before it hardens. Denatured alcohol and many common industrial solvents are suitable for removing uncured adhesive. Consult your supplier's information pertaining to the safe and proper use of solvents.

Bond Strength Performance

Tensile Lap Shear Strength - tested per ASTM D1002 after curing for 5 days @ 77°F/25°C. Adherends are 2024-T3 bare aluminum treated with phosphoric acid anodized per ASTM D3933.

<u>Test Temperature, °F/°C</u>	<u>Typical Results</u>	
	<u>psi</u>	<u>MPa</u>
-67/-55	3,300	22.7
77/ 25	4,200	28.9
180/82	3,000	20.7
200/93	2,900	20.0
250/121	2,300	15.8
300/149	1,600	11.0
350/177	1,200	8.3
400/204	600	4.1

LOCTITE EA 9394 AERO

Epoxy Paste Adhesive

(KNOWN AS Hysol EA 9394)

After Exposure to/Test Temperature

	Typical Results	
	<u>psi</u>	<u>MPa</u>
Room Temperature Control (no exposure)	4,300	29.6
77°F/25°C Water - 7 days @77°F/25°C	4,100	28.2
Isopropyl Alcohol - 7 days @77°F/25°C	4,000	27.6
Hydraulic Oil - 7 days @77°F/25°C	4,100	28.2
JP-4 Fuel - 7 days @ 77°F/25°C	4,200	28.9

Peel Strength

T-Peel strength tested per ASTM D1876 after curing for 5 days @ 77°F/25°C. Adherends are 2024-T3 AlClad aluminum treated with phosphoric acid anodized per ASTM D3933.

<u>Test Temperature, °F/°C</u>	Typical Results	
	<u>Lb/in</u>	<u>N/2 mm</u>
77/25	5	22

Bell Peel strength tested per ASTM D3167 after curing for 7 days @ 77°F/25°C. Adherends are 2024-T3 AlClad aluminum treated with phosphoric acid anodized per ASTM D3933.

<u>Test Temperature, °F/°C</u>	Typical Results	
	<u>Lb/in</u>	<u>N/25mm</u>
77/25	20	89

Service Temperature

Service temperature is defined as that temperature at which this adhesive still retains 1000 psi/6.9 MPa) using test method ASTM D1002 and is 350°F/177°C.

Bulk Resin Properties

Tensile Properties - tested using 0.125 inch/ 3.18 mm castings per ASTM D638.

Tensile Strength @ 77°F/25°C	6,675 psi	46.0 MPa
Tensile Modulus @ 77°F/25°C	615 ksi	4,237 MPa
Shear Modulus, dry @ 77°F/25°C	212 ksi	1,461 MPa
Shear Modulus, wet @ 77°F/25°C	149 ksi	1,027 MPa
Elongation at Break @77°F/25°C	1.66%	
Shore D Hardness, @ 77°F/25°C	88	
Tg dry	172°F	78°C
Tg wet	154°F	68°C

LOCTITE EA 9394 AERO

Epoxy Paste Adhesive

(KNOWN AS Hysol EA 9394)

Compressive Properties - tested with rectangular specimens 0.5 in/12.7 mm width by 1.0 in/25.4 mm length by 0.5 in/12.7 mm height per ASTM D695.

<u>Compressive Strength, °F/°C</u>	<u>psi</u>	<u>MPa</u>
77/25	10,000	68.9

Electrical Properties - tested per ASTM D149, D150.

	<u>0.1 KHz</u>	<u>1.0 KHz</u>	<u>10.0 KHz</u>
Dielectric Constant	7.72	7.51	7.20
Dissipation Factor	.017	.022	.033
Thermal Conductivity	7.92 x 10 ⁻⁴ cal/sec-cm-°C		[0.331 W/(m•K)]
Volume Resistivity	4.05 x 10 ¹³ ohm-cm		[4.05 x 10 ¹¹ ohm]
Surface Resistivity	4.60 x 10 ¹³ ohm		
Coefficient of Thermal Expansion	55.6µm/m°C @ 40°C		
	80.6µm/m°C @ 100°C		

Handling Precautions

Do not handle or use until the Material Safety Data Sheet has been read and understood.
For industrial use only.

DISPOSAL INFORMATION

Dispose of spent remover and paint residue per local, state and regional regulations. Refer to HENKEL TECHNOLOGIES MATERIAL SAFETY DATA SHEET for additional disposal information.

PRECAUTIONARY INFORMATION

General:

As with most epoxy based systems, use this product with adequate ventilation. Do not get in eyes or on skin. Avoid breathing the vapors. Wash thoroughly with soap and water after handling. Empty containers retain product residue and vapors so obey all precautions when handling empty containers.



LOCTITE EA 9394 AERO Epoxy Paste Adhesive (KNOWN AS Hysol EA 9394)

PART A

CAUTION! This material may cause eye and skin irritation or allergic dermatitis. It contains epoxy resins.

PART B

WARNING! This material causes eye and skin irritation or allergic dermatitis. It contains amines.

Before using this product refer to container label and HENKEL TECHNOLOGIES MATERIAL SAFETY DATA SHEET for additional precautionary, handling and first aid information.

Note

The data contained herein are furnished for information only and are believed to be reliable. We cannot assume responsibility for the results obtained by others over whose methods we have no control. It is the user's responsibility to determine suitability for the user's purpose of any production methods mentioned herein and to adopt such precautions as may be advisable for the protection of property and of persons against any hazards that may be involved in the handling and use thereof. In light of the foregoing, **Henkel Corporation specifically disclaims all warranties expressed or implied, including warranties of merchantability or fitness for a particular purpose, arising from sale or use of Henkel Corporation's products. Henkel Corporation specifically disclaims any liability for consequential or incidental damages of any kind, including lost profits.** The discussion herein of various processes or compositions is not to be interpreted as representation that they are free from domination of patents owned by others or as a license under any Henkel Corporation patents that may cover such processes or compositions. We recommend that each prospective user test his proposed application before repetitive use, using this data as a guide. This product may be covered by one or more United States or foreign patents or patent applications.

Rev. 9/2013

Henkel Corporation Aerospace | 2850 Willow Pass Road | Bay Point, CA 94565
PHONE: +1.925.458.8000 | FAX: +1.925.458.8030 | www.henkel.com/aerospace

Trademark usage

Except as otherwise noted, all trademarks in this document are trademarks of Henkel Corporation in the U.S. and elsewhere. ® denotes a trademark registered in the U.S. Patent and Trademark Office.

The data contained herein are furnished for information only and are believed to be reliable. We cannot assume responsibility for the results obtained by others over whose methods we have no control. It is the user's responsibility to determine suitability for the user's purpose of any production methods mentioned herein and to adopt such precautions as may be advisable for the protection of property and of persons against any hazards that may be involved in the handling and use thereof. In light of the foregoing, **Henkel Corporation specifically disclaims all warranties expressed or implied, including warranties of merchantability or fitness for a particular purpose, arising from sale or use of Henkel Corporation's products. Henkel Corporation specifically disclaims any liability for consequential or incidental damages of any kind, including lost profits.** The discussion herein of various processes or compositions is not to be interpreted as representation that they are free from domination of patents owned by others or as a license under any Henkel Corporation patents that may cover such processes or compositions. We recommend that each prospective user test his proposed application before repetitive use, using this data as a guide. This product may be covered by one or more United States or foreign patents or patent applications.



LOCTITE® EA 3450™

May 2014

PRODUCT DESCRIPTION

LOCTITE® EA 3450™ provides the following product characteristics:

Technology	Epoxy
Chemical Type (Resin)	Epoxy
Chemical Type (Hardener)	Epoxy
Appearance (Resin)	Black thixotropic paste
Appearance (Hardener)	White thick paste
Appearance (Mixture)	Metallic gray
Components	Two component - requires mixing
Mix Ratio, by volume - Resin : Hardener	1 : 1
Mix Ratio, by weight - Resin : Hardener	1 : 1
Cure	Room temperature cure after mixing
Application	Bonding

LOCTITE® EA 3450™ is a two component epoxy adhesive which cures rapidly at room temperature after mixing. It is a metal bonding adhesive which develops high strength. The gap filling properties make this adhesive system suitable for rough and poorly fitting surfaces made from metal, ceramic, rigid plastics or wood. Applications include bonding aluminum window frames and GRP panels.

TYPICAL PROPERTIES OF UNCURED MATERIAL

Resin:

Specific Gravity @ 25 °C 1.7

Casson Viscosity @ 25 °C, Pa·s Plate-plate 25

Flash Point - See SDS

Hardener:

Specific Gravity @ 25 °C 1.8

Casson Viscosity @ 25 °C, Pa·s Plate-plate 40

Flash Point - See SDS

Mixed:

Pot life @ 25 °C, 20 gram mass, ISO 9514, minutes 5

TYPICAL CURING PERFORMANCE

Fixture Time

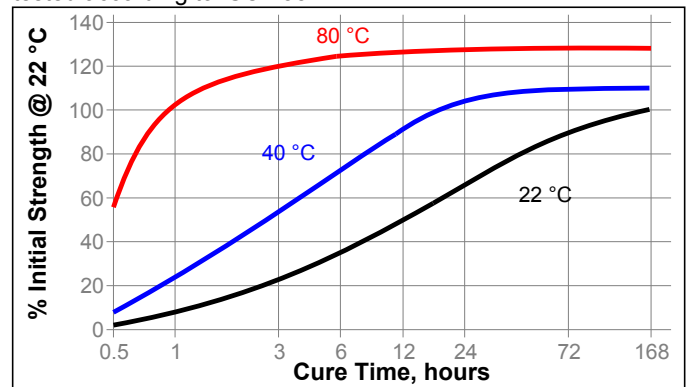
Fixture time is defined as the time to develop a shear strength of 0.1 N/mm².

Fixture Time, ISO 4587, minutes:

Steel (grit blasted) 15

Cure Speed vs. Temperature

The rate of cure will depend on the ambient temperature. The graph below shows the shear strength developed with time on grit blasted steel lap shears at different temperatures and tested according to ISO 4587.



TYPICAL PROPERTIES OF CURED MATERIAL

Physical Properties

Shore Hardness, ISO 868 68

Glass Transition Temperature, ISO 11359-2, °C 37

Coefficient of Thermal Expansion, K⁻¹:

Below Tg 53×10⁻⁰⁶

Above Tg 160×10⁻⁰⁶

TYPICAL PERFORMANCE OF CURED MATERIAL**Adhesive Properties**

After 1 week @ 22 °C

Shear Strength

Lap Shear Strength, :

Mild steel	N/mm ² 21 (psi) (3,070)
Grit Blasted Mild Steel (GBMS)	N/mm ² 25 (psi) (3,560)
Aluminum	N/mm ² 11 (psi) (1,650)
Aluminum (Gritblasted)	N/mm ² 21 (psi) (3,050)
Polycarbonate	N/mm ² 5 (psi) (740)
PVC	N/mm ² 2 (psi) (290)
Nylon	N/mm ² 3 (psi) (440)
ABS	N/mm ² 2 (psi) (280)
Wood (Beech)	N/mm ² 11 (psi) (1,610)

TYPICAL ENVIRONMENTAL RESISTANCE

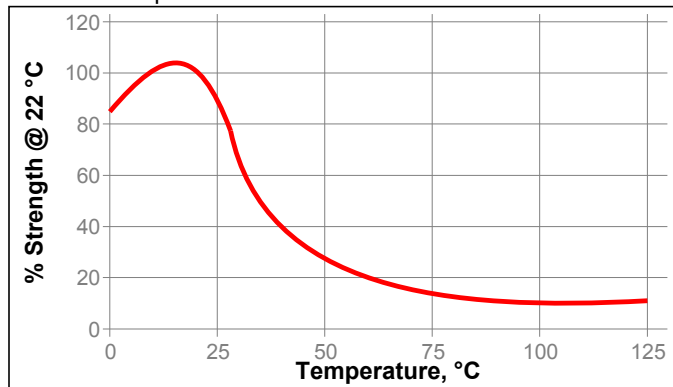
Cured for 1 week @ 22 °C

Lap Shear Strength, ISO 4587:

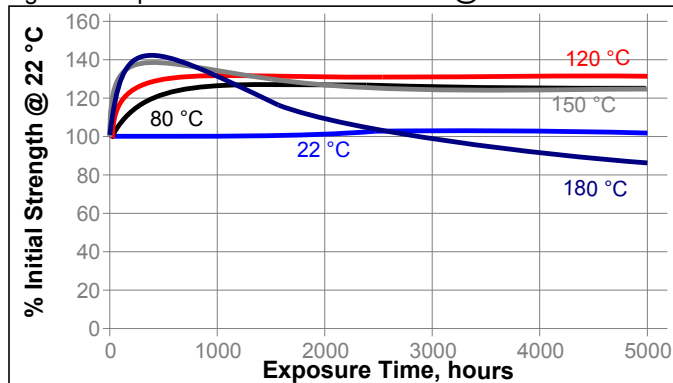
Grit Blasted Mild Steel (GBMS)

Hot Strength

Tested at temperature

**Heat Aging**

Aged at temperature indicated and tested @ 22 °C



Cured for 1 week @ 22 °C

Lap Shear Strength, ISO 4587:

Grit Blasted Mild Steel (GBMS)

Chemical/Solvent Resistance

Aged under conditions indicated and tested @ 22 °C.

Environment	°C	% of initial strength			
		100 h	1000 h	3000 h	5000 h
Motor oil	87	130	130	130	130
Unleaded gasoline	22	110	95	95	95
Water/glycol 50/50	87	40	25	20	15
Acetone	22	90	95	95	95
Isopropanol	22	105	95	95	95
Ethanol	22	95	90	90	90
Water	22	110	95	85	75
Water	60	80	40	40	40
Water	90	35	35	35	35
98% RH, 40°C	40	110	55	45	35

GENERAL INFORMATION

For safe handling information on this product, consult the Safety Data Sheet (SDS).

This product is not recommended for use in pure oxygen and/or oxygen rich systems and should not be selected as a sealant for chlorine or other strong oxidizing materials.

Directions for use:

- For best performance part surfaces should be clean and free of grease.
- For high strength structural bonds, remove surface contaminants such as paint, oxide films, oils, dust, mold release agents and all other surface contaminants.
- Dual Cartridges:** To use simply insert the cartridge into the application gun and start the plunger into the cylinders using light pressure on the trigger. Next, remove the cartridge cap and expel a small amount of adhesive to be sure both sides are flowing evenly and freely. If automatic mixing of resin and hardener is desired, attach the mixing nozzle to the end of the cartridge and begin dispensing the adhesive. For hand mixing, expel the desired amount of the adhesive and mix thoroughly. Mix for approximately 15 seconds after uniform color is obtained.
Bulk Containers: Mix thoroughly by weight or volume in the proportions specified in Product Description section. Mix vigorously, approximately 15 seconds after uniform color is obtained.
- For maximum bond strength apply adhesive evenly to both surfaces to be joined.
- Application to the substrates should be made within 20 minutes. Larger quantities and/or higher temperatures will reduce this working time.
- Join the adhesive coated surfaces and allow to cure at 25 °C for 24 hours for high strength. Heat up to 93 °C, will speed curing.
- Keep parts from moving during cure. Contact pressure is necessary. Maximum shear strength is obtained with a 0.1 to 0.2 mm bond line.

8. Excess uncured adhesive can be wiped away with organic solvent (e.g. Acetone).
9. After use and before adhesive hardens mixing and dispensing equipment should be cleaned with hot soapy water.

Not for product specifications

The technical data contained herein are intended as reference only. Please contact your local quality department for assistance and recommendations on specifications for this product.

Storage

Store product in the unopened container in a dry location. Storage information may be indicated on the product container labeling.

Optimal Storage: 8 °C to 21 °C. Storage below 8 °C or greater than 28 °C can adversely affect product properties.

Material removed from containers may be contaminated during use. Do not return product to the original container. Henkel Corporation cannot assume responsibility for product which has been contaminated or stored under conditions other than those previously indicated. If additional information is required, please contact your local Technical Service Center or Customer Service Representative.

Conversions

$(^{\circ}\text{C} \times 1.8) + 32 = ^{\circ}\text{F}$
 $\text{kV/mm} \times 25.4 = \text{V/mil}$
 $\text{mm} / 25.4 = \text{inches}$
 $\mu\text{m} / 25.4 = \text{mil}$
 $\text{N} \times 0.225 = \text{lb}$
 $\text{N/mm} \times 5.71 = \text{lb/in}$
 $\text{N/mm}^2 \times 145 = \text{psi}$
 $\text{MPa} \times 145 = \text{psi}$
 $\text{N}\cdot\text{m} \times 8.851 = \text{lb}\cdot\text{in}$
 $\text{N}\cdot\text{m} \times 0.738 = \text{lb}\cdot\text{ft}$
 $\text{N}\cdot\text{mm} \times 0.142 = \text{oz}\cdot\text{in}$
 $\text{mPa}\cdot\text{s} = \text{cP}$

Note:

The information provided in this Technical Data Sheet (TDS) including the recommendations for use and application of the product are based on our knowledge and experience of the product as at the date of this TDS. The product can have a variety of different applications as well as differing application and working conditions in your environment that are beyond our control. Henkel is, therefore, not liable for the suitability of our product for the production processes and conditions in respect of which you use them, as well as the intended applications and results. We strongly recommend that you carry out your own prior trials to confirm such suitability of our product.

Any liability in respect of the information in the Technical Data Sheet or any other written or oral recommendation(s) regarding the concerned product is excluded, except if otherwise explicitly agreed and except in relation to death or personal injury caused by our negligence and any liability under any applicable mandatory product liability law.

In case products are delivered by Henkel Belgium NV, Henkel Electronic Materials NV, Henkel Nederland BV, Henkel Technologies France SAS and Henkel France SA please additionally note the following:

In case Henkel would be nevertheless held liable, on whatever legal ground, Henkel's liability will in no event exceed the amount of the concerned delivery.

In case products are delivered by Henkel Colombiana, S.A.S. the following disclaimer is applicable:

The information provided in this Technical Data Sheet (TDS) including the recommendations for use and application of the product are based on our knowledge and experience of the product as at the date of this TDS. Henkel is, therefore, not liable for the suitability of our product for the production processes and conditions in respect of which you use them, as well as the intended applications and results. We strongly recommend that you carry out your own prior trials to confirm such suitability of our product.

Any liability in respect of the information in the Technical Data Sheet or any other written or oral recommendation(s) regarding the concerned product is excluded, except if otherwise explicitly agreed and except in relation to death or personal injury caused by our negligence and any liability under any applicable mandatory product liability law.

In case products are delivered by Henkel Corporation, Resin Technology Group, Inc., or Henkel Canada Corporation, the following disclaimer is applicable:

The data contained herein are furnished for information only and are believed to be reliable. We cannot assume responsibility for the results obtained by others over whose methods we have no control. It is the user's responsibility to determine suitability for the user's purpose of any production methods mentioned herein and to adopt such precautions as may be advisable for the protection of property and of persons against any hazards that may be involved in the handling and use thereof. In light of the foregoing, **Henkel Corporation specifically disclaims all warranties expressed or implied, including warranties of merchantability or fitness for a particular purpose, arising from sale or use of Henkel Corporation's products. Henkel Corporation specifically disclaims any liability for consequential or incidental damages of any kind, including lost profits.** The discussion herein of various processes or compositions is not to be interpreted as representation that they are free from domination of patents owned by others or as a license under any Henkel Corporation patents that may cover such processes or compositions. We recommend that each prospective user test his proposed application before repetitive use, using this data as a guide. This product may be covered by one or more United States or foreign patents or patent applications.

Trademark usage

Except as otherwise noted, all trademarks in this document are trademarks of Henkel Corporation in the U.S. and elsewhere. ® denotes a trademark registered in the U.S. Patent and Trademark Office.

Reference 0.0

Version: 1.1
Last update: 16-02-2022

Technical datasheet

Prusament PLA by Prusa Polymers



Identification

Trade Name	Prusament PLA/PLA (Blend)
Chemical Name	Polylactic Acid
Usage	FDM/FFF 3D printing
Diameter	1.75 ± 0.02 mm (± 0.03 mm for PLA Blend)
Manufacturer	Prusa Polymers a.s., Prague, Czech Republic

Recommended print settings

Nozzle Temperature [°C]	210 ± 10
Heatbed Temperature [°C]	40-60
Print Speed [mm/s]	up to 200
Cooling Fan Speed [%]	100
Bed Type	smooth PEI sheet; powder coated sheet; satin sheet
Additional Info	The brim is not necessary in general.

Typical material properties

	Typical Value	Method
MFR [g/10 min](1)	9-11	ISO 1133
MVR [cm ³ /10 min](1)	8-10	ISO 1133
Density [g/cm ³]	1.24	ISO 1183
Moisture Absorption in 24 hours [%](2)	0.13	Prusa Polymers
Moisture Absorption in 7 days [%](2)	0.19	Prusa Polymers
Heat Deflection Temperature (0.45 MPa) [°C]	55	ISO 75
Heat Deflection Temperature (1.80 MPa) [°C]	55	ISO 75
Tensile Yield Strength for Filament [MPa]	57 ± 1	ISO 527
Hardness - Shore D	81	Prusa Polymers
Interlayer Adhesion [MPa]	17 ± 3	Prusa Polymers

(1) 2.16 kg; 210 °C

(2) 24 °C; humidity 22 %

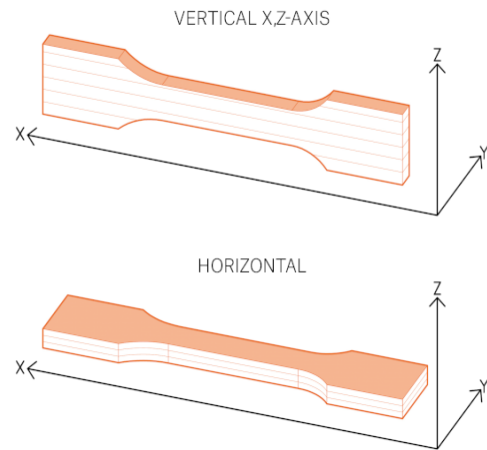
Mechanical properties of 3D printed testing specimens(3)

Property\Print Direction	Horizontal	Vertical xz	Method
Tensile Yield Strength [MPa]	51 ± 3	59 ± 2	ISO 527-1
Tensile Modulus [GPa]	2.3 ± 0.1	2.4 ± 0.1	ISO 527-1
Elongation at Yield Point [%]	2.9 ± 0.3	3.2 ± 1.0	ISO 527-1
Flexural Strength [MPa]	83 ± 6	99 ± 1	ISO 178
Flexural Modulus [GPa]	3.1 ± 0.1	3.2 ± 0.1	ISO 178
Deflection at Flexural Strength [mm]	7.4 ± 0.2	8.3 ± 0.2	ISO 178
Impact Strength Charpy [kJ/m ²](4)	13 ± 1	14 ± 1	ISO 179-1
Impact Strength Charpy Notched [kJ/m ²]	not applicable	not applicable	ISO 179-1

(3) Original Prusa i3 MK3 3D printer was used to print testing specimens. Slic3r Prusa Edition 1.40.0 was used to create G-code following settings:

Prusament PLA Filament;
Print Settings 0.20 mm FAST (layers 0.20 mm);
Solid Layers Top: 0, Bottom: 0;
Perimeters: 2;
Infill 100% rectilinear;
Infill Print Speed 200 mm/s;
Nozzle Temperature 215 °C all layers;
Bed Temperature 60 °C all layers;
Other parameters are set as default.

(4) Charpy Unnotched – Edgewise direction of blow according to ISO 179-1



Disclaimer:

The results presented in this data sheet are just for your information and comparison. Values are significantly dependent on print settings, operator experiences, and surrounding conditions. Everyone has to consider suitability and possible consequences of printed parts usage. Prusa Polymers can not carry any responsibility for injuries or any loss caused by using Prusa Polymers material. Before using Prusa Polymers material read properly all the details in the available safety data sheet (SDS).